Collective Spin-Oscillators for Light-Atom Interfaces

Applications as an on-demand single-photon source and for quantum-enhanced sensing

PhD Thesis

Rebecca Schmieg

This thesis has been submitted to the PhD School of The Faculty of Science, University of Copenhagen

QUANTOP
Center for Quantum Optics
Niels Bohr Institute
Faculty of Science
University of Copenhagen
Copenhagen, Denmark
February 2023

Academic Supervisor:	Prof. Eugene S. Polzik
External referees:	Prof. Dmitry Budker Prof. Morgan Mitchell
Thesis submitted:	February 27th, 2023
Disputation:	April 12th, 2023

Abstract

Light-atom interfaces have been of fundamental interest due to their varied applications as magnetometers, atomic clocks, and as fundamental building blocks for quantum communication and cryptography. Especially room-temperature atomic ensembles have drawn much interest as they offer experimental simplicity while not relying on cryogenic cooling. These practical advantages make room-temperature atomic ensembles a promising candidate and experimental platform within the field of quantum optics in terms of potential scalability. This thesis focuses on two applications of room-temperature atomic ensembles: on-demand single-photon generation and storage, as well as quantum-enhanced sensing. Both applications exploit the atomic ensembles' collective spin state.

This thesis covers our on-demand room-temperature single-photon source with built-in memory exploiting a herald-retrieve scheme. We observe a conditional auto-correlation as low as $g^{(2)}_{\mathrm{RR}\,|\,\mathrm{W}=1} = 0.20 \pm 0.07$ verifying the single-photon character of our source. Further, high cross-correlations of $g^{(2)}_{\mathrm{WR}} = 10 \pm 1$ between the heralding and retrieval light fields confirm the success of our protocol, indicating highly non-classical correlations between the heralding and retrieval scattered photons. The herald-retrieve scattered photons maintain non-classical correlations for a duration of 0.68 ± 0.08 ms.

The second application covered in this thesis is quantum-enhanced magnetic induction tomography (QMIT). We introduce the technique of stroboscopic back-action evasion along with conditional spin-squeezing to the well-known technique of magnetic induction tomography. We test this new quantum-enhanced measurement protocol in a proof-of-principle experiment. We verify the quantum enhancement by observing 42 % lower quantum noise exploiting conditional spin-squeezing of $\xi^2 = (-1.8 \pm 0.1)$ dB between unconditional and conditional measurement, corresponding to a signal-to-noise improvement from 0.72 to 1.2.

Sammenfatning

Interaktioner imellem lys og atomer har været af fundamental interesse på grundet af deres forskellige anvendelsmuligheder som magnetometre, atomurer, som grundlæggende byggesten til kvantekommunikation og kvantekryptografi. Stuetemperatur atomare ensembler har særlig interesse, da de tilbyder eksperimentel enkelhed, mens de ikke er afhængige af kryogen køling. Disse praktiske fordele gør stuetemperatur atomare ensembler til en prominent kandidat og eksperimentel platform inden for kvanteoptik med hensyn til den potentielle skalerbarhed. Den her afhandling er fokuseret på to anvendelser af stuetemperatur atomare ensembler. Den første er en klik enkeltfotonkilde og hukommelse. Den anden er kvanteforbedret måling. Begge applikationer udnytter atomernes kollektive spin-tilstand som kvantisering.

Denne afhandling dækker vores klik stuetemperatur enkeltfotonkilde med indbygget hukommelse, der udnytter et advarsels-modtagelses-protokol. Vi observerer en betinget autokorrelation så lav som $g^{(2)}_{\mathrm{RR}\,|\,\mathrm{W}=1} = 0.20 \pm 0.07$, hvilket verificerer enkeltfoton-karakteren af vores kilde. Yderligere bekræfter høje krydskorrelationer af $g^{(2)}_{\mathrm{WR}} = 10 \pm 1$ mellem advarsels og modtagelses succesen af vores protokol, hvilket indikerer høj ikke-klassiske korrelationer mellem advarelse og modtagelse af spredte fotoner. Advarelses fotoner opretholder ikke-klassiske korrelationer i en varighed på 0.68 ± 0.08 ms.

Det andet emne dækket i denne afhandling er kvanteforstærket magnetisk induktionstomografi (quantum-enhanced magnetic induction tomography – QMIT). Vi introducerer teknikken til stroboskopisk backaction annullering sammen med betinget spin-squeezing til den velkendte teknik af magnetisk induktionstomografi. Vi tester denne nye kvantum-forbedrede måleprotokol med et bevis for eksperimental potentiale. Vi verificerer kvanteforbedringen ved at observere 42 % lavere kvantestøj ved at udnytte betinget spin-squeezing på $\xi^2 = (-1.8 \pm 0.1)$ dB mellem ubetinget og betinget måling. Dette svarer til en signal-til-støj forbedring fra 0.72 til 1.2.

Zusammenfassung

Licht-Atom-Schnittstellen sind aufgrund ihrer vielfältigen Anwendungen als Magnetometer, Atomuhren und als grundlegende Bausteine für Quantenkommunikation und Quantenkryptographie von herausragendem Interesse. Besonders Raumtemperatur-Atomkollektive haben ein besonders großen Forschungsdrang hervorgerufen. Dieser liegt daring begründet, dass sie experimentell einfacher in der Handhabung sind, da auf kryogene Temperaturen in den Experimenten verzichtet werden kann. Diese praktischen Vorteile machen Raumtemperatur-Atomkollektive zu einem vielversprechenden Kandidaten und einer praktischen Ressource auf dem Gebiet der Quantenoptik, vor allem im Hinblick auf die potenzielle Skalierbarkeit der Versuchsaufbauten. Diese Dissertation konzentriert sich auf zwei Beispielen der Anwendung von Raumtemperatur-Atomkollektiven: die Einphotonenerzeugung auf Knopfdruck, basierend auf der Speicherung eben jener Photonen in Form einer kollektiven Erregung, sowie die Möglichkeit zur quantenmechanisch verbesserten Messpräzision. Beide Anwendungen nutzen den gemeinsamen Spinzustand des Atomkollektivs für das jeweilige experimentelle Protokoll aus.

Das erste Thema dieser Dissertation befasst sich mit unserer Raumtemperatur-basierten, auf Abruf operierenden Einphotonenquelle mit eingebautem Speicher. Diese basiert auf einem Verkünder-Abruf-Schema. Wir beobachten eine konditionierte Autokorrelation mit einem Wert von $g^{(2)}_{\mathrm{RR\,|\,W=1}} = 0.20 \pm 0.07$. Dies bestätigt den Einphotonencharakter unserer Quelle. Darüber hinaus bestätigt eine hohe Kreuzkorrelationen von $g^{(2)}_{\mathrm{WR}} = 10 \pm 1$ zwischen den verkündenden und gewonnenen Einphotonenlichtfeldern den Erfolg unseres Protokolls, was auf starke, nicht-klassische Korrelationen zwischen den ankündigenden und gewonnenen gestreuten Photonen hinweist. Die nicht-klassischen Korrelationen zwischen den Verkünder- und Abgerufe-nen-Photonen werden für eine Dauer von 0.68 ± 0.08 ms beibehalten.

Die zweite in dieser Arbeit behandelte Anwendung ist die quantenverstärkte magnetische Induktionstomographie (QMIT). Wir führen die Technik der stroboskopischen Umgehung der Rückwirkung, zusammen mit konditionierten, gequetschten Spinzuständen, in die bekannte Technik der magnetischen Induktionstomographie ein. Wir testen dieses neue quantenerweiterte Messprotokoll in einem Experiment zum Beweis des Prinzips durch. Wir

verifizieren die Quantenverbesserung, indem wir ein um 42 % niedrigeres Quantenrauschen beobachten. Dies wird durch Ausnutzen von gequetschten Spinzuständen mit einem Wert von $\xi^2 = (-1.8 \pm 0.1)$ dB möglich. Durch die gequetschten Spinzustände ist es möglich, zwischen nicht konditionierten und konditionierten Messungen eine Signal-Rausch-Verbesserung von 0.72 auf 1.2 zu erreichen.

List of Publications

Peer-reviewed articles:

Authors marked with * contributed equally.

Karsten B. Dideriksen*, Rebecca Schmieg*, Michael Zugenmaier* and Eugene S. Polzik:
Room-temperature single-photon source with near-millisecond built-in memory,
Nature Communications (2021) 12:36

Michael Zugenmaier, Rebecca Schmieg, Karsten B. Dideriksen and Eugene S. Polzik:
Single-Photon Source with Near-Millisecond Memory based on Room-Temperature Atomic Vapour,
2021 Conference on Lasers and Electro-Optics Europe & European Quantum Electronics Conference (CLEO/Europe-EQEC) (2021)

Articles in preparation:

Authors marked with * contributed equally.

Wenqiang Zheng*, Hengyan Wang*, Rebecca Schmieg*, Alan Oesterle and Eugene S. Polzik:
Entanglement-enhanced magnetic induction tomography
Manuscript submitted. Preprint available here: arXiv:2209.01920.

Conference contributions:

Rebecca Schmieg, Wenqiang Zheng, Hengyan Wang, Alan Oesterle and Eugene S. Polzik:
Quantum enhanced conductivity measurement with room-temperature RF magnetometer
Quantum sensing with hot vapors - macQsimal symposium June 2022 (contributed talk)

Rebecca Schmieg, Karsten B. Dideriksen, Michael Zugenmaier and Eugene S. Polzik:
Room-temperature single-photon source with built-in memory
CLEO/Europe-EQEC 2021
(contributed talk)

Rebecca Schmieg, Karsten B. Dideriksen, Michael Zugenmaier and Eugene S. Polzik:
Single-Photon source with built-in memory
Hot Vapor Workshop - Stuttgart 2021
(contributed talk)

Rebecca Schmieg, Karsten B. Dideriksen, Michael Zugenmaier and Eugene S. Polzik:
Observation of non-classical photon pairs from room-temperature atomic ensembles
YAO 2019 - Hamburg 2019
(contributed poster)

List of Abbreviations

While there is no fundamental reason to use abbreviations in a written thesis, sometimes it is still convenient for a smoother flow of the text to use them. While some of the abbreviations are fairly common, others might not be or can be ambiguous due to different meanings in different contexts. For this reason, the following list covers the abbreviations used in this thesis.

AM	Atomic magnetometer
AOM	Acousto-optic modulator
APD	Avalanche photo detector
AR	Anti-reflection (coating)
CSS	Coherent spin state
DLCZ	Duan-Lukin-Cirac-Zoller (quantum repeater protocol)
DOE	Diffractive optical element
EOM	Electro-optic modulator
FID	Free induction decay
FWHM	Full width at half maximum
GWD	Gravitational wave detection
HWHM	Half width at half maximum
HWP	Half waveplate
LIA	Lock-in amplifier
MIT	Magnetic induction tomography
MORS	Magneto-optical resonance spectroscopy
MOT	Magneto-optical trap
MZI	Mach-Zehnder-Interferometer
NBI	Niels Bohr Institute
PBS	Polarizing beam splitter
PGF	Probability generating function
pMORS	Pulsed magneto-optical resonance spectroscopy
PN	Projection noise
PSD	Power spectral density
QBA	Quantum back-action
QMIT	Quantum-enhanced magnetic induction tomography
QND	Quantum non-demolition
QWP	Quarter waveplate

RF	Radio-frequency (field)
SN	Shot noise
SNU	Shot noise units
SPDC	Spontaneous parametric downconversion
SQL	Standard quantum limit
TBS	Tophat beam shaper
TH	Tophat
TN	Thermal noise
TSS	Thermal spin state
VCA	Voltage controlled attenuator
VCO	Voltage controlled oscillator

Preface

Already during my project outside the course scope and the consecutive master's project, I knew that doing a PhD in Quantop would be an exciting challenge I wanted to take on. Fortunately for me, I was given the opportunity. Here, I express my gratitude towards Prof. Eugene S. Polzik for giving me this opportunity to pursue my wish to dive deep into experimental quantum optics, all his support, challenging me at times, and providing guidance and criticism. I would also thank him for his trust and all the responsibilities he trusted me with.

Given the complexity of our experiments, guidance and experimental and theoretical insight from experienced people was needed. Two people that always strove to help me solve problems were Jörg H. Müller and Jean-Baptiste Beguin. For the QMIT experiment, former group member Kasper Jensen provided valuable input allowing us to push the experiment to where it is. A few months of intermission from my usual research were due to vapor cell testing and the visit of Mikhail Balabas at Quantop. I am impressed by the skill and the resulting vapor cells, and I am thankful for all the thorough discussions and explanations relating to the coating and manufacturing of these vapor cells.

During all my time at Quantop, I was part of the "cell lab". First, by being part of the single-photon experiment. I got to continue my work from my master's project alongside two dedicated and devoted people who always made me happy about coming to the lab and showed much patience when I started. Karsten B. Dideriksen and Michael Zugenmaier, I am very grateful to have had you as fellow lab mates. I am very thankful that you welcomed me to your team and for the collaborative and supportive atmosphere in the lab. The long nights (and days) spent counting single-photons were less tedious with you as teammates. I really enjoyed the time in and out of the lab with you!
The second experiment I joined was the quantum-enhanced MIT. Wenqiang Zheng and Hengyan Wang, it was always a pleasure working with you. Also, the time spent together outside the lab. I am impressed by your commitment and passion, pushing the experiment to its goal! You both have been great collaborators, your support extending beyond your time at Quantop. Thanks for letting me join you and introducing me to the subtleties of the experiment and the many interesting discussions.

During my PhD, multiple students who contributed to the experiments joined our cell lab. I want to thank you for all your work. It was a pleasure working with you: Jeppe Detlefsen, as a master's student and research assistant; master students Alan Oesterle (QMIT) and Isaac R. Caritg (Tophat Implementation); Project student Veronika Kaminski (Subset of spin noise measurements). To all of you, thank you for all your help and for keeping me on my toes with your questions!

I was fortunate to visit Warsaw University during my external stay, despite the difficulties arising from the Corona pandemic. Thanks for letting me see beyond room-temperature atomic ensembles by joining your lab for a while, Wojciech Wasilewski and Michal Parniak. I enjoyed my time there very much.

In Quantop, but also the whole of the QO-section, many people made the experience of this PhD a pleasure by going out for drinks to Søerne's, doing fun activities, biking together, or just sharing and listening. Many of you contributed significantly to making the past few years a great adventure – at and outside of Quantop. Moreover, thanks go to everyone who read a chapter or two and gave me valuable feedback. Christian, Emil, Karsten, Michael, and Rodrigo: thank you for your helpful input and raising questions! Also, Jacob and Christian, thank you for proofing my attempt in writing a Danish abstract. And Ivan, I am grateful for your positive spirit and the joint support of each other while we both had to write our thesis. And Anna, I really enjoyed having a writing buddy going through the same process as me and our sessions via skype helped me stay motivated along the way.

I want to thank my parents, Susanne and Werner, for all their support, whom I could always count on despite my choice to move to another country. Also, my brother Tobias and grandmother Uta deserve special thanks. They always motivated me to push myself further alongside many other extended family members who cheered me on along the way. I want to thank some of my year-long friends. By now, you are more like family. Your support helped me through all of this! You believed in me, even when I doubted myself. Thank you Veronika, Kithi, Sandra, Ronja, Isabelle, Anna, Alex, Matze, Weikai and Jan!

About this work - Thesis structure

This thesis covers our efforts on the DLCZ-type single-photon source and the quantum-enhanced MIT experiment during the time of my PhD program. While both experiments are somewhat different in their operation principle and goals, the common feature is cesium vapor cells containing macroscopic spin-ensembles.

A significant part of my PhD program was spent on improving the DLCZ-type single-photon experiment I had already joined during my master's project. Key to our experimental approach is that we exploit a two-step herald-retrieve scheme. It allows retrieval of single-photons on-demand after initially

loading the source, the heralding step. After the heralding step, the readout of the single-photon can be delayed due to the source's intrinsic memory.

Quantum sensing and quantum metrology have emerged as significant fields exploiting quantum mechanical effects to improve beyond sensitivities attainable by classical means. During my time at Quantop, I was fortunate enough to join an experiment that combined two well-established techniques – spin-squeezing and magnetic induction tomography (MIT) – as a new protocol exploiting quantum mechanical effects for a quantum-enhanced MIT.

This thesis is structured into four main parts and an additional part for the supplements. In **part I**, we present an overview of the relevant theoretical background for both experiments covered in this thesis. It focuses on the relevant descriptions required for the general light-atom interaction relevant to both experiments (chapter 2). It then proceeds to introduce specifics for the quantum-enhanced MIT (chapter 3) and DLCZ-type experiment (chapter 4), respectively. General experimental techniques are introduced in **part II**. This part is rather broad and has applications for the experiments presented throughout this thesis and beyond. It contains information about optical pumping and our lasers (chapter 5) and techniques for the atomic state characterization (chapter 6). This part also contains a summary of the cell testing endeavors (chapter 7) and presents the techniques required to quantify the performance of vapor cells. **Part III** focuses on the DLCZ-type on-demand single-photon source with built-in memory. It will give an overview of the experimental setup (chapter 9) and covers and elaborates on the results presented in our paper Dideriksen et al. (2021) (chapter 10). Further, it contains an overview of our efforts to investigate experimental limitations and possible improvements (chapter 11). **Part IV** covers the quantum-enhanced MIT experiment. Similar to before, the experimental setup is introduced first (chapter 13). We then discuss the back-action evasion and spin-squeezing implementation and optimization (chapter 14). Finally, we will present the proof-of-principle experiment of quantum-enhanced MIT measurements (chapter 15). Both topics have been covered in our publication Zheng et al. (2022). We discuss the current limitations and possible ways to address them in the future (chapter 16). The central part of this thesis concludes with a summary of the whole thesis (chapter 17). This thesis contains supplementary information in **part V** with additional practical descriptions for internal knowledge transfer. Further, we provide the references used within this thesis.

As a personal note, I tried to provide all relevant information for all experiments presented throughout this thesis. However, since the DLCZ-type experiment has been shown in other theses before, I chose to refrain from showing all details and instead provide recommendations where specifics can be found if I deemed the information not fundamental for the general understanding of this thesis. For the quantum-enhanced MIT, I provided more details to consider it a practical manual for future students at Quantop since this does not exist for this experiment yet. Therefore, I present the experimental optimization and specifics more thoroughly for the QMIT experiment than for

the DLCZ-type experiment.

Many figures illustrating the experimental setups throughout this thesis are made using a vector graphics library for optical components and electronics. It is available as ComponentLibrary by Alexander Franzen, licensed under a Creative Commons Attribution-NonCommercial 3.0 Unported License.

Contents

Part I

Theoretical overview

Chapter 1

Introduction

1.1 Spin-ensemble experiments at Quantop

This thesis will consider two somewhat different applications of atomic spin ensemble-based experiments. One experiment employs the collective spin state of the ensemble – collective spin-oscillator – to store and retrieve collective excitations of the ensemble to generate a single-photon on demand. In contrast, the other experiment employs collective spins to detect the presence of a conductive object. Exploiting spin ensembles with various applications in mind has a long tradition at Quantop. Throughout the years, many protocols have been proposed and implemented at Quantop. For example, Hammerer et al. (2005) proposed a teleportation scheme between light and atoms and spin-squeezing. The underlying description provided for the latter will prove helpful throughout this thesis. Sherson et al. (2006) proposed arbitrary light state storage and retrieval based on Faraday interaction using an atomic ensemble. While the two previous papers were more of theoretical nature, their relevance to our group makes them essential to the vapor cell-based experiments at Quantop. Apart from the efforts towards ensemble-based sources of the DLCZ-type (e.g., Borregaard et al. (2016); Zugenmaier et al. (2018); Dideriksen et al. (2021)), cavity-enhanced non-degenerate parametric down-conversion has been successfully investigated at Quantop as well by Neergaard-Nielsen et al. (2007).

Within our group, efforts toward sensing magnetic fields have been pursued in various ways. Quantum noise limited sensitivity and entanglement-assisted magnetometry has been shown in Wasilewski et al. (2010). Detrimental back-action noise in the system is evaded by combining two oppositely oriented atomic ensembles. Exploiting two-mode squeezed states generated using two spatially separated cells, entangled continuous-variable states could be stored on the millisecond level in Jensen et al. (2011). Efforts in the cell lab of Quantop continued pursuing two vapor-cell configurations and were used to show deterministic quantum teleportation between two spatially separated atomic objects in Krauter et al. (2013). A different approach of back-action evasion not requiring a two-cell setup is the stroboscopic back-action

evasion measurement for squeezed-state generation of a spin-oscillator inside a cavity as pursued by Vasilakis et al. (2015). This approach will be introduced more thoroughly later in chapter 3 since it will be a crucial component of our quantum-enhanced magnetic induction tomography (QMIT).

Then, efforts on a room-temperature single-photon source and magnetic field sensing continued in parallel at Quantop. On the one hand, non-invasive detection of nerve impulses (Jensen et al. (2016)) and magnetocardiography of isolated animal hearts (Jensen et al. (2018)), culminating in the detection of low-conductivity saltwater phantoms using magnetic induction tomography (MIT) (Jensen et al. (2019)), was pursuit. Following in these footsteps, our quantum-enhanced MIT experiment tries to combine different ingredients from Jensen et al. (2016) and Vasilakis et al. (2015). Our results have led to the manuscript Zheng et al. (2022), available as a pre-print at the time of this thesis, which will be one of the main topics presented in this thesis. On the other hand, efforts toward implementing a deterministic single-photon source with built-in memory continued. Motional averaging[1] – a property that will prove vital for successful write-in and retrieval of collective excitations – together with some initial proof-of-concept measurements has been presented in Borregaard et al. (2016). Non-classical correlations between write and read scattered photons from a room-temperature spin-oscillator were successfully implemented in Zugenmaier et al. (2018). However, the single-photon character of the retrieval light field could not be shown due to detrimental four-wave mixing processes limiting the overall performance of the scheme. The necessary changes and efforts leading us to achieve an on-demand single-photon source with built-in memory of the DLCZ-type are the second central part of this thesis. Our efforts have led to the publication Dideriksen (2021), which we will discuss in-depth in this thesis.

In the consecutive sections, we will introduce key concepts such as single-photon sources (section 1.2), quantum memories (section 1.3), long-distance entanglement generation (section 1.4), and quantum sensing (section 1.5), before diving into the required theoretical descriptions starting from chapter 2 onward.

1.2 Single-photon sources

Single-photon sources are a fundamental building block for many applications of quantum information protocols. Many quantum communication schemes (section 1.4) rely on the efficient and high-fidelity generation of single-photons. Generally, one can distinguish two very different types of single-photon sources – probabilistic and deterministic. A probabilistic source relies, as the name suggests, on probabilistic processes. They create single-photons with a finite probability but can also create multiple photons due to their probabilistic nature. With a finite likelihood of multiple photons being generated, probabilistic sources are often operated such that they create a vacuum state most of the time. Examples of probabilistic sources are based on spontaneous

[1] Motional averaging is the term that we use to describe that for long interaction times between light and atoms, the atomic motion and the inhomogeneous interaction is averaging out. It will be introduced and discussed thoroughly in chapter 4.

parametric downconversion or spontaneous four-wave mixing. In both approaches, photon pairs are generated with low probability, where one of the photons is used to herald the existence of the other photon. For example, a single-photon source based on a non-degenerate parametric downconversion process is presented in Neergaard-Nielsen et al. (2007). On the other hand, deterministic single-photon sources deliver one – and only one – photon at a time.

In this thesis, we are interested in a deterministic single-photon source, particularly for applications in quantum communication. A popular choice of system for these types of sources has been solid-state[2] based. These solid-state-based single-photon sources have been implemented, for example, in rare-earth-ion-doped crystals (Kutluer et al. (2017); Laplane et al. (2017)), quantum dots embedded in a micropillar (Ding et al. (2016)) or using a planar nanobeam waveguide (Kiršanske et al. (2017)), or also exploiting color centers (Wan et al. (2020)). Many of these previously mentioned deterministic single-photon sources require cryogenic temperatures to operate successfully. While solid-state systems have been shown to allow for a combination of high single-photon extraction efficiency, single-photon purity, and single-photon indistinguishably (Ding et al. (2016)), the cryogenic cooling adds to their experimental complexity and potential scalability. Another popular choice of platform for generating single-photons has been ultracold atoms. While ultracold atoms do not require cryogenic temperatures, the cooling apparatus in the form of magneto-optical traps (MOTs) or the like is often experimentally challenging in itself. For example, this system of choice has been pursued in Corzo et al. (2019), coupling a register of atoms trapped along a waveguide. On-demand retrieval of single-photons from a cold atomic memory has also been shown by exploiting cavity enhancement (Bimbard et al. (2014); Mücke et al. (2013)), where the latter exploits a single atom. It has also been shown successfully that combining a cold atomic memory with telecom-wavelength conversion is possible (Radnaev et al. (2010)).

Compared to ultracold and cryogenic experiments, room-temperature systems have attracted much interest given their more straightforward experimental setup avoiding the necessity of a sophisticated cooling apparatus. For example, on-demand single-photon generation has been shown in room-temperature systems exploiting Rydberg blockades and giant Rydberg atoms (Ripka et al. (2018)). Other examples of room-temperature single-photon sources have been shown with atomic vapors using ladder schemes (Finkelstein et al. (2018); Kaczmarek et al. (2018)), bi-photon generation (Shu et al. (2016)) or EIT (Eisaman et al. (2005)). Many of the preceding single-photon sources already incorporate an atomic memory through the physical system used within itself. The natural compatibility with atomic memories makes atomic single-photon sources good candidates as fundamental building blocks in quantum repeater protocols, such as, for example, proposed in Duan et al. (2001).

[2] For the interested reader, a review of a variety of solid-state single-photon emitters can be found in Aharonovich et al. (2016).

1.3 Quantum memory

Quantum memories are another critical building block for quantum computation and communication applications. In principle, a quantum memory facilitates the means to store a quantum state in a quantum system and retrieve it at a later point in time. For quantum computation, maintaining and storing a state can allow for quantum error correction protocols (Brown et al., 2016), for example, discussed in Shor (1996), Steane (1996), and Lidar and Brun (2013).

We will see throughout this thesis that single-photon sources used in quantum communication protocols are of particular interest in combination with means of storing and retrieving single-photons efficiently. It is easy to imagine interfacing a single-photon source with a dedicated quantum memory, as, for example, done in Pang et al. (2020) or Makino et al. (2016). From an experimental point of view, intrinsic generation and storage capabilities are favorable as they reduce issues with compatibility between the systems and the experimental complexity arising thereof. Memories of photonic qubits have evolved along two main paths, optically controlled memories and engineered absorption (Heshami et al. (2016)), where our DLCZ-type of source and memory falls into the former category.

For room-temperature atomic systems, the intrinsic atomic motion is one of the main challenges of retrieving a single-photon on demand from a quantum memory. A fundamental problem here is efficiently addressing and retrieving a single excitation as a single-photon. Not only efficiency but also spurious noise photons contaminating the memory output are detrimental to the retrieval from the memory and the fidelity of the retrieved single-photon (Heshami et al. (2016)). One way to overcome atomic motion is using buffer gas, which effectively slows down or even prevents atomic motion. Considering only single-photon level storage, Dou et al. (2018) successfully implemented single-photon storage using buffer gas vapor cells, observing a few microseconds of memory time.

While we focus here on single-photon memories, it should be noted that a remarkable achievement for storing coherent light pulses in a room-temperature – or at elevated temperatures exceeding room-temperature – system has been achieved in Katz and Firstenberg (2018). The authors showed a memory time of up to one second. The same group has also shown hour-long coherence times exploiting strong coupling of alkali-metal spins to noble-gas nuclear spins (Shaham et al. (2022)). These pose other attractive candidates for future applications as a quantum memory for quantum-repeater protocols if compatibility with single-photon storage and retrieval can be shown. The potential application of the latter system as a quantum memory for single-photons has also been addressed in Katz et al. (2022).

1.4 Long-distance entanglement generation

Quantum communication exploits intrinsic properties of the quantum nature of, for example, photonic qubits. One well-known protocol is the BB84 protocol, a protocol for quantum key distribution, which was already proposed in 1984 by Bennett and Brassard (1984). It relies on two independent, non-orthogonal measurement bases. The intrinsic security of the protocol arises from encoding the information in the non-orthogonal states protected by the non-cloning theorem.

Another example is the Ekert protocol (Ekert (1991)), which relies on two fully entangled qubits, i.e., in the Bell states. If using photons, we, for example, could choose to exploit the polarization states of light exploiting horizontal ($|\mathrm{H}\rangle$) and vertical ($|\mathrm{V}\rangle$) polarization. In this case, the four Bell states[3] would be:

$$|\Psi^{\pm}\rangle = \frac{1}{\sqrt{2}}\left(|\mathrm{H}\rangle_1 |\mathrm{V}\rangle_2 \pm |\mathrm{V}\rangle_1 |\mathrm{H}\rangle_2\right) \tag{1.1}$$

$$|\Phi^{\pm}\rangle = \frac{1}{\sqrt{2}}\left(|\mathrm{H}\rangle_1 |\mathrm{H}\rangle_2 \pm |\mathrm{V}\rangle_1 |\mathrm{V}\rangle_2\right) \tag{1.2}$$

The two photonic qubits have to be generated reliably in one of the four Bell states, for example, $|\Psi^{-}\rangle$, and distributed between the two (spatially separated) locations, A and B. However, sending photonic qubits over long distances through a fiber will limit the efficiency of any protocol simply due to the losses associated with fibers. Typically, the error probability (losses and fidelity) scales exponentially with the length of the channel (Briegel et al. (1998)). Losses are a general problem for quantum communication protocols relying on entanglement.

Amplification, in analogy to classical signals using repeaters, is not an option due to the non-cloning theorem (Wootters and Zurek (1982); Dieks (1982); Sangouard et al. (2011)). Therefore, overcoming limitations on long-distance entanglement distribution is necessary for quantum networks and communication exploiting entanglement-based quantum key distribution. One way of remedying this is to exploit entanglement in itself for something that has come to be known as *quantum repeater* by dividing a larger distance into smaller links. First, entanglement is created on these smaller links. Consecutive entanglement swapping between the smaller links creates entanglement over a more considerable distance. This idea stems from Briegel et al. (1998), proposing a nested protocol with purification and auxiliary connection points. The protocol by Briegel et al. (1998) induced the development of more proposals focusing on implementing and realizing quantum repeaters using different physical systems. One example is the DLCZ protocol (Duan et al. (2001)), exploiting atomic ensembles and linear optics for realizing quantum repeaters for long-distance entanglement generation. We will introduce the protocol and discuss the underlying physics in chapter 4. Based on the DLCZ protocol, more sophisticated proposals have emerged, for example, Jiang et al. (2007) or Chen et al. (2007). All these protocols have induced various kinds of

[3] A thorough discussion of the implications of such entangled states and their generation is covered in chapter 9 of the book *Introductory Quantum Optics* by Gerry and Knight (2004).

experimental implementations. A more thorough review that considers different implementations of quantum repeaters and schemes can be found in Sangouard et al. (2011).

1.5 Quantum metrology and quantum-enhanced sensing

The field of metrology deals with sensing and measurement sensitivity. Metrology is ultimately the reason why we have standardized units and the like, thus a rather fundamental science with an enormous impact. Many institutes worldwide are working and offering services ensuring proper calibration and standardization of measurements and measurement devices, such as NIST[4] or – for our Danish friends – Danmarks Nationale Metrologiinstitut[5] (DFM). Due to the relevance of standardized measurements, nearly every country has its national metrology institute.

Apart from classical metrology, many efforts went into going beyond the standard quantum limits (SQL) of measurement sensitivity. These are fundamental measurement limits arising from the Heisenberg uncertainty principle that classical means cannot overcome. Therefore, quantum metrology has emerged as a field of interest. By exploiting quantum mechanical effects, standard quantum limits can be overcome. While the Heisenberg uncertainty principle is a fundamental limit set by laws of nature about the combined measurement uncertainty of the observables of two non-commuting operators, it is possible to reduce the uncertainty in one of the two observables at the expense of the uncertainty associated with the other. One way of achieving this is, for example, a stroboscopic back-action evading measurement, which we will introduce later in chapter 3.

Quantum-enhanced sensing beyond the standard quantum limit of measurement sensitivity is still challenging in many areas. However, many proposals and experimental reports have harnessed quantum enhancement to improve the attainable measurement sensitivities, sometimes beyond the SQL. Entanglement between the trapped ions in a two-dimensional crystal has improved the sensitivity to electric field displacements below the respective SQL in Gilmore et al. (2021). Another field within quantum metrology where quantum enhancement has been proposed is atomic clocks, for example, by entangling multiple lattice clocks (Derevianko and Katori (2011); Weinstein et al. (2010)). In Nichol et al. (2022), entanglement over a macroscopic distance between two atomic clocks has been shown. The authors observed a reduction in the measurement uncertainty as predicted by the Heisenberg limit. The authors of Appel et al. (2009) exploited entanglement to beat the SQL present in atomic interferometry.

Another field where quantum enhancement was proposed is gravitational wave detection, for example, in Caves et al. (1980). Nearly 40 years later, Tse et al. (2019) reported quantum-enhanced detection of gravitational waves. Atomic magnetometry has also been an active field of interest in exploiting quantum resources to enhance measurement sensitivity. For example, Sewell

[4] National Institute of Standards and Technology, a government institution of the US. I can only recommend that interested readers check out their online resources and publications. They are really doing impressive things. Web page: `https://www.nist.gov/`

[5] While DFM is a Danish institution, they also have good online resources available in English. Our institute - NBI - also has scientific collaborations with them. `https://dfm.dk/en/`

et al. (2012) exploited spin-squeezing and entanglement in a cold rubidium cloud to improve the measurement sensitivity. Quantum-noise limited sensitivity has also been reported in Wasilewski et al. (2010). All this motivates that spin-squeezing and back-action evasion can also benefit magnetic induction tomography of conductive objects beyond the classical results presented in Jensen et al. (2019) and beat the standard quantum limit. Therefore, introducing a quantum enhancement to the existing technique of magnetic induction tomography is one of the two main experimental results presented throughout this thesis.

Chapter 2

Describing light and spin oscillator interactions

We deal throughout this thesis with the interaction between macroscopic ensembles of atomic spins and laser pulses. Here, we use cesium atoms as our atomic ensemble. We will start this chapter with a general description of the cesium atom and its properties. To describe the interaction of light and atoms, a common language is needed to describe light and atoms and their quantum mechanical properties. We will introduce canonical operators capable of describing light fields (section 2.2) and atomic ensembles (section 2.3). Having a shared language for both systems, we can describe the interaction between light and atoms (section 2.4). This chapter is just an overview; sometimes, we will not provide the derivations to reach certain expressions. There are plenty of resources available that provide more rigorous derivations and descriptions. Throughout this chapter, and this thesis, we will point to the relevant resources as guidance for the readers. As a general recommendation for this chapter, the following publications from Quantop are considered relevant for readers unfamiliar with the topic: Julsgaard (2003), Hammerer et al. (2010) or also Krauter (2011). External and even more fundamental resources can be found in Gerry and Knight (2004); Foot (2005); Auzinsh et al. (2010).

2.1 The cesium atom

In Quantop, we are mainly dealing with room-temperature cesium atomic vapors. While cesium has many different isotopes, cesium-133 is the only stable one. Commonly, it is denoted as ^{133}Cs. ^{133}Cs is a common choice in experimental quantum optics due to its uncomplicated level structure arising from its alkali metal properties originating from a single valence electron. Other alkalis that are used within atomic physics experiments are Rubidium (Rb), for example, Dąbrowski et al. (2016), or Strontium (Sr), for example, Schäffer et al. (2020). The properties of alkali atomic ensembles have led to many interesting research fields, including atomic clocks, gravitational wave detection beyond the standard quantum limit (Khalili and Polzik (2018)), quantum communica-

tion, and more. In the following, we will briefly introduce the electronic level structure of cesium resembling that of hydrogen and the effects of magnetic fields on the level structure.

The valence electron in ^{133}Cs occupies the $6S_{1/2}$ orbital in its ground state and has an electron spin of $S = 1/2$. The nuclear spin of ^{133}Cs is given by $I = 7/2$. The interaction between electron and nuclear spin gives rise to a hyperfine splitting, introducing a hyperfine structure to the ground state determined as $\mathbf{F} = \mathbf{I} \pm \mathbf{J} = \mathbf{I} \pm \mathbf{S}$. Here, J refers to the total electron angular momentum (Steck, 2019). With an orbital angular momentum quantum number of $L = 0$ for the ground state of cesium, the hyperfine splitting gives rise to two hyperfine levels described by the total atomic angular momentum $F = \{3, 4\}$[1]. In all experiments presented in this thesis, we are only concerned with transitions between the ground-state Zeeman levels to the first excited state levels of ^{133}Cs, the $6P$ orbital with $L = 1$. The $6P$ orbital is split into two distinct excited states due to the spin-orbit coupling as $J = L \pm S = \{1/2, 3/2\}$. The first excited states of alkali atoms are commonly referred to as D_1 and D_2 lines. The D_1 line is the transition from $6S_{1/2} \rightarrow 6P_{1/2}$ at $\lambda = 894.6\,\text{nm}$, while the D_2 line refers to the transition from $6S_{1/2} \rightarrow 6P_{3/2}$ at $\lambda = 852.3\,\text{nm}$. Figure 2.1 shows the resulting level structure.

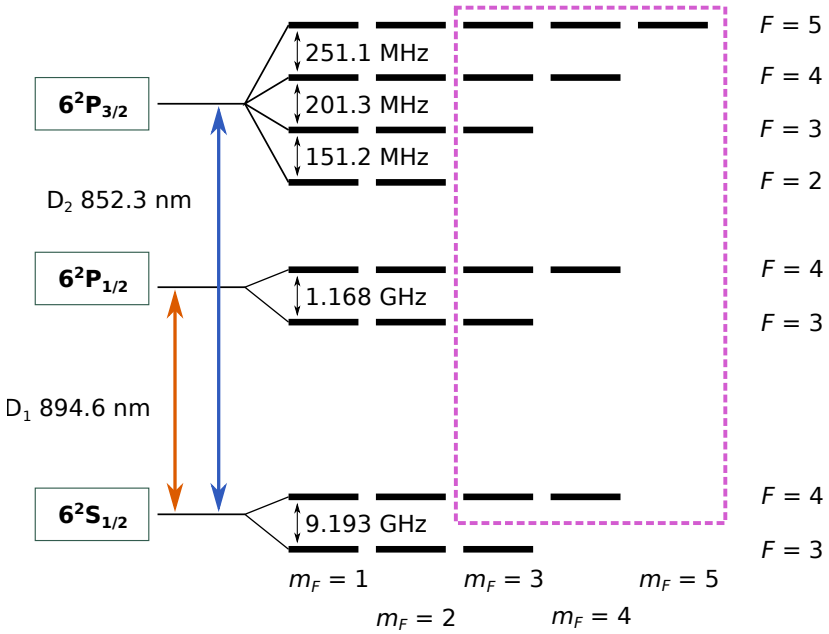

Figure 2.1: Level structure of cesium. Shown is the level structure of cesium with the first two excited states, including hyperfine levels. For simplicity, only a subset of Zeeman levels is indicated. The purple box marks the most appropriate Zeeman levels for the experiments presented in this thesis (idea adapted from Dideriksen (2021)). The numbers for the energetic splittings are taken from Steck (2019)

[1] A thorough introduction into atomic physics describing the origin of the hyperfine structure can be found in Foot (2005). A summary of ^{133}Cs data can be found in Steck (2019).

Similar to the ground state, the first excited state levels exhibit a hyperfine

structure. For $6P_{1/2}$, the hyperfine numbers are $F' = \{3, 4\}$, where the prime denotes that we refer to an excited level. For the other excited level, $6P_{3/2}$, the hyperfine structure splits into four hyperfine levels with $F' = \{2, 3, 4, 5\}$.

When applying a magnetic field, each hyperfine level splits further into $2F + 1$ Zeeman levels, denoted by $m_F = \{-|F|, -|F| + 1, ..., |F|\}$. They reflect the projection onto the quantization axis of the total atomic angular momentum (Steck, 2019). We refer to the hyperfine levels as manifolds. The degeneracy of the levels is only lifted when subjected to a magnetic field (illustrated in figure 2.2). The energy difference between Zeeman levels depends on the applied magnetic field strength and can be described using the Breit-Rabi formula (Steck (2019)):

$$E_{F,m_F} = \frac{-\Delta E_{\text{hfs}}}{2\,(2I+1)} + g_I \mu_B m_F B \pm \frac{\Delta E_{\text{hfs}}}{2}\left(1 + \frac{4 m_F x}{2I+1} + x^2\right)^{1/2} \tag{2.1}$$

where $\Delta E_{\text{hfs}} = h\nu_{\text{hfs}}$ is the hyperfine splitting, μ_B is the Bohr magneton, $B = |\mathbf{B}|$ is the magnetic field strength and g_I is the nuclear g-factor. The $\pm$ is used depending on the orientation of electronic and nuclear spin to each other $F = I \pm S$. In equation (2.1), the x is given by (Steck (2019)):

$$x = \frac{(g_J - g_I)\,\mu_B B}{\Delta E_{\text{hfs}}} \tag{2.2}$$

with g_J and g_I as the Landé factors for the total electron angular and the total nuclear angular momentum.

In our experiments, we operate in the weak-field regime, in which the square root in (2.1) can be expanded around $x = 0$. For small magnetic fields $\vec{B}$, the energy difference between two neighboring m_F levels is linear in B, while a quadratic part has to be taken into account for increasing magnetic field strengths. The higher the magnetic field, the more terms in the expansion would need to be considered. Throughout this thesis, we remain in a magnetic field regime where an expansion to the second order is sufficient. The linear energetic splitting can be expressed in terms of frequency, the Larmor precession frequency ν_L. The quadratic splitting leads to nonlinear splitting across the Zeeman levels that we exploit to resolve the different levels in the magneto-optical resonance spectra (section 6.2). The quadratic splitting can also be related to frequency. In the following, we denote the quadratic splitting as ν_{QZ}. In Julsgaard et al. (2004), the Larmor frequency ν_L and the quadratic splitting ν_{QZ} are derived to be:

$$\nu_L = \frac{g_F \mu_B B}{h} \tag{2.3}$$

$$\nu_{QZ} = \frac{2\nu_L^2}{\nu_{\text{hfs}}} \tag{2.4}$$

Here, g_F is the hyperfine Landé factor[2] and takes the value for the two mani-

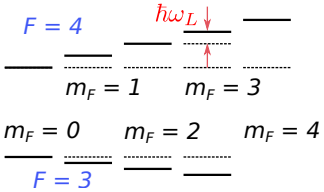

Figure 2.2: Zeeman level splitting. In the presence of a magnetic field, the degeneracy of the Zeeman levels is lifted. The energetic splitting is linear for low magnetic field strengths and can be expressed with the Larmor frequency $h\nu_L = \hbar\omega_L$. Only a subset of m_F levels is shown. Dashed levels indicate Zeeman levels in the absence of a magnetic field.

[2] An overview of the different Landé factors and their underlying expressions can be found in Steck (2019).

folds as follows:

$$g_F(F=4) \approx \quad 0.2504 \tag{2.5}$$
$$g_F(F=3) \approx -0.2512 \tag{2.6}$$

The sign difference indicates that the energetic splitting due to the Zeeman effect (increase or decrease) is behaving oppositely for the two ground state manifolds.

All these properties make cesium a good choice for using it in atomic physics experiments. The popularity across different research fields has driven the development of commercially available lasers and optics fitting the wavelengths of the D_1 and D_2 lines of cesium.

2.2 Light

Before introducing the light-atom interaction, we want to describe and discuss light and its polarization representation using Stokes operators. Both the total number of photons and the polarization of the photons are of relevance. To describe these properties, we introduce the four Stokes operators with the choice of light propagating along the z-axis:

$$\hat{S}_x = \frac{1}{2}\left(\hat{n}_x - \hat{n}_y\right) \tag{2.7a}$$
$$\hat{S}_y = \frac{1}{2}\left(\hat{n}_{+45^\circ} - \hat{n}_{-45^\circ}\right) \tag{2.7b}$$
$$\hat{S}_z = \frac{1}{2}\left(\hat{n}_{\sigma_+} - \hat{n}_{\sigma_-}\right) \tag{2.7c}$$
$$\hat{S}_0 = \frac{1}{2}\left(\hat{n}_{\sigma_+} + \hat{n}_{\sigma_-}\right) \tag{2.7d}$$

Here, the first three Stokes operators[3] describe three different orthogonal bases for the polarization of photons. The polarization bases are linear polarization comprised of horizontal and vertical polarization (x, y-direction), the diagonal ($\pm 45^\circ$-direction), and the circular basis ($\sigma_\pm$ polarized). The fourth Stokes operator $\hat{S}_0$ counts the total number of photons[4]. It should be noted that we use, for brevity, in this and the following sections $\hbar = 1$.

We will see later in this thesis how the different Stokes operators can be measured. It should be noted that there are different definitions of these operators. Without explicit time dependence, the Stokes operators count photons within a fixed time duration T and are dimensionless. Following Sherson (2006), it can be shown that by introducing explicit time and space dependency, the Stokes operators can count photons per unit length or per unit time, depending on their precise definition. They are connected according to $\hat{S}_i(t) = c\hat{S}_i(z,t)$, where $\hat{S}_i(z,t)$ has the units 1/length such that multiplying with the speed of light c converts it into units of 1/time. This will become relevant later when working with the effective interaction Hamiltonian in section

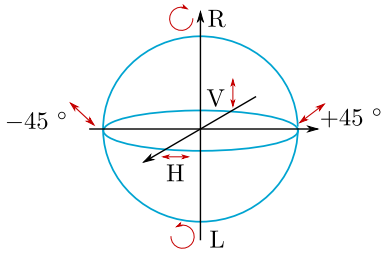

Figure 2.3: Poincaré sphere. Illustration of polarization states for the Stokes operators. On the surface, light is said to be polarized, while inside the sphere, the light is partially polarized. The origin of the Poincaré sphere signifies unpolarized light.

[3] For a thorough introduction including visualization of quantum fluctuations on Stokes operators, one can consider Schnabel et al. (2003).

[4] The number operator $\hat{n}_i$ is defined via the creation and annihilation operators:

$$\hat{n}_i = \hat{a}_i^\dagger \hat{a}_i$$

For more information about the origin of this notation, the book "Introductory Quantum Optics" by Gerry and Knight (2004) might be considered.

2.4, as well as when dealing with the input-output relations in section 3.1. For now, it will be sufficient to proceed without explicit dependencies, as the expressions can easily be extended following the appendices in Julsgaard (2003). The Stokes operators obey the angular momentum commutation relations:

$$\left[\hat{S}_i, \hat{S}_j\right] = \mathrm{i}\epsilon_{ijk}\hat{S}_k \tag{2.8}$$

where we use the Levi-Civita symbol representing the different permutations of x, y, z.

Common to our experiments is that we choose our light propagation direction along the z-axis. Especially for this thesis's second experiment, the probe light polarization choice is essential and selected to be along x. Using a highly linearly polarized beam, $\hat{S}_x$ approaches the classical value $\sqrt{\langle \hat{S}_x \rangle} = \sqrt{S_x}$ [5]. This allows us to define canonical light operators in analogy to a harmonic oscillator[6]:

$$\hat{x}_L = \frac{\hat{S}_y}{\sqrt{S_x}}, \quad \hat{p}_L = \frac{\hat{S}_z}{\sqrt{S_x}}, \quad \Rightarrow \quad [\hat{x}_L, \hat{p}_L] = \mathrm{i} \tag{2.9}$$

as follows from equation (2.8). In our experiments, we rely on polarization homodyne detection of our light fields, as it allows us to detect the effects of Faraday interaction between light and atoms, discussed later on. Atoms exposed to a magnetic field exhibit a precession of the atomic spins with the Larmor frequency. As we will see later, the interaction of light and atoms leads to a sideband modulation of the light field, with sidebands at the atomic Larmor frequency $\pm\nu_\mathrm{L}$ compared to the frequency of the probe light frequency. The relevant signal of our quantum fields is hence encoded in these sidebands. It is therefore instructive to describe our light fields in sine and cosine components oscillating at the Larmor frequency $\omega_\mathrm{L} = 2\pi \cdot \nu_\mathrm{L}$ (see chapter 2.1) when detecting them using photodetectors in a polarization homodyne detection scheme as (Hammerer et al. (2010)):

$$\hat{x}^c_\mathrm{L} = \sqrt{\frac{2}{T}} \int \mathrm{d}t \hat{x}_\mathrm{L}(t) \cos(\omega_\mathrm{L} t) \tag{2.10a}$$

$$\hat{x}^s_\mathrm{L} = \sqrt{\frac{2}{T}} \int \mathrm{d}t \hat{x}_\mathrm{L}(t) \sin(\omega_\mathrm{L} t) \tag{2.10b}$$

$$\hat{p}^c_\mathrm{L} = \sqrt{\frac{2}{T}} \int \mathrm{d}t \hat{p}_\mathrm{L}(t) \cos(\omega_\mathrm{L} t) \tag{2.10c}$$

$$\hat{p}^s_\mathrm{L} = \sqrt{\frac{2}{T}} \int \mathrm{d}t \hat{p}_\mathrm{L}(t) \sin(\omega_\mathrm{L} t) \tag{2.10d}$$

where we indicate the sine and cosine components using the superscripts s, c, while the subscript L again indicates that we refer to light. T is the duration of the light pulse and hence determines the measurement length. These newly introduced operators follow the canonical commutation relation for the measurement durations much longer than periods of the Larmor precession, see Hammerer et al. (2005).

[5] Replacing an operator by its expectation value relies on the Hostein-Primakoff approximation, introduced in Holstein and Primakoff (1940). Here, the underlying assumption is that we only weakly perturb the system while considering many photons, and the approximation holds. Then, $\hat{S}_y$ and $\hat{S}_z$ follow the Heisenberg uncertainty:

$$\mathrm{Var}\left(\hat{S}_y\right) \cdot \mathrm{Var}\left(\hat{S}_z\right) \geq \frac{S_x^2}{4}$$

[6] Many resources derive this and other relations of the light operators. Julsgaard (2003) is probably the most extensive one, but also Hammerer et al. (2010); Krauter (2011) are rather thorough resources.

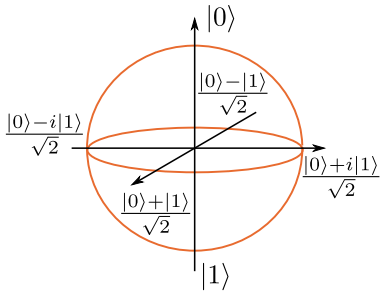

Figure 2.4: Bloch sphere. Illustration of spin 1/2 system. Subjecting a spin aligned with a magnetic field to an RF field would correspond to displacements on the surface and hence effective mean projections of the other components.

2.3 Atomic spin oscillators

While we were describing the atomic physics using our favorite isotope, cesium-133, in chapter 2.1, this section will be on the quantum mechanical description of atomic spins as a collective spin-oscillator consisting of many atoms. While we described the total angular momentum of a cesium atom before using the quantum number F, we will choose to follow suit of previous theses at Quantop (see, for example, Jensen (2011); Krauter (2011); Julsgaard (2003)) by using the more common choice of $\mathbf{J}$ to describe the total angular momentum of the collective spin state of an atomic ensemble and an individual atom by $\mathbf{j}$. Given the significant hyperfine splitting (see chapter 2.1), most of the time throughout this thesis, it is sufficient to consider ourselves only with atoms in $F = 4$ hyperfine level. We choose to describe the ensemble's total angular momentum as follows:

$$\mathbf{J} = \sum_{i=1}^{N_\mathrm{A}} \mathbf{j}^{(i)}, \tag{2.11}$$

with N_A reflecting the total number of atoms in $F = 4$, while $\mathbf{j}^{(i)}$ is the i-th atom's total angular momentum.

Common to our experiments is that we wish to have atoms in a coherent spin state (CSS) where all atoms are prepared in $F = 4, m_F = 4$. The quantization axis choice is the bias magnetic field direction aligning the spins along the x-axis to $\hat{J}_x$. Due to the large ensemble size of typically $10^8 - 10^9$ atoms, $\hat{J}_x$ is like a macroscopic property. As done for the Stokes operators, we can replace the operator $\hat{J}_x$ with the classical number J_x when considering a highly polarized atomic ensemble. With all atoms in $F = 4, m_F = 4$, this leads to a spin component of maximal magnitude $J_x = 4 \cdot N_\mathrm{A}$ along the x-axis (Krauter, 2011). While J_x is a macroscopic property, the spin components $\hat{J}_y$ and $\hat{J}_z$ have a vanishing expectation value and remain governed by their quantum nature. Similar to the description of the light polarization, we can define commutator relations and the Heisenberg uncertainty relation for the total angular momentum operators (Krauter, 2011):

$$\left[\hat{J}_y, \hat{J}_z\right] = iJ_x \tag{2.12}$$

$$\mathrm{Var}\left(\hat{J}_y\right) \cdot \mathrm{Var}\left(\hat{J}_z\right) \geq \frac{J_x^2}{4} \tag{2.13}$$

For the coherent spin state, equality in equation (2.13) will be fulfilled[7]. For a more generic quantum mechanical description, we define dimensionless canonical operators for the atomic ensemble as follows:

$$\hat{x}_\mathrm{A} = \frac{\hat{J}_y}{\sqrt{J_x}},\ \hat{p}_\mathrm{A} = \frac{\hat{J}_z}{\sqrt{J_x}}, \quad \Rightarrow \quad [\hat{x}_\mathrm{A}, \hat{p}_\mathrm{A}] = \mathrm{i} \tag{2.14}$$

When the ensemble of atoms is in the coherent spin state, all atoms are in the same state with $F = 4, m_F = 4$. With the beforementioned assumptions, we assume that changes to the projections along J_x are vanishingly small

[7] For the coherent state and a large number of atoms in the ensemble, $\langle J_x^2 \rangle \approx F^2 N_\mathrm{A}$ such that $\mathrm{Var}\left(\hat{J}_y\right) = \mathrm{Var}\left(\hat{J}_z\right) = F/2 \cdot N_\mathrm{A} = J_x/2$. See Krauter (2011) for more details.

and will not change in our systems. For our DLCZ-type experiment, we rely on describing collective excitations of the collective spin-oscillator despite the macroscopic properties of J_x. Therefore, it is instructive to define our coherent spin state as the ground state of a kind of harmonic oscillator and think of it as a collective spin-oscillator. This can be understood as follows. If all atoms are in the same state, any change due to the coherent interaction with light corresponds to an excitation in analogy to a harmonic oscillator (Hammerer, 2006). Therefore, we describe these excitations of our spin-oscillator using bosonic creation $\hat{b}^\dagger$ and annihilation $\hat{b}$ operators (Hammerer, 2006):

$$\hat{J}_x = J_x - \hat{b}^\dagger \hat{b} \tag{2.15}$$

with $\hat{b}^\dagger$ acting on the state of our spin-oscillator as follows:

$$\hat{b}^\dagger \left|0, 0, ..., 0, 0\right\rangle = \frac{1}{\sqrt{N_\mathrm{A}}} \sum_i \left|0, 0, ..., 0, 1^{(i)}, 0, ..., 0\right\rangle \tag{2.16}$$

where the superscript (i) indicates the i-th atom. Note how the operator acts symmetrically onto the collective state. The created excitation is shared between all atoms, each atom contributing a fraction $1/N_\mathrm{A}$ to the collective excitation[8].

With the atomic creation and annihilation operators, we can define raising and lowering operators along the macroscopic spin component $\hat{J}_x$ in the limit of $\langle \hat{b}^\dagger \hat{b} \rangle \ll N_\mathrm{A}$ corresponding to only a small fraction of the atoms not being in the $F = 4, m_F = 4$ state as (Hammerer, 2006):

$$\hat{J}_+ = \sqrt{N_\mathrm{A}} \hat{b} \tag{2.17a}$$

$$\hat{J}_- = \sqrt{N_\mathrm{A}} \hat{b}^\dagger \tag{2.17b}$$

We can interpret this as follows. If our atomic ensemble is initially in a coherent spin state, corresponding to the ground state of our collective spin-oscillator, applying $\hat{b}^\dagger$ will add one excitation while reducing the projection along $\hat{J}_x$. The symmetry of the collective excitation is one of the fundamental ingredients for storing a collective excitation in the spin-oscillator for the DLCZ-type experiment. Given our approximation of the numbers of excitations being small compared to the number of atoms in our ensemble, changes in the projection along J_x will remain to be treated as a classical number where changes in the few excitations regime remain negligible.

Using the lowering and raising operators as defined in equation (2.17), we can rewrite the expressions from equation (2.14) as (Krauter, 2011):

$$\hat{x}_A = \frac{1}{\sqrt{2}} \left(\hat{b} + \hat{b}^\dagger \right) \tag{2.18a}$$

$$\hat{p}_A = \frac{-\mathrm{i}}{\sqrt{2}} \left(\hat{b} - \hat{b}^\dagger \right) \tag{2.18b}$$

As we apply a magnetic field along the x-axis, the interaction of the spins with the magnetic field can be expressed through the Hamiltonian $H_B = \hbar \omega_\mathrm{L} \hat{J}_x$

[8] This symmetric excitation of the spin-oscillator is one of the fundamental building blocks of the DLCZ-type experiment. This symmetric state is also referred to as the symmetric Dicke state as introduced in Dicke (1954).

(Krauter (2011)). This interaction will lead to a precession of the spin components $\hat{J}_y$ and $\hat{J}_z$ at the Larmor frequency[9] $\omega_\mathrm{L} = 2\pi \cdot \nu_\mathrm{L}$ around the macroscopic spin component $\hat{J}_x$. Due to this precession, it is convenient to express the operators in the rotating reference frame with respect to ω_L:

$$\hat{x}'_A = \hat{x}_A \cos(\omega_\mathrm{L} t) + \hat{p}_A \sin(\omega_\mathrm{L} t) \tag{2.19a}$$
$$\hat{p}'_A = \hat{p}_A \cos(\omega_\mathrm{L} t) - \hat{x}_A \sin(\omega_\mathrm{L} t) \tag{2.19b}$$
$$\iff \quad \hat{x}_A = \hat{x}'_A \cos(\omega_\mathrm{L} t) - \hat{p}'_A \sin(\omega_\mathrm{L} t) \tag{2.19c}$$
$$\hat{p}_A = \hat{p}'_A \cos(\omega_\mathrm{L} t) + \hat{x}'_A \sin(\omega_\mathrm{L} t) \tag{2.19d}$$

In the following, we primarily use the rotating reference frame representation and drop the prime for convenience unless otherwise specified.

2.3.1 Spin coherence times

Before turning toward light-atom interaction, we have to slide in a short interlude to introduce the spin components and their coherence times as preparation for the experimental techniques used in chapters 6 and 7, but also for the main experiments. In our spin-oscillator, we distinguish two main spin components. The macroscopic spin component $\hat{J}_x$, oriented along the bias magnetic field direction, is the longitudinal spin component. Throughout our experiments, we operate with pulsed laser beams for optical pumping. Due to decoherence effects, we expect the atoms to thermalize their spin state after turning off the optical pumping. The time it takes for the longitudinal spin component $\hat{J}_x(t)$ to decay to its $1/e$-value is defined as the longitudinal spin coherence time T_1. While Graf et al. (2005) describes the decay of the longitudinal spin decay using two decay rates, a fast and a slow rate, for our experiments, it is sufficient to approximate it using a single exponential decay (Shen (2014)). This only accounts for the slow decay rate considered in Graf et al. (2005). The decay of our longitudinal spin component is then described by:

$$\langle \hat{J}_x(t) \rangle = \langle \hat{J}_x(0) \rangle \, e^{-t/T_1} \tag{2.20}$$

where we have introduced the longitudinal spin coherence time T_1. We will discuss measuring the longitudinal spin component and its decay as part of the vapor cell testing (chapter 7).

For our experiments, the spin component transverse to the bias magnetic field, $\hat{J}_\perp$, and its respective coherence time is of uttermost interest. The transverse spin coherence time is denoted T_2. It limits, for example, how long we can store coherences between two neighboring Zeeman levels, an essential consideration for our DLCZ-type experiment (chapters 4 and 10). We parameterize the decay of the transverse spin component also using a single exponential decay $\langle \hat{J}_\perp(t) \rangle = \langle \hat{J}_\perp(0) \rangle \, e^{-t/T_2}$. Different effects contribute to the transverse spin coherence time T_2. These include wall collisions, diffusion of atoms in and out of our cell channel, and magnetic field (in)homogeneity

[9] The effect of a magnetic field on an atomic spin has been introduced in chapter 2.1.

and stability. A thorough description of the different mechanisms contributing to $1/T_2 = \gamma$ can, for example, be found in Krauter (2011), including how to quantify the individual contributions experimentally. Experimentally, we can deduce T_2 from the linewidth of the resolved pulsed magneto-optical resonance spectroscopy (pMORS) spectra. The technique of pMORS will be introduced in chapter 6.

2.4 Light - spin ensemble interaction

Following the introduction of the light and the collective spin ensemble operator description in the previous two sections, we are now ready to describe light-spin interaction. This section will introduce the general form of the interaction Hamiltonian. The interaction between light and spin will form the basis for describing the dynamics exploited for the QMIT experiment (chapter 3) and the DLCZ-type experiment (chapter 4).

Throughout this thesis, we are interested in the interaction of a highly polarized atomic spin ensemble with polarized light. The thorough derivation of the full description of this interaction has been covered in many different resources, the most relevant for the present work being Julsgaard (2003) and Hammerer et al. (2010). Here, we will only focus on the key components. The total Hamiltonian H describing our system consists of three contributions. Two contributions describe the intrinsic dynamics of the atomic spin ensemble, H_A, and the dynamics of the light field H_L. Only the third part of H describes the interaction between the light and the atomic spins and is denoted H_int. The interaction Hamiltonian for a single atom with a light field is simply given by the dipole interaction with an electric field[10]:

$$H_\mathrm{int}^{(i)} = -\mathbf{d}^{(i)} \cdot \mathbf{E}(\mathbf{r}_i) \tag{2.21}$$

with $\mathbf{d}^{(i)}$ being the dipole moment of the i-th atom and $\mathbf{E}$ the electric field operator evaluated at the position $\mathbf{r}_i$ of the i-th atom. It is instructive to decompose the operators in positive and negative frequency components (Hammerer et al. (2010); Julsgaard (2003)):

$$\begin{aligned}\mathbf{E} &= \mathbf{E}^{(+)} + \mathbf{E}^{(-)} \\ &= \mathbf{E}_0^+ e^{-\mathrm{i}\omega t} + \mathbf{E}_0^- e^{+\mathrm{i}\omega t} \qquad (2.22)\\ \mathbf{d} &= \mathbf{d}^{(+)} + \mathbf{d}^{(-)} \\ &= \sum_{m,n} \mathbf{d}_{g_n,e_m} |g_n\rangle \langle e_m| + \mathbf{d}_{g_n,e_m} |e_m\rangle \langle g_n| \qquad (2.23)\end{aligned}$$

where we have omitted the atom label i for brevity. In the case of the electric field, $(+)$ and $(-)$ reflect frequency components oscillating with positive ($\propto \exp(-\mathrm{i}\omega t)$) and negative ($\propto \exp(\mathrm{i}\omega t)$) frequencies, respectively, in consistency with the notation used in Gerry and Knight (2004) and Hammerer et al. (2010). For the dipole operator, $(+)$ and $(-)$ reflect transitions from or to the m-th excited state $|e_m\rangle$. $\mathbf{d}_{g_n,e_m}$ is the vector of matrix elements corresponding

[10] It should be noted that the same expression can be found with a minus. Two versions can be found in the literature, and one needs to pay attention to which convention is used.

to the dipole moments along x, y, z. It determines the transition strength between ground state $|g_n\rangle$ and excited state $|e_m\rangle$ and vice versa for the i-th atom. The ground and excited state can be expressed in a time-dependent fashion. It can be shown that $\mathbf{d}^{(+)}$ and $\mathbf{d}^{(-)}$ include positive and negative oscillating terms, respectively (Schliesser (2016)). If we are interested in time scales slow compared to the optical frequency, we can exploit the rotating wave approximation and neglect contributions to the interaction Hamiltonian oscillating at twice the optical frequency, reducing it to (Hammerer et al., 2010):

$$H_{\text{int}} = -\left(\mathbf{E}^{(+)}\mathbf{d}^{(-)} + \mathbf{d}^{(+)}\mathbf{E}^{(-)}\right) \tag{2.24}$$

In our experiments, we are working with probe light fields that are far-detuned[11]. We have stable ground states of the atoms, given by their Zeeman levels. Instead of considering transitions from a ground state to the excited state manifold and then from the excited state to some other ground state, adiabatic elimination of the excited state can be performed[12]. In Julsgaard (2003), the derivation of a concise expression for the effective interaction Hamiltonian suitable for describing cesium atoms in the $F = 4$ manifold as the ground state and coupling to the allowed excited states on the D_2 line. The derivation involves adiabatic elimination of the excited states and is valid when considering weak interaction (Hammerer et al. (2010)). Further, Julsgaard (2003) shows that the resulting effective interaction Hamiltonian can be rewritten in terms of the Stokes operators (see equations (2.7a-d)) and spin vector components (see equations (2.17)). Here, we will consider only the result that Julsgaard (2003) arrives at for brevity[13]:

$$\begin{aligned} H_{\text{int}}^{\text{eff}} = -\frac{\hbar c \gamma \lambda^2}{16 A \Delta \pi} \int_0^L \big(a_0 \cdot \hat{S}_0(z,t) + a_1 \cdot \hat{S}_z(z,t)\hat{j}_z(z,t) \\ + a_2\left[\hat{S}_0(z,t)\hat{j}_z^2(z,t) - \hat{S}_-(z,t)\hat{j}_+^2(z,t) - \hat{S}_+(z,t)\hat{j}_-^2(z,t)\right]\big)\,\rho A \mathrm{d}z \end{aligned} \tag{2.25}$$

with dimensionless coefficients a_i

$$a_0 = \frac{1}{4}\left(\frac{1}{1-\Delta_{35}/\Delta} + \frac{7}{1-\Delta_{45}/\Delta} + 8\right) \longrightarrow 4 \tag{2.26a}$$

$$a_1 = \frac{1}{120}\left(\frac{-35}{1-\Delta_{35}/\Delta} - \frac{21}{1-\Delta_{45}/\Delta} + 176\right) \longrightarrow 1 \tag{2.26b}$$

$$a_2 = \frac{1}{240}\left(\frac{5}{1-\Delta_{35}/\Delta} - \frac{21}{1-\Delta_{45}/\Delta} + 16\right) \longrightarrow 0 \tag{2.26c}$$

Here, λ refers to the wavelength of the light (852 nm), while c is the speed of light. γ is the FWHM of the excited state, given by $\gamma = 2\pi \cdot 5.21\,\text{MHz}$ (Steck (2019)). The area and length of the atomic spin ensemble are reflected by A and L, respectively, while ρ is the atomic density. Positive and negative detuning Δ reflect red and blue detuning. To account for the hyperfine structure, Δ_{45} accounts for the frequency shift between $F' = 4$ and $F' = 5$, while Δ_{35} accounts for the frequency shift between $F' = 3$ and $F' = 5$, used in the a_j coefficients in equations (2.26a-c).

[11] Details about our probe laser can be found in chapter 5. We commonly use a blue-detuning of the probe laser of >1.9 GHz.

[12] A generic derivation of adiabatic elimination can be found in Schliesser (2016). In contrast, a specific but reduced derivation for our system can be found in Hammerer et al. (2010).

[13] Please note that we corrected for the factor 2 that was wrong in Julsgaard (2003), instead of 1/8 it is supposed to be the 1/16 as stated here. For example, this mistake has also been corrected in Krauter (2011); Jensen (2011); Sherson (2006).

This effective interaction Hamiltonian consists of three contributions, leading to three distinct effects. The first term, proportional to a_0 – referred to as scalar polarizability – counts photons in units of 1/length. As mentioned in section 2.2, we can, with appropriate normalization, convert the Stokes vectors from "counting" photons to allowing us to estimate the photon flux, i.e., photons per unit time ($c\hat{S}_0(z,t) = \hat{S}_0(t)$) at a position z in our ensemble passing through the cross-section A of the ensemble. This contribution to the Hamiltonian interacts with all ground state levels to the same extent, adding only a constant energetic shift. The second term, proportional to the vector polarizability a_1, describes the interaction of the Faraday rotation type. The interaction rotates our macroscopic spin $\mathbf{J}$ at a rate proportional to $\hat{S}_z(z,t)$ around the z-axis, while the Stokes vector $\mathbf{S}$ is rotated around the z-axis by a rate proportional to $\hat{j}_z(z,t)$. Here, $\hat{j}_k(z,t) = \sum_{i=1}^{N_A} \delta(z - z_i)\hat{j}_k^{(i)}(t)$ are the time- and position-dependent dimensionless spin operators for $k = x, y, z$ (Krauter, 2011). Multiplying $\hat{j}_k(z,t)$ with $A\rho\mathrm{d}z$ yields the respective total angular momentum within dz in units of $\hbar$ (Jensen (2011)). Thus, the total angular momentum of all atoms within our ensemble in units of $\hbar$ can be determined as $\mathbf{J}(z,t) = \int_0^L \mathbf{j}(z,t)\rho A\mathrm{d}z$ (Jensen, 2011).

The interaction described in equation (2.25) will prove vital for the quantum-enhanced sensing protocol (chapter 15). Starting from light polarized along x, the light-atom interaction in equation (2.25) leads to a polarization rotation of the light depending on the state of the atoms. Hence, recording the Stokes component $\hat{S}_y$ after the light-atom interaction allows us to gain information about the light-atom interaction and the atomic spin ensemble. The third term is proportional to the tensor polarizability a_2, containing higher order terms of the interaction. Overall, we usually can neglect the higher order terms due to our choice of detuning $|\Delta| > 1.9\,\mathrm{GHz}$, rendering contributions in equation (2.25) proportional to the tensor polarizability a_2 negligible. An interesting observation regarding all terms comprising equation (2.25) is that they individually conserve the combined atom-light projection along the z-axis. This stems from the axial symmetry of the physical system along the light propagation direction (Julsgaard, 2003; Sherson, 2006).

The a_j parameters have also been calculated in Julsgaard (2003) for the $F = 3$ manifold[14]:

$$a_0 = \frac{1}{28}\left(\frac{25}{1+\Delta_{24}/\Delta} + \frac{63}{1+\Delta_{23}/\Delta} + 24\right) \longrightarrow 4 \tag{2.27a}$$

$$a_1 = \frac{1}{56}\left(\frac{45}{1+\Delta_{24}/\Delta} - \frac{21}{1+\Delta_{23}/\Delta} - 80\right) \longrightarrow -1 \tag{2.27b}$$

$$a_2 = \frac{1}{112}\left(\frac{5}{1+\Delta_{24}/\Delta} - \frac{21}{1+\Delta_{23}/\Delta} + 16\right) \longrightarrow 0 \tag{2.27c}$$

These will become relevant later for the QMIT experiment discussed in chapters 14 and 15, where we need a_1 for both manifolds to extrapolate the influence from atoms in $F = 3$.

[14] Please note that we use the a_1 from the erratum to Julsgaard (2003). Therefore the expression does not fit the one stated in the main text of Julsgaard (2003). The changes are only signs, most importantly a_1 approaches -1 instead of 1.

Chapter 3

Toward quantum non-demolition measurements for QMIT

This chapter will introduce the theoretical background more specifically to the quantum-enhanced magnetic induction tomography (QMIT) experiment. The theory for the DLCZ-type experiment is presented in a dedicated chapter. Nevertheless, some topics within this chapter are also relevant to the DLCZ-type experiment. It might seem like an odd choice to treat the QMIT first while it is presented last in this thesis. It is on purpose since the topics presented here are more directly building on the spin dynamics introduced in the previous chapter on collective light-atom interactions. First, we will look at the input-output relations for the light-atom interaction, which is the first topic of the two sections of this chapter (section 3.1). To derive the required relations, we will use various theses and articles, most importantly Julsgaard (2003) an Sherson (2006), and adapt their notation. Based on the derivation of the expressions for the input-output relations, the second section of this chapter (section 3.2) will introduce a technique for avoiding back-action noise in our measurement using stroboscopic probing toward realizing a quantum non-demolition (QND) measurement. For this, we will mainly use the derivations provided in Vasilakis et al. (2015) and Shen (2014).

3.1 Input-output relations

For our experiments, we use light to probe the atomic spins. Thus, we rely on atom-light interaction to imprint information from the atoms onto the light. From the light, we can extract the information using polarization homodyne detection. For this purpose, we need to determine the relationship between the in- and output light fields involved in the interaction with our collective spin-oscillator. The relationship between in- and output light fields can be found using propagation equations. The problem has been treated extensively in Julsgaard (2003),Sherson (2006), Jensen (2011), and Shen (2014). We will refrain from presenting the complete derivation here and present only key steps. The starting point for the derivation is the Heisenberg equation of

motion for the spin operators $\hat{j}_i$ (Sherson, 2006):

$$i\hbar \frac{\partial \hat{j}_i}{\partial t} = \left[\hat{j}_i, \hat{H}\right] \tag{3.1}$$

while we will use the Maxwell-Bloch equation for the Stokes operators $\hat{S}_i(z,t)$. Here, it takes the form (Julsgaard, 2003; Sherson, 2006):

$$\left(\frac{\partial}{\partial t} + c\frac{\partial}{\partial z}\right)\hat{S}_i(z,t) = \frac{1}{i\hbar}\left[\hat{S}_i(z,t), \hat{H}\right] \tag{3.2}$$

For simplicity, we will consider the case where the probe light detuning Δ is ample enough that the tensor polarizability coefficient a_2, as defined in equation (2.25) in chapter 2, approaches the limit $a_2 \to 0$. This allows us to neglect contributions to the effective interaction Hamiltonian (equation (2.25)) proportional to the tensor polarizability $\left(H_{\text{int}}^{\text{eff}} \propto a_2\right)$ in the following. Secondly, we will exploit that the polarization of the coherent drive light and the macroscopic spin orientation are both along the x-axis as introduced in sections 2.2 and 2.3. Under these assumptions, we can treat the corresponding components as classical variables by making the replacements $\hat{S}_x \to S_x$ and $\hat{j}_x \to j_x$ (see chapter 2). These assumptions will remain valid as long as the mean value and variations in the transverse quantum components can be considered negligible (Julsgaard (2003)). The probe light propagates along the z-direction. It reads out the quantum fluctuations of the transverse spin components. Under the assumption that j_x and S_x remain classical properties after the light-atom interaction, the previously introduced continuous notation for the spin operators $\hat{J}_i(t) = \int_0^L \hat{j}_i(z,t)\rho A \mathrm{d}z$ (section 2.3) can be used (Sherson, 2006). As before, this collective notation incorporates all atomic spins within our interaction volume. For the Stokes operators, we are only interested in the light operators before and after the interaction of the light with the spin-oscillator (Sherson, 2006). We define $\hat{S}_i^{\text{in}}(t) = c\hat{S}_i(z=0,t)$ describing our probe light field at the "input of the vapor cell" before interacting with the atomic spin ensemble. Analogously, we define the Stokes vectors after the interaction with the spin-oscillator as $\hat{S}_i^{\text{out}}(t) = c\hat{S}_i(z=L,t)$, where L is the length of our interaction volume, i.e., the length of the vapor cell. In a sense, $\hat{S}_i^{\text{out}}(t)$ corresponds to the "light at the output of the vapor cell". Hence, we can remove any explicit space dependency for our description as shown in Sherson (2006). As mentioned in section 2.2, this conversion means that the Stokes operators count photons per unit of time. Combining all these assumptions, it can be shown that the input-output relations and the spin evolution equations reduce, in the absence of a bias magnetic field, to (Sherson (2006)):

$$\hat{S}_y^{\text{out}}(t) = \hat{S}_y^{\text{in}}(t) + aS_x\hat{J}_z(t) \tag{3.3a}$$

$$\hat{S}_z^{\text{out}}(t) = \hat{S}_z^{\text{in}}(t) \tag{3.3b}$$

$$\frac{\partial}{\partial t}\hat{J}_y(t) = aJ_x\hat{S}_z^{\text{in}}(t) \tag{3.3c}$$

$$\frac{\partial}{\partial t}\hat{J}_z(t) = 0 \tag{3.3d}$$

where $a = \frac{\gamma\lambda^2}{16A\Delta\pi}a_1$. $\hat{J}_z(t)$ remains time-independent without a bias magnetic field. However, we see that the interaction of the Stokes component $\hat{S}_z^{\text{in}}(t)$ with the macroscopic spin component J_x, introduces changes in the spin component $\hat{J}_y(t)$ which we refer to as back-action. On the other hand, $\hat{J}_z(t)$ can be measured without being impacted by back-action. Considering a large interaction strength aS_x such that the imprecision shot noise originating from the contribution $\hat{S}_y^{\text{in}}(t)$ is small in equation (3.3a), recording $\hat{S}_y^{\text{out}}(t)$ provides information on $\hat{J}_z(t)$ through a QND type measurement (Sherson, 2006).

Typically, we are placing our vapor cell inside a bias magnetic field, lifting the energetic degeneracy of Zeeman levels (chapter 2). In the description above, we have not included these dynamics emerging from the bias magnetic field along the x-axis. The interaction with a magnetic field is described by the Hamiltonian $H_{\text{B}} = \hbar\omega_{\text{L}}\hat{J}_x$ where $\omega_{\text{L}} = 2\pi\nu_{\text{L}}$ (see equation (2.3)). This is just an addition to the effective Hamiltonian for the light-atom interaction discussed in section 2.4 (Sherson (2006)). The magnetic field Hamiltonian H_{B} alters equations (3.3a-d), as it adds a time-dependent precession of the collective spin components around $\hat{J}_x$ (compare section 2.3). We will therefore consider the rotating-frame variables for the collective spin, indicated with a prime. For the rest of this section, we will choose to follow the conventions presented in Sherson (2006)[1]:

$$\begin{pmatrix} \hat{J}'_y(t) \\ \hat{J}'_z(t) \end{pmatrix} = \begin{pmatrix} \cos(\omega_{\text{L}}t) & \sin(\omega_{\text{L}}t) \\ -\sin(\omega_{\text{L}}t) & \cos(\omega_{\text{L}}t) \end{pmatrix} \begin{pmatrix} \hat{J}_y(t) \\ \hat{J}_z(t) \end{pmatrix} \tag{3.4}$$

Expressing equations (3.3a-d) with the rotating frame spin operators allows us to describe the dynamics resulting from the equations of motion[2] as follows (Julsgaard (2003); Sherson (2006)):

$$\hat{S}_y^{\text{out}}(t) = \hat{S}_y^{\text{in}}(t) + aS_x\left(\hat{J}'_y(t)\sin(\omega_{\text{L}}t) + \hat{J}'_z(t)\cos(\omega_{\text{L}}t)\right) \tag{3.5a}$$

$$\hat{S}_z^{\text{out}}(t) = \hat{S}_z^{\text{in}}(t) \tag{3.5b}$$

$$\frac{\partial}{\partial t}\hat{J}'_y(t) = aJ_x\hat{S}_z^{\text{in}}(t)\cos(\omega_{\text{L}}t) \tag{3.5c}$$

$$\frac{\partial}{\partial t}\hat{J}'_z(t) = aJ_x\hat{S}_z^{\text{in}}(t)\sin(\omega_{\text{L}}t) \tag{3.5d}$$

Now both spin components are imprinted with back-action from the light. At the same time, we can measure both spin components with a single light pulse if it is longer than the spin precession period ($T > 1/\omega_{\text{L}}$). This measurement is, of course, limited in precision due to the non-commuting nature of the operators. We note that in equation (3.5a), the atomic signals are encoded at sidebands of $\omega_{\text{L}}/(2\pi)$ to the light frequency ν_0. The atomic contribution to our signal $\hat{S}_y^{\text{out}}(t)$ has an in-phase (cosine) and an out-of-phase (sine) component. As in sections 2.2 and 2.3, we can express these equations utilizing canonical operators for the atomic spins and light variables. This changes

[1] The unfamiliar reader should be aware that different conventions exist, and the signs in other works might differ from the convention used throughout this thesis.

[2] Here we use that our additional interaction with the magnetic field changes the differential equations in (3.3c,d) to:

$$\frac{\partial}{\partial t}\hat{J}_y(t) = aJ_x\hat{S}_z^{\text{in}}(t) - \omega_{\text{L}}\hat{J}_z(t)$$

$$\frac{\partial}{\partial t}\hat{J}_z(t) = \omega_{\text{L}}\hat{J}_y(t)$$

Using the slowly-varying rotating-frame variables introduced in (3.4), the laboratory-frame variables can be replaced to obtain the final result in equations (3.5 a-d).

equations (3.5) to[3]:

$$\hat{x}_{\mathrm{L}}^{\mathrm{out}}(t) = \hat{x}_{\mathrm{L}}^{\mathrm{in}}(t) + \frac{\kappa}{\sqrt{T}}\left(\hat{x}_{\mathrm{A}}(t)\sin(\omega_{\mathrm{L}}t) + \hat{p}_{\mathrm{A}}(t)\cos(\omega_{\mathrm{L}}t)\right) \tag{3.6a}$$

$$\hat{p}_{\mathrm{L}}^{\mathrm{out}}(t) = \hat{p}_{\mathrm{L}}^{\mathrm{in}}(t) \equiv \hat{p}_{\mathrm{L}}(t) \tag{3.6b}$$

$$\frac{\partial}{\partial t}\hat{x}_{\mathrm{A}}(t) = \frac{\kappa}{\sqrt{T}}\hat{p}_{\mathrm{L}}(t)\cos(\omega_{\mathrm{L}}t) \tag{3.6c}$$

$$\frac{\partial}{\partial t}\hat{p}_{\mathrm{A}}(t) = \frac{\kappa}{\sqrt{T}}\hat{p}_{\mathrm{L}}(t)\sin(\omega_{\mathrm{L}}t) \tag{3.6d}$$

where we have introduced the coupling constant $\kappa = a\sqrt{J_x S_x T}$. Since $\hat{p}_{\mathrm{L}}(t)$ does not change upon interaction with the atoms, we can exploit this to integrate the equations (3.6c) and (3.6d) to obtain:

$$\hat{x}_{\mathrm{A}}(t) = \hat{x}_{\mathrm{A}}(0) + \frac{\kappa}{\sqrt{T}}\int_0^t \hat{p}_{\mathrm{L}}(t')\cos\left(\omega_{\mathrm{L}}t'\right)\mathrm{d}t' \tag{3.7a}$$

$$\hat{p}_{\mathrm{A}}(t) = \hat{p}_{\mathrm{A}}(0) + \frac{\kappa}{\sqrt{T}}\int_0^t \hat{p}_{\mathrm{L}}(t')\sin\left(\omega_{\mathrm{L}}t'\right)\mathrm{d}t' \tag{3.7b}$$

Here we identify the previously defined sine and cosine modes introduced in equation (2.10). Using these and the coupling constant κ, we can simplify the atomic input-output relations in equation (3.7) for a total interaction time of T to:

$$\hat{x}_{\mathrm{A}}^{\mathrm{out}} = \hat{x}_{\mathrm{A}}^{\mathrm{in}} + \frac{\kappa}{\sqrt{2}}\hat{p}_{\mathrm{L}}^{c} \tag{3.8a}$$

$$\hat{p}_{\mathrm{A}}^{\mathrm{out}} = \hat{p}_{\mathrm{A}}^{\mathrm{in}} \pm \frac{\kappa}{\sqrt{2}}\hat{p}_{\mathrm{L}}^{s} \tag{3.8b}$$

where we have introduced $\hat{x}_{\mathrm{A}}^{\mathrm{in}} \equiv \hat{x}_{\mathrm{A}}(0)$ as the atomic operator before the interaction, while $\hat{x}_{\mathrm{A}}^{\mathrm{out}} \equiv \hat{x}_{\mathrm{A}}(T)$ describes the atomic operator after the interaction (Hammerer (2006)) and vice versa for $\hat{p}_{\mathrm{A}}^{i}$. We illustrate the effect of this back-action from the light onto the atomic operators in figure 3.1 for three different times. Without light, we expect the transverse spin projection noise to remain constant in time (neglecting decoherence effects). However, when interacting with light, according to the coupling to the light in equation (3.8), we expect the noise in the atomic projection noise to grow. How much noise is introduced, depends of the coupling constant κ.

The alternative sign $-$ in equation (3.8b) arises when dealing with an ensemble whose macroscopic component is oppositely oriented. Throughout this thesis, we will not concern ourselves with this case but want to make the reader aware of the different existing notations. We see that the two atomic quadratures in equation (3.8) are both affected by the light noise in the $\hat{p}$ quadrature. The atomic input-output relations can be used in the expression for the output light field (equation (3.6a)). Following the derivations and approximations presented, for example, in Hammerer et al. (2005), Hammerer (2006), and Sherson (2006), one can find expressions for the sine and cosine component of the light quadrature $\hat{x}_{\mathrm{L}}^{\mathrm{out}}(t)$. To obtain the cosine mode

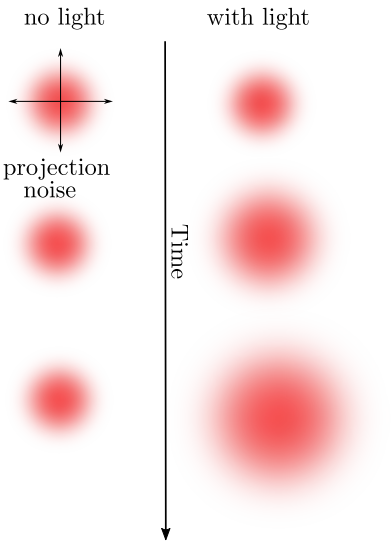

Figure 3.1: Atomic projection noise evolution. Simplified illustration of back-action introduced by the light (right) compared to the constant atomic projection noise in the absence of light (left) interacting with the collective spin state. The growth is shown for three different times.

[3] From sections 2.2 and 2.3, we use:

$$\hat{x}_{\mathrm{L}} = \frac{\hat{S}_y}{\sqrt{S_x}}$$

$$\hat{p}_{\mathrm{L}} = \frac{\hat{S}_z}{\sqrt{S_x}}$$

$$\hat{x}_{\mathrm{A}} = \frac{\hat{J}_y}{\sqrt{J_x}}$$

$$\hat{p}_{\mathrm{A}} = \frac{\hat{J}_z}{\sqrt{J_x}}$$

Please note that we dropped the prime for convenience.

of $\hat{x}_{\mathrm{L}}^{\mathrm{out}}(t)$, we multiply the expression in equation (3.6a) with $\sqrt{\frac{2}{T}}\cos(\omega_{\mathrm{L}}t)$. Here, the constant prefactor $\sqrt{\frac{2}{T}}$ corresponds to assuming a flat envelope function and the expression for $\hat{x}_{\mathrm{L}}^{\mathrm{out},c}$ as the cosine mode is obtained by integrating the total expression for the total measurement duration $T \gg 2\pi/\omega_{\mathrm{L}}$:

$$\hat{x}_{\mathrm{L}}^{\mathrm{out},c} = \sqrt{\frac{2}{T}} \int_0^T \mathrm{d}t\, \hat{x}_{\mathrm{L}}^{\mathrm{out}} \cos(\omega_{\mathrm{L}}t) \tag{3.9}$$

Following this approach, it can be shown that the cosine and sine modes for the light quadratures can be determined as (Sherson (2006)):

$$\hat{x}_{\mathrm{L}}^{\mathrm{out},c} = \hat{x}_{\mathrm{L}}^{\mathrm{in},c} + \frac{\kappa}{\sqrt{2}}\hat{p}_{\mathrm{A}}^{\mathrm{in}} \pm \frac{\kappa^2}{4}\hat{p}_{\mathrm{L}}^{\mathrm{in},s} \pm \frac{\kappa^2}{4\sqrt{3}}\hat{p}_{\mathrm{L}}^{\mathrm{in},s1} \tag{3.10a}$$

$$\hat{x}_{\mathrm{L}}^{\mathrm{out},s} = \hat{x}_{\mathrm{L}}^{\mathrm{in},s} \pm \frac{\kappa}{\sqrt{2}}\hat{x}_{\mathrm{A}}^{\mathrm{in}} \pm \frac{\kappa^2}{4}\hat{p}_{\mathrm{L}}^{\mathrm{in},c} \pm \frac{\kappa^2}{4\sqrt{3}}\hat{p}_{\mathrm{L}}^{\mathrm{in},c1} \tag{3.10b}$$

$$\hat{p}_{\mathrm{L}}^{\mathrm{out},c} = \hat{p}_{\mathrm{L}}^{\mathrm{in},c} \tag{3.10c}$$

$$\hat{p}_{\mathrm{L}}^{\mathrm{out},s} = \hat{p}_{\mathrm{L}}^{\mathrm{in},s} \tag{3.10d}$$

with

$$\hat{p}_{\mathrm{L}}^{\mathrm{in},s1} = \sqrt{3}\left(\frac{2}{T}\right)^{3/2} \int_0^T \mathrm{d}t \left(\frac{T}{2} - t\right) \sin(\omega_{\mathrm{L}}t)\, \hat{p}_{\mathrm{L}}^{\mathrm{in}}(t) \tag{3.11}$$

and similar expression for the cosine component, including a cosine instead of sine in the integral for $\hat{p}_{\mathrm{L}}^{\mathrm{in},c1}$. To achieve the results in equation (3.10), contributions with $\sin(\omega_{\mathrm{L}}t)\cos(\omega_{\mathrm{L}}t)$ are neglected since they average out on the timescales considered. The alternate signs in the equations indicate dealing with an oppositely oriented atomic ensemble as covered in Sherson (2006). Here, we will not use this and only state it to make the reader aware of alternate notations. For a more thorough mathematical derivation of the results stated in equations (3.10) and (3.11), Hammerer (2006) explains the underlying approximations and mathematical assumptions very thoroughly.

Let us examine the different contributions to the light output field. As before, the $\hat{p}_{\mathrm{L}}^{\mathrm{out}}$ quadrature of the light field is conserved (both the sine and cosine components). Only the light components $\hat{x}_{\mathrm{L}}^{\mathrm{out},s/c}$ are affected by the light-atom interaction and are suited for retrieving information about the collective state of the spin-oscillator. For convenience, we will only consider the cosine mode $\hat{x}_{\mathrm{L}}^{\mathrm{out},c}$ of the light output field here. It will become apparent in the following section why this is our preferred choice. In equation (3.10a), we have contributions from both light quadratures to our output light field. For example, $\hat{x}_{\mathrm{L}}^{\mathrm{in},c}$ and $\hat{p}_{\mathrm{L}}^{\mathrm{in},s}$ both contribute to $\hat{x}_{\mathrm{L}}^{\mathrm{out},c}$ in equation (3.10a). We call the contribution to $\hat{x}_{\mathrm{L}}^{\mathrm{out},c}$ from the conjugate light quadrature $\hat{p}_{\mathrm{L}}^{\mathrm{in},s}$ oscillating out-of-phase with our input light quadrature $\hat{x}_{\mathrm{L}}^{\mathrm{in},c}$ the back-action noise of light. It is reflected in the last two terms of equation (3.10a), proportional to $\hat{p}_{\mathrm{L}}^{\mathrm{in},s}$ and $\hat{p}_{\mathrm{L}}^{\mathrm{in},s1}$. In addition, we have the desired atomic contribution $\hat{p}_{\mathrm{A}}^{\mathrm{in}}$, enabling us to retrieve information about the atomic spin ensemble.

The noise variance of the output light field for the cosine component $\hat{x}_{\mathrm{L}}^{\mathrm{out},c}$ is given by:

$$\mathrm{Var}\left(\hat{x}_{\mathrm{L}}^{\mathrm{out},c}\right) = \frac{1}{2}\left(1 + \frac{\kappa^2}{2} + \frac{\kappa^4}{12}\right) \tag{3.12}$$

where we have exploited that $\mathrm{Var}\left(\hat{x}_{\mathrm{L}}^{\mathrm{in},c}\right) = \mathrm{Var}\left(\hat{p}_{\mathrm{L}}^{\mathrm{in},s}\right) = \mathrm{Var}\left(\hat{p}_{\mathrm{L}}^{\mathrm{in},s1}\right) = 1/2$ and $\mathrm{Var}\left(\hat{x}_{\mathrm{A}}^{\mathrm{in}}\right) = \mathrm{Var}\left(\hat{p}_{\mathrm{A}}^{\mathrm{in}}\right) = 1/2$. We are measuring the y-component of the Stokes vector $\hat{S}_y^{\mathrm{out},c}$ oscillating in phase with the cosine component. We can rewrite the expression in equation (3.12) using equation (2.9), converting the canonical light operators to Stokes vectors, and equation (2.14), relating the canonical atomic operators to the spin operators, leading to:

$$\mathrm{Var}\left(\hat{S}_{\mathrm{y}}^{\mathrm{out},c}\right) = \frac{N_{\mathrm{ph}}}{4}\left(1 + \frac{\kappa^2}{2} + \frac{\kappa^4}{12}\right) \tag{3.13}$$

where N_{Ph} is the mean number of photons interacting with the atomic ensemble in the detection interval $[0, T]$. It should be noted that we exploited here that $\left|\hat{S}_x\right| = N_{\mathrm{ph}}/2$ and hence $\mathrm{Var}\left(\hat{S}_y^{\mathrm{in},c}\right) = N_{\mathrm{ph}}/4$ (Shen (2014)). Further, we assumed that our spin-oscillator is in a coherent spin state with $\mathrm{Var}(\hat{J}_z) = J_x/2$. As before, we can identify the previously mentioned noise contributions in equation (3.13). The first term is the imprecision shot noise contribution (SN), while the second is the contribution arising from the atomic projection noise (PN). The third term describes the light's back-action noise (BAN) onto itself via the oscillator response. It should be noted that the back-action contribution to the noise variance is proportional to $\kappa^4 \propto T^2$. This means that the contribution from the back-action to the signal grows faster with $\kappa \propto \sqrt{T}$ than any other contribution, and the stronger – or longer – we measure, the more back-action we introduce to the system.

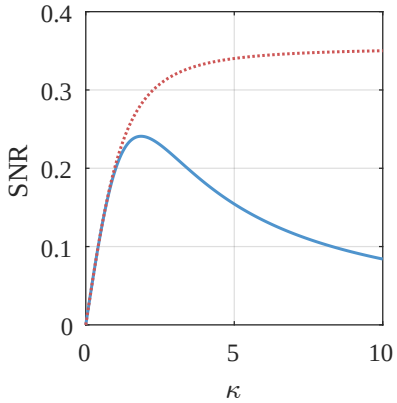

Figure 3.2: Relative SNR versus κ. κ-dependence of the SNR for two cases. The expected SNR is shown in blue as described by equation (3.14). The red dotted line shows the expected SNR in the absence of SNR.

When considering detecting a non-zero-mean transverse spin component created using an RF pulse, the signal-to-noise ratio can be calculated by exploiting the mean of the vacuum input light field in the y-direction is $\langle \hat{S}_y^{\mathrm{in}} \rangle = 0$. At the same time, the output light field in the y-direction following the light-atom interaction should have then a non-vanishing contribution ($\langle \hat{S}_y^{\mathrm{out}} \rangle \neq 0$). This can be seen in the expression of equation (3.3a), where we select only the cosine component of our signal in our measurement. From this, we expect our signal to follow $\langle \hat{S}_y^{\mathrm{out},c}(t) \rangle \propto a S_x \langle \hat{J'}_z(t) \cos(\omega_{\mathrm{L}} t) \rangle \propto \sqrt{N_{\mathrm{Ph}}}\kappa$. Further, we can determine the noise compromising our signal as the square root of the noise variance as determined in equation (3.13). Combining these considerations, we determine the signal-to-noise ratio (SNR) to follow:

$$\mathrm{SNR} \propto \frac{\kappa\sqrt{N_{\mathrm{Ph}}}}{\sqrt{\frac{N_{\mathrm{Ph}}}{4}}\sqrt{1 + \frac{\kappa^2}{2} + \frac{\kappa^4}{12}}}. \tag{3.14}$$

where the nominator is our expected signal, while the denominator describes noise. Due to the different scaling of the noise contribution with κ, we expect

a clear optimum in equation (3.14), illustrated in figure 3.2. In addition, we show the expected growth of the SNR in the absence of the detrimental back-action noise in figure 3.2, indicated by the dotted line. The SNR is maximized for $\kappa^4 = 12$, allowing us to define the SQL for a classical, continuous measurement. We can express the minimal noise variance scaled to the projection noise:

$$\mathrm{SQL}\,[\mathrm{PN}] = \frac{1 + \kappa^2/2 + \kappa^4/12}{\kappa^2/2} = (1 + 2/\sqrt{3})\mathrm{PN} \tag{3.15}$$

To put this expression into words: The minimum noise variance that one can observe for a continuous measurement of light-atom interaction operating at the standard quantum limit exhibits a noise variance $(1 + 2/\sqrt{3})$ times the projection noise variance. This limit will be our reference for quantifying our improvement compared to continuous measurements when exploiting back-action evasion and conditional spin-squeezing.

3.2 Back-action evasion for QND measurements

As we have seen in the previous section, standard continuous measurements of two non-commuting variables are commonly limited by a standard quantum limit (SQL). Such a SQL sets, for example, a limit on the sensitivity attainable with an atomic magnetometer[4]. In principle, measuring a quantum mechanical observable with arbitrary precision is possible when the measurement does not perturb the observable in question. However, simultaneously, the conjugate observable will suffer perturbation, and its uncertainty will increase such that the combined uncertainties still follow the Heisenberg uncertainty principle (Braginsky et al., 1992). Measurements of this type, i.e., that do not alter the observable, are called *quantum non-demolition* (QND) measurements. A measurement of the QND type leaves the observable unchanged, whereas the distribution for the conjugate variable is widened.

As we have seen in the previous section, the measurement of $\hat{J}_z$ leads to back-action in the conjugate variable $\hat{J}_y$. In the presence of a magnetic field, the Larmor precession ($\omega_\mathrm{L} \neq 0$) rotates the back-action acting on $\hat{J}_y(t)$ into $\hat{J}_z(t)$, where $\hat{J}_z(t)$ is our observable in the non-rotating lab-frame. Hence, considering a continuous stream of light with constant intensity will ultimately disturb our quantum measurement of the spin quadrature by introducing additional noise in the form of extraneous back-action noise from the light. Suppose we want to perform a quantum non-demolition (QND) measurement, where our observable retains the same value for repeated measurements and is of the QND type (Braginsky et al. (1992)). A way to realize this was already proposed in Braginskii et al. (1978), Caves et al. (1980), and Braginsky et al. (1980). These works introduce theoretical proposals to circumvent back-action when probing a harmonic oscillator, mainly in the framework of gravitational wave detection. The idea is to choose an observable that remains free of back-action throughout the probing.

[4] Often classical noise sources like technical noise already preclude one from attaining the SQL. Technical noise sources can prevent one from reaching quantum noise limited operation of a sensor.

In the previous section, we observed that the cosine component of $\hat{x}_{\mathrm{L}}^{\mathrm{out}}$ suffers from the back-action of the conjugate light quadrature ($\hat{p}_{\mathrm{L}}$) for the canonical light operators. To realize a quasi-QND measurement in our system of light-atom interaction, where our measurements are always performed in the laboratory frame, we must fulfill some criteria. First, our interaction must be of the QND type. This means that for repeated measurements and free evolution of the system in between measurements, the conjugate observable should not feed its perturbations into our desired observable (Caves et al. (1980)). We can understand this as follows. Back-action disturbing and altering our measurement of an observable $\hat{p}$ can either directly originate from the measurement or be mediated by the conjugate observable $\hat{x}$ during the free evolution of the system. Both cases prevent us from repeatedly measuring a desired observable $\hat{p}$ to arbitrary precision, and, in this case, we cannot avoid detrimental back-action (Caves et al., 1980). We can rephrase this observation into a requirement for measuring $\hat{J}_z$, without $\hat{J}_z$ suffering from undesired back-action. Therefore, we require an interaction fulfilling $\left[\hat{H}, \hat{J}_z\right] = 0$ as derived in Braginsky and Khalili (1996). In our case, the interaction Hamiltonian is $H_{\mathrm{I}} \propto \hat{S}_z \hat{J}_z \propto \hat{S}_z \left(\hat{J}'_z \cos(\omega_{\mathrm{L}} t) + \hat{J}'_y \sin(\omega_{\mathrm{L}} t)\right)$ which is solely valid in the case of large detuning of the probe light[5]. The condition for QND interaction is hence not generally fulfilled except for $\omega_{\mathrm{L}} = 0$. The presence of the bias magnetic field makes our transverse spin projections precess with the Larmor frequency $\omega_{\mathrm{L}} \neq 0$. As we have seen in the previous section, adding a bias magnetic field introduces an additional interaction described by the Hamiltonian $H_{\mathrm{B}} = \hbar \omega_{\mathrm{L}} \hat{J}_x$. As the reader can easily verify, this contribution to the overall interaction does not generally commute with $\hat{J}_z$, thus preventing realizing QND interaction. For this collective spin-oscillator, the proposal of stroboscopic back-action evasion, as discussed in Braginsky et al. (1980), can be exploited. While we cannot realize a continuous measurement that does not suffer from back-action onto the collective spin state, probing $\hat{J}_z$ using stroboscopic pulses at twice the spin precession frequency ω_{L} can circumvent this. Then, for certain times we will fulfill $\left[\hat{H}_{\mathrm{I}}, \hat{J}_z\right] = \left[\hat{H}_{\mathrm{I}}, \hat{J}'_z\right] = 0$, allowing us to realize a non-continuous QND type interaction.

Experimentally, we detect the signal in the sideband at ν_{L} with respect to the carrier frequency. Typically, we record only the cosine component oscillating at the Larmor frequency of our quantum light field $\hat{S}_y^{\mathrm{out}}(t)$ using a lock-in amplifier. This light component contains information about $\hat{J}_z(t)$ in the laboratory frame that contains information about both transverse spin observables in the rotating frame (equation (3.5)) for measurement durations $T > 1/\nu_{\mathrm{L}}$ if we probe our system continuously but will not contain any information about $\hat{J}'_y$ if we modulate the drive light intensity accordingly. We already established that we can treat $\hat{S}_x$ as a classical property. This means that the detected atomic signal $\hat{J}_z(t) \propto \hat{J}'_z \cos(\omega_{\mathrm{L}} t) + \hat{J}'_y \sin(\omega_{\mathrm{L}} t)$ is analyzed only for its Fourier component oscillating in phase with $\cos(\omega_{\mathrm{L}} t)$. Since we want to modulate the probe light intensity, we account for the stroboscopic modulation and hence mod-

[5] We will later show in, e.g., chapter 5, that we commonly use probe light locked more than 1.9 GHz away from any atomic transition. Therefore, contributions from the interaction Hamiltonian in (2.25) proportional to a_2 are neglected.

ulated atom-light interaction by multiplying with a time-dependent intensity modulation function $\Phi(t)$, defined such that the overlap with the recorded cosine component is optimized (Vasilakis et al. (2015))[6]:

$$\Phi(t) = \begin{cases} 1: & -DT/4 + kT \leq t \leq DT/4 + kT \\ 0: & DT/4 + kT < t < -DT/4 + (k+1/2)T \\ 1: & -DT/4 + (k+1/2)T \leq t \leq DT/4 + (k+1/2)T \end{cases} \tag{3.16}$$

with k being an integer number and T now being given as the oscillation period, not the total measurement duration as before. As illustrated in figure 3.3, the envelope function describing the modulation of the probe light pulses $\Phi(t)$ has an oscillation period of $T = 2\pi/\omega_L$, with probe pulses arriving at a rate of $2\nu_L$ with a width determined by the duty cycle D. These stroboscopic probing pulses enable us to avoid adding back-action noise from the light onto our spin state in the limit of $D \to 0$. The reason is that probing $\hat{J}_z$ in this way singles out the cosine component and hence only probes $\hat{J}_z \propto \hat{J}'_z \cos(\omega_L t)$. Only the combination of this stroboscopic probing together with choosing to look only at the cosine component of S_y^{out} enables us to get rid of the quantum back-action, while the latter alone would not allow us to do so. Therefore, no additional back-action is added when modulating the probe light intensity. The observable under investigation is unchanged when measured, fulfilling $\left[\hat{J}_z(t_1), \hat{J}_z(t_2)\right] = 0$ only for specific times, making $\hat{J}_z(t)$ not a continuous but rather stroboscopic QND variable (Caves et al. (1980); Braginsky et al. (1980).

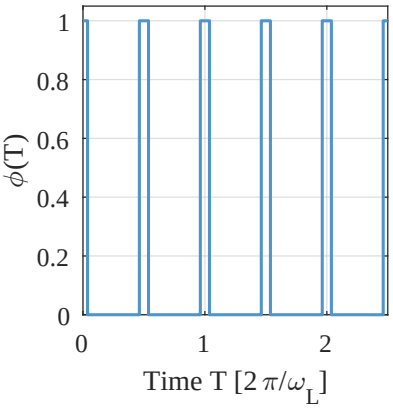

Figure 3.3: Illustration of envelope function. Plot of $\Phi(t)$ as stated in equation (3.16) with $D = 0.15$ and time axis scaled to units of oscillation period $T = 1/\nu_L$.

Experimentally, we record a signal over many oscillation periods, corresponding to $\tau = NT$, where T is one Larmor precession period. For experimental simplicity, we do not consider any weighting of our data, such that we can describe our observable as (Vasilakis et al., 2015; Shen, 2014):

$$\hat{S}_{y,NT}^{\text{out},c} = \sum_{k=0}^{N} \left[\hat{S}_y(kT) + a\bar{\phi}_x T \hat{j}_z(kT)\right] \tag{3.17}$$

$$\hat{S}_y(kT) = \int_{kT}^{(k+1)T} \mathrm{d}t \hat{S}_y^{\text{in}}(t)\Phi(t)\cos(\omega_L t) \tag{3.18}$$

where we introduce $\bar{\phi}_x$ as the average photon flux per period and the collective spin component $\hat{j}_z(kT)$. The input light operator $\hat{S}_y^{\text{in}}(t)$ does not interact with the spin-oscillator, and hence if it is assumed to be independent of the initial spin state, this remains true for all times. Further, the correlations between light states with different k for the k-th oscillation considered in (3.18) vanish. Under these assumptions, the simplified expression derived in Vasilakis et al. (2015) explicitly depending on the choice of probe duty cycle D can be obtained:

$$\langle \hat{S}_y(k_1 T)\hat{S}_y(k_2 T)\rangle = \frac{\bar{\phi}_x T}{4}\left[1 + \mathrm{sinc}(\pi D)\right]\delta_{k_1,k_2}, \tag{3.19}$$

where we introduced the average photon flux per oscillation $\bar{\phi}_x$ such that $\bar{\phi}_x T$ determines the number of photons incident during a single oscillation period. We also introduced δ_{k_1,k_2}, representing the Kronecker δ.

[6] It should be noted that in the following we are not using the canonical operators as used in Shen (2014) and Vasilakis et al. (2015), but rather express it in the notation used in our manuscript Zheng et al. (2022).

The second contribution to equation (3.17) contains the collective spin component $\hat{j}_z(kT)$, which is given by (Shen (2014)):

$$\hat{j}_z(kT) = \frac{1}{TD}\int_{kT}^{(k+1)T} \mathrm{d}t \hat{J}_z(t)\Phi(t)\cos(\omega_{\mathrm{L}}t) \tag{3.20}$$

and accounts for analyzing cosine mode and the modulation of our probe light intensity as defined by $\Phi(t)$ (equation (3.16)). The expression in equation (3.20) describes the signal obtained from the demodulated cosine quadrature of a single oscillation period depending on our choice of stroboscopic probing duty cycle D. To evaluate the full expression of equation (3.17), we need a description for $\hat{j}_z(kT)$. We will keep following the authors of Vasilakis et al. (2015) and Shen (2014) and express $\hat{j}_z(kT)$ as two uncorrelated contributions:

$$\hat{j}_z(kT) = \hat{j}_z^{\mathrm{free}}(kT) + \hat{j}_z^{\mathrm{BA}}(kT) \tag{3.21}$$

The first contribution originates from the spin-oscillator state before the light atom interaction (Vasilakis et al. (2015)), while the latter describes the influence of the back-action arising from our measurement. In Shen (2014) and Vasilakis et al. (2015), the free spin-oscillator evolution $\hat{j}_z(kT)$ is found to be:

$$\begin{aligned} a\bar{\phi}_x T\hat{j}_z^{\mathrm{free}}(kT) &= \frac{a\bar{\phi}_x T}{TD}\int_{kT}^{(k+1)T} \mathrm{d}t \left(\hat{j}'_z\cos(\omega_{\mathrm{L}}t) + \hat{j}'_y\sin(\omega_{\mathrm{L}}t)\right)\Phi(t)\cos(\omega_{\mathrm{L}}t) \\ &= \frac{a\bar{\phi}_x T}{2}\hat{j}'_z\left[1+\mathrm{sinc}(\pi D)\right] \end{aligned} \tag{3.22}$$

Contributions proportional to the free atomic evolution governed by the slowly varying spin components of the initial-time atomic operators in $\hat{j}_z(kT)$ then lead to a variance of:

$$\begin{aligned} \mathrm{Var}\left(a\bar{\phi}_x T\hat{j}_z^{\mathrm{free}}(kT)\right) &= \frac{a^2\bar{\phi}_x^2T^2}{4}\mathrm{Var}\left(\hat{j}'_z\right)\left[1+\mathrm{sinc}(\pi D)\right]^2 \\ &= \frac{a^2\bar{\phi}_x^2T^2}{4}\frac{J_x}{2}\left[1+\mathrm{sinc}(\pi D)\right]^2 \end{aligned} \tag{3.23}$$

The second contribution to equation (3.21) arises from the back-action of the interaction with light. As the calculation to find the correlation between different periods k_i is rather extensive, we will refrain from going through it here but rather state the result, derived in Shen (2014), only:

$$\langle \hat{j}_z^{\mathrm{BA}}(k_1T)\hat{j}_z^{\mathrm{BA}}(k_2T)\rangle \propto \left[K+2\min(k_1,k_2)\right]\left[1-\mathrm{sinc}(\pi D)\right]\left[1+\mathrm{sinc}(\pi D)\right]^2 \tag{3.24}$$

with K as a numerical factor on the order of unity (Shen (2014)). Following Shen (2014), the end result for the full expression of the recorded variance over many oscillations $N \gg 1$ for the cosine quadrature of $\hat{S}_{y,NT}^{\mathrm{out},c}$ is obtained as:

$$\begin{aligned} \mathrm{Var}\left(\hat{S}_{y,NT}^{\mathrm{out},c}\right) = \frac{N\bar{\phi}_x T}{4}\left[1+\mathrm{sinc}(\pi D)\right]\Bigg(1+\frac{\kappa^2}{2}\left[1+\mathrm{sinc}(\pi D)\right] \\ +\frac{\kappa^4}{12}\left[1+\mathrm{sinc}(\pi D)\right]\left[1-\mathrm{sinc}(\pi D)\right]\Bigg) \end{aligned} \tag{3.25}$$

We recover the result from the previous section for the continuous probing for the case $D = 1$, as $\mathrm{sinc}(\pi) = 0$. With the definitions used here, $N\bar{\phi}_x T$ is the total number of photons N_{Ph} interacting with the atomic spin ensemble over the total duration of the acquired signal over N cycles. However, we can simplify this expression by introducing the following:

$$\eta = 1 + \mathrm{sinc}(\pi D) \tag{3.26}$$

$$C = \frac{1 - \mathrm{sinc}(\pi D)}{1 + \mathrm{sinc}(\pi D)} \tag{3.27}$$

$$\tilde{\kappa} = \sqrt{\eta}\kappa \tag{3.28}$$

allowing us to rephrase equation (3.25) to:

$$\mathrm{Var}\left(\hat{S}^{\mathrm{out},c}_{y,NT}\right) = \frac{\eta N_{\mathrm{Ph}}}{4}\left(1 + \frac{\tilde{\kappa}^2}{2} + C\frac{\tilde{\kappa}^4}{12}\right) \tag{3.29}$$

The value of C depends on the choice of duty cycle D, illustrated in figure 3.4. What can easily be seen is that for $D \to 0$, and hence $C \to 0$, the back-action contribution to equation (3.29) vanishes. In this case, the only noise contributions will be the shot noise of the light and the contribution arising from the atomic projection noise. The stroboscopic probing pulses and the sine and cosine function matching the Larmor frequency of our system are shown in figure 3.5 to illustrate why the back-action introduced to our system reduces for smaller duty cycles. For an infinitely short duty cycle, our measurement does not overlap with the sine mode in, for example, equation (3.8a), causing the back-action noise in our measurement. How much back-action noise is introduced to our measurement is what the constant C represents. In the limit of continuous probing, it approaches 1 (see figure 3.4), reflecting the back-action noise contribution introduced to our system for continuous measurement. For $D \to 0$, the value of C also approaches the same limit ($C \to 0$). Hence, we will start introducing back-action into our measurement for any finite duty cycle value D. This is independent of our choice of considering only the cosine component of our recorded light signal when imagining a larger duty cycle in figure 3.5. We would also like to comment on the coupling constant $\tilde{\kappa}$ depending on the duty cycle D. For $D = 1$, we recover $\tilde{\kappa} = \kappa$, while in the limit $D \to 0$, our coupling constant increases and approaches the maximal value of $\tilde{\kappa} \to \sqrt{2}\kappa$.

The expression for the expected best signal-to-noise ratio will improve compared to the measurement suffering from back-action stated in equation (3.14). Exploiting complete back-action evasion ($D \to 0$), the SNR should be given as follows:

$$\mathrm{SNR} \propto \frac{\tilde{\kappa}}{\sqrt{1 + \frac{\tilde{\kappa}^2}{2}}} \tag{3.30}$$

For the eddy current detection, the application of this back-action evading measurement of a single transverse spin component of the collective spin os-

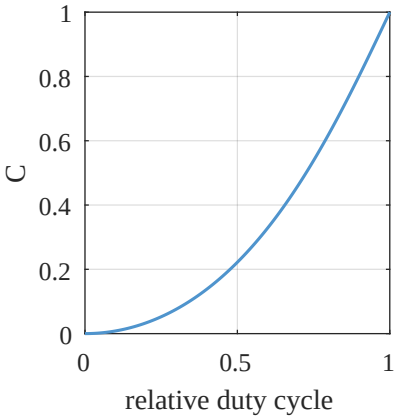

Figure 3.4: C versus duty cycle. Value of parameter C (equation (3.27)) versus the choice of duty cycle D for the stroboscopic probing pulses as defined in (3.16).

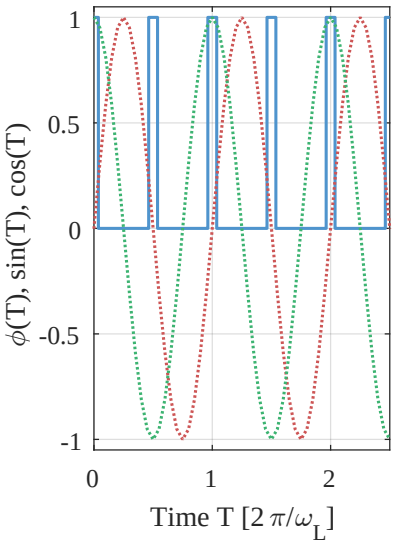

Figure 3.5: Illustration overlap modes and stroboscopic probing. Cosine (green) and sine (red) function scaled to unit period and plotted together with our stroboscopic probe pulses ($D = 15\,\%$).

cillator, we should observe a scaling of its sensitivity inverse to the SNR:

$$\delta B_{\mathrm{ec}} \propto \frac{\sqrt{1+\frac{\tilde{\kappa}^2}{2}}}{\tilde{\kappa}} \tag{3.31}$$

Let us sum up what we have seen throughout this chapter. We have found ways to describe the collective dynamics via input-output relations based on the description of the interaction between a spin-oscillator and light. One of the key findings was that for a continuous interrogation of the spin with light, we would add back-action noise to our system. However, we want to realize a QND-type measurement. While it is impossible to implement an experimental configuration allowing us to measure one observable continuously with a QND-type measurement, stroboscopic probing should allow for a stroboscopic QND measurement. We are probing the spin-oscillator at twice its precession frequency, allowing us to probe only one of the slowly-varying quadratures while only adding back-action to the orthogonal quadrature. Since we add noise to the slowly-varying observable in quadrature, overall, the Heisenberg uncertainty principle is maintained. To quantify the improvement from back-action evasion in the light quadrature of our choice, we have found expressions for the signal-to-noise ratios for continuous and stroboscopic measurements. While imagining infinitely short stroboscopic pulses is theoretically easy, practical reality will be limited to a finite duty cycle. We have developed a toy model to realize a QND-type measurement for δ-peak probing ($D \to 0$). We will exploit the description introduced here in the chapters focusing on the QMIT experiment, starting from chapter 12 onward.

Chapter 4

Single-photon interface of the DLCZ-type

This chapter will describe the deterministic single-photon generation from a room-temperature atomic ensemble. The underlying idea stems from the DLCZ protocol originally proposed in Duan et al. (2001). The DLCZ protocol is a quantum repeater scheme for long-distance entanglement generation aimed at quantum communication using atomic ensembles and linear optics. Our experiment focuses on the room-temperature implementation of one of the fundamental nodes for a quantum repeater of the DLCZ protocol.

In this chapter, we will first cover the generic idea of the DLCZ protocol as introduced by Duan et al. (2001) (section 4.1) and motivate why we can use this approach as an on-demand single-photon source with built-in memory. Intrinsic to the protocol is that the single-photon generation follows a two-step scheme: the creation or write step and the retrieval or read step. We will introduce the underlying processes for the write step in section 4.2.1 and the read step in section 4.2.2. After introducing the write and read step, the three consecutive sections will cover how we overcome physical limitations. First, we discuss how we benefit from cavity enhancement (section 4.3). Then we will address how to overcome detrimental noise from the four-wave mixing processes during the read process (section 4.4). Lastly, we explain the technique of *motional averaging* (section 4.5) ensuring efficient single-photon retrieval. The last part of this chapter, section 4.6, will introduce the second-order correlation functions used to quantify the performance of our single-photon source and quantum memory.

4.1 Idea of the DLCZ protocol

Exploiting quantum mechanical effects such as superposition and entanglement, but also the non-cloning theorem, allowed the invention of quantum communication protocols that would be intrinsically secure and allow for detecting the presence of eavesdroppers (see section 1.4). Many of these protocols rely on a quantum channel, for example, entanglement between two

points. One of these protocols focusing on creating such a quantum channel is the DLCZ protocol (Duan et al. (2001)). It relies on atomic ensembles and linear optics to generate entanglement over a large distance.

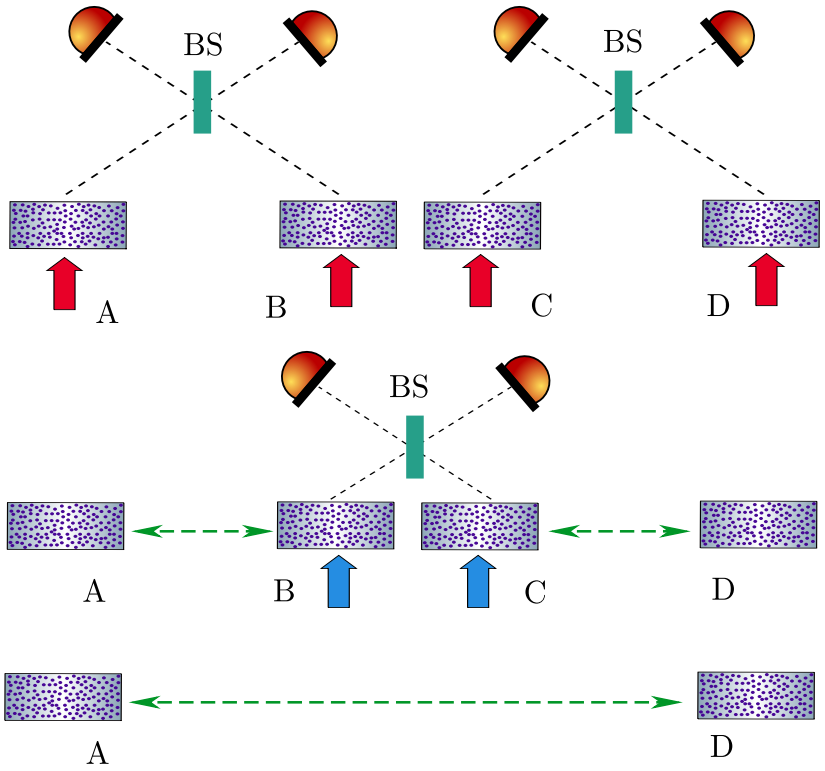

Figure 4.1: Illustration of DLCZ protocol. Sequential entanglement generation between points A and D by first generating entanglement between links A-B and C-D (top). After the successful entanglement of elementary links, the entanglement is swapped by reading out the atomic ensembles at points B and C, which form a quantum repeater (mid). Reading out the stored excitations at points B and C and combining the retrieval light fields with a beamsplitter will swap the entanglement shared between points A and B, and, C and D, respectively, to be shared among points A and D (bottom). See text for more details.

The underlying idea of the DLCZ protocol is to create entanglement over a large distance by dividing the length into smaller segments and generating entanglement first on these elementary links. The DLCZ protocol exploits atomic ensembles at each end of the elementary links to generate entanglement on the elementary links. In the first step, a collective excitation is created inside each atomic ensemble with low probability in parallel. The success is indicated by scattering a heralding photon (section 4.2.1). The scattered light fields are combined using a beamsplitter with detectors placed at its output ports as illustrated in figure 4.1 (top part). Then, detecting a single heralding photon entangles the two atomic ensembles at each end of the elementary link. This process is inherently probabilistic. Therefore, the successful operation requires the atomic ensembles to act as a quantum memory to allow for

repetitions of the entanglement generation in parallel links until the entanglement generation of all elementary links is completed. In the next step, the entanglement between neighboring links is swapped by retrieving the stored excitation and combining the retrieval light fields on a beamsplitter as indicated in the center of figure 4.1. Through this entanglement swapping, one can create entanglement over a larger distance. Sequentially repeating the entanglement swapping would allow the creation of entanglement over larger and larger distances. This entanglement swapping not only relies on maintaining the stored collective excitation within the ensemble (quantum memory) but also relies on the retrieval of a single-photon on-demand (section 4.2.2).

4.2 Ensemble-Light interaction for herald-retrieve scheme

In the following, we will revisit the generic light-atom interaction introduced in section 2.4 and develop a description of the herald-retrieve scheme of the DLCZ protocol from this point. The starting point will be equations (2.22) and (2.23), along with the interaction Hamiltonian exploiting the rotating wave approximation (2.24).

We employ the herald-retrieve scheme of the DLCZ-type for a room-temperature ensemble of cesium atoms, exploiting a λ-level scheme. It consists of one excited level, $|e\rangle$, and two distinct ground states, denoted $|g\rangle$ and $|s\rangle$. The single-photon generation consists of two distinct steps. The first step, which we refer to as *write*, is inherently probabilistic (subsection 4.2.1). For this, we write a collective excitation into the ensemble, which coincides with the scattering of a *heralding* photon (see figure 4.2 a). In a second step - the *read*, we read out the previously stored excitation in the form of an on-demand single-photon – the *retrieval* photon (see figure 4.2 b). We address the retrieval in subsection 4.2.2.

Before looking into the two processes exploited for the heralding and consecutive retrieval step, we need to introduce some simplifications to equation (2.24). Our total Hamiltonian describing the dynamics of light, atoms, and their interaction contains three contributions $\hat{H} = \hat{H}_\mathrm{A} + \hat{H}_\mathrm{L} + \hat{H}_\mathrm{int}$. In the case of being far-detuned and weak excitation, adiabatic elimination can be exploited to effectively remove the excited state $|e\rangle$ from the description. Using this adiabatic elimination, we can describe the dynamics utilizing an effective ground state Hamiltonian $\hat{H}'_\mathrm{int}$. It can be generalized to multiple excited and ground state levels, taking the form (Hammerer et al. (2010)):

$$\hat{H}'_\mathrm{int} = \sum_{m,m'} \left[-\hbar \sum_{m''} \frac{\Omega_{m,m''} g^*_{m',m''}}{2\Delta_{m''}} \right] |g_{m'}\rangle \langle g_m| \tag{4.1}$$

Here, the first sum (m, m') accounts for all transitions between the distinct ground state levels. The second sum (m'') accounts for all excited state levels with their respective light detuning $\Delta_{m''}$ mediating the coherent population transfer. We can understand $\Omega_{m,m''} g^*_{m',m''} / (2\Delta_{m''})$ as the effective Rabi frequency between the two ground states. It is governed by the detuning

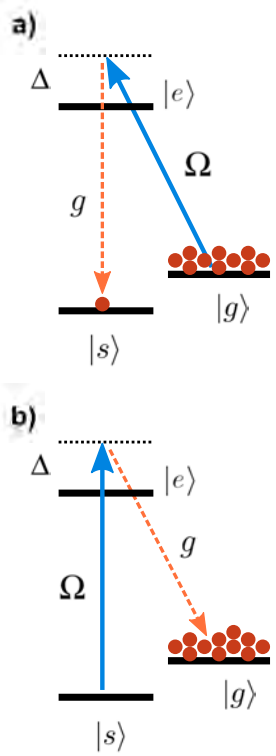

Figure 4.2: λ-schemes for herald-retrieve scheme. Top: Creation of a collective excitation using classical light field with Ω with all atoms initially prepared in $|g\rangle$ and scattering an atom into groundstate $|s\rangle$ by scattering a photon into quantum field g. Bottom: Retrieval of stored excitation in $|s\rangle$ by using strong classical field Ω and scattering quantum light field g.

$\Delta_{m''}$ from the m''-th excited state, the classical field Rabi frequency Ω and the single-photon Rabi frequency g of the quantum field (Hammerer et al. (2010)). The following will describe the write and read step more detailed.

4.2.1 Write

For the deterministic single-photon generation based on the two steps of the DLCZ scheme, we will first describe the dynamics allowing us to create a collective excitation within the atomic ensemble. Exploiting a λ-scheme with the classical drive field with coupling constant Ω that is far-detuned, a spontaneous Raman scattering process can be used to coherently transfer an atom from groundstate $|g\rangle$ to a different ground state, denoted by $|s\rangle$. Figure 4.2 a illustrates the level structure and light fields for this spontaneous Raman scattering process.

The starting point of our description is a cesium atomic ensemble, which we prepare employing optical pumping (see section 5.2) in a coherent spin state. This coherent spin state describes the state where all atoms of the ensemble are prepared in the $|F = 4, m_F = 4\rangle$ state. This collective state will be the first of our two ground states $|g\rangle$ required for the λ-level structure of our protocol. Using a far-detuned light pulse ($|\Delta| \gg 1$), as indicated in figure 4.2 a, coupling to the ground state $|g\rangle$, a spontaneous Raman scattering process can be induced, mediated via a virtual excited level (dashed line in 4.2 a). This scattering process produces a collective excitation, effectively exciting an atom into $|s\rangle$. Due to energy conservation, this coincides with the scattering of a photon. Since the photon indicates success in creating a collective excitation, we refer to this photon as the *heralding* photon. The collective excitation that can be described by the operator $b^\dagger$ in equation (2.16) assumes equal contribution from all atoms to the collective excitation. However, this is different from the description above. We have to account for the asymmetric coupling between the atoms and the light during the interaction. This means the collective excitation is not necessarily shared equally between all atoms. One can interpret this as knowing how likely the photon was scattered from specific atoms. In Hammerer et al. (2010), it is shown how equation (2.16) can be extended to account also for asymmetric modes. The term asymmetric mode refers to the case where different atoms contribute with different magnitudes to the collective spin excitation. Considering that excitation and scattered light field both propagate along the z, Hammerer et al. (2010) show that the atomic operators can be expressed using mode functions $u_m(\vec{r}_\perp, z)$ as (Hammerer et al. (2010)):

$$\hat{b}_m(z) = \int \mathrm{d}^2\vec{r}_\perp u_m(\vec{r}_\perp, z)\hat{b}(\vec{r}) \tag{4.2}$$

In analogy to the atomic operator $\hat{b}(z)$, light operators can be defined, which we will denote $\hat{a}(z)$ to avoid confusion with the atomic operators. Preparing a single excitation in our atomic ensemble while heralding the success by scattering a photon is a type of interaction known as the parametric gain-type

$H \propto \hat{a}^\dagger \hat{b}^\dagger + \hat{a}\hat{b}$. This parametric gain Hamiltonian can be understood as the write-in of a collective excitation coinciding with the creation of an excitation in the scattered light field and vice versa for the annihilation. Suppose that scattered light field and collective atomic excitations start with zero excitations. Only the first part of the parametric gain Hamiltonian will be relevant for describing our system. Under this condition, the parametric gain interaction creates states of the two-mode squeezer type (Sangouard et al. (2011)):

$$\begin{aligned} |\xi\rangle_2 &= \frac{1}{\cosh(\xi t)} \sum_{n=0}^{\infty} (-\mathrm{i})^n \tanh^n(\xi t) \, |n_\mathrm{A}, n_\mathrm{L}\rangle \\ &= \sqrt{1-p_0} \sum_{n=0}^{\infty} (-\mathrm{i})^n p_0^{n/2} \, |n_\mathrm{A}, n_\mathrm{L}\rangle \end{aligned} \tag{4.3}$$

where we have introduced the excitation probability as $p_0 = \tanh(\xi t)$. The indices A and L indicate the atomic and scattered light modes, respectively, with n as the number of excitations.

Assuming perfect atomic state preparation of all atoms in $|g\rangle$, and π-polarized write excitation light, we can effectively realize a three-level λ-system as shown in figure 4.3 a. With this, assuming a flat transverse profile for the interaction and the z-axis as the light propagation direction, the light-atom interaction describing our desired write processes is found to be (Hammerer et al. (2010)):

$$\begin{aligned} \hat{H}_\mathrm{W} = \hbar \int_0^L \mathrm{d}z \Bigg[&\frac{|\Omega(z,t)|^2}{4\Delta} \sum_m \hat{b}_m^\dagger(z) \hat{b}_m(z) \\ &- \left(\frac{\Omega(z,t) g^*(z)}{2\Delta} e^{\mathrm{i}\Delta k_\mathrm{W} z} \sum_m \hat{a}_m^\dagger(z) \hat{b}_m^\dagger(z) + \mathrm{h.c.} \right) \Bigg] \end{aligned} \tag{4.4}$$

Here, the first part of the Hamiltonian is just a constant energetic shift, an AC Stark shift, affecting the atomic ground state. The second part of the write Hamiltonian contains the parametric gain interaction with the coupling constant $g(z) \propto n_\mathrm{A}(z) \propto N_\mathrm{A}$ depending on the atomic density via N_A. In a vapor cell, the density within the interaction volume is constant when keeping the ambient conditions constant. The number of atoms interacting governs the coupling constant, providing an essential advantage over a single atom. This dependency makes atomic ensembles one of the core elements of the DLCZ protocol in Duan et al. (2001). The overall interaction is enhanced when increasing the atomic density in a vapor cell, for example, by heating it. The expression in equation (4.4) is summed over all possible modes m. The integration of the Hamiltonian is reduced to one dimension along the length of the ensemble. We have to include the phase $e^{\mathrm{i}\Delta k z}$ since our two ground states are non-degenerate but are energetically separated by the Larmor frequency ν_L. This phase will be referred to as a spin wave. It will play a crucial role in the success of retrieving a single-photon (section 4.2.2). The name *spin wave* can be understood when considering that the spontaneous Raman scattering pro-

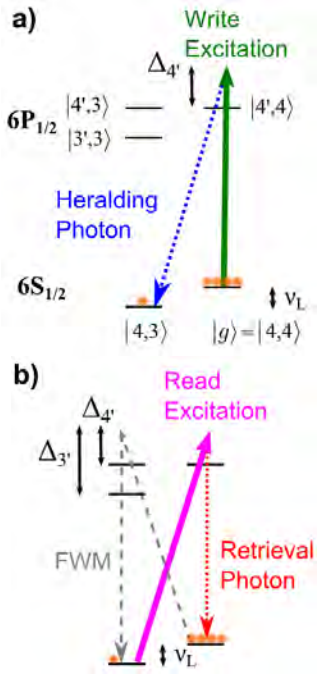

Figure 4.3: Illustration of four-wave mixing process. Atomic levels involved in the heralding (top) and retrieval (bottom) step. During the retrieval, four-wave mixing processes are mediated by excited levels and choice of retrieval light polarization. Figure adapted from Dideriksen et al. (2021).

cess, a two-photon process, effectively "flips" atomic spins by changing their value of m_F.

Due to the nature of the interaction in equation (4.4), the detection of a single scattered photon will project the atomic state onto one specific atomic mode (Lukin (2003)). The scattered light photon is often referred to as *Stokes*-photon, in analogy to the convention used in Raman scattering. However, this requires that the storage state $|s\rangle$ has higher energy than the ground state $|g\rangle$ (Sangouard et al. (2011)), which is not the case in our specific choice of Zeeman level storage. Nevertheless, we will sometimes still use this notation of Stokes and anti-Stokes photons to illustrate the analogy to other schemes.

4.2.2 Readout

Deterministic single-photon generation can be achieved in the case of the DLCZ protocol as a consecutive retrieval of a previously stored excitation. Given that we herald the existence of a collective excitation during the write step of the protocol, as discussed in the previous section 4.2.1, this should be possible by the correct choice of interaction.

As opposed to the write step, where creating a collective excitation should coincide with an excitation created in the scattered light field, the read requires a slightly different process. This time, the previously created atomic excitation should be annihilated while scattering, and hence retrieving, a single-photon. The process in a simplified three-level λ-scheme is illustrated in figure 4.2 b. We, therefore, are interested in finding a process of the type $\hat{H} \propto \hat{a}^\dagger \hat{b}$. As before, $\hat{b}$ describes the atomic annihilation operator, while $\hat{a}^\dagger$ corresponds to the creation operator acting on the quantum light field. The process can be realized by swapping which of the two ground states the classical light couples to in order to address the collective excitation directly. The light-atom system dynamics, illustrated in figure 4.2 b, are derived in Hammerer et al. (2010). For this, mode functions similar to equation (4.2) with the replacement $u_m(\vec{r}_\perp, z) \leftrightarrow u_m^*(\vec{r}_\perp, z)$ are used. The Hamiltonian used for describing the read step is then given by (Hammerer et al. (2010)):

$$\hat{H}_\mathrm{R} = -\hbar \int_0^L \mathrm{d}z \left[\frac{|\Omega(z,t)|^2}{4\Delta} \sum_m \hat{b}_m^\dagger(z)\hat{b}_m(z) + \frac{|g(z)|^2}{\Delta} \sum_m \hat{a}_m^\dagger(z)\hat{a}_m(z) + \left(\frac{\Omega(z,t)g^*(z)}{2\Delta} e^{\mathrm{i}\Delta k_\mathrm{R} z} \sum_m \hat{a}_m^\dagger(z)\hat{b}_m(z) + \mathrm{h.c.} \right) \right] \tag{4.5}$$

This Hamiltonian consists of three parts. First, as before, we have an AC Stark shift affecting the atomic state. However, the direction of the energetic shift is in the other direction compared to the write Hamiltonian (equation (4.4)). The second contribution affects only the scattered quantum light field, corresponding to the index of refraction arising from the gaseous cesium atoms in the vapor cell. The interesting part of equation (4.5) is the last contribution to the Hamiltonian. It connects the atomic and scattered field modes with an exchange of quanta for modes with the same mode number m. This type of

interaction is referred to as beamsplitter interaction. As for the write step, we also have to account for a phase arising from the energetic difference between the two ground states involved in the process. The phase term got the index R here to indicate that different processes can be involved. Assuming that we have a single collective excitation stored, this retrieval process should allow us to read out this excitation in the form of a single-photon. Due to the preceding heralding of the collective excitation, this retrieval is deterministic. Like the write process, this retrieval photon is often denoted as the *Anti-Stokes* photon. However, we have to be careful since the Anti-Stokes photon, in our case, has a higher energy than the drive light. We will still follow this commonly used convention for convenience here.

While this description allows us to describe and understand the dynamics, this alone will not suffice to ensure the success of the protocol. As a first step, we will have to consider the two phases and the respective implications arising from these. In Sangouard et al. (2011), this issue of the spin wave is discussed thoroughly. Here, we will only introduce it briefly. To illustrate the problem arising from the phases acquired during the write and read processes, let us consider the following. If we succeed in the retrieval of the read single-photon, our atomic ensemble should be in its ground state we started out with initially. However, due to the phase terms in equations (4.4) and (4.5), the final state will have an amplitude proportional to:

$$|\Psi_{\mathrm{R}}\rangle \propto \sum_{n=1}^{N_{\mathrm{A}}} \exp(\mathrm{i}(\vec{k}_{\mathrm{W}} - \vec{k}_{\mathrm{S}})\vec{x}_n) \exp(\mathrm{i}(\vec{k}_{\mathrm{R}} - \vec{k}_{\mathrm{AS}})\vec{x}'_n) \tag{4.6}$$

We refer to the wave vectors of our write and read classical light fields as W and R, while we indicate the wave vectors for the Stokes and Anti-Stokes photon as S and AS. The sum is over all atoms of the ensemble, where we indicate the position of the n-th atom as $\vec{x}_n$. For atoms not moving, e.g., atoms in a cell with buffer gas or cold atomic clouds[1], the amplitude is maximal if the acquired phases fulfill the following condition to ensure constructive interference (Sangouard et al., 2011):

$$\vec{k}_{\mathrm{W}} - \vec{k}_{\mathrm{S}} = -(\vec{k}_{\mathrm{R}} - \vec{k}_{\mathrm{AS}}) \tag{4.7}$$

The condition in equation (4.7) is trivially fulfilled if the levels are degenerate. However, spatial separation of the photons is required in this case, as spectral filtering will not be possible. A thorough discussion of the impact of dephasing of the atoms where scattered light fields are detected at an angle θ can be found in Zhao et al. (2009). In addition, one needs to avoid that the atomic motion on the scale of the imprinted phase leads to significant dephasing. In the case of our experiment, the wavelength of the imprinted spin wave will be significantly larger than the spatial extent of the atomic ensemble, making dephasing a minor effect in our case (Zugenmaier (2018)). The long wavelength of our spin wave and the forward scattering in our comparably short ensemble lead only to minuscule changes in the phase factors for different atomic

[1] Of course, one cannot consider the atoms as fully immobile either, but their diffusion motion opposed to our anti-relaxation coated cells is significantly reduced. Diffusion, so the motion of the atoms in and out of the interaction region is still one of the main limitations, e.g., Felinto et al. (2005) in cold atoms limiting the coherence time to a millisecond, and Eisaman et al. (2005) observed a few µs coherence time for warm ensembles. This issue will be covered more in detail in section 4.5.

positions in equation (4.6). This makes the precise position of atoms irrelevant. Instead, the mode of the spin wave will govern the success, as we will see in the following.

In our choice of system, we operate in the collinear configuration, and spectral filtering will be used to filter out the desired scattered light fields (see sections 9.4.1 and 9.4.2). Furthermore, despite the atomic motion, we rely on the spin wave not decaying. Due to our choice of geometry, the phase affects only the spin state along the z-axis, the light propagation direction. Because the cavity is creating an effective standing wave together with our drive light being far-detuned, we effectively remove the impact of Doppler effects due to the light field inside the cavity that can be viewed as a superposition of two counter-propagating light fields (Borregaard et al. (2016)). Due to the atomic motion, only the symmetric mode can easily be stored and consecutively retrieved. The reason for this can be intuitively understood when considering the impact of atomic motion on an asymmetric mode. Let us assume that one specific asymmetric mode is written into the ensemble. Since it is subjected to atomic motion, it cannot be easily addressed during the readout as the "configuration," so the atoms' momentary position and velocity distribution has already changed by then. This makes the symmetric mode the only accessible mode in our case.

In Shaham et al. (2020), the dynamics of highly polarized atomic ensembles are modeled for coated and uncoated vapor cells. When the atoms undergo many wall collisions while not changing their spin state, the atomic ensemble is in the diffusive regime (Shaham et al. (2020)). The authors find that only the symmetric mode is long-lived for those anti-relaxation coated cells, while all asymmetric mode contributions decay much faster. The findings by Shaham et al. (2020) indicate and verify previous findings (see Borregaard et al. (2016)) that only the symmetric mode is long-lived and suited for adequate storage and consecutive retrieval of a collective excitation in our experimental configuration. Since the excitation is spread out across all atoms, additional spin wave decay mechanisms, such as atomic motion, do not affect the symmetric mode. Therefore, the decay of this mode should be governed by the lifetime of coherences across Zeeman levels. However, this we previously introduced as the transverse spin decay time T_2, and hence we expect the lifetime of the symmetric collective excitations to be governed by the same decay mechanisms. How to overcome this limitation in the case of moving atoms and efficient selection of the symmetric collective excitation for the write and read will be discussed further in section 4.5.

4.3 Cavity enhancement

For the success of our write-read scheme, we rely on efficient interaction between the light and the atoms. A common technique to enhance the interaction between light and atoms is to place the atomic ensemble inside a cavity. Our experiment is no exception here; already in the original proposal for the

DLCZ protocol, the authors suggested placing the ensemble inside a cavity (Duan et al. (2001)). While we will introduce the experimental specifics of our cavity and cell in section 9.3, we will look at the generic description of the expected enhancement during write and read.

We will consider a standing wave cavity for our description and place the cell in the center (figure 4.4). The enhancement compared to the free space case has been discussed in Tanji-Suzuki et al. (2011).

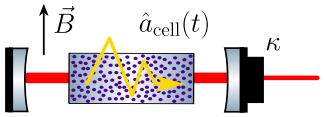

Figure 4.4: Illustration cell in cavity. Simplified illustration of one-sided cavity used for efficient outcoupling κ, together with the vapor cell at the center. The arrows indicate the transverse magnetic field direction and scattered photon wave packet.

In terms of on-resonance optical depth d, the free-space cooperativity η_{fs} can be expressed as $\eta_{\text{fs}} = d/2$ (Dideriksen (2021); Tanji-Suzuki et al. (2011)). The on-resonance optical depth can readily be determined from the absorption measurement presented in section 7.3 as $d(\nu = 0) = \rho\sigma(\nu = 0)L_z$ with $\alpha(\nu) = \sigma(\nu)L_z$ as the detuning-dependent absorption governed by Clebsch-Gordan coefficients (section 7.3). In Tanji-Suzuki et al. (2011), the authors find that the cooperativity inside the cavity can be related to the free-space cooperativity as:

$$\eta_{\text{cav}} = \frac{2\mathcal{F}\eta_{\text{fs}}}{\pi} = \frac{dF}{\pi} \tag{4.8}$$

with $\mathcal{F}$ as the finesse of the cavity. This equation illustrates that the cavity enhances the effective optical depth d by a factor of $2\mathcal{F}/\pi$. It should be noted that this is the case where the light interacts twice per round trip with the atoms. For a traveling cavity, i.e., a cavity with a single pass per round trip, only half of the enhancement will be achieved, as shown for example in Gorshkov et al. (2007).

So far, this cavity enhancement has been an abstract property, leading to an enhanced interaction due to a higher effective optical depth. Furthermore, this enhanced interaction and the finite outcoupling efficiency of light out of the cavity reduces the filter requirement as the scattering rate of photons is proportional to the optical depth d. We can understand the cavity enhancement as follows. For the same number of scattered photons, the cavity enhancement of the optical depth will reduce the required number of classical photons to create a scattered photon by a factor of $\pi/(2\mathcal{F})$. We will investigate and discuss this further in the later chapters 9 and 11. Furthermore, a more rigorous description and derivation can be found in Dideriksen (2021).

4.4 Four-wave mixing and its suppression

In the experimental implementation of the herald-retrieve scheme, the level structure of a real cesium atom will lead to experimental effects posing challenges for the experimental success. In figure 4.5, we indicate the appropriate Zeeman levels relevant to our write and read scheme. Experimentally, we use optical pumping to prepare all atoms in $|F = 4, m_F = 4\rangle$, which will form our ground state. For the write step, discussed in 4.2.1, we use π-polarized light to scatter a heralding photon with a low excitation probability p_0. In this process, our level structure is not leading to any unwanted effects. However, during the read step, indicated in the lower part of figure 4.3,

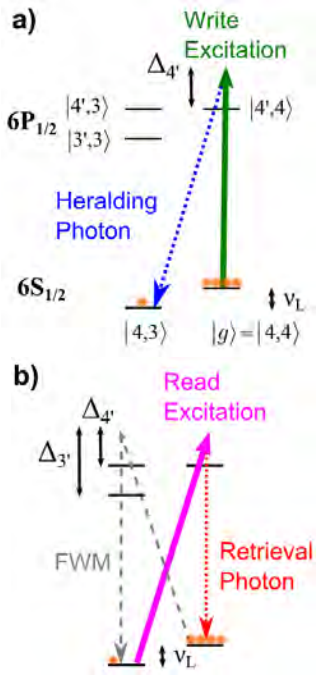

Figure 4.5: Illustration of the four-wave mixing process. Atomic levels involved in the heralding (top) and retrieval (bottom) step. During the retrieval, four-wave mixing processes are mediated by excited state levels and choice of retrieval light polarization. The solid arrow indicates the desired retrieval process, while the gray dashed arrows indicate the undesired write process during the readout. See the text for more details on four-wave mixing and its suppression. Figure adapted from Dideriksen et al. (2021).

our choice of experimental configuration leads, unfortunately, to unwanted effects. Due to the orientation of bias magnetic field and light propagation direction, along with the cell inside a cavity, the σ-polarized light is a superposition of σ_+ and σ_- for the atoms. For the successful retrieval, only the σ_+-polarized light is of interest (compare bottom part figure 4.5).

The undesired four-wave mixing processes lead to the detrimental effect that our retrieval drive light field also creates additional excitations. While the scattered photons from these false write processes are a problem, we at least can avoid their detection due to our spectral filtering. However, over the total duration of the read pulse, these new excitations can also be read out again. These false retrieval scattered photons are indeed a problem for us, as those are not correlated with any previously detected heralding photons during the write pulse. This four-wave mixing process during the retrieval was identified as the primary constraint in the previous incarnation of our DLCZ-type experiment, presented in Zugenmaier et al. (2018).

In order to understand the underlying dynamics of the detrimental four-wave mixing, we will consider Dąbrowski et al. (2014). The four-wave mixing for a Raman memory during the readout is discussed using the example of hyperfine storage using Rubidium-87. As mentioned before, four-wave mixing creates in our experimental configuration additional collective excitations during the readout that can consecutively be read out again. Therefore, the Hamiltonian contains terms resembling the beamsplitter-type Hamiltonian (compare equation (4.5)) and the parametric gain-type Hamiltonian (compare equation (4.4)). The dynamics of the four-wave mixing are illustrated in figure 4.6.

The dynamics combining a parametric gain-type and beamsplitter-type interaction can be described using the Hamiltonian as introduced in Dąbrowski et al. (2014):

$$\hat{H}_R = i\hbar \left(\chi \hat{a}_\chi^\dagger \hat{b} + \xi \hat{a}_\xi^\dagger \hat{b}^\dagger \right) + \text{h.c.} \tag{4.9}$$

where χ is the strength of the desired beamsplitter interaction, the associated scattered light field is proportional to $\hat{a}_\chi^\dagger$. The unwanted parametric gain interaction strength and scattered light field are given by ξ and $\hat{a}_\xi^\dagger$, respectively. As discussed in section 4.2.2, the desired part of this Hamiltonian is proportional to χ. In Dąbrowski et al. (2014), the mean expectation value for the anti-Stokes scattered photons is calculated assuming the initial scattered light field is in a vacuum state. The mean number of spin waves initially present is under this assumption given by $n_{\text{exc}} = \langle \hat{b}^\dagger(0)\hat{b}(0) \rangle$. The authors in Dąbrowski et al. (2014) reach:

$$\langle \hat{a}_\chi^\dagger(t)\hat{a}_\chi(t) \rangle = \chi^2 e^{(\xi^2-\chi^2)t} n_{\text{exc}} + \frac{\xi^2\chi^2}{\xi^2-\chi^2} \left(e^{(\xi^2-\chi^2)t} - 1 \right) \tag{4.10}$$

This expression shows that any contribution of four-wave mixing, i.e., $\xi > 0$, our dynamics cannot be fully described by a simple retrieval of previously stored excitations in the ensemble. If both processes are included in equation

(4.9), there will be coupled dynamics between the two scattered light fields causing additional readout noise.

In the trivial case, $\xi = 0$, our desired retrieval light field is simply dependent on the stored excitations and the coupling strength. The retrieval follows a simple exponential decay. Also, the Hamiltonian includes only the beamsplitter-type interaction then. Experimentally more interesting are the cases where $\xi > 0$. For $\xi > \chi$, the second term in equation (4.10) will lead to an exponential growth of "false" retrieval photons in the scattered light field. This would severely limit the expected cross- and auto-correlations of our experiment. For $\chi > \xi > 0$, we expect influence from false readout originating from four-wave mixing processes. In this case, it is possible to retrieve more excitations than initially written into the ensemble during the write process. However, an equilibrium level will ultimately be reached, governed by the prefactor of the second term in equation (4.10). Different experimental approaches are aimed at reducing or even suppressing contributions to the parametric gain interaction driven by the coupling constant ξ, but they come with different challenges on their own. These include, for example, the exploitation of cavities only resonant with the desired scattered photons and anti-resonant with the undesired scattered photons as pursued in Saunders et al. (2016) and Nunn et al. (2017).

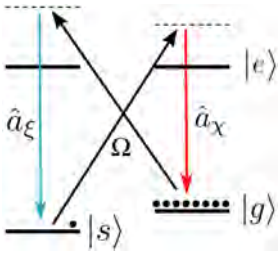

Figure 4.6: Four-wave mixing process. Simplified level structure indicating the involved states and transitions for the four-wave mixing. $\hat{a}_\chi$ illustrates the desired readout, while $\hat{a}_\xi$ indicates the undesired write process during the read pulse. Figure adapted from Dideriksen (2021).

For our experimental approach exploiting Zeeman level storage, we are interested in avoiding Raman scattering processes mediated via the excited level(s) driving false write processes during the read step. In Vurgaftman and Bashkansky (2013), Zeeman level storage in different hyperfine levels was chosen with $\Delta m_F = 2$ for a Rubidium vapor cell. The transitions mediated by different excited states interfered destructively, effectively suppressing them. Similar to the observation in Vurgaftman and Bashkansky (2013), this sparked the interest in Zugenmaier (2018) to investigate exploiting a *magic detuning*, for which the undesired write transitions mediated via different excited states would destructively interfere. For the D_2 line, such a magic detuning does not exist outside the Doppler-width of the excited states. However, for transitions on the D_1 line, it is possible to find a detuning where the two transitions driving detrimental "false" write processes during the read pulse have equal coupling strengths but are of opposite signs. This is the case for a detuning of $\Delta = 924\,\mathrm{MHz}$ from $|4', 4'\rangle$, where the four-wave mixing process is effectively suppressed, and only the desired readout process is possible. The specifics about the calculation can be found in Zugenmaier (2018), and have also been covered in Dideriksen (2021).

To conclude this section, we wish to summarize the reason for four-wave mixing and the necessity to suppress it. Due to our choice of geometry and Zeeman level storage with $\Delta m_F = 1$ and placing the cell inside a cavity, our σ-polarized read drive light is seen as a superposition of σ_+- and σ_--polarized light. The coupling of our system to the undesired σ_--polarized light has to be suppressed to avoid driving false write excitations causing undesired four-wave mixing processes. Choosing a magic detuning, we can get the two tran-

sitions coupling to the σ_--polarized light to destructively interfere, effectively leaving us with only the desired beamsplitter-type interaction for the retrieval process. This process is illustrated in the bottom part of figure 4.5.

4.5 Motional averaging

In our lab, we make use of vapor cells that are anti-relaxation coated to allow atoms to maintain their spin state upon hitting the walls of the channel. This also means that our atoms are free to move within the interaction volume, as opposed to buffer gas cells, where the atoms are immobilized using a buffer gas. The interaction volume is the channel of our vapor cell, confining the atoms in a well-defined volume[2]. While the movement of the atoms leads to the dephasing of atomic modes, we will in the following introduce the technique of *motional averaging* as introduced by Borregaard et al. (2016), effectively turning the detrimental atomic motion into an advantage by enabling addressing the long-lived symmetric mode during write and read steps. At the same time, the motional averaging enabled by high finesse cavities will ensure that when we detect a single-photon, the correlation with the momentarily atomic position remains washed out, as otherwise instantaneous detection would project the atomic ensemble onto an asymmetric mode. In order to not get this detrimental "which-way" information[3], a high-finesse cavity also acts as a random delay before the detection of the single-photon, washing out any atomic position and scattered photon correlations.

In the following, we will introduce the key ideas and concepts of Borregaard et al. (2016)[4], as these form one of the three pillars for our experimental results presented in chapter 10. First, let us consider our experiment's configuration and Zeeman level structure. As previously introduced (section 4.3), we enhance the light-atom interaction by placing the cell inside a low-finesse cavity. This means that in our case, the Gaussian beam intensity profile determined by the cavity mode is illuminating the vapor cell channel with a square cross-section of $300 \times 300\,\mu m^2$ and length of 10 mm. In order to average the interaction of the atoms with the drive light, a good filling factor – how well the transverse beam profile fills the cross-section of the channel – is required. Further, temporally long laser pulses and an anti-relaxation coating that allows the atoms to move back and forth through the light are exploited to average out the inhomogeneous light-atom interaction. Combining these allows us to enhance the interaction with the symmetric mode.

A second cornerstone in Borregaard et al. (2016) is the exploitation of additional spectral filter cavities with narrow linewidth. A narrow filter cavity is relevant as it ensures averaging the interaction between atoms and light, as the cell cavity itself with a low finesse on the order of 10 will not suffice. While we can easily employ polarization filtering of our scattered light (e.g., see section 4.2.1), spectral filtering is also possible and even needed, as we will see later (section 9). In the following, we will describe the dynamics. Figure 4.7 indicates the simplified experimental setup and level scheme.

[2] We will thoroughly introduce cells and their design in chapter 7.

[3] In analogy to the double slit experiment where the double slit interference pattern vanishes if we observe which path the photon takes, we would obtain information about the scattered photon origin if we detect the photon package instantaneously.

[4] It should be noted that the paper considered hyperfine storage as opposed to our choice of Zeeman level storage. Where necessary, we will comment on the differences throughout this section.

Let us start by considering the write-in of a collective excitation into an ensemble of moving atoms. As opposed to the sections 4.2.1 and 4.2.2, we need to account for the inhomogeneous coupling of the light to the moving atoms due to the Gaussian intensity profile. This is done by explicitly including spatial dependency into the expressions for the couplings g and Ω of each atom (Borregaard et al. (2016)):

$$\Omega^{(j)}(t) = \Omega e^{-\frac{x_j^2(t)-y_j^2(t)}{\omega^2}} \sin(k_W z_j(t)) \tag{4.11}$$

$$g^{(j)}(t) = g e^{-\frac{x_j^2(t)-y_j^2(t)}{\omega^2}} \sin(k_S z_j(t)) \tag{4.12}$$

We use g and Ω to denote the couplings as indicated in figure 4.7. The subscripts W and S refer to the write drive light field and scattered light field (Stokes photon[5]), respectively.

In order to find the scattered light field at the detector, indicated in figure 4.7 as $\hat{a}$, the scattered light field has to be propagated through the filter cavity ($\hat{a}_{\text{filter}}(t)$). For this, one first needs to find the field inside the cell cavity, described by $\hat{a}_{\text{cell}}(t)$. The authors in Borregaard et al. (2016) find the dynamics by formally integrating the equations of motion.

$$\hat{a} = -\frac{\kappa_2\sqrt{\kappa_1}}{4} \sum_{j=1}^{N_A} \theta_j(t)\hat{\sigma}_{10}^{(j)} \tag{4.13}$$

where κ_1 and κ_2 are the cavity decay rates of the cell and filter cavity. The sum accounts for all N_A atoms in the interaction volume. In addition, the dynamics are governed by population transfer $\sigma_{10}^{(j)}$ alone. This is a result of treating the light-atom interaction as a perturbation and that all atoms are initially in $|g\rangle = |0\rangle^{\otimes N_A}$. The j-th time-dependent atomic coupling $\theta_j(t)$ is given as (Borregaard et al. (2016)):

$$\theta_j(t) = \int_0^t dt' \int_0^{t'} dt'' \int_0^{t''} dt''' e^{-\kappa_2(t-t')/2} e^{-\kappa_1(t'-t'')/2} \times e^{-(\gamma/2-i\Delta)(t''-t''')} g_j^*(t'')\Omega_j(t''') \tag{4.14}$$

Here, the first integral describes the dynamics arising from the filter cavity (dt'), effectively shifting the atomic response compared to the detection and hence washing out the correlations between detection and atomic position correspondence. The second integral describes effects due to the cell cavity (dt''), and the third stems from the formal integration of the equation of motion (dt''') including the spontaneous decay γ of the atoms. The full derivation is shown in the supplements of Borregaard et al. (2016).

One figure of merit in our experiment is the write efficiency during the write step of the scheme. The detection of a scattered photon projects the ensemble onto a collective state. Good detection events will correspond to projection onto the symmetric collective state, which has to be scaled by the overall probability of detecting a photon, including symmetric and asymmetric collective excitations. For a write drive pulse duration of t_{int}, the authors

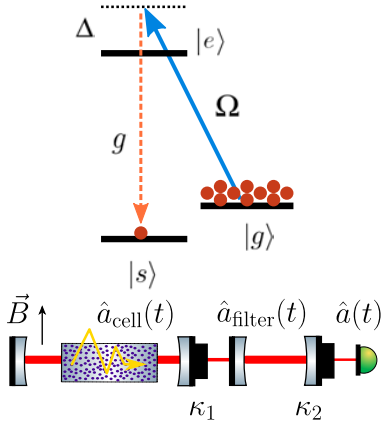

Figure 4.7: Motional averaging. Setup as proposed by Borregaard et al. (2016) for exploiting the motional averaging principle. Top: Write process with strong classical drive Ω and scattered field g between ground states $|g\rangle$ and $|s\rangle$ mediated via the excited level $|e\rangle$. Bottom: Setup for motional averaging. The operators refer to the quantum field in the cell cavity (subscript "cell"), the filter ("filter"), and the detector (no subscript). The two coupling constants of the cavities are denoted by κ_i Figure inspired by figure 1 in Borregaard et al. (2016).

[5] As in section 4.2, we will use the common choice of referring to the write (read) scattered photon as (Anti-)Stokes photon. We further note that this is formally incorrect due to the Stokes photon being of higher energy than the Anti-Stokes photon.

in Borregaard et al. (2016) find the general expression for the write efficiency to be governed by the time-dependent atomic coupling constants $\theta_j(t)$ as:

$$\eta_{\mathrm{W}} \approx \frac{\int_0^{t_{\mathrm{int}}} \left| \langle \theta_j(t) \rangle_e \right|^2 \mathrm{d}t}{\int_0^{t_{\mathrm{int}}} \langle \left| \theta_j(t) \right|^2 \rangle_e \, \mathrm{d}t} \tag{4.15}$$

where $\langle \ldots \rangle_e = \frac{1}{N_{\mathrm{A}}} \sum_{j-1}^{N_{\mathrm{A}}} \langle \ldots \rangle$ indicates that the ensemble average is taken. In order to determine the write efficiency based on the individual atomic coupling coefficients, the two contributions in equation (4.15) need to be analyzed. The denominator contains correlations between the atomic positions. The authors of Borregaard et al. (2016) find the expression of the correlation to be given by $\langle g_j(0) g_j(t) \rangle = \langle g_j(0)^2 \rangle \, e^{-\Gamma t} + \langle g_j(0) \rangle^2 \, (1 - e^{-\Gamma t})$ and verify their assumptions using Monte-Carlo simulation. Here, Γ is the decay rate of atomic position correlations. The first term contains correlations of individual atoms, only relevant on short time scales (Borregaard et al. (2016)). The second term dominates on long time scales and is proportional to correlations averaged over the atoms. Using this, together with the assumption that the linewidth of the filter cavity is much narrower than that of the cell cavity, the effective interaction time is governed by $1/\kappa_2$. The authors of Borregaard et al. (2016) reach, assuming a detuning beyond the Doppler width:

$$\begin{aligned} \eta_{\mathrm{W}} &\approx \frac{1}{1 + \frac{\kappa_2}{2\Gamma + \kappa_2} \left(\frac{4L^2}{\pi \omega_0^2} - 1 \right)} \\ &\approx 1 - \frac{1}{N_{\mathrm{pass}}} \end{aligned} \tag{4.16}$$

where the size of the beam is ω_0 and $2L$ is the diameter of the cell channel. We see that the filling factor, so how good the beam profile ($\pi \omega_0^2$) fills the transverse cross-section of the cell channel ($4L^2$), limits the potential write efficiency. The better the filling factor, the better the write efficiency. The second part influencing the write efficiency is how the filter cavity decay κ_2 scales compared to the decay rate Γ of the atomic coupling correlations. The higher the finesse of the filter cavity, and hence smaller κ_2, the closer we will approach unity in the write efficiency. The last approximation in equation (4.16) states that the write efficiency scales as the effective number of passes an atom can travel through the beam for a decay rate of $\kappa_2 \ll \Gamma$ of the filter cavity (Borregaard et al. (2016)).

More details on how the filling factor and decay rates impact the write efficiency η_{W}, including simulation and estimation for variable parameters, can be found in Borregaard et al. (2016). It has also been discussed extensively in Zugenmaier (2018). It should be noted that the different mode contributions have also been discussed in Shaham et al. (2020). There, the spectral composition of the spin noise spectrum has been considered as parameters of the cell cross-section and beam profile. Shaham et al. (2020) find that the broad contribution to the spin noise spectrum is a superposition of different Lorentzians with variable widths.

Following Borregaard et al. (2016), we use their simulation result, for an experimental setup very close in geometry to ours, of $\Gamma \approx 1.3 v_{\mathrm{th}}/\omega_0$ with v_{th} as the mean thermal velocity of the atoms and ω_0 as the waist of the beam to estimate the HWHM width of the broadband contribution. With a beam waist of $\omega_0 = 90\,\mu\mathrm{m}$ and a temperature of $T = 42\,^{\circ}\mathrm{C}$, the decay rate of the correlations is estimated to be on the order of $\Gamma = 2\pi \cdot 0.46\,\mathrm{MHz}$. Figure 4.8 shows the expected write spectrum. The broadband contribution, illustrating asymmetric collective excitations, is plotted with the desired narrowband feature illustrating the coupling to the symmetric collective excitation. As discussed, the symmetric mode is governed by the transverse spin coherence time. Therefore, the width of the narrow contribution to the spectrum is determined by our T_2 time. Experimentally, the spectral contributions as illustrated in figure 4.8 allow us to determine the write efficiency η_{W} as the ratio between the narrow peak height to the total peak height. We will exploit this later in chapter 10 when discussing our experimental results.

For the read process, Borregaard et al. (2016) determine the read efficiency η_{R} to be given by:

$$\eta_{\mathrm{R}} = \frac{\kappa_2^2 \kappa_1}{4} \int_0^{\tau_{\mathrm{R}}} \mathrm{d} \int_0^t \mathrm{d}t' \int_0^t \mathrm{d}t'' e^{-\kappa_2 (2t - t' - t'')/2} \left\langle \hat{a}^\dagger_{\mathrm{cell}}(t') \hat{a}_{\mathrm{cell}}(t'') \right\rangle \tag{4.17}$$

where τ_{R} is the duration of the read pulse. In order to find an expression for the retrieval efficiency, Borregaard et al. (2016) considers the case with $\Omega \to 0$ and $\tau_{\mathrm{R}}, \kappa_2 \to \infty$. The latter can be understood as using infinitely long readout pulses and an infinitely narrow filter cavity. This allows us to find a convenient expression for the retrieval efficiency to zeroth order, $\eta_{\mathrm{R}}^{(0)}$, as (Borregaard et al. (2016)):

$$\eta_{\mathrm{R}}^{(0)} \approx \frac{1}{1 + \frac{\pi}{d\mathcal{F}}} \tag{4.18}$$

where $\mathcal{F}$ is the finesse of the cell cavity and d is again referring to the optical depth. It should be noted that this expression is just an approximation and reflects the case of perfect motional averaging and considering long time scales. It also resembles the expression found for the retrieval efficiency in cold atoms as presented in Gorshkov et al. (2007).

Due to decoherence, we wish in our experiment to retrieve a stored excitation with read light pulses shorter than the finite lifetime of the stored collective excitations. Therefore, higher orders constituting the retrieval efficiency must be considered. The authors of Borregaard et al. (2016) address this issue. The retrieval efficiency is reduced when considering higher-order contributions, as those contain losses due to spontaneous emission. However, this also means that there will be a trade-off between how fast we can read out a stored excitation, as this coincides with using higher read drive light power, which speeds up spontaneous emission. For more details and the derivation of the higher order contributions to the retrieval efficiency η_{R}, please consider the supplements of Borregaard et al. (2016).

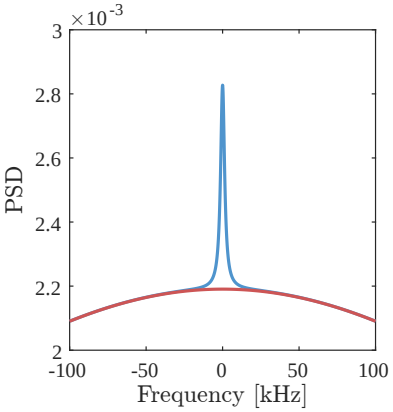

Figure 4.8: Expected write spectrum. Estimated write spectrum considering our experimental parameters for $\Gamma = 2\pi \cdot 0.46\,\mathrm{MHz}$ for the broadband contribution (red) and γ for the narrowband contribution (blue) based on our T_2 measurements. The ratio between contributions is chosen to aid the visualization. Figure inspired by figure 2.5 in Zugenmaier (2018).

4.6 Non-classical correlations

When dealing with single-photons, we are dealing with highly non-classical light. In order to quantify the statistics of our generated light fields, and hence how well we can create collective excitations and retrieve them again, we need a formalism allowing us to determine the correlations and statistics of the different light fields involved. In the following, we will describe the statistics of the different light fields involved and how we can find a criterion to relate the scattered light fields during write and read to each other.

We will be starting by introducing the classical second-order correlation function used to, for example, describe the coincidences of detector counts after a beamsplitter with detectors at each output port after a delay τ as (Gerry and Knight (2004)):

$$\gamma^{(2)}(\tau) = \frac{\langle I(t)I(t+\tau)\rangle}{\langle I(t)\rangle^2} \tag{4.19}$$

This second-order correlation function can be defined analogously for quantum fields using a quantized electric field. This allows us to describe the second-order correlation function using creation and annihilation operators $\hat{a}(t)$ and $\hat{a}^\dagger(t)$. Here, we stated the explicit time dependency. In the following, we will refrain from that. It will become more apparent why we can do this in our case throughout this section. Following Gerry and Knight (2004), the quantum second-order correlation function is given by:

$$G^{(2)}(\vec{r}_1, t_1, \vec{r}_2, t_2) = \left\langle \hat{a}_1^\dagger \hat{a}_2^\dagger \hat{a}_1 \hat{a}_2 \right\rangle \tag{4.20}$$

It will often be more practical for comparison between fields to deal with the normalized second-order correlation functions:

$$g^{(2)}(\vec{r}_1, t_1, \vec{r}_2, t_2) = \frac{\langle \hat{a}_1^\dagger \hat{a}_2^\dagger \hat{a}_1 \hat{a}_2 \rangle}{\langle \hat{a}_1^\dagger \hat{a}_1 \rangle \langle \hat{a}_2^\dagger \hat{a}_2 \rangle} \tag{4.21}$$

In the following, we will use equation (4.21) to find expressions for describing the properties of our recorded detection events in the experiment. The first measure is the second-order auto-correlation function of the write (W) and read (R) scattered light fields. For this, we rewrite the creation and annihilation operators in terms of number operators $\hat{n}_i$ exploiting $\left[\hat{a}, \hat{a}^\dagger\right] = 1$, since we will be "counting photons" in our experiments [6]:

$$g_{ii}^{(2)} = \frac{\langle \hat{n}_i (\hat{n}_i - 1)\rangle}{\langle \hat{n}_i \rangle^2} \text{with } i = [\mathrm{R}, \mathrm{W}] \tag{4.22}$$

which we will use to describe the correlations within the individual scattered light fields.

In addition, we can also use equation (4.21) to define the cross-correlation between the write and read scattered light fields. In this case, the expression takes a slightly different form as the operators commute in this case:

$$g_{\mathrm{WR}}^{(2)} = \frac{\langle \hat{n}_\mathrm{W} \hat{n}_\mathrm{R} \rangle}{\langle \hat{n}_\mathrm{W} \rangle \langle \hat{n}_\mathrm{R} \rangle} \tag{4.23}$$

[6] see Loudon and von Foerster (2000); Sekatski et al. (2012) for more details

which allows us to obtain information about the distribution of the photon number between the two fields (see Sekatski et al. (2012)). Our experiment will use well-defined time windows for write and read duration and consider the number of recorded photons during these. This is possible since our single photon detectors can be considered number resolving in our experiment (see 9.4.3 for details).

Elemental for the success of our write-read scheme is that the retrieval of single-photons is not only correlated with the successful detection of a heralding write scattered photon but also that we only retrieve a single scattered photon during the retrieval light pulse. For this purpose, we define the conditional second-order auto-correlation function of the read scattered light field. Conditional means that we consider the auto-correlation of the read light field, considering only cases where we detected a single write scattered photon during the preceding write pulse. We define:

$$g^{(2)}_{\mathrm{RR}\,|\,\mathrm{W}=1} = \frac{\langle \hat{n}_\mathrm{R}\,(\hat{n}_\mathrm{R}-1)\rangle_{\mathrm{W}=1}}{\langle \hat{n}_\mathrm{R}\rangle^2_{\mathrm{W}=1}} \tag{4.24}$$

and will always refer to this expression here when talking about our conditional auto-correlation. This expression tells us how likely it is to detect two photons in the scattered retrieval light field during the read pulse, given that we detected a single write heralding photon during the write pulse. Therefore, it can be considered a measure of how likely triple photon events (2 R, 1 W) are to occur. In the case of photon-number states $|n\rangle$, we can easily see that a perfect single-photon character of our read scattered light field with $|n_\mathrm{R}=1\rangle$ would give a conditional second-order auto-correlation of $g^{(2)}_{\mathrm{RR}\,|\,\mathrm{W}=1}=0$. Experimentally, we will have noise counts arising from background counts and the like (see subsection 9.4.3). Consequently, we consider the expected conditional auto-correlation for a two-photon state, which exhibits $g^{(2)}_{\mathrm{RR}\,|\,\mathrm{W}=1}=1/2$, as an upper bound of the read scattered light field statistics. Thus, we say the read light field exhibits significant single-photon character if the observed conditional auto-correlation $g^{(2)}_{\mathrm{RR}\,|\,\mathrm{W}=1}$ is statistically significant below $1/2$.

We want to consider the non-classicality witness based on the Cauchy-Schwarz inequality $2I_1I_2 \leq I_1^2 + I_2^2$ (Loudon and von Foerster (2000)). Assuming classical light fields, one can find classical bounds for the second-order correlation functions [7] that cannot be violated by classical fields:

$$g^{(2)}_{ii} \geq 1 \quad \text{with} \quad i=[\mathrm{R},\mathrm{W}] \tag{4.25a}$$

$$g^{(2)}_{\mathrm{WW}}g^{(2)}_{\mathrm{RR}} \geq \left(g^{(2)}_{\mathrm{WR}}\right)^2 \tag{4.25b}$$

We note that the upper expression fulfills equality in the case of a coherent light field, while for thermal light fields, it takes the value $g^{(2)}_{ii}=2$. Please note that these classical bounds and their violation have also been considered already in Clauser (1972, 1974)[8].

[7] A very thorough derivation and also discussion of the implications can be found in Gerry and Knight (2004).

[8] Further, similar considerations of coincidences of two entangled single-photons were considered by J. Clauser and used for experimental violation of the Bell-inequality, discussed at length in Clauser and Shimony (1978). His efforts were rewarded with last year's Nobel prize (2022).

From equation (4.25b) one typically defines the Cauchy-Schwarz parameter $\mathcal{R}$, sometimes also referred to as non-classicality witness:

$$1 \geq \mathcal{R} = \frac{\left(g^{(2)}_{\mathrm{WR}}\right)^2}{g^{(2)}_{\mathrm{WW}} g^{(2)}_{\mathrm{RR}}} \tag{4.26}$$

As before, equality is obtained in the particular case of coherent light fields.

Often, $g^{(2)}_{\mathrm{WR}} > 2$ alone is taken as a sign of non-classicality. Commonly, assuming that our independent light fields originate from a perfect two-mode squeezed state (Sangouard et al. (2011)), the unconditional light fields should follow a thermal distribution (Gaussian statistics) with $g^{(2)}_{\mathrm{WW}} = g^{(2)}_{\mathrm{RR}} = 2$, exhibiting clear photon bunching. Then, an observation of a cross-correlation $g^{(2)}_{\mathrm{WR}} > 2$ alone is sufficient to violate the inequality. However, even for $g^{(2)}_{\mathrm{WR}} < 2$, it is possible to verify non-classicality using the Cauchy-Schwarz parameter $\mathcal{R}$ with scattered light field auto-correlations smaller than that of a thermal light field. For example, this approach has been used in Zugenmaier et al. (2018), and Kuzmich et al. (2003). Using the Cauchy-Schwarz parameter $\mathcal{R}$ is beneficial, as often losses and detection imperfections reduce the observed cross-correlations[9].

In Sekatski et al. (2012), a thorough analysis of the impact of imperfect detector efficiencies, and hence losses, on the Cauchy-Schwarz parameter $\mathcal{R}$ and second-order cross-correlation functions are considered. They show that the expression is also valid in the presence of imperfect detection and losses and if the detectors are not photon-number resolving.

In order to avoid double excitations and only create a two-mode squeezed state with one photon in each mode, we only use a very low excitation probability p_0. For a perfect two-mode squeezed state, the respective cross-correlation scales as (Sangouard et al. (2011)):

$$g^{(2)}_{\mathrm{WR}} = 1 + \frac{1}{p_0} \tag{4.27}$$

where we see that the overall attainable cross-correlation is limited by the excitation probability[10]. We usually remain in the low excitation probability regime to observe high cross-correlations and ensure that double or triple excitations are negligible.

At the same time, the conditional read auto-correlation function is also governed by the excitation probability p_0 for $p_0 \ll 1$ (Chou et al. (2004)):

$$g^{(2)}_{\mathrm{RR\,|\,W}} \approx 4p_0 \tag{4.28}$$

[9] For a thorough description, consult the supplementary information of Kuzmich et al. (2003).

[10] It should be noted that the expression only holds for number resolving photon detection, in the case of non-number-resolving, it scales only as $1/p_0$.

4.6.1 Modelling correlations in the presence of noise

In the following, we will shortly introduce the method we used to model the correlations obtained experimentally. This has been part of our joint publication in Dideriksen et al. (2021). It was described extensively in Dideriksen (2021), and we will summarize it here.

Limited detector efficiencies, losses along the optical path, and background noise counts introduce losses and noise into our cross- and auto-correlations. Consequently, we wish to find expressions describing our real experimental system. The derivation is performed using probability-generating functions, also referred to as PGFs. We exploit the assumption that all recorded light fields are quantized, including coherent and noise contributions to read and write scattered light fields. All detection events are performed in the Fock basis ("counting photons"); hence, the phase relations between different light states are neglected.

In the following, we will describe the combined observed detection events as an independent sum of the coherent and noise counts as W = X + A for write and R = Y + B for read, where the noise processes are denoted A and B with mean numbers λ_A and λ_B for the detection events. The coherent contributions from the two-mode squeezed state are X and Y for write and read, respectively. These follow a joint thermal distribution of photon pairs, the probability for n photon pairs given as (compare equation (4.3)):

$$p_n = (1 - p_0)p_0^n \tag{4.29}$$

for an excitation probability p_0 and mean excitation $\mu = \frac{p_0}{1-p_0}$. In order to include the experimental reality of losses, we have to account for different effects. During both write and read, we suffer from outcoupling losses from the cell cavity[11], leading to a finite escape efficiency η_{esc}, affecting write and read scattered photons to the same extent. We use dedicated filtering and detection setups for write and read scattered photons. We determine the detection efficiencies of each setup experimentally (compare sections 9.4.1 and 9.4.2) and indicate them as η_{det}^W and η_{det}^R. For the read, we additionally have to account for the finite retrieval efficiency of the stored excitation in the form of the desired on-demand single-photon. We will denote the retrieval efficiency η_R^*. The combined efficiencies are therefore given by $\eta_X = \eta_{esc}\eta_{det}^W$ for coherent write detection events and $\eta_Y = \eta_R^*\eta_{esc}\eta_{det}^R$ for coherent read detection events.

Cross-correlation

In Dideriksen (2021), the cross-correlation is derived as:

$$g_{WR}^{(2)} = 1 + \frac{\mu(1+\mu)}{(\mu + \lambda_A/\eta_X)\,(\mu + \lambda_B/\eta_Y)} \tag{4.30}$$

using the PGFs and the previously introduced mean excitation μ, detection efficiencies for write, η_X, and read, η_Y, along with the mean noise detection events λ_A and λ_B. Let us have a brief look at different cases. In general, this function can be understood as a function of three variables: μ, λ_A/η_X and λ_B/η_Y. In the case of no noise, the latter two being zero, we recover the result stated in equation (4.27). When noise contributions are considered and have a finite contribution, this reduces the maximally obtainable cross-correlation. As soon as the mean noise detection events reach $\lambda_{A/B} \approx \eta_{X/Y}\mu$,

[11] For enhancing the light-atom interaction, we place the atomic ensemble in a cavity. This, at the same time, limits the outcoupling efficiency of the scattered photon. The experimental limitations are presented in detail in section 9.3, and the theoretical description has been provided in the preceding section 4.3.

the cross-correlation reduces to $g^{(2)}_{\mathrm{WR}} = 1 + 1/(4p_0)$, which is significantly reduced compared to the noise-free case.

Auto-correlation

We expect the true auto-correlation of the coherent write and read scattered light fields to be governed by the thermal distribution of the modes of the two-mode squeezed state. Hence $g^{(2)}_{\mathrm{XX}} = g^{(2)}_{\mathrm{YY}} = 2$, while we expect the experimentally observed auto-correlations to be compromised by noise. The noise auto-correlation of the write and read process will be referred to as $g^{(2)}_{\mathrm{AA}}$ and $g^{(2)}_{\mathrm{BB}}$. The observed auto-correlations for write $g^{(2)}_{\mathrm{WW}}$ and read $g^{(2)}_{\mathrm{RR}}$ should therefore be a mixture of the noise and coherent auto-correlations. In Dideriksen (2021), the expressions are found to be:

$$g^{(2)}_{\mathrm{WW}} = \frac{\eta_{\mathrm{X}}^2\mu^2 g^{(2)}_{\mathrm{XX}} + \lambda_{\mathrm{A}}^2 g^{(2)}_{\mathrm{AA}} + 2\eta_{\mathrm{X}}\mu\lambda_{\mathrm{A}}}{\eta_{\mathrm{X}}^2\mu^2 + \lambda_{\mathrm{A}}^2 + 2\eta_{\mathrm{X}}\mu\lambda_{\mathrm{A}}} \tag{4.31a}$$

$$g^{(2)}_{\mathrm{RR}} = \frac{\eta_{\mathrm{Y}}^2\mu^2 g^{(2)}_{\mathrm{YY}} + \lambda_{\mathrm{B}}^2 g^{(2)}_{\mathrm{BB}} + 2\eta_{\mathrm{Y}}\mu\lambda_{\mathrm{B}}}{\eta_{\mathrm{Y}}^2\mu^2 + \lambda_{\mathrm{B}}^2 + 2\eta_{\mathrm{Y}}\mu\lambda_{\mathrm{B}}} \tag{4.31b}$$

As before, we used the previously defined detection efficiencies and mean detection events. Let us have a look at the expressions. We see that there are three contributions in both expressions, the two auto-correlations for the respective write or read process and their respective noise auto-correlations, scaled with their respective mean counts squared as they deal with two-photon events. The third contribution accounts for uncorrelated coincidences of coherent- and noise-detection events. This "mixing" of the auto-correlations is responsible for the deviation of experimentally observed auto-correlations from those of a thermal state (see results in chapter 10).

Conditional auto-correlation

Verifying our retrieved light field's single-photon character is of utmost importance for our experiment. Finding an expression reflecting the dynamics in the presence of noise and losses will allow us to verify our experimental findings and help us identify how different contributions impact them. In order to find a similar expression as stated in (4.31b) for the conditional auto-correlation, one needs to find some additional expressions. In Dideriksen (2021), the conditional auto-correlation for the coherent readout conditioned on a single write scattered photon is found to be:

$$\begin{aligned} g^{(2)}_{\mathrm{YY}\,|\,\mathrm{W}=1} =& 2(1-\eta_{\mathrm{X}})\left(\lambda_{\mathrm{A}} + \eta_{\mathrm{X}}\mu + \lambda_{\mathrm{A}}\eta_{\mathrm{X}}\mu\right)\cdot \\ & \cdot \frac{\left(\lambda_{\mathrm{A}} + 2\eta_{\mathrm{X}} - \lambda_{\mathrm{A}}\eta_{\mathrm{X}} + 3\eta_{\mathrm{X}}\mu - \eta_{\mathrm{X}}^2\mu + \lambda_{\mathrm{A}}\eta_{\mathrm{X}}\mu - \lambda_{\mathrm{A}}\eta_{\mathrm{X}}^2\mu\right)}{\left(\lambda_{\mathrm{A}} + \eta_{\mathrm{X}} - \lambda_{\mathrm{A}}\eta_{\mathrm{X}} + 2\eta_{\mathrm{X}}\mu - \eta_{\mathrm{X}}^2\mu + \lambda_{\mathrm{A}}\eta_{\mathrm{X}}\mu - \lambda_{\mathrm{A}}\eta_{\mathrm{X}}^2\mu\right)^2} \end{aligned} \tag{4.32}$$

Further, since we consider only a subset of our measurements where we successfully heralded a collective excitation, we need an expression reflecting the

conditional mean excitation probability and conditional retrieval efficiency. In Dideriksen (2021), it was found to be:

$$\tilde{\mu} = \frac{\mu\left(\lambda_{\mathrm{A}} + \eta_{\mathrm{X}} - \lambda_{\mathrm{A}}\eta_{\mathrm{X}} + 2\eta_{\mathrm{X}}\mu - \eta_{\mathrm{X}}^2\mu + \lambda_{\mathrm{A}}\eta_{\mathrm{X}}\mu - \lambda_{\mathrm{A}}\eta_{\mathrm{X}}^2\mu\right)}{\left(1 + \eta_{\mathrm{X}}\mu\right)\left(\lambda_{\mathrm{A}} + \eta_{\mathrm{X}}\mu + \lambda_{\mathrm{A}}\eta_{\mathrm{X}}\mu\right)} \tag{4.33}$$

allowing to determine the conditional retrieval efficiency as $\eta_{\mathrm{R}} = \eta_{\mathrm{Y}}\tilde{\mu}$.

Now we have the necessary expressions to determine the conditional read auto-correlation in analogy to equation (4.31b), leading to (Dideriksen (2021)):

$$g^{(2)}_{\mathrm{RR}\,|\,\mathrm{W}=1} = \frac{\eta_{\mathrm{Y}}^2\tilde{\mu}^2 g^{(2)}_{\mathrm{YY}\,|\,\mathrm{W}=1} + \lambda_{\mathrm{B}}^2 g^{(2)}_{\mathrm{BB}} + 2\eta_{\mathrm{Y}}\tilde{\mu}\lambda_{\mathrm{B}}}{\eta_{\mathrm{Y}}^2\tilde{\mu}^2 + \lambda_{\mathrm{B}}^2 + 2\eta_{\mathrm{Y}}\tilde{\mu}\lambda_{\mathrm{B}}} \tag{4.34}$$

We will use these functions later in our analysis (chapter 10). The data obtained during our experimental runs will be used to fit $g^{(2)}_{\mathrm{WR}}$, η_R, and the mean number of read detection events $\langle n_R \rangle$. The results are used to overlay our experimental results for $g^{(2)}_{\mathrm{RR}\,|\,\mathrm{W}=1}$ with the model prediction from the fit model result. This will be discussed further in chapter 10.

Part II

Experimental methods and characterizations

Chapter 5

Laser system and optical pumping

This chapter and the consecutive chapters will introduce standard experimental methods used to prepare and characterize our experiments at Quantop. In this chapter, we will introduce the light sources used for all the experiments covered in this thesis, along with our method of optical pumping. As will become clear throughout the thesis, optical pumping for the coherent spin state (CSS) preparation is one of the fundamental building blocks for the successful operation of our experiments.

5.1 Light sources

For our experiments, we rely on different laser sources. Across all of the experiments covered in this thesis, we rely on three main lasers[1]. We refer to the lasers as the probe, pump, and repump laser, respectively. Their names originate from the purpose they are used for: the probe laser "probes" or interrogates the atoms. The pump and repump laser have names indicating their purpose in the optical pumping for the atomic spin state preparation. The latter's names will become apparent when the scheme for optical pumping is introduced in section 5.2.

Common to all our lasers is that they are external cavity diode lasers – often just referred to by their acronym ECDL. We lock them using saturated absorption spectroscopy. This allows us to lock to atomic transitions with higher precision than the Doppler broadening $\Delta\omega_D$ would usually allow for. In simple terms, the working principle relies on two counter-propagating light beams traveling through a so-called spectroscopy cell filled with cesium, as depicted in figure 5.1. The first beam is acting as a pumping beam due to its high intensity exceeding the saturating intensity of the atomic transition $\left(I_{\text{pump}} \gtrsim I_{\text{sat}}\right)$ (Foot (2005)). The counter-propagating, weaker probe beam then interacts with the atoms depending on their velocity along the probing direction. Depending on the atoms' velocity along the probing and pumping direction, their resonance frequency is shifted with respect to their velocity as $\omega = \omega_0 \pm kv$. Given that the beams are counter-propagating, scanning the laser frequency away from atomic resonances will lead to probe absorption

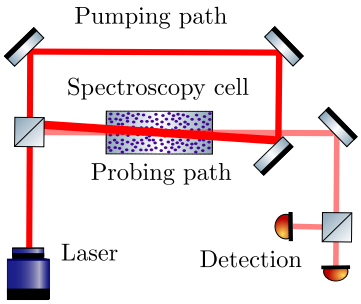

Figure 5.1: Saturated spectroscopy. Simplified setup of the saturated spectroscopy illustrating the beam paths used for generating a Doppler-free locking signal for locking the lasers. No waveplates are shown for simplicity.

[1] For the DLCZ-type experiment, we have one additional laser, but as it is particular to that experiment, the additional laser will be presented in the respective experimental setup for the DLCZ-type experiment (chapter 9).

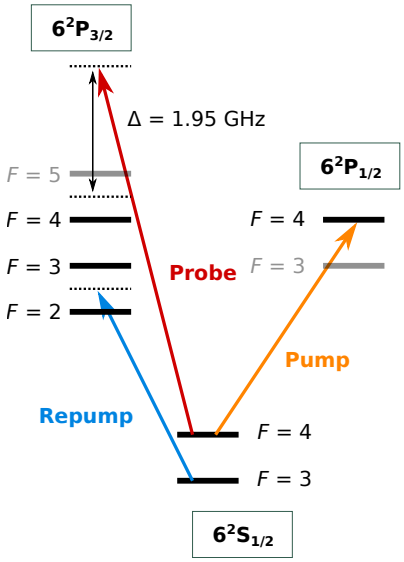

Figure 5.2: Laser transitions for locking. Transitions used for locking the probe laser ($F = 4 \rightarrow F' = 4,5 + 1.95\,\text{GHz}$), repump laser ($F = 3 \rightarrow F' = 2,3$ on D_2 line) and pump laser ($F = 4 \rightarrow F' = 4$ on D_1 line). Figure inspired by figure 3.1 in Thomas (2020).

as the probe and pump beam are resonant with atoms of different velocity classes since they are counter-propagating. The probe beam absorption is reduced when both beams are resonant with the atoms due to the transition being saturated from the much stronger pumping beam. Saturation is only the case when atoms have no mean velocity ($v = 0$) along the probing and pumping direction. No mean velocity along the beam propagation direction is only valid for a subset of the atoms subjected to Doppler broadening. When scanning the laser frequency, we only observe less probe absorption when this resonance condition is fulfilled for atoms exhibiting $v = 0$ along the probing direction. The obtained probe signal is a wide Doppler-broadened absorption dip with a narrow peak around the atomic resonance frequency (Foot (2005)). To get the strongest signal, we want the overlap between the two counter-propagating beams to be as considerable as possible. At the same time, we need to be capable of spatially separating the probe beam for the detection as indicated in figure 5.1. Modulating the laser frequency and monitoring the probe beam signal allows us to generate an error signal to lock the laser to an atomic reference. For more details on the specific experimental setups, one can consider Krauter (2011), while a general, more in-depth description of saturated absorption spectroscopy can be found in Foot (2005).

We lock the three lasers of our experiment to three different transitions, indicated in figure 5.2. The pump laser is locked on resonance to the $F = 4 \rightarrow F' = 4$ transition on the D_1 line (figure 5.2). The laser is a Toptica *DL100 pro design* laser, which includes a tunable grating and an optical isolator. The repump laser, a Toptica *DL pro* laser, is locked to the $F = 3 \rightarrow F' = 2,3$-cross-over transition on the D_2 line. This transition exists due to the Doppler width $\Delta\omega_D$ exceeding the energetic separation between the transitions to the different excited states (figures 2.1 and 5.2). In this case, additional cross-over transitions can be locked to as the resonance condition can also be fulfilled with atoms traveling at a velocity matching half of the energy difference between two different resonances[2]. The specific choice of locking for the repump will be discussed in sections 5.2 and 6.2 and was thoroughly analyzed in Thomas (2020).

We use a Toptica *DL pro* laser lasing on the D_2 line for our probe laser. Unique about this laser compared to the pump and repump laser is that we do not want to lock it close to any atomic transition. However, its frequency should also not be free running. Therefore, we use a fiber-coupled EOM to modulate the probe light to generate sidebands of the error signal of atomic transitions. This allows us to lock the probe laser with a fixed detuning to an atomic transition. In our case, we choose the second sideband to the blue. Depending on the precise modulation frequency[3], we lock the laser approximately 1.9 to 2.0 GHz from the $F = 4 \rightarrow F' = 4,5$-cross-over transition as it exhibits the most prominent error signal.

[2]For more details, consider chapter 8.3.2 on cross-over resonances in saturation spectroscopy in Foot (2005).

[3]It will become clear why we make slight adjustments to the modulation frequency when working with the DLCZ-type experiment.

5.2 The principle of optical pumping

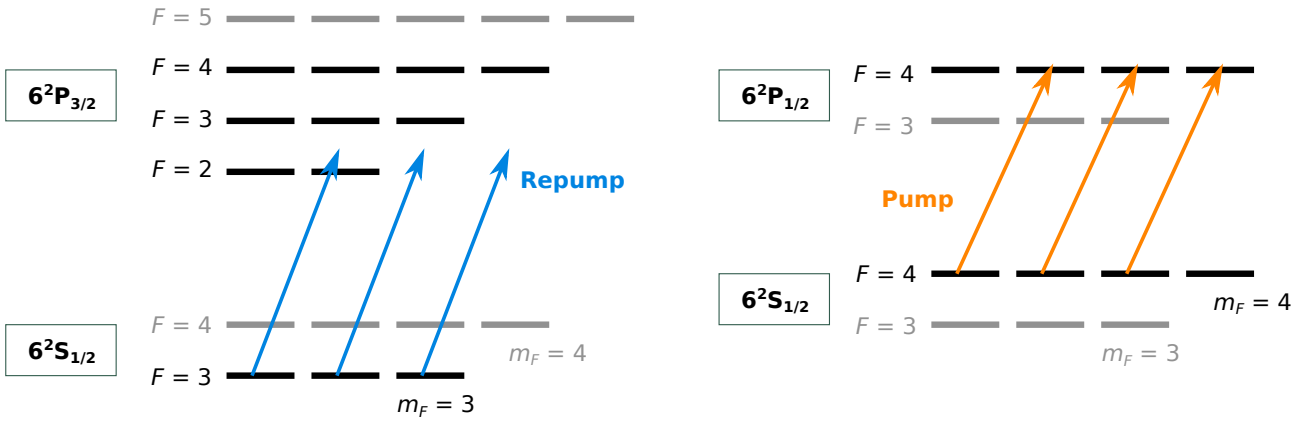

Figure 5.3: Optical pumping. Left: Relevant levels for repumping atoms from $F = 3$ using light locked to the $F = 3 \rightarrow F\prime = 2, 3$ crossover transition on the D2 line. Right: Pump transitions exploited for trapping atoms in the dark state $F = 4, m_F = 4$ using light locked to $F = 4 \rightarrow F\prime = 4$ on the D1 line. Diagonal arrows reflect σ_+ polarized light. Levels indicated in grey do not couple to the drive light due to selection rules or due to a detuning exceeding the Doppler width multiple times (far-detuned). Scattering processes not indicated. This figure was inspired by figure 4.8 in Julsgaard (2003).

Both experiments presented in this thesis rely on the collective spin oscillator being prepared in a coherent spin state (CSS). In this state, all cesium atoms are in the desired $F = 4, m_F = 4$ state exhibiting minimal projection noise. The spin ensemble is then said to be fully polarized along the quantization axis, determined by the bias magnetic field orientation.

To achieve this, starting from the equilibrium distribution of the atoms, we exploit the technique of optical pumping[4]. In order to polarize an atomic ensemble, we need to exploit polarized light. In our optical pumping scheme, we use two lasers, pump and repump, to collectively move the atoms in our spin ensemble to $F = 4, m_F = 4$ using σ_+-polarized light. There are two different purposes for the lasers, reflected in their names. The pump laser pumps the atoms in $F = 4$ towards higher m_F levels (figure 5.3). The selection rules for atomic transitions determine which transitions are dipole-allowed, which we will refrain from discussing here. For a derivation and introduction to the selection rules, the interested reader is referred to Foot (2005). Using σ_+-polarized light will, on average, increase the m_F level as shown in the simplified scheme for the pump showing the scattering processes in figure 5.4. As shown in that figure of the dipole-allowed transitions, m_F will never decrease using σ_+ polarized light. Since the $F = 4, m_F = 4$ has no dipole-allowed transition for σ_+-polarized light, atoms in this state do not couple to the pump light. The state is said to be a "dark" state. Applying the pump laser to the atomic ensemble will lead to atoms accumulating in this dark state.

Starting initially from an equilibrium distribution of the atomic ensemble, along with additional atoms scattered to the 3-manifold by the pump laser, a portion of atoms are "stuck" in $F = 3$ as the pump laser does not address

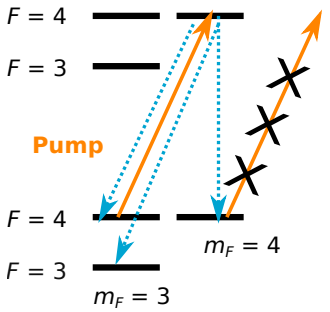

Figure 5.4: Allowed scattering transitions. Simplified level structure for the pump beam addressing atoms in $F = 4, m_F = 3$ (orange) and the allowed scattering processes (blue), as well as the dark state for $F = 4, m_F = 4$.

[4]For a comprehensive discussion on various optical pumping schemes, one might want to consider chapter 9 of "Optically polarized atoms - understanding light-atom interactions" (Auzinsh et al. (2010)).

them. To remedy this and increase the macroscopic spin for our experiments, we must remove the atoms in $F = 3$. Removing atoms from the 3-manifold can be done using the repump laser, addressing atoms in the 3-manifold. The repump process is illustrated in the left part of figure 5.3. Due to the Doppler-broadening and selection rules, the repump couples to three excited hyperfine levels. When optimizing the atomic state polarization, the best result has been obtained by locking the repump to the $F = 3 \rightarrow F' = 2, 3$-cross-over transition (see Thomas (2020)).

After some duration of optical pumping pulses, the atomic orientation, defined as (Julsgaard (2003))

$$p = \frac{1}{F} \sum_{m_F=-F}^{F} m_F \left\langle \hat{\sigma}_{m_F,m_F} \right\rangle , \tag{5.1}$$

can be determined. For a thermal state, all m_F levels exhibit equal populations $\left\langle \hat{\sigma}_{m_F,m_F} \right\rangle$, and hence $p = 0$. However, after optical pumping, we expect $p = 1$ if all atoms are successfully prepared in $F = 4, m_F = 4$. How to quantify our success with optically pumping the atomic ensemble toward preparing a highly polarized atomic ensemble, we need means of characterizing the atomic population distribution, which will be introduced in the following chapter 6.

Chapter 6

Atomic state characterization

Our experiments rely on the atomic spins prepared in specific collective spin states. The starting point for all experiments is the coherent spin state (CSS). We prepare our ensemble using optical pumping as described in the previous chapter (chapter 5). In the following, we will discuss the different experimental methods employed in our lab to optimize the optical pumping and determine the atomic spin orientation for our experiments.

This chapter will mainly present the techniques regarding (pulsed) MORS – magneto-optical resonance spectroscopy – by focusing on data obtained for the experimental setup of the DLCZ-type experiment. The choice originates from the fact that for the DLCZ-type experiment, we spent an extensive amount of time improving the optical pumping and coherent state preparation. We use the pulsed MORS technique to quantify the success, we have investigated this technique and the underlying model used to analyze the data. The principles presented throughout this chapter are also valid and have (partially) been adapted to the quantum-enhanced MIT covered from chapter 12 onward. The specifics for the experimental setup and characterization for the QMIT will be addressed in chapter 13.

6.1 MORS

The magneto-optical resonance spectroscopy (MORS) method can be used to determine the atomic spin polarization p of a macroscopic spin ensemble. Initially, this method was presented in Julsgaard (2003); Julsgaard et al. (2004). MORS allows us to determine the distribution of the atomic population across the different Zeeman levels of the ground-state hyperfine manifolds. This can be done using continuous probing and optically pumping while slowly sweeping the frequency of the RF field, driving Rabi oscillations between neighboring Zeeman levels. The RF field, oriented transverse to the bias magnetic field, creates a non-vanishing transverse spin component $\hat{J}_\perp$. The transverse spin component $\hat{J}_\perp$ precesses with the Larmor frequency $\omega_L = 2\pi \cdot \nu_L$. Similar to the Faraday angle measurement (section 7.4), this alters the birefringence of a far-detuned, linearly polarized probe. The orientation of optical

pumping and probing beams, along with bias and RF magnetic field orientation, is illustrated in figure 6.1.

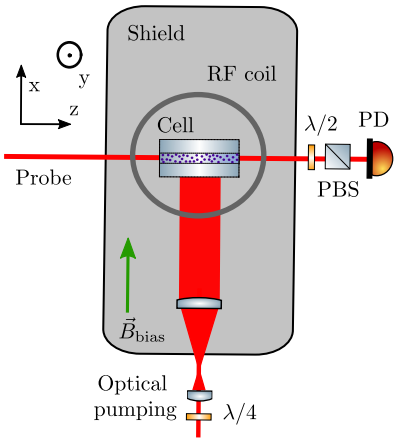

Figure 6.1: Experimental (p)MORS configuration. Illustration of the beam and magnetic field orientations used for exciting and reading out the transverse spin component for (p)MORS. See text for more details.

In the following, we will consider the macroscopic spin $\hat{J}_i$ and light $\hat{S}_i$ operators as introduced in chapter 2. Following the input-output relation presented in equation[1] (3.3a) in section 3.1, we can read out the orthogonal spin component by recording $\hat{S}_y^{\text{out}}(t)$. Please note that we use horizontally polarized input light such that S_x is again a macroscopic property. We use a half-wave plate after the vapor cell together with a polarizing beamsplitter to record the desired Stokes component $\hat{S}_y^{\text{out}}(t)$. For small rotation angles, the recorded photo current $I(t)$ of the detector – ignoring the linear DC component – allows us to gain access to the transverse spin component since $I(t) \propto \langle \hat{S}_y^{\text{out}}(t) \rangle \propto \langle \hat{J}_z(t) \rangle$ (Julsgaard, 2003).

To understand the MORS signal, we need to develop a description of the dynamics. Here, we will follow Julsgaard (2003) but provide only the key steps to reach the expressions required and only motivate the steps required to achieve the stated results. First, we will consider the spin state of the atomic ensemble containing N_{A} atoms in the hyperfine manifold F. We can describe the collective spin operators as (Julsgaard, 2003):

$$\hat{J}_x = N_{\text{A}} \sum_{m_F=-F}^{F} m_F \hat{\sigma}_{m_F,m_F} \tag{6.1a}$$

$$\hat{J}_y = N_{\text{A}} \sum_{m_F=-F}^{F} \frac{C(F,m_F)}{2} \left(\hat{\sigma}_{m_F+1,m_F} + \hat{\sigma}_{m_F,m_F+1} \right) \tag{6.1b}$$

$$\hat{J}_z = N_{\text{A}} \sum_{m_F=-F}^{F} \frac{C(F,m_F)}{2\text{i}} \left(\hat{\sigma}_{m_F+1,m_F} - \hat{\sigma}_{m_F,m_F+1} \right) \tag{6.1c}$$

where $C(F,m_F) = \sqrt{F(F+1) - m_F(m_F+1)}$ and $\hat{\sigma}_{i,j} = \frac{1}{N_{\text{A}}} \sum_{k=1}^{N_{\text{A}}} |i\rangle_k \langle j|_k$. The indices i,j can take all values in the range $i,j = [-F, -F+1, ..., F]$. Typically, we are interested in $F = 4$ for our experiments. However, the description can also be used for $F = 3$ when adjusting relevant information, such as the number of Zeeman levels, for example. Further, we need to consider the dynamics introduced to our collective spin system when applying a transverse RF magnetic field oscillating with $\omega_{\text{RF}} = 2\pi \cdot \nu_{\text{RF}}$ as $B_{\text{RF}}(t) = |B_{\text{RF}}| \cos(\omega_{\text{RF}} t + \phi)$ (along y-axis) while the spin-oscillator is subjected to a constant bias magnetic field[2] B_{bias} (along x-axis). For reference, the orientation of the fields is indicated in figure 6.1. Concerning ourselves only with the first-order interaction between the collective spins and the applied magnetic fields, the Hamiltonian describing the dynamics is given as follows (Julsgaard, 2003):

$$\hat{H} = g_F \mu_{\text{B}} \mathbf{J} \cdot \mathbf{B}$$

[1] For simplicity, we provide the expression here again:

$$\hat{S}_y^{\text{out}}(t) = \hat{S}_y^{\text{in}}(t) + a S_x \hat{J}_z(t)$$

[2] According to equation (2.3) the Larmor frequency is determined by the bias magnetic field as:

$$\nu_{\text{L}} = g_F \mu_{\text{B}} B_{\text{bias}} / h$$

$$= \sum_{m_F=-F}^{F} \hbar\omega_{m_F} \cdot \hat{\sigma}_{m_F,m_F} + \frac{g_F\mu_B}{4} \sum_{m_F=-F}^{F} \left(C(F, m-F)\hat{\sigma}_{m_F+1,m_F} B_{RF} e^{i\omega_{RF}t} + \text{h.c.} \right) \tag{6.2}$$

where the second equality exploits the definitions introduced in equations (6.1b,c). Further, we have introduced $B_{RF} = |B_{RF}|\, e^{-i\phi}$ as the complex amplitude of the RF field.

Finally, we are interested in finding an expression for the population differences between neighboring Zeeman levels in order to evaluate the distribution of atoms across a hyperfine manifold and determine the atomic polarization of the atomic spin ensemble. Therefore, Julsgaard (2003) employs the Heisenberg equation using the Hamiltonian in equation (6.2) and adds decay terms ($\Gamma/2$) by hand to account for the interaction of the system with the environment. This, together with defining $\hat{\tilde{\sigma}}_{ij} = \hat{\sigma}_{ij} e^{i\omega_{RF}t}$ as slowly varying operator, Julsgaard (2003) reaches the following:

$$\frac{\partial \hat{\tilde{\sigma}}_{m_F,m_F+1}}{\partial t} = \left(i\Delta\omega_{m_F} - \frac{\Gamma}{2} \right) \cdot \hat{\tilde{\sigma}}_{m_F,m_F+1} + \frac{i g_F \mu_B}{4\hbar} C(F, m_F) B_{RF} \left[\hat{\sigma}_{m_F+1,m_F+1} - \hat{\sigma}_{m_F,m_F} \right] \tag{6.3}$$

Here, we have introduced $\Delta\omega_{m_F} = \omega_{RF} - \omega_{m_F+1,m_F}$, reflecting the frequency difference between the RF field oscillation and the resonance frequency between two neighboring Zeeman levels. Since we wish to operate in the resolved regime, meaning that the quadratic splitting[3] ν_{QZ} exceeds the linewidth of the resonances between neighboring Zeeman levels, each resonance will be subject to its resonance frequency in the first term of equation (6.3):

$$\frac{\omega_{m_F+1,m_F}}{2\pi} = \nu_L - \nu_{QZ}\,(m_F + 1/2) \tag{6.4}$$

For the continuous MORS as discussed here, we are interested in finding the equilibrium solution to equation (6.3). Considering a stationary RF field, the solution to equation (6.3) is determined by Julsgaard (2003) to be given by:

$$\hat{\tilde{\sigma}}_{m_F,m_F+1}(t) = \hat{\tilde{\sigma}}_{m_F+1,m_F}(0) e^{(i\Delta\omega_{m_F} - \Gamma/2)t} - \frac{i\chi}{i\Delta\omega_{m_F} - \Gamma/2} \left[\hat{\sigma}_{m_F+1,m_F+1} - \hat{\sigma}_{m_F,m_F} \right] \left(1 - e^{(i\Delta\omega_{m_F} - \Gamma/2)t} \right) \tag{6.5}$$

$$\text{with } \chi = g_F \mu_B B_{RF} C(F, m_F)/(4\hbar)$$

where we note that the steady-state solution is obtained when all oscillations have averaged out ($e^{-\Gamma t/2} \to 0$). Further, we can then easily obtain $\hat{\sigma}_{m_F+1,m_F}(t)$ by reverting the transformation to the rotating frame through $\hat{\sigma}_{ij} = \hat{\tilde{\sigma}}_{ij} e^{-i\omega_{RF}t}$. From equation (6.6a), we can obtain the dynamics for the collective

[3] As previously introduced in equation (2.4), the quadratic splitting ν_{QZ} can be determined from the Larmor frequency ν_L and the hyperfine splitting ν_{hfs} as

$$\nu_{QZ} = \frac{2\nu_L^2}{\nu_{hfs}}.$$

spin operators in equations (6.1b,c) as (Julsgaard, 2003):

$$\hat{J}_y = \mathrm{Re}\left(\sum_{m_F=-F}^{F-1} \frac{\mathrm{i}\chi \cdot e^{\mathrm{i}\omega_{\mathrm{RF}}t}}{-\mathrm{i}\Delta\omega_{m_F} - \Gamma_{m_F+1,m_F}/2}\left(\hat{\sigma}_{m_F+1,m_F+1} - \hat{\sigma}_{m_F,m_F}\right)\right) \tag{6.6a}$$

$$\hat{J}_z = \mathrm{Im}\left(\sum_{m_F=-F}^{F-1} \frac{\mathrm{i}\chi \cdot e^{\mathrm{i}\omega_{\mathrm{RF}}t}}{-\mathrm{i}\Delta\omega_{m_F} - \Gamma_{m_F+1,m_F}/2}\left(\hat{\sigma}_{m_F+1,m_F+1} - \hat{\sigma}_{m_F,m_F}\right)\right) \tag{6.6b}$$

where we have reused the previously introduced expressions for $C(F, m_F)$, χ, and $\Delta\omega_{m_F}$. Please note that the expressions are proportional to $\hat{\sigma}_{ii}$ instead of the previous dependency on $\hat{\sigma}_{ij}$ in equations (6.1b,c). The dynamics induced from an RF magnetic field onto our transverse spin components will also be of interest when performing the quantum-enhanced eddy current detection in chapter 15. For our desired Fourier signal, the frequency-dependent magneto-optical resonance spectroscopy signal – MORS(ω_{RF}) – Julsgaard (2003) finally reaches:

$$\begin{aligned}\mathrm{MORS}(\omega_{\mathrm{RF}}) \propto \Bigg| N_{\mathrm{A}} \sum_{m_F=-F}^{F-1} &\frac{[F(F+1) - m_F(m_F+1)]}{\mathrm{i}(\omega_{m_F+1,m_F} - \omega_{\mathrm{RF}}) - \Gamma_{m_F+1,m_F}/2} \cdot \\ &\cdot \left\langle \hat{\sigma}_{m_F+1,m_F+1} - \hat{\sigma}_{m_F,m_F} \right\rangle \Bigg|^2\end{aligned} \tag{6.7}$$

where we see that the spectrum consists of a superposition of $2F$ Lorentzian, each centered around their respective resonance frequency ω_{m_F+1,m_F}. The height of each Lorentzian depends on the population difference between the two neighboring Zeeman levels, where the population of the i-th Zeeman level is determined as $\langle \hat{\sigma}_{i,i} \rangle$. Overall, the total spectrum depends on the number of atoms N_A within the hyperfine manifold F of the atomic ensemble. Furthermore, the transverse spin decay rate Γ_{m_F+1,m_F} determines the spectral width of the Lorentzian resonances of the Fourier spectrum. Experimentally, we record the desired spectrum by using a lock-in amplifier. Further, the RF frequency is slowly swept within the range of interest.

Typically, we use the (continuous) MORS only to optimize alignment and polarization of the optical pumping beams since changes lead to an instantaneous change in the observed spectrum[4]. Further, we use the technique of colinear MORS to test the homogeneity of a magnetic field profile. There, we exploit a small vapor cell, move it along the magnetic field profile, and record the center Larmor frequency. The magnetic field profile can be obtained by plotting the center Larmor frequency versus the position of the cell. We use this technique rather commonly for magnetic field homogeneity optimization. An example and accurate description of the technique are presented in appendix B.

However, considering that the experiments presented within this thesis are operated in a pulsed fashion, we have to extend our MORS technique to pulsed MORS to get a proper estimate of the atomic polarization for our experiments.

[4] For an example description of how this is exploited, consider Krauter (2011), or Schmieg (2019).

6.2 pMORS

Commonly, we extend the method of MORS to pulsed operation. We refer to the pulsed version of MORS as pMORS. This originates from the fact that all experiments presented throughout this thesis rely on pulsed measurement sequences. For a reliable estimate of the atomic polarization after the respective optical pumping pulse, only pMORS can be employed to determine the atomic spin state reliably. Therefore, we employ a sequence consisting of optical pumping pulses (section 5.2), followed by a short RF pulse of roughly 50 µs for our pulsed version of MORS and consecutive optical readout using a probing pulse extending multiple milliseconds. The precise RF pulse duration is chosen to fit an integer number of oscillations. As for MORS, the RF pulse is used to excite the transverse spin component. This short pulse can be seen as a "kick" of the macroscopic spin, creating a non-vanishing transverse spin component $\hat{J}_\perp$. Instead of sweeping the RF frequency, we choose a temporally short RF pulse much shorter than the transverse spin coherence time ($t_{\mathrm{RF}} \ll T_2$), making it spectrally broad. This allows us to address all resonances between neighboring Zeeman levels despite their different energetic splitting ($1/\nu_{\mathrm{QZ}} \gg t_{\mathrm{RF}}$). Figure 6.2 illustrates the pulse sequence. For pMORS, we record time traces instead of directly recording the spectra using lock-in detection. Typically, we record not only a single pulse sequence but rather average it 500 times to remove incoherent noise from the time trace. Further, optical pumping and probing duration is chosen to be significantly longer than the transverse spin coherence time T_2.

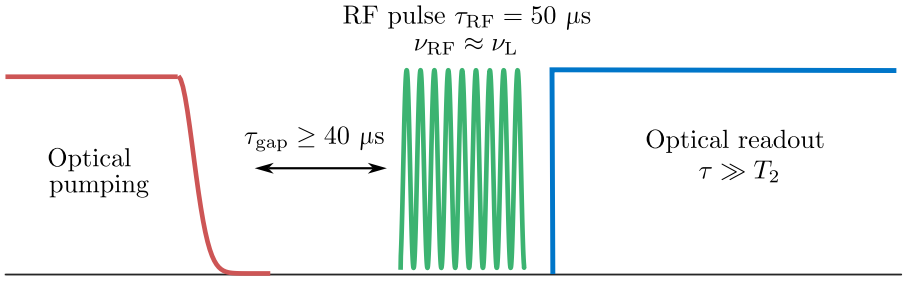

Figure 6.2: Pulse sequence pMORS. Illustration of the pulse sequence for the pMORS measurement. The sequence starts with a long optical pumping duration, followed by a short RF pulse of approximately 50 µs before the mean transverse spin is optically read out with a probing pulse extending multiple T_2 times. The RF and probing pulse can be delayed to test the polarization decay.

We determine the Fourier spectrum from the recorded time traces in the analysis. A quadratic splitting exceeding the linewidth of the individual resonances allows for a resolved spectrum and is fundamental to reliably estimating the population differences for the atomic polarization. To motivate this, let us consider how we estimate the atomic polarization p. In an atomic ensemble, different atoms will occupy different Zeeman levels. Depending on the value of m_F, the projection along J_x will differ. We estimate the atomic

spin orientation p by weighing Zeeman levels according to their relative occupation, normalized to the maximally polarized state ($p = 1$, all atoms in $m_F = F$). Then we obtain (compare equation (5.1)):

$$p = \frac{1}{F} \sum_{m_F=-F}^{F} m_F \langle \hat{\sigma}_{m_F,m_F} \rangle \tag{6.8}$$

For a reliable estimate of p, we require reliable knowledge of the occupation in each Zeeman level $\langle \hat{\sigma}_{m_F,m_F} \rangle$. Their estimate will improve when the spectrum is fully resolved.

The RF pulse, inducing Rabi oscillations between neighboring Zeeman levels, is followed by an optical probing pulse, reading out the transverse spin component. The underlying principle is the same as for MORS. However, the dynamics in the pulsed case are more involved. Due to the free evolution, the induced coherences between neighboring Zeeman levels are damped. Further, the free evolution also leads to relative phases between the coherences. The following will introduce the two models we use to estimate atomic polarization. The first population model is the thermal population model as introduced in Julsgaard (2003); Julsgaard et al. (2004). We refer to it as the thermal model, as one of the basic assumptions is a thermal distribution of the occupation. The eight population differences in the spectrum (equation (6.7)) are replaced by two fitting parameters:

$$\langle \hat{\sigma}_{m_F+1,m_F+1} - \hat{\sigma}_{m_F,m_F} \rangle = A \cdot \epsilon^{4-m_F} (\epsilon^{-1} - 1) \tag{6.9}$$

where A describes an overall scaling parameter of the spectrum, and ϵ represents the population differences following an exponential distribution. This significantly reduced the number of free parameters to describe a pMORS spectrum and enabled reliable fitting. Overall, the thermal model requires only five parameters. The remaining three are the linewidth Γ, the center frequency of the spectrum's first peak, and a parameter accounting for the resonance shift due to the quadratic splitting.

As we have seen in chapter 4, one of the main limitations for the readout in the DLCZ-type experiment is the residual population in $|F = 4, m_F = 3\rangle$. Therefore, we spent a significant part of our efforts on improving the optical pumping between Zugenmaier et al. (2018) and the more recent publication Dideriksen et al. (2021). Therefore, the results and considerations regarding atomic polarization optimization and pMORS analysis throughout this chapter are based on the DLCZ-type experiment. However, the techniques and improvements also apply to other experiments and are partially revisited for the QMIT experiment later on (chapter 13 onwards). When we improved the optical pumping, we started to observe discrepancies between the thermal model and the recorded pMORS spectra (see figure 6.3). The main issue with the thermal model is its ability to reflect the third peak correctly. Likewise, the valleys in-between neighboring peaks cannot be reproduced with it. These issues drove the investigation of alternative models in Schmieg (2019) and consecutively in Dideriksen (2021). We developed a model with three individual

peak heights to allow for more flexibility of the fitting model at the expense of excluding the remaining five peaks to be expected in the spectrum for the 4-manifold.

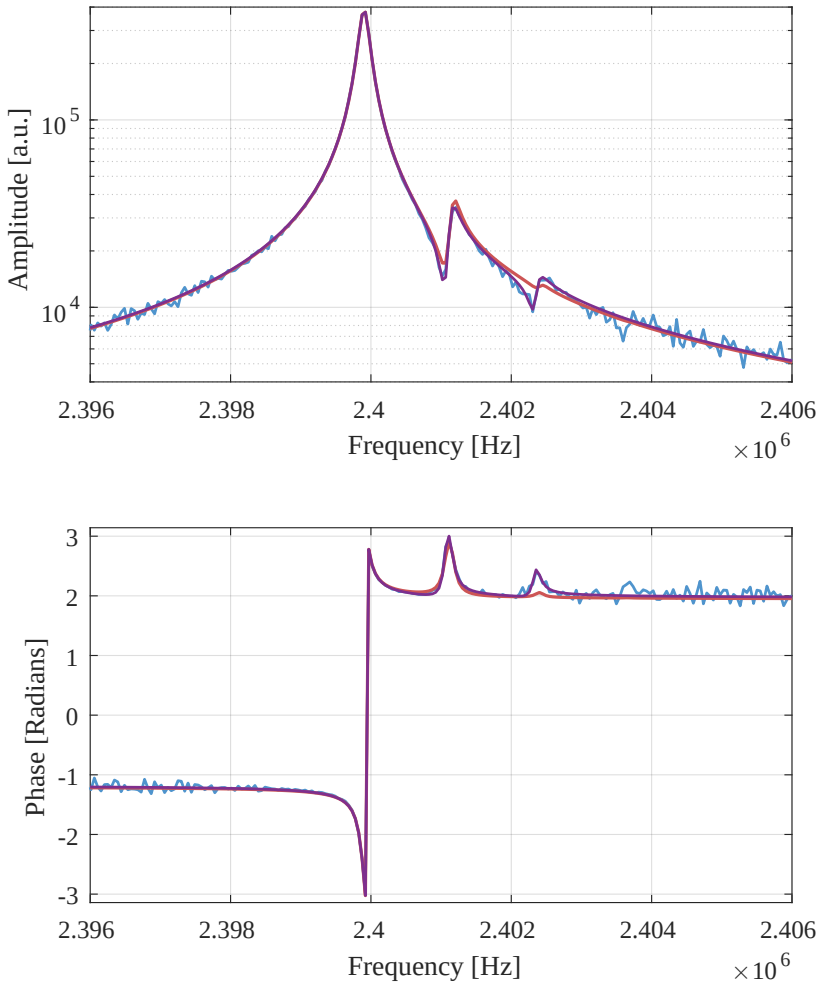

Figure 6.3: Comparison pMORS model fits. Shown is the amplitude (top) and phase (bottom) of our complex Fourier signal (blue) recorded with the pMORS technique. The fit obtained with the thermal model is shown in red, while our free model fit is shown in purple. See text for more details. The same experimental data is presented in figure 3.10 in Dideriksen (2021).

Further, we added two phase factors between the complex Lorentzian motivated by the expression in equation (6.6a). Our motivation for doing so lies in the slightly different resonance frequencies that should lead to relative phases acquired during the spin's free evolution after the optical pumping stops. Therefore, our fit model, which we refer to as the free model, is given

as follows (Schmieg (2019)):

$$\mathrm{pMORS}\,(\omega) = N \cdot \Bigg(\frac{A_1}{(\omega_\mathrm{L} - \omega + \frac{\mathrm{i}\Gamma}{2})} + \frac{A_2 e^{i\phi_1}}{(\omega_\mathrm{L} - \omega + G + \frac{\mathrm{i}\Gamma}{2})} + \frac{A_3 e^{i\phi_2}}{(\omega_\mathrm{L} - \omega + 2G + \frac{\mathrm{i}\Gamma}{2})} \Bigg) \tag{6.10}$$

Here, we use N as an overall scaling factor, while A_i are the amplitudes of the respective Lorentzian. Further, we have the central Larmor frequency ω_L and account for the frequency shift due to the quadratic splitting by introducing G. Also, we have the two complex phases ϕ_1 and ϕ_2. The linewidth of the resonances if estimated by the fit parameter Γ. We observed in Schmieg (2019) some instability of the fit regarding the phase factor for repeated measurements. We extended our fitting routine to include the phase information instead of only fitting the power spectral density. The fit exploiting the complex Fourier signal was first introduced in Dideriksen (2021). Including the phase information in our fitting routine improved the reproducibility of the fitting results for repeated measurements. We observe a better agreement between the data and the fit for the free model compared to the thermal model, as becomes apparent in figure 6.3.

While it is straightforward to calculate the population based on the thermal model (equation (6.9)), we want to address the assumptions in our free model. To estimate the polarization according to equation (6.8) based on the fit result of the three complex amplitudes of the free model, we have to make some assumptions regarding the occupation of Zeeman levels (Schmieg (2019); Dideriksen (2021)):

$$\begin{aligned} \langle \hat{\sigma}_{4,4} - \hat{\sigma}_{3,3} \rangle &\rightarrow A_{4,3} \\ \langle \hat{\sigma}_{3,3} - \hat{\sigma}_{2,2} \rangle &\rightarrow A_{3,2} \\ \langle \hat{\sigma}_{2,2} \rangle &\rightarrow A_{2,1} \end{aligned}$$

where we assume for the last one that the remaining Zeeman levels have no occupation, i.e., $\langle \hat{\sigma}_{m_F,m_F} \rangle = 0$ for $m_F \in [-4, 1]$. With this at hand, we can calculate the respective atomic polarization from the two fit results shown in figure 6.3. For the thermal model, we obtained $p_\mathrm{thermal} \approx 99.1\,\%$, while for the free model, we only estimate an atomic spin polarization of $p_\mathrm{thermal} \approx 98.8\,\%$. The discrepancy between the two estimates can be explained by the thermal model underestimating the third peak in the spectrum significantly. Hence the thermal model underestimates the residual population of atoms in Zeeman levels with $m_F < 3$, leading to an overestimation of the spin polarization in the ensemble according to equation (6.8).

While 98.8 % of atomic spin polarization within our ensemble seems like a relatively high level of polarization, we kept investigating how to improve it further. Considering that the residual population in $|F = 4, m_F = 3\rangle$ is the main limitation in the DLCZ-type experiment, the residual population in the $F = 3$ manifold is not a problem. Therefore, we investigated how delaying the

pump turn-off later than the repump laser alters our initial atomic polarization. Delaying the pump turn-off comes at the expense of the available optical depth since we effectively reduce the number of atoms in the $F = 4$ manifold. In figure 6.4, a comparison of the two spectra[5] for no delay of the pump laser

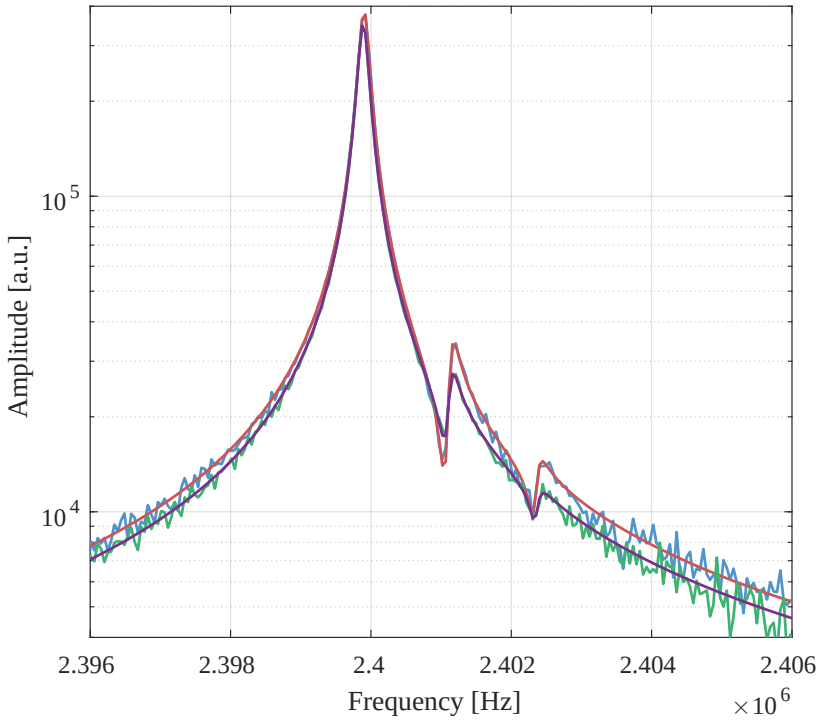

Figure 6.4: Comparison pump delays. PMORS spectra for pump turn-off 0 µs (blue) together with the free model fit (red) in comparison to spectrum with pump turn-off delayed by 40 µs (green) together with the free model fit (purple). At the expense of the overall signal and optical depth, the relative height of the second and third peaks is reduced. This figure contains the same data as figure 3.13 in Dideriksen (2021).

turn-off compared to 40 µs delayed pump laser turn-off is presented. For the latter, the atomic spin polarization increases to $p_{\text{free}} \approx 99.2\,\%$. Extending the delayed turn-off of the pump laser beam further does not improve the atomic polarization further (see Dideriksen (2021)).

The pMORS also allows us to determine the evolution of the transverse spin component by delaying the probing pulse by variable gaps. Appendix C provides an example of that. Further, the T_2 in the dark, meaning in the absence of other decoherence processes due to probing and the RF field, can be determined. Similar to the T_1 time (chapter 7), this can be done by extrapolating the RF power and probe power to zero by recording pMORS for different values.

Let us summarize the key facts regarding optical pumping optimization and quantification using the technique of pMORS. Optical pumping and coherent spin state preparation are fundamental requirements for many exper-

[5] Only the amplitude is shown. However, the fit was still containing the phase portion as well.

iments throughout this thesis and beyond. Calibrating and estimating the atomic spin state using pMORS allows quantifying the atomic spin state in an experimental sequence. Further, the information about the population distribution across Zeeman levels allows us to identify limitations and evaluate possible improvements. Combining the pMORS spectra with respective fitting models, the information about the Zeeman level populations can be extracted. The free model reproduces the spectrum better than the thermal model for a very high atomic spin polarization. The technique pMORS can also be imagined to quantify other optical pumping schemes as proposed in Chalupczak et al. (2018), not necessarily limited to preparing the spin ensemble in a coherent spin state. However, depending on the choice of spin state preparation, a suitable fitting model is required to extract and quantify the relevant information from the pMORS spectrum. An alternative approach to pMORS is to monitor higher-order Zeeman coherences as presented in Pustelny et al. (2006). The authors excite and read out higher-order Zeeman coherences as nonlinear magneto-optical rotation with frequency-modulating the light. In appendix C, we further present the evolution of the atomic spin polarization versus delay time and our efforts of combining pMORS with a second measurement to get absolute estimates of the Zeeman level occupation as opposed to the relative ones we exploited throughout this chapter.

Chapter 7

Cell testing

During the time of this PhD program, we were fortunate enough to get a visit by **Mikhail Balabas**, a master at crafting anti-relaxation coated atomic vapor cells. In the following, we will introduce vapor cells and the subtleties of quantifying their performance. Given that the various experiments in our group have different requirements on the vapor cells, a variety of cells has been manufactured during the visit of Mikhail Balabas. While these measurements provide information about newly fabricated cells, some of the techniques used are also relevant for the day-to-day operation of our experiments. Apart from the experimental performance of newly fabricated cells, denoted **Generation O** to indicate their fabrication time and properties, procedures regarding the cell fabrication and specifics in the approach for this generation will be introduced briefly.

During the cell testing efforts, the master student **Isaac Roca Caritg** was introduced to the different techniques used for vapor cell characterization. He joined in the cell testing efforts for a small subset of measurements. Therefore, this chapter has some overlap with the data presented in the master thesis by Isaac Roca Caritg (see: Caritg (2022)).

7.1 Vapor cells

Many room-temperature experiments in quantum optics use so-called vapor cells – glass containers usually filled with one or more atomic or molecular vapors. Vapor cells are versatile due to their broad applicability. Vapor cells can be made with different atomic species – in this thesis, we only use cesium – and come in various sizes and geometries, depending on the application they are intended for. Sensing and detection applications of atomic vapors range from terahertz electrometry (Chen et al. (2022)) or imaging (Downes et al. (2020)), eddy current detection (Jensen et al. (2019)), unshielded magnetoencephalography (Zhang et al. (2020)), as an optogalvanic gas sensor (Schmidt et al. (2020)) or even as a possible application for improved gravitational wave detection (Khalili and Polzik (2018)). Other applications are, for example, within the field of quantum communication as building blocks for DLCZ-

Figure 7.1: Vapor cells. Assortment of cesium vapor cells with different geometries. All displayed cells are of encapsulated design with a channel of a variable cross-section diameter and channel length. The channel is contained within a half-inch glass cylinder. All cells are coated with an anti-relaxation coating and have a drop of cesium in the attached stem as the atomic reservoir. Jun Jia kindly provided the picture.

type of experiments (Borregaard et al. (2016); Dideriksen et al. (2021)), EIT-based quantum memory (Ma et al. (2015)) or parametric downconversion based single-photon generation and matched atomic vapor storage (Buser et al. (2022)).

In our group, we employ vapor cells for various experimental applications. A subset of the experiments has already been covered in the introduction in chapter 1. All of our experiments have in common that we use anti-relaxation coated vapor cells. We exploit anti-relaxation coatings to prevent loss of atomic spin orientation when the atoms collide with the channel walls due to their thermal motion. We do not suppress thermal atomic motion in our vapor cells, as opposed to buffer gas cells, where a buffer gas consisting of one or more atomic or molecular species is used to slow down the atomic motion to elongate spin coherence times. A better coating enables longer coherence times of atomic spin states, which are an essential performance parameter of vapor cells for us. Other figures of merit are the transmission and atomic density of a vapor cell. These vapor cell properties depend on the tolerable temperature of the anti-relaxation coating and the manufacturing process. All cells are handcrafted. Hence, there is a limit to the reproducibility of each cell parameter, and we require individual testing of each cell.

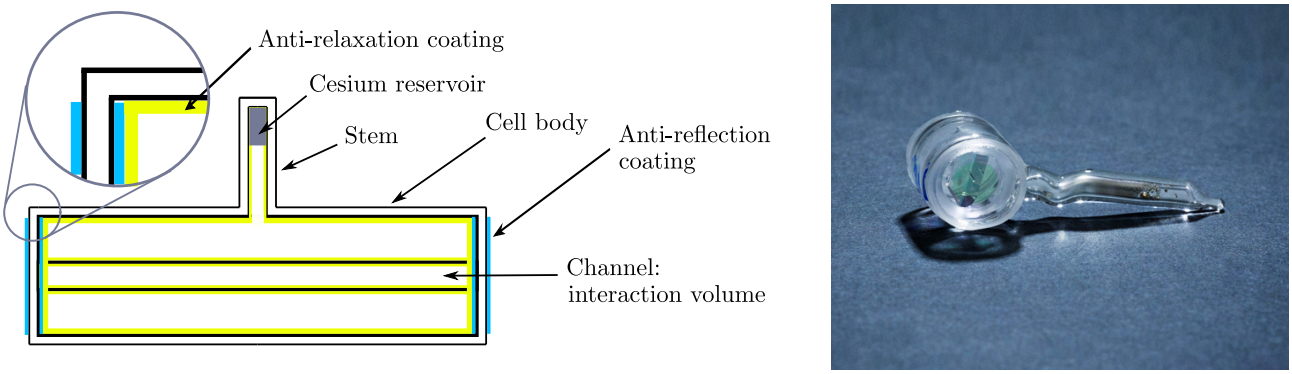

Figure 7.2: Illustration cell parts. Left: Schematic of cell with channel showing the stem with cesium, the anti-relaxation coating (yellow), and anti-reflection (AR) coating (blue). Figure inspired by Figure 3.1 in Enault-Dautheribes (2017). Right: Picture of encapsulated glass chip micro-cell. Photo: Carsten Seidel for University Post.

7.1.1 Information about Generation O

The vapor cells manufactured as part of Generation O were all made in winter '21 to spring '22. All of them are produced similarly, while their dimensions vary to accommodate the needs of their intended practical application. Two main types of cells can be distinguished in this vapor cell generation. One design is the encapsulated chip cell, while the other type is a simple encapsulated glass channel. Figure 7.1 is a picture of an assortment of vapor cells illustrating the various designs and geometries. For small interaction volumes, glass chips are used for improved stability in the encapsulated design. Independent of the precise geometry, all channels/chips are placed inside a half-inch glass tube forming the vapor cell body. The cell body is connected to a stem containing a drop of pure cesium. A schematic illustrating the generic design of our vapor cells is provided in figure 7.2. All glass parts consist of Borofloat, sometimes referred to as Duran or Pyrex. The channels, chips, and glass tubes are obtained from *Vitrocom*, partially as off-the-shelf parts and partially as a custom order. The bare windows originate from *Foctek China* but were coated with an AR coating on both sides by the Danish company *Ferroperm*.

In order to attach the windows to the cell body, the outer rim of the AR coating had to be polished off. Polishing off the outer rim can cause minor scratches on the surface, leading to unwanted scattering and losses in transmission of the vapor cell. The channel/chip is placed inside a half-inch glass tube of the same length. The glass tube has a smaller glass capillary attached to it that will enable the filling of the cell and form the stem of the cell. The window and cell body are fused by melting the rim of the window and glass tube. The windows are attached to each side of the cell body, clamping the channel/chip in between the windows. The procedure is the same for all cell geometries. For an overview of the geometries realized, see table A.1 in appendix A.2. A connection between the cell channel and the atomic reservoir in

the stem requires a physical connection. For this, one of the channel surfaces is scratched, creating a connection between the channel and the cell body. When heating the cell, this allows for atoms from the cesium reservoir to evaporate and reach the cell channel[1]. The manual scratching process leads to a natural variance in how big the connection between the channel and the cell body is. In an experiment, a more significant scratch allows more atoms to leave and enter the channel from the cell body. The scratch also enables coating the inside of the channel during the filling process.

The anti-relaxation coating made for cells of Generation O is based on normal alpha olefins "AlphaPlus C30+HA" from *Chevron Phillips Chemical – CPChem*. The C30+ mixture contains more than 95 % of carbon chains with at least 30 carbon atoms (CPChem (2010)). It is an alkene type, also referred to as the unsaturated hydrocarbon type, with one double bond between two carbon atoms. The C30+ mixture is distilled to increase the amount of long-chained molecules allowing for higher operating temperatures of the coating. Since this has to be done for each set of cells manufactured, each coating has a slightly different composition. However, the higher operational temperatures, meaning increased atomic density and optical depth, are at the expense of possible spin relaxation times. Typically, anti-relaxation coatings that allow for more wall collisions and enable longer spin coherence times come with the limitation that they only endure lower experimental operation temperatures. The relation between longer coherence times with low-temperature anti-relaxation coatings has been experimentally verified for older generations of cells with different coatings in our lab, for example, in Zugenmaier et al. (2018), and externally by the authors of Balabas and Tretiak (2013). Coating material with shorter carbon chains allows, on average, longer relaxation times at the expense of enduring lower operational temperatures in the experiments.

The cell is cleaned and evacuated before the distilled coating material is deposited inside the cells at high temperatures ranging for Generation O between 320 and 350 °C. Afterward, the residual gaseous coating material is removed, and the cell is evacuated once more before finally adding a drop of cesium to the cell. As a last step, the cell is disconnected and sealed from the manufacturing glass construction.

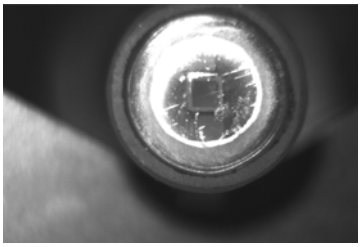

Figure 7.3: Picture scratched window Frontal view of a vapor cell. The window has visible scratches from the manual manufacturing process. Polishing off the rim of the AR coating or other mechanical forces led to scratches on the cell window.

7.2 Transmission and Losses of vapor cells

High levels of transmission for newly fabricated cells are essential. A low transmission indicates losses that can harm an experiment's performance, making cell transmission a figure of merit for us. The transmission of a cell is influenced by the anti-reflection (AR) coating of the windows or other issues during the manual manufacturing process of the vapor cells. These include, for example, bending or twisting the channel (illustrated in figure 7.5) or alignment of the windows at an odd angle (figure 7.6). Also, the outer rim of the windows was coated and had to be polished off, sometimes causing

[1] This is not the case for the cell of encapsulated design used for the DLCZ-type experiment (chapters 8 to 11). This cell is from an older generation and has a micro-drilled hole connecting the channel with the cell body.

scratches on the coated windows when removing the outer part of the AR coating (figure 7.3). A too-thick coating layer or condensed cesium on the windows reduces a cell's transmission.

We adapt the beam size to match the cross-section of the cell under investigation for a reasonable estimate of the cell transmission. A too-big beam diameter would lead to clipping and scattering losses, while a too-small beam does not accurately reflect the transmission through the whole channel cross-section. The maximal local transmission for a small beam might exceed and not reflect the expected transmission for a beam with an adequate filling factor. For small cross-sections, it is crucial to verify the alignment of the beams using a camera. The alignment of a probe beam inside a chip cell is illustrated in figure 7.4.

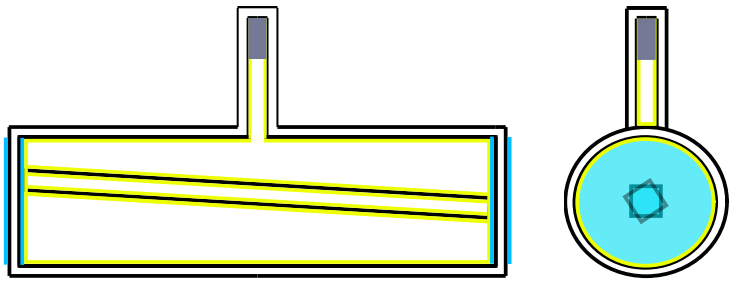

Figure 7.5: Illustration of channel misalignment. Left: Schematic of cell visualizing tilt of the channel inside the cell body. Right: Frontal view for illustrating a twisted channel inside a vapor cell.

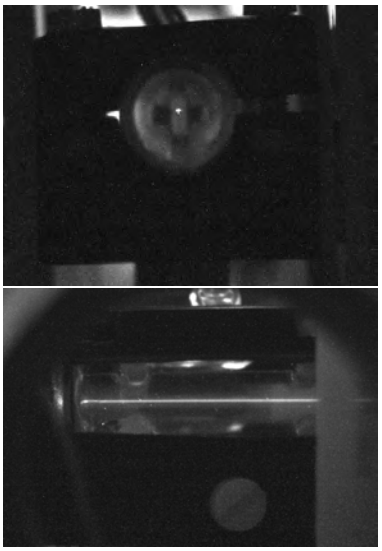

Figure 7.4: Alignment chip cell. We verify the proper alignment of a probing beam through the channel with a camera for the front (top) and side view (bottom). We increase the contrast by shining light from the top into the shield with a flashlight.

Measuring all cells of Generation O for their transmission leads to the results stated in table A.1, visualized in figure 7.7. Most of the cells exhibit between 94 and 97 % of transmission. Fortunately, the transmission is not dependent on the cross-section of the cells. The AR-coated windows are specified for 99.5 % transmission, leading to 99 % of expected transmission for the cells. This value does not agree with our observation. We investigated the possible causes for the lower transmission. Therefore, we checked the transmission through windows and cells at different manufacturing steps to identify where the losses originate.

We compared uncoated and coated cells to rule out the anti-relaxation coating as the reason for the diminished transmission. Coating and filling the cells with cesium could also be ruled out. Instead, the attachment of the windows to the cell body was identified as the problem. Testing bare and filled cells, we observed hardly any difference. However, we measured 1.5 % of reflection of the attached windows as opposed to the bare AR-coated windows. This was measured and confirmed together with Jeppe Detlefsen for multiple cells, angle of incidence, and more. The increase in reflection identifies the glass-blowing process as the problem. We suspect that heating the rim of the windows to the melting point adds much stress to the window and the AR coating. The melting can cause cracks and stress within the AR coating or the window substrate.

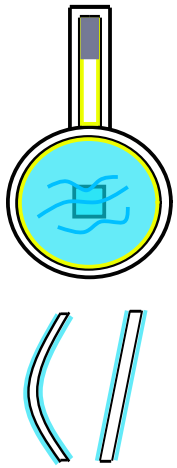

Figure 7.6: Illustration issues with windows. Top: Scratches/dirt obscuring transmission through the channel. Bottom: Example of windows bending and alignment issues during the attachment of the windows to the glass body.

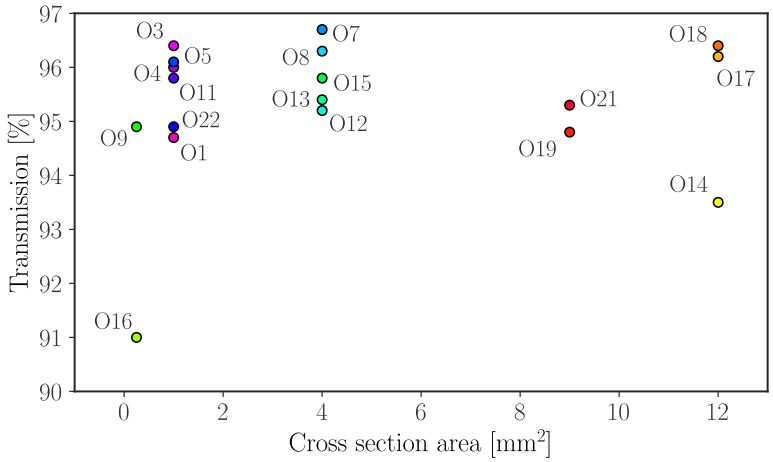

Figure 7.7: Transmission of cells. The different transmission values obtained for Generation O, each cell reflected with label and individual color, plotted versus their cross-section. It should be noted that for better visibility, cell "O10" has been excluded due to its bad transmission (table A.1).

As lessons learned, this means that windows with a thick, flat center but thinner rim could be tested in the future. The idea here is that a thinner rim could help during the attachment process. Less material must be melted for the attachment process, thus reducing the AR-coating and window substrate distress due to the glass-blowing. Hopefully, this will allow for a higher transmission of vapor cells. Also, twisting and bending of the glass channels could be remedied by using glass wares with thicker walls, making the parts sturdier. We also plan to coat only the center of the window substrates with the AR-coating to not remove part of it again and damage the center of the coating layer in the process.

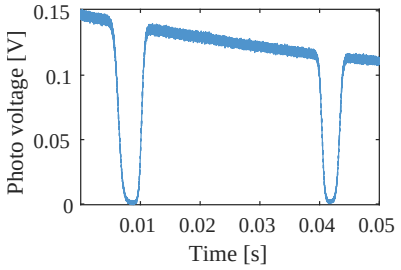

Figure 7.8: Recorded absorption signal cell O19. Offset corrected absorption signal recorded with APD. The left dip is the $F = 4$ manifold, while the right dip corresponds to the $F = 3$ manifold. The signal was averaged ten times to remove uncorrelated high-frequency noise.

7.3 Atomic absorption measurement

Another figure of merit for vapor cells is their atomic density, from which the number of atoms inside the interaction volume and the expected optical depth (OD) can be calculated. To measure the atomic density, we use what we refer to as "absorption measurement". The absorption measurement exploits the detuning-dependent light absorption of atomic transitions. Scanning the probe laser over the two hyperfine ground state transitions allows recording an absorption spectrum (figure 7.8). For the D_2 line, we expect the absorption spectrum to consist of two dips corresponding to the Doppler-broadened transitions for the $F = 4$ and $F = 3$ manifold, determined by the selection rules[2].

The optical power used should not saturate the atomic transitions and avoid broadening effects to get a reliable estimate of the number of atoms.

[2]For an introduction to the selection rules, one might consider Foot (2005), or Steck (2007).

The probe laser should scan slowly enough that we can assume an equilibrium distribution of the atoms. A too-fast or a too-high probe power would lead to asymmetry in the absorption dips for the up-and-down scan of the laser frequency. The transmission signal through the vapor cell is recorded with an APD due to the low optical powers used for this measurement (figure C.2). Figure 7.8 shows an offset-corrected absorption signal. We see the probe power is not constant when scanning the probe laser frequency. For a more reliable estimate of the atomic density, the signal is normalized to correct for the frequency-dependent power change of the probe laser.

The absorption spectrum can be integrated for low optical depths to estimate the atomic density (Fabricant (2014)). Increasing the length of cells to 80 mm or operating at elevated temperatures, complete absorption limits the applicability of this method. Therefore, a fitting algorithm taking the temperature-dependent Doppler broadening leading to Voigt profiles of the atomic transitions, including their relative transition strengths, was developed in Schmieg (2018). This fitting routine allowed for more reliable estimates, even for the case of total absorption. The method was also successfully used, for example, in Thomas (2020); Dideriksen (2021). The two dips in the absorption spectrum are separated by the hyperfine splitting of 9.2 GHz. The frequency and temporal separation between the two dips allow us to convert the time trace into a spectrum. Due to the nonlinearity of the probe laser scan, an asymmetric Mach-Zehnder-Interfero-meter (MZI) of 2.58 m path difference is exploited to improve the time-frequency conversion by recording the interference signal on a simple reference photo detector (PD). Details can be found in Schmieg (2018). The experimental setup is shown in figure 7.9, illustrating the separate path for the MZI together with the transmission measurement. In the following, we will summarize the approach developed in Schmieg (2018) and present the core concepts of the model and the fitting routine here.

The atomic density can be determined from the absorption spectrum from the Beer-Lambert law describing the probe attenuation through a medium:

$$\frac{I_\nu(L_z)}{I_\nu(0)} = \exp\left(-\rho\sigma(\nu)L_z\right) = \exp\left(-\alpha(\nu)L_z\right) \tag{7.1}$$

where ρ refers to the atomic density, L_z is the length of the atomic medium, in our case, the length of the cell, and $\sigma(\nu)$ is the frequency-dependent absorption cross-section. Lastly, $\rho\sigma(\nu) = \alpha(\nu)$ is the absorption coefficient.

Due to the finite temperature, all atomic transitions are subjected to Doppler broadening. This Doppler broadening means that each transition is a convolution of the Lorentzian atomic spectral line and the Gaussian Boltzmann velocity distribution[3] (Schmieg, 2018):

$$S_{FF'}(\nu) = \int_{-\infty}^{\infty} \frac{\frac{\gamma_{F'}}{2}}{(\nu-\nu_{FF'})^2 - \left(\frac{\gamma_{F'}}{2}\right)^2} \cdot \frac{\exp\left(-\ln 2\frac{(\nu-\nu')^2}{\Gamma_D^2}\right)}{\sqrt{\frac{\pi}{4\ln 2}}\Gamma_D}\,\mathrm{d}\nu' \tag{7.2}$$

[3] For readers interested in broadening effects of atomic transitions might want to consider Foot (2005) as an extensive resource.

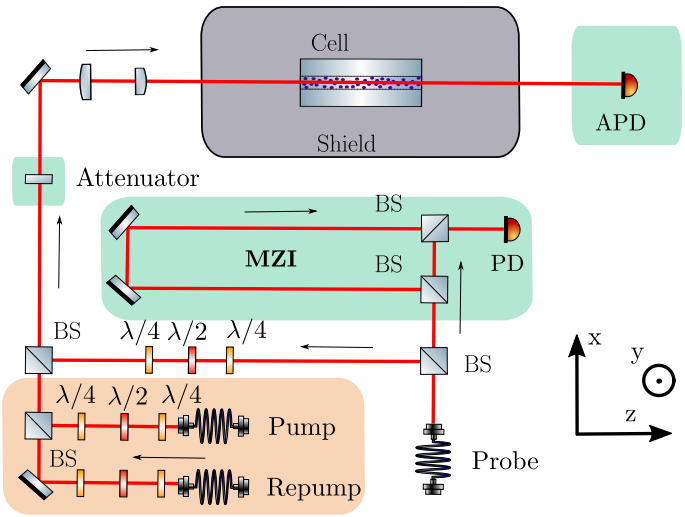

Figure 7.9: Experimental setup: Absorption measurement. Relevant optical paths for the absorption measurement for a vapor cell, including the asymmetric Mach-Zehnder-interferometer (MZI) for linearizing the probe scan. BS indicates a beam-splitter, $\lambda/2$, and $\lambda/4$ represent half- and quarter-waveplates. Green tiles represent parts of the experimental setup relevant only to the absorption measurement of the cell testing. Paths in Orange tiles are part of the setup but not used for the absorption measurement.

where Γ_D refers to the temperature-dependent Doppler width (HWHM) and $\gamma_{F'}$ is the excited state decay rate. The total absorption spectrum is then a superposition of all six allowed transitions weighted according to their Glebsch-Gordan coefficients[4], incorporated into $A_{FF'}^{m_F}$ in equation (7.3). Using this spectrum and introducing an overall scaling factor allows incorporating the atomic density of the medium:

$$c_1 \alpha(\nu) = c_1 \cdot \sum_{F,F'} \sum_{m_F} A_{FF'}^{m_F} S_{FF'}(\nu) \tag{7.3}$$

Combining the above expressions, the overall fitting model can be expressed as:

$$\frac{I_\nu(L)}{I_\nu(0)} = \exp\left(-c_1 \cdot \alpha\left((\nu - c_2) \cdot c_3\right) \cdot L_z\right) \tag{7.4}$$

where the two additional fit parameters are a shift along the frequency axis, given by c_2, and a frequency scaling factor allowing for corrections in the time-frequency conversion, denoted c_3[5]. The latter serves the purpose of adjusting the frequency scale of the spectrum to the data. Only c_1 defines the steepness of the absorption spectrum. The fitting parameter c_1 thus allows us to retrieve the information from our measurement required to determine the atomic density ρ.

Using equation 7.1, we can calculate ρ from the fit of the data to the spec-

[4]The values for the Glebsch-Gordan coefficients can be found, for example, in Steck (2019).

[5]Typically, the value of this parameter is within the range $[0.99, 1.01]$, therefore acts only as a really minor correction to our calibration.

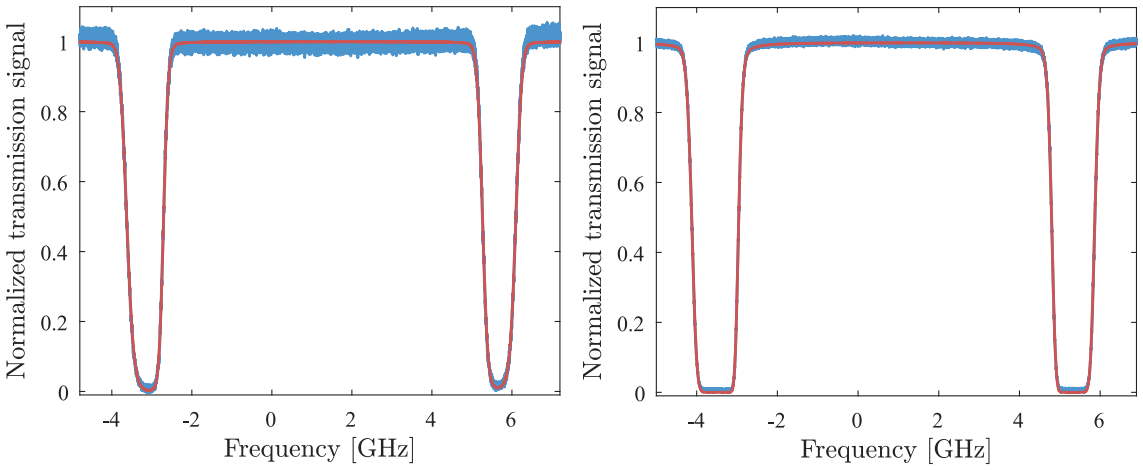

Figure 7.10: Comparison absorption spectra for different temperatures Left: Normalized absorption spectrum with obtained fit for cell O19 at room-temperature. Right: Same, but at an elevated temperature of 41 degrees.

trum as:

$$\begin{aligned}\rho &= \frac{\int_{-\infty}^{\infty} c_1 \cdot \alpha\left((\nu - c_2)\cdot c_3\right)\,\mathrm{d}\nu}{\int_{-\infty}^{\infty}\sigma(\nu)\,\mathrm{d}\nu} \\ &= \frac{1}{\pi c r_e f}\int_{-\infty}^{\infty} c_1 \cdot \alpha\left((\nu - c_2)\cdot c_3\right)\,\mathrm{d}\nu \end{aligned} \tag{7.5}$$

where we have used that the integral over the atomic absorption cross-section is given as $\int_\nu \sigma(\nu)\,\mathrm{d}\nu = (\pi r_e f c)$ (Fabricant (2014)). Here, c is the speed of light, r_e is the electron radius, and f is the absorption oscillator strength. For the D_2 line of cesium, it takes the value $f = 0.7164$ (Steck (2019)). As an example, we have performed the absorption measurement for cell O19 at two different temperatures. Figure 7.10 presents the respective absorption spectra. The values of the atomic density were determined to be:

$$\rho_{23^\circ\mathrm{C}} = (3.78 \pm 0.02)\cdot 10^{16}\,\frac{1}{\mathrm{m}^3} \tag{7.6}$$

$$\rho_{40^\circ\mathrm{C}} = (1.40 \pm 0.01)\cdot 10^{17}\,\frac{1}{\mathrm{m}^3} \tag{7.7}$$

where we estimate the uncertainties from an error on the temperature of 1 °C since we cannot place our thermistor arbitrarily close to the cell, we also note that statistical uncertainties lead to uncertainties of the same magnitude. The difference between the two atomic densities corresponds roughly to a factor of 3.7, which agrees with the expected increase in vapor density for cesium provided in figure 1 in Steck (2019).

The summary table A.1 in appendix A.2 shows the results at room-temperature for all cells of Generation O. The results are presented in figure 7.11 versus the order the cells were manufactured for easier comparison. This figure shows

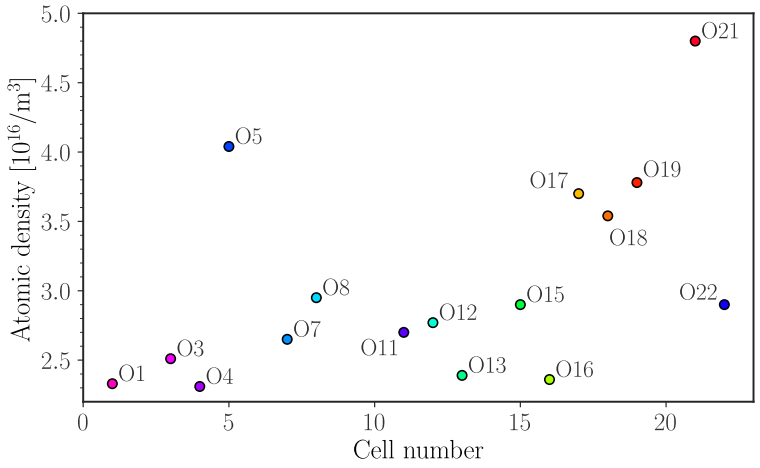

Figure 7.11: Measured atomic densities. The measured atomic densities were determined using the fit model described in the text. All densities correspond to room-temperature measurements. The densities are plotted versus the manufacturing order of the vapor cells to identify possible manufacturing dependencies of their performance.

that most cells exhibit a vapor density within a factor 2 of each other. The differences could be related to different amounts of cesium in the stem or the size of the scratch, connecting the reservoir via the cell body to the cell channel. Another explanation is the different composition and thickness of the anti-relaxation coating as investigated in Li et al. (2017). Variations in the cell coating would explain why the cells O17-O19 have a slightly higher atomic density, as they were manufactured simultaneously. Cell O22 was a cell that we discovered at the end but was suspected to be already manufactured as one of the first but not tested initially.

Another explanation for the variance in the atomic densities observed is that the volume or the length could be a factor that introduces biases to our results. A bias due to the cell channel volume could explain why cells O17-O19 and O21 have a higher atomic density than those with smaller volumes, as can be seen in figure 7.12. If we consider that the channel length mainly determines the optical depth and hence the observed absorption, this would speak against a bias of the fitting routine and model towards bigger channel volumes, as the cells O7, O8, O12, O13, and O15 also have a length of 80 mm. Nevertheless, the cells with smaller volumes are consistently lower in atomic density, except for cell O5. Given that the cells were mainly manufactured in sets with similar dimensions, we cannot rule out either explanation for the variation of atomic densities. One way to investigate this in the future is to manufacture and fill cells in sets of mixed geometry. Then comparing tendencies in the atomic density plotted versus manufacturing order and interaction volume should give a better idea of the underlying reason and help identify

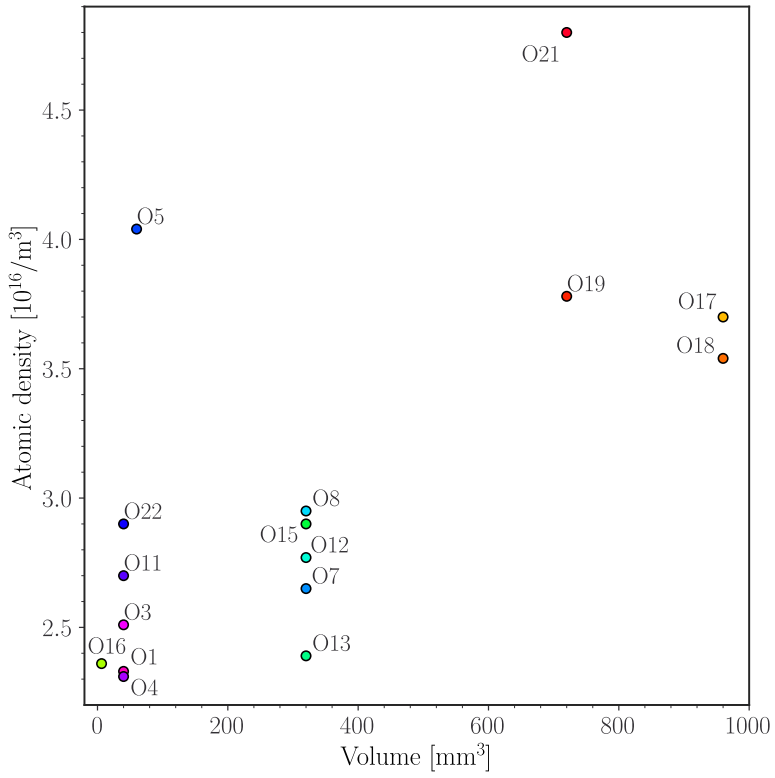

Figure 7.12: Measured atomic densities versus channel volume. The measured atomic densities obtained from the respective absorption spectra, similar to figure 7.10, versus the volume of the channel. For identification, each cell is shown in a different color and their number is indicated.

possible biases and errors in the measurement or its analysis.

7.4 Measuring relaxation time T_1

For many of our experiments, we must achieve a good spin polarization of our ensemble, but we also need to know how fast the coherent spin state (CSS) decays. For this purpose, we are interested in T_1, the spin population decay time (longitudinal spin $\hat{J}_x(t)$), and in T_2, the spin coherence decay time (transverse spin component $\hat{J}_\perp(t)$) as introduced in section 2.3.1. Since magnetic field inhomogeneity and the like impact T_1 less, it reflects the vapor cell performance, while T_2 reflects both cell properties and magnetic field homogeneity. We already discussed determining the transverse spin coherence time T_2 as part of the atomic state characterization in the preceding chapter 6. Here, we will focus on one of the experimental techniques used to quantify the longitudinal spin coherence time T_1. For many experiments at Quantop, the transverse spin coherence time T_2 is of more relevance. However, it is also

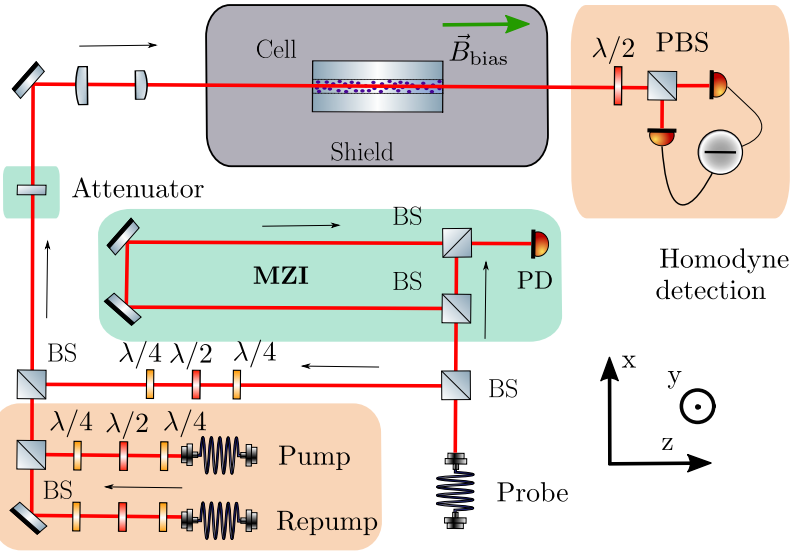

Figure 7.13: Experimental setup: Absorption measurement. Relevant optical paths for the T_1 measurement, including the optical pumping path and the homodyne detection marked in the orange tiles. BS indicates a beamsplitter, $\lambda/2$, and $\lambda/4$ represent half- and quarter-waveplates. Optics in green tiles are not used for the T_1 measurement but are part of the whole setup for cell testing.

more tedious to measure, especially given the vastly different sizes of the cells to be tested. Therefore, we investigate T_1 for all vapor cells, while only for a subset T_2 was also measured[6]. From this, we hope to have some way of gauging the expected cell performance from the much simpler T_1 measurement to the expected T_2 times. A note of caution: T_2 is highly dependent on magnetic field inhomogeneity and magnetic field fluctuations. Therefore, extrapolations from one setup to the other must be taken with a grain of salt. However, since all T_1 will be measured within the same setup with the same magnetic field settings, we can evaluate the cells reasonably well with respect to each other.

Figure 7.14: Coil system T_1 measurement. Picture of the 3D printed coil frame used for the T_1 measurement. We use multiple coil pairs to optimize the magnetic field homogeneity along the cell channel.

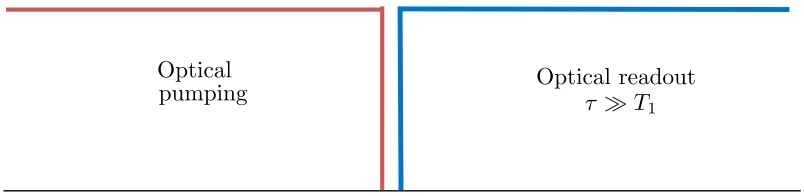

Figure 7.15: T_1 measurement sequence. Measurement sequence for the Faraday angle readout to estimate the T_1 time. The atomic ensemble is first optically pumped (red). In a second step, the optical probing is turned on and the decay of the Faraday angle is recorded using an optical probing pulse with $\tau \gg T_1$.

For the T_1 measurement, we use the magnetic shield used for the DLCZ-type experiment. However, we removed the innermost aluminum layer with

[6] T_2 was measured in the "GWD lab" by Jun Jia and Ryan Yde.

the coil frame. We exchanged it with a 3D-printed coil frame, generating a field along the probing direction as indicated in figure 7.13. Figure 7.14 depicts a picture of the new coil system. We use a combination of multiple coil pairs whose current ratio has been optimized to create a homogeneous magnetic field along the cell channel. More details on the coils used for the T_1 measurement can be found in Caritg (2022) and are not reproduced here for brevity.

When performing the T_1 measurement, we rely on the Faraday effect and the respective light polarization rotation due to atom-light interaction. The macroscopic spin $\langle J_x(t)\rangle$, prepared via optical pumping (compare chapter 5), rotates the polarization axis of linearly polarized light propagating along the magnetic field direction due to circular birefringence. The rotation angle is often referred to Faraday angle θ_F and is given by (Krauter, 2011):

$$\theta_\mathrm{F}(t) = \frac{\gamma a_1 \lambda^2 \langle J_x(t)\rangle}{32 A \Delta \pi} \tag{7.8}$$

The rotation angle depends on the polarization state of the atomic spin state, meaning the magnitude of $\langle J_x(t)\rangle$. In principle, equation (7.8) equips us to calculate the maximal Faraday angle for a given detuning and the number of atoms for a fully polarized atomic ensemble. For convenience, we are not interested in measuring the maximal rotation angle but rather in exploiting that the decay in the atomic state will decrease the rotation angle over time. Hence, this change in light polarization can be monitored using polarization homodyne detection. Figure 7.15 illustrates the pulse sequence. Due to the decay of the atomic spin state, we can describe the dynamics by a simple exponential decay as $\langle J_x(t)\rangle = \langle J_x(0)\rangle\, e^{-t/T_1}$ (see also section 2.3.1). In order to record the decay of the DC-Faraday rotation[7], we use a simple sequence that switches between optical pumping (circularly polarized) and probing (linearly polarized) beams.

We use the setup shown in figure 7.13, indicating relevant optical paths and components, for measuring the DC-Faraday rotation and its decay. We, of course, adapted the beam sizes to match the respective channel cross-sections with lenses. We use a simple sequence of 500 ms optical pumping, 100 ns delay, and then probing the DC-Faraday rotation either continuously (m̃ultiple $T1$ times) or pulsing the probe light to reduce the depumping effects. Pulsing the probe corresponds, in a sense, to applying lower mean probing powers. We use a function generator and AOMs to control the light pulses[8].

We record the time trace of the decay of the DC-Faraday rotation signal for different probing powers. We fit an exponential decay to the DC-Farday rotation signal for each optical probing power. An example recording with respective fit is shown in figure 7.16 for cell O16 with a probe power of 20 µW. The higher the probing power, the faster we expect the signal to decay as the probe laser induces more and more decoherence. Plotting the respective T_1 times for each cell versus various probe powers, we can fit a linear function to extrapolate the expected T_1 time in the dark. The linear extrapolation of the

[7] This method has been subject in many previous theses, we will therefore refrain from reproducing all the details here. The interested reader should consult Fabricant (2014) for a more experimentalist's take on the measurement or Julsgaard (2003) for a more in-depth mathematical description.

[8] We used a RIGOL DG1032 for the trigger generation of the switches for the light pulses.

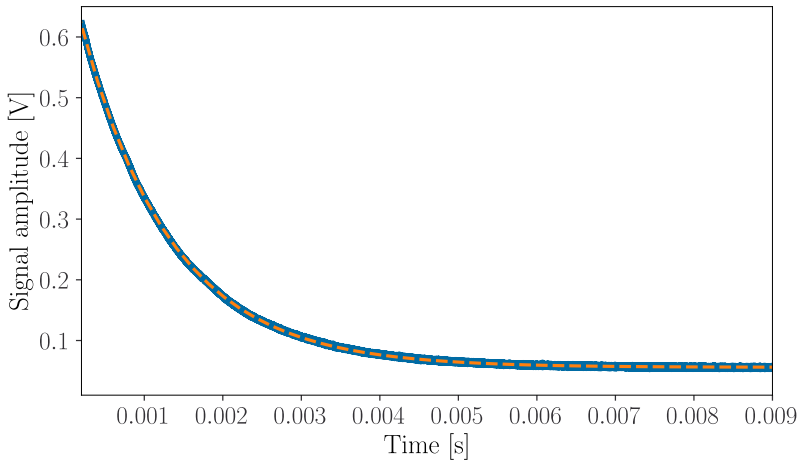

Figure 7.16: Decay of Faraday rotation. Exemplary recording of the measured Faraday angle decay (blue) for cell O16 with a simple exponential fit (dashed orange line) of type $f(t) = a + b\exp(-t/T_1)$ to extrapolate the T_1 time after turning off optical pumping at $t = 0$. This measurement is repeated for many different probe powers.

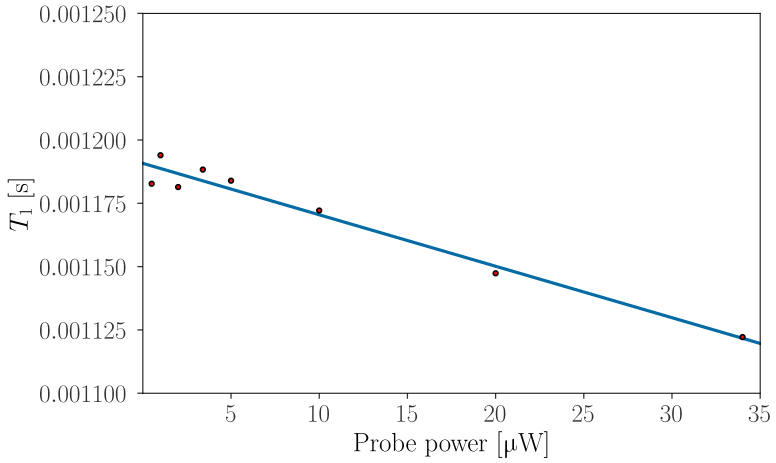

Figure 7.17: T_1 versus probe power. Obtained T_1 times (red dots) for cell O16 as obtained from the Faraday rotation decay as presented in figure 7.16 versus different probing powers. From this, we extrapolate the decoherence time in the dark for zero probe power to be $T_1 = (1.19 \pm 0.01)$ ms using the fit function (blue).

T_1 time in the dark is shown for cell O16 in figure 7.17. The extrapolated T_1 times in the dark are the values we stated in table A.1 and plot for comparison versus the channel cross-section in figure 7.18. Typically, we choose T_1 in the dark for comparison, as this time should be independent of the applied probing power, enabling us to compare cells of different geometries and beam sizes. We see a variance in the observed T_1 times for cells. We expect the av-

erage T_1 time to increase with the mean free path of the atoms towards larger channel cross-sections. However, we expect cells of the same cross-section to exhibit similar longitudinal spin coherence times. Precise anti-relaxation coating compositions and thickness variations are likely cause the observed coherence time differences. We can rule out that the variances are related to day-to-day drifts, as we tested the same cell over multiple days and observed a high level of reproducibility.

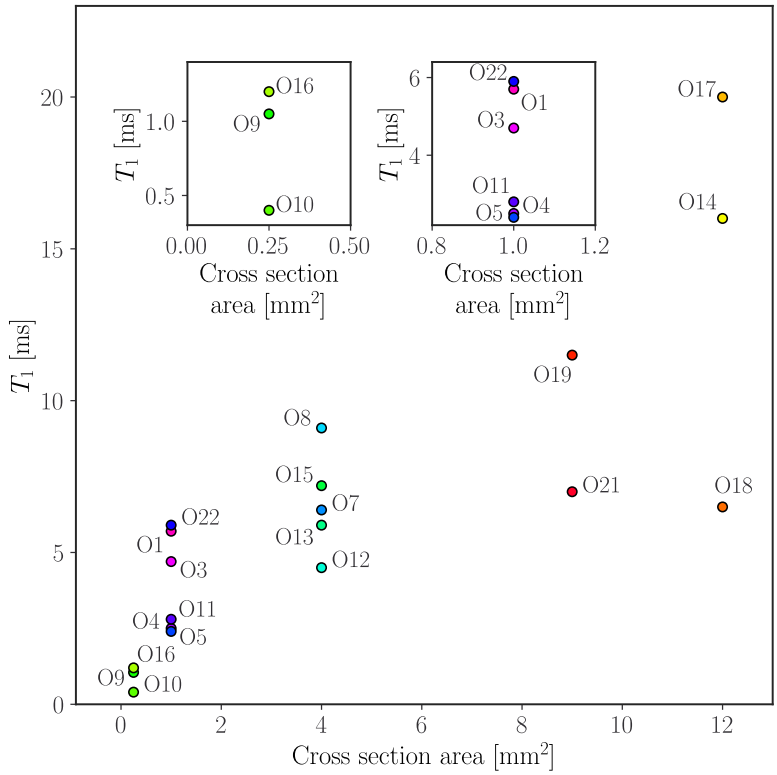

Figure 7.18: T_1 times in the dark versus channel cross-section. Observed T_1 times in the dark for all cells (individual colors and labels) versus their respective cross-section diameter. The two insets are zoom-ins of the data points to allow better data visibility.

Naturally, one would easily anticipate some correlation between different cell performance parameters when observing variations in different parameters. For example, one could expect a correlation between a low transmission of the vapor cells and the observed coherence times. However, there is no clear trend that long T_1 times coincide with the high transmission of a vapor cell. The absence of correlations illustrates the natural variability across vapor cells due to their manufacturing process. The high level of the individuality of cell performance is why we go through so much trouble in having many cells fabricated and tested with the same geometry. The individuality of the cells makes it hard to predict the precise outcome in cell performance, and hav-

ing a variety will ensure that we can take our pick, accommodating a specific experiment's needs.

Comparison T_1 and T_2

As mentioned, we are interested in extrapolating the T_2 times of newly fabricated cells based on the much simpler T_1 measurement. The hope is to find a linear dependence between both measurements to extrapolate the remaining cells' expected performance. The values for the T_2 times have been obtained by **Jun Jia** and **Ryan Yde** in the "GWD lab".

In figure 7.19, we plot the measured T_1 and T_2 times in the dark versus each other. We fitted a polynomial of the first order to the result and observed rather good agreement. The linearity hints that each method seems to reproduce the relative performance. Otherwise, lower T_2 would not necessarily correspond to observing lower T_1. One outlier is cell O12, but there we had the problem that between its T_2 measurement and the T_1 measurement, we had observed a sudden degradation of the cell. This sudden cell degradation has often been observed across many cell generations (e.g., Zugenmaier et al. (2018); Thomas (2020)). For cell O12, we had to recure the cell[9] multiple times before a proper T_1 measurement with a reasonable outcome could be performed. Therefore, this data point is likely, not reliable. Nevertheless,

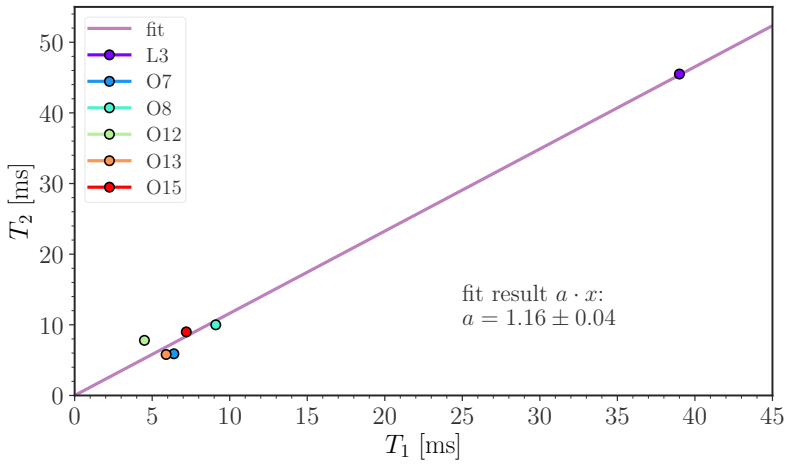

Figure 7.19: Polynomial of first order fitted to T_2 times versus T_1 times in the dark, individual colors for each cell, to extrapolate the expected proportionality factor. The purple line illustrates the fitting result. Cell O12 is an outlier, but removing it did not alter the result significantly. More information about O12 is provided in the text.

[9]Recuring refers to heating the cell to an elevated temperature to remove atoms that are stuck to the coating or the window and "reinitialize" the cell in a sense. The method is described in appendix A.1.

using the relation in figure 7.19 allows for a rough estimate of the expected T_2. However, one should be careful and not extrapolate the absolute expected T_2 values from the various T_1 in the dark shown in table A.1 in appendix A.2. It is limited to how comparable T_1 and T_2 measurements are since they were per-

formed in different experimental setups and regimes. For example, T_1 measurements were performed at significantly higher magnetic field strength than T_2. Also, the magnetic field used for the T_2 measurements has been specifically designed to achieve an incredibly high magnetic field homogeneity[10], decreasing the decoherence rate due to magnetic inhomogeneity compared to other experimental setups. However, due to the linear agreement, using the values to relatively judge the cells compared with respect to each other is possible.

[10] This has been a rather long endeavor for our fellow Quantoppies in the GWD lab, extending over more than a year. The results have been part of the Master thesis by Ryan Yde (Yde (2020))

Part III

DLCZ-type experiment

Chapter 8

A room-temperature atomic ensemble as single-photon source

Single-photons and their sources are fundamental building blocks for many schemes establishing secure communication channels. Characteristics of single-photons are their statistical properties, manifesting in the anti-bunching of photons. This allows us to quantify the performance of single-photon sources by investigating the auto-correlation function of their light field. There are two fundamentally different ways of generating single-pho-tons: probabilistic and deterministic single-photon generation. The fundamental difference here is that probabilistic sources will generate single-photons with some finite probability but most of the time zero photons. With a finite probability, two or more photons are generated. Multi-photon generation can be detrimental to specific quantum cryptography protocols. However, a truly deterministic single-photon source will generate a single-photon – and a single-photon only – each time. Many efforts have been aimed at developing single-photon sources across many different physical platforms, as seen in the introductory chapter of this thesis (section 1.2).

Often, a single-photon source by itself is of limited use with probabilistic operating schemes, as the photons are generated with low probabilities, and successful generation can be random in time. Therefore, these sources are often combined with a quantum memory (section 1.3). A quantum memory allows the successful storage of a quantum state, for example, single-photons. After a variable storage time, the stored state can be retrieved from the memory again. While it is easy to think of combining two systems, one dedicated to the single-photon generation and one dedicated to the storage of said single-photon, it is technologically simpler to have one system combine both properties. The advantage of having source and memory within one physical is that one does not need to worry about how to interface both systems. A single experimental setup and control suffice. The DLCZ protocol exploits storage and consecutive retrieval of single-photons on demand for long-distance entanglement generation using atomic ensembles. The protocol aims to overcome limits set by losses when sending qubits through fiber to create entanglement

over a distance. It exploits storing and retrieving a collective excitation to generate a single-photon on-demand to implement so-called *quantum repeaters* to create entanglement over long distances. Many efforts have gone into realizing the herald-retrieval scheme as proposed in the DLCZ protocol (Duan et al. (2001)). Early experimental realizations, verified by the observation of non-classical correlations, were using cold atomic clouds, e.g., in Kuzmich et al. (2003), or an atomic memory in a dense cloud of Rubidium atoms van der Wal (2003), however, not on the single-photon level.

This part of the thesis covers our approach toward implementing a DLCZ-type single-photon source with built-in memory. The following chapter will first focus on the experimental setup used for the DLCZ-type experiment (chapter 9) where we will emphasize the changes and steps taken towards our publication Dideriksen et al. (2021). Here, we will describe the differences and improvements implemented since Zugenmaier et al. (2018) and Schmieg (2019). Afterward, chapter 10 will present and elaborate on the results presented in our joint publication *Room-temperature single-photon source with near-millisecond built-in memory* (Dideriksen et al., 2021). All the main results presented have been achieved in collaboration with **Michael Zugenmaier** and **Karsten B. Dideriksen**. Due to this very close collaboration, there is a significant overlap in the presented information with the PhD thesis by Karsten B. Dideriksen (Dideriksen (2021)). This part of the thesis will conclude with a discussion and outlook chapter, where the steps towards improving our single-photon source and memory are presented (chapter 11).

Chapter 9

Experimental Setup

This chapter will introduce the setup used to implement the DLCZ-type single-photon source with in-built memory as presented in our publication Dideriksen et al. (2021). We will emphasize the changes made since Dideriksen (2017); Zugenmaier et al. (2018); Zugenmaier (2018) and Schmieg (2019), as those were the contributing factors allowing us to improve our experimental setup and scheme to reach the level of performance as presented in chapter 10. However, most of the experimental setup details will significantly overlap with the previously presented theses. Further, the same status of the experimental setup has been reported in Dideriksen (2021) due to the close collaboration.

Due to the complexity of the experimental setup, we will illustrate and describe individual parts of the setup in the following sections. We will start this chapter by introducing the characteristics of the vapor cell used for our experiment and details on the magnetic field and shielding (section 9.1). In addition, we will introduce the narrow linewidth laser used to derive the two drive light fields for the write and read step, along with the respective locking frequencies for the scattered light fields in section 9.2. Further, we will discuss the properties of our cavity surrounding the vapor cell and address some of the experimental difficulties arising from the cell cavity in section 9.3. As we have motivated in the theory part of this thesis (chapter 4), efficient filtering and rejection of the drive light are essential for the success of our herald-retrieve scheme. The two dedicated write and read detection setups and our choice of single-photon detectors will be covered in section 9.4. This chapter will commence with a description of our experimental control and pulse sequence used to perform our measurements (section 9.5).

Figure 9.1: Photo of microcell. Microcell of encapsulated design, where a glass chip with a small channel is placed inside a half-inch glass tube. A micro-drilled hole connects the channel and cell body, allowing cesium atoms from the cesium reservoir in the stem to travel to the channel. Due to the stem and chip's orientation, optical pumping must be applied through the thick side of the chip. Photo: Carsten Seidel for University Post.

9.1 Vapor cell

In the case of the DLCZ-type experiment, we use a vapor cell internally known as G2. Generic details about vapor cells have already been introduced in chapter 7, and technical details were covered in the first section 7.1 of that

chapter. Therefore, we will only describe specifics of cell G2 that have not been covered yet and are relevant to the DLCZ-type experiment.

Cell G2 is an encapsulated chip cell with an effective interaction volume of $0.3 \times 0.3 \times 10\,\mathrm{mm}^3$. Due to its size and design, we refer to it as a microcell. The chip is contained in a half-inch glass tube with a stem connected to it. A drop of cesium in the tip of the stem is the atomic reservoir. The reservoir is connected to the interaction volume (cell channel) through a microdrilled hole as opposed to the scratch used for cells of Generation O, covered in chapter 7. We have an alkane-based paraffin coating, allowing for $>10^4$ wall collisions of atoms before they depolarize while at the same time allowing for operating temperatures of up to 60 °C. We typically heat our cell to $\approx 42\,°\mathrm{C}$. Using the absorption measurement presented in section 7.3, we determine the number of atoms in our interaction volume at 42 °C to be $\rho_{42°\mathrm{C}} = (0.22 \pm 0.02) \cdot 10^9$ atoms. Following Dideriksen (2021), we estimate the on-resonance optical depth d between the ground and excited states and assume a fully polarized atomic ensemble for convenience. Then we only need to consider $|F = 4, m_F = 4\rangle \longrightarrow |F' = 4, m_{F'} = 4\rangle$ with π-polarized light in analogy to our theoretical description of the write step in section 4.2.1. We estimate the optical depth of our ensemble to be (Dideriksen (2021)):

$$d \quad = \quad \frac{\lambda^2}{2\pi}\rho_{42°\mathrm{C}} L_z \quad = \quad (0.32 \pm 0.03) \cdot 10^3 \tag{9.1}$$

where $L_z = 10\,\mathrm{mm}$ is the length of our cell channel and λ is the wavelength of the D_1 line. The prefactor of exactly one is related to the excited state branching ratio and can be found, for example, in Steck (2019).

In the DLCZ-type experiment, we are limited by two figures of merit of our vapor cell. First, we need a long transverse spin coherence time T_2 to efficiently store and retrieve single collective excitations in our herald-retrieve scheme. Secondly, we rely on a high transmission of the cell. Since we exploit a cavity around the cell, any additional losses inside the cavity are detrimental to our performance. Therefore, avoiding as many losses as possible for each pass inside the cavity is elemental (section 9.3). Typically, we observe $T_{\mathrm{cell}} = 87.8\,\%$ for the transmission of the cell.

9.1.1 Magnetic field and shielding

As for the cell testing (chapter 7), or later on in this thesis for the entanglement-enhanced MIT (chapter 13), we rely on a homogeneous magnetic field and avoid disturbing our collective spins by magnetic fields originating from surrounding electronics or the power grid, for example. To this end, we place our vapor cell inside a magnetic shield. However, compared to the cell testing, the channel is not oriented along the axis of the magnetic shield cylinder (x-direction) but transverse to it (z-direction). The shield for the DLCZ-type experiment consists of an outer layer of iron and three layers of mu-metal. These serve the purpose of reducing low-frequency magnetic fields. An additional layer of aluminum serves the purpose of shielding our collective spin-

oscillator from external RF frequency magnetic fields. This aluminum shield simultaneously serves as a frame for our coil system generating the bias magnetic field. The bias magnetic field is generated using three pairs of coils. Since our bias magnetic field is transverse to the cell channel, we are sensitive to the radial dependency of the magnetic profile. Our bias field alone will not be sufficient for that. Therefore, a double saddle coil is introduced to reduce the radial inhomogeneity. Unlike the quantum-enhanced MIT setup (chapter 13), we do not have a compensation coil for the DLCZ-type experiment.

With careful optimization of the magnetic fields, our magnetic field homogeneity is good enough to resolve a pulsed MORS spectrum at a Larmor frequency of $\nu_L = 2.4\,\mathrm{MHz}$. This corresponds roughly to $B \approx 7 \cdot 10^{-4}$ T. Using pulsed MORS, we determine the transverse spin coherence time T_2 in the dark for cell G2 to amount to $T_2 = 1/(\pi \cdot 158\,\mathrm{Hz}) = 2.0\,\mathrm{ms}$. In order to perform pulsed MORS, we need to drive transitions across neighboring Zeeman levels. We "kick" the macroscopic spin using a pair of RF coils, generating an RF field oriented along the y-axis. The RF coils are the only coil pair placed inside the aluminum shield.

These magnetic field and shielding configurations have been discussed many times before. We refrain from presenting them here further. The experimental details on them are found, for example, in Fabricant (2014) or Stærkind (2015).

9.1.2 Optical Pumping and atomic state preparation

As discussed in the theory section 2.4, a fundamental prerequisite for implementing the DLCZ scheme successfully in a room-temperature vapor cell is the successful preparation of the atomic ensemble in a coherent spin state (CSS). Our scheme is intrinsically limited to the residual population in the $m_4 = 3$ Zeeman level. We previously identified this as one of our leading experimental limitations compromising the successful retrieval of stored collective excitations (Zugenmaier (2018); Schmieg (2019)). Continuing our previous efforts to improve the optical pumping remained a key factor. We have introduced the principle of optical pumping in section 5.2 and discussed some of our efforts as part of the chapter on atomic spin state characterization. Here, we will focus more on the experimental setup and specifics.

As previously discussed, we use the pump and repump lasers for optical pumping. We combine them in front of the cell using a beam splitter (figure 9.2). With an interaction volume of $0.3 \times 0.3 \times 10\,\mathrm{mm}^3$, optical pumping from the side poses some challenges. First, due to the encapsulated chip design of the cell, we have to optically pump through the thick side of the chip the curvature of the cell body. In addition, we require a very narrow beam waist in the vertical direction. In contrast, the horizontal dimension of the optical pumping beams has to cover a large extent of the channel length. We achieve this highly asymmetric beam profile with cylindrical lenses (figure 9.2). The technique of pulsed MORS is key to investigating the optical pumping effi-

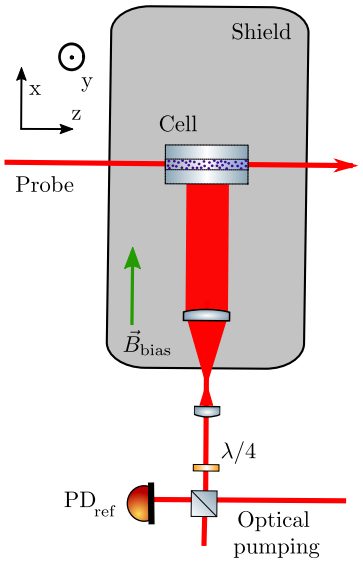

Figure 9.2: Optical pumping configuration. To optimize the optical pumping along the bias magnetic field and match the cell channel, we exploit cylindrical lenses to widen the beam along the z-direction. We monitor the pump and repump powers using a reference photodetector.

ciency as presented in 6.2, as it allows us to determine the population differences between neighboring Zeeman levels. Employing this technique, we optimize the polarization of the optical pumping beams, their optical power, and their temporal shape. Implementing smooth optical pumping turn-off and delaying the pump turn-off to the repump beam allowed us overall to achieve an atomic polarization of 98.8 % using our free model for a Larmor frequency of $\nu_L = 2.4\,\mathrm{MHz}$. Delaying the pump turn-off in our experimental pulse sequence by 40 µs at the expense of optical depth allowed us to reach 99.2 % atomic spin polarization. The experimental sequence is discussed at the end of this chapter in section 9.5. More details on the optical pumping optimization can be found in the chapter on atomic state characterization (chapter 6). Further, readers interested in different efforts people at Quantop have pursued throughout time might want to consider checking the relevant (p)MORS chapters provided in Zugenmaier (2018); Schmieg (2019); Dideriksen (2021) for the steps taken in the DLCZ-type experiment. Valuable information is provided in Thomas (2020) for a different experiment from our group. A rather old but somewhat more educational resource exploiting continuous MORS for optical pumping optimization is Krauter (2011).

9.2 Excitation light

The light used to drive the scattering processes during the write and read part of our scheme is derived from a single narrowed ECDL laser. The optical setup, including relevant optical paths for the feedback, is shown in figure 9.3. This narrowed laser has been part of the experiment for a long time and has been covered previously. Here, we will only introduce the basic working principles, and more details can be found in Dideriksen (2014a) and Zugenmaier (2018). Both resources cover the setup when the light on the D_2 line at 852 nm was used. A more recent description describing the setup after changing to the D_1 line can be found in Dideriksen (2021).

The laser is locked using a triangular cavity, where the reflection of the incoupling mirror is analyzed using a Hänsch-Couillaud analyzer, and an error signal is derived (Hansch and Couillaud (1980)). The error signal is used to actuate the piezo attached to the feedback mirror that sends a small fraction of the light back into the ECDL. The piezo-actuated feedback ensures that the phase of the feedback light is stabilized.

As we have seen in section 4.4, our experiment needs to operate the write and read drive light at a magic detuning to avoid four-wave mixing processes during the readout. In order to lock the laser to an atomic transition, a second feedback loop is used to stabilize the laser at the desired wavelength. For this, we beat part of the ECDL laser light against the light of our pump laser (locked to $F = 4 \rightarrow F' = 4$), and the recorded signal is analyzed for its beating signal using an RF electronic interferometer based on Schünemann et al. (1999). The error signal controls the piezo of the triangular locking cavity using an analog PID controller. The advantage of using a triangular cavity in this setup is

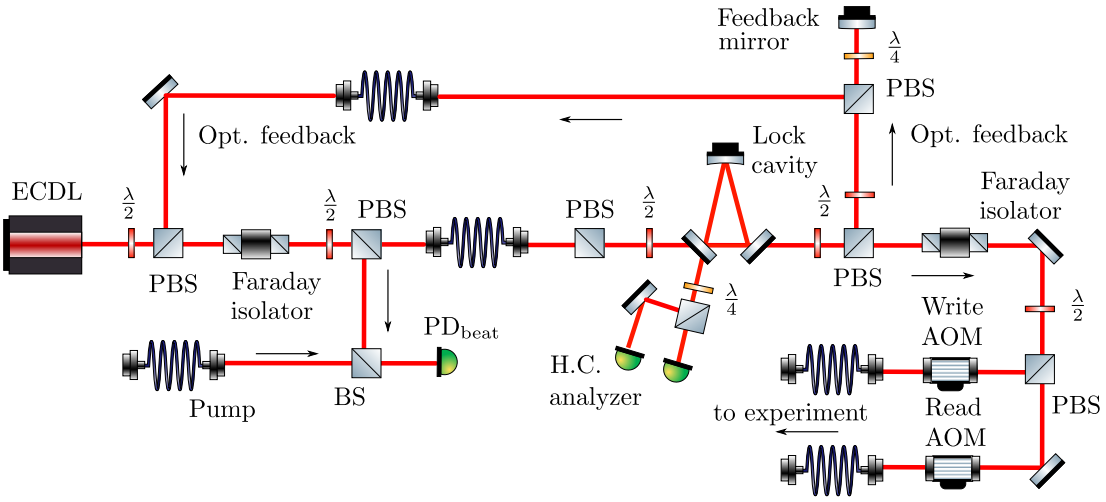

Figure 9.3: Narrowed laser setup. Schematic of the narrowed external cavity diode laser (ECDL), including the optical feedback, the H.-C. locking, and relevant other optics. The optical path towards the experiment includes the dedicated AOMs and fiber for write and read pulse generation. The triangular cavity is used for locking and as a spectral filter of our narrowed laser light. A piezo-controlled feedback mirror stabilizes the phase of the optical feedback light. For locking the laser to an absolute atomic reference, it is beaten against the pump light. The feedback from the beat note signal is used to control the length of the lock cavity. Figure inspired by figure 3.1 in Zugenmaier (2018).

that we can exploit the locking cavity simultaneously as a spectral filter for our drive light used in the experiment. The drive light is split and sent to two AOMs – one for write and one for read (see figure 9.3). The frequencies for write and read are then obtained using the first-order diffraction of the respective AOM.

The narrow linewidth of our laser is one of the building blocks for the success of our scheme. The linewidth of the laser light would limit us if our spectral filters were narrower than our scattered photons. Spectral filters narrower than our scattered light would lead to spectral mismatch and inadvertently filter out part of our "good" scattered light fields. In Dideriksen (2014b), and further discussed in Dideriksen (2021), the linewidth of the laser was determined to be FWHM $< 30\,\text{kHz}$ over $200\,\mu\text{s}$ as an upper limit using a beat note measurement.

9.3 Cell cavity

We place the vapor cell G2 used for our experiment inside a low finesse cavity to enhance the light-atom interaction (compare section 4.3). The cavity is designed to be one-sided to ensure efficient outcoupling of the light and guide it toward the dedicated filtering and detection setups. One-sided means that our incoupling mirror is a high-reflector with $R_1 = 99.6\,\%$, while our outcoupling mirror has a lower reflectivity of $R_2 = 80.5\,\%$. Then, losses out of the cavity through R_1 are negligible, and we can assume that our scattered

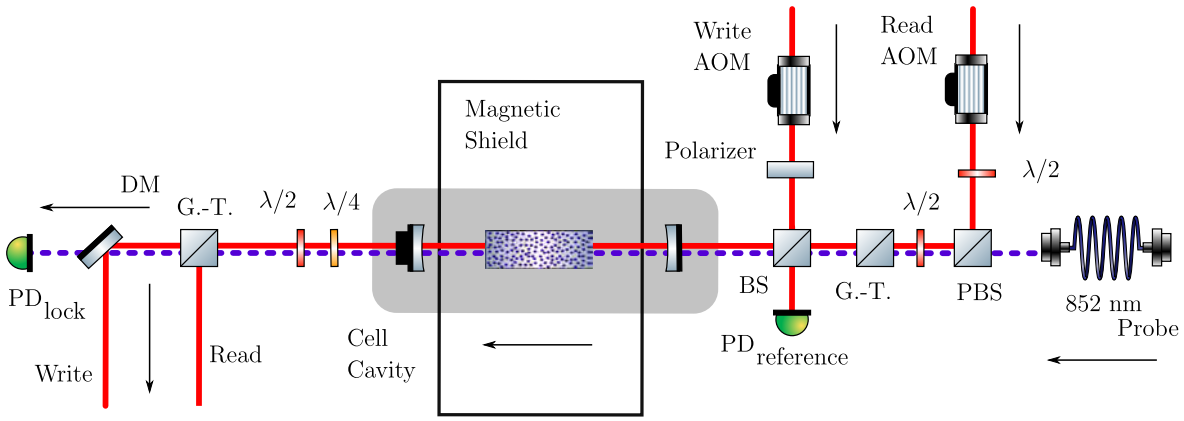

Figure 9.4: Beam paths incident on cell cavity and cell cavity locking signal. Illustration of write and read path incident on the cell cavity. In addition, the probe path (blue dashed line) for locking the cell cavity in transmission, exploiting a dichroic mirror (DM), is shown. For polarization cleaning before the cell cavity and filtering between drive and scattered light fields, Glan-Thompson polarizers (G.-T.) are used. (P)BS indicates a (polarizing) beamsplitter. Arrows indicate the light propagation directions to aid the reader.

photons will effectively leave the cell cavity solely through R_2. Both cavity mirrors have a curvature of $R = 110\,\text{mm}$. As indicated in figure 9.4, we built the cavity around the magnetic shield. By varying the separation between the mirrors, we can adjust the waist at the center of the cavity. This allowed us to increase the waist radius from $\omega_0 = 55\,\mu\text{m}$, used for the results presented in, for example, Zugenmaier et al. (2018), to $\omega_0 = 90\,\mu\text{m}$, effectively improving our filling factor. As previously introduced (section 4.5, the motional averaging is faster for a beam profile that illuminates the cell cross-section better. For a waist of $\omega_0 = 90\,\mu\text{m}$, we observe a cell transmission of $T_{\text{cell}} = 87.8\,\%$.

One practical limit to our scheme is how well a generated scattered photon can leave the cell cavity, which we refer to as escape efficiency η_{esc}. Considering only the out-coupling mirror with R_2 and approximating $R_1 = 1$, together with the cell transmission T_{cell}, we determine the escape efficiency η_{esc} as follows:

$$\eta_{\text{esc}} \quad = \quad \frac{T_{\text{cell}}(1 - R_2)}{1 - R_2 T_{\text{cell}}^2} \quad = \quad 0.45 \pm 0.02 \tag{9.2}$$

This equation can be interpreted as the transmission of the scattered photon through the outcoupling mirror $(1 - R_2)$, where a scattered photon has passed through the cell once (T_c), divided by the total round-trip loss $(1 - R_2 T_{\text{cell}}^2)$. The escape efficiency of scattered photons out of the cell cavity significantly reduces our scheme's success rate, as more than half of the scattered photons are not even leaving the cell cavity. The high number of lost scattered photons limits our attainable retrieval efficiency of a heralded collective excitation. It slows down the rate of successful write-read detection events. However, these losses do not compromise our performance. They only increase the number of trials required (success rate) and require us to operate in the low excitation

regime to render double-excitations negligible.

The cell cavity is locked using our probe laser (see chapter 5), as the probe laser is far-detuned from any atomic resonances. An off-resonant laser avoids depolarizing the atomic ensemble during our experimental sequence's optical pumping and locking stage (section 9.5). The far-detuned laser for locking the cavity allows us to prepare the atomic ensemble in a coherent spin state within the same time window during the experimental pulse sequence. When using the probe laser to lock the cell cavity, we must ensure that our scattered light field resonances and probe laser resonance coincide despite their vastly different wavelengths. We achieve this by scanning the cell cavity and recording the signals of drive light fields tuned to the scattered light field frequency and the probe light used for locking. The co-propagating beams are illustrated in figure 9.4. To overlap the resonances of the scattered light field and the probe light, we adjust the precise probe EOM modulation frequency to overlap the resonance of all three light fields. These adjustments to the EOM modulation frequency are why our probe light detuning is not fixed but instead varies between 1.8 and 2 GHz.

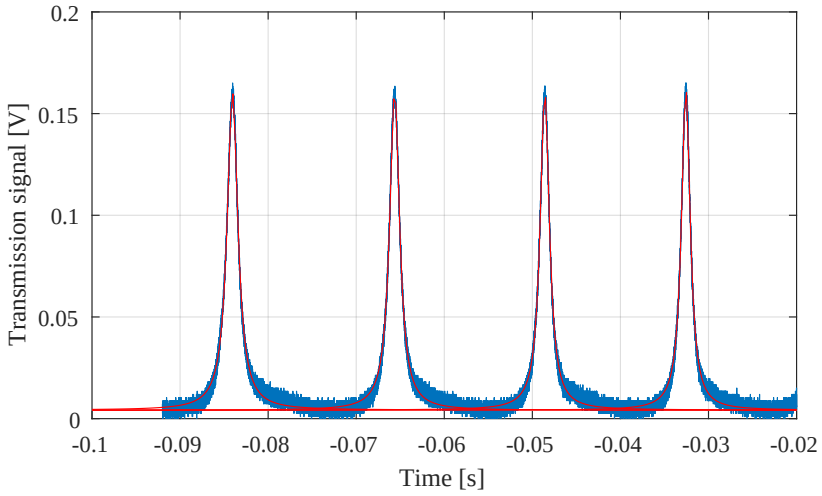

Figure 9.5: Cell cavity scan. Obtained transmission signal when scanning the cavity piezo over multiple resonances. Each resonance is fitted with a Lorentzian lineshape to estimate the average finesse. See the main text for more details about the fits.

Before we run our experiments, we verify the proper alignment of the cell channel inside the cell cavity by scanning the piezo to scan over multiple resonance peaks. This allows us to determine the observed finesse by fitting a Lorentzian to each scanned resonance and determining the free spectral range (FSR) between each resonance. A good scan of the transmission signal, including four individual Lorentzian fits, is shown in figure 9.5. We fitted four individual Lorentzians in the time domain:

$$\mathcal{L}(t) \quad = \quad \frac{a}{(t-t_0)^2 + (\gamma/2)^2} + b \tag{9.3}$$

where the fit parameters are given by the amplitude a and offset b, while t_0 determines the peak location and γ the width. These fits allow us to determine the finesse $\mathcal{F} = \gamma/\mathrm{FSR}$ in the time domain. Due to the nonlinearity of the piezo scan, we determine the finesse as the average over the observed four resonances. Typically, we observe for our light at the scattered photon frequencies a finesse of $\mathcal{F} = 13.0 \pm 0.4$. The linewidth γ in the frequency domain can be determined using the finesse $\mathcal{F}$, together with FSR = 725 MHz, leading to $\gamma = 55.8 \pm 1.7\,\mathrm{MHz}$. This relatively broad spectral linewidth of the cell cavity ensures that drive and scattered light fields have both high transmissions through the cell cavity despite their separation by the Larmor frequency $\nu_\mathrm{L} = 2.4\,\mathrm{MHz}$.

Another essential feature of the cell cavity – or more of a challenge – is its different, atomic polarization-dependent birefringence. We observe for our vertically-polarized σ-light and horizontally-polarized π-light a shift in the resonance frequencies with respect to each other. The resonance frequency shift due to the birefringence is maximal when dealing with a highly polarized atomic ensemble. It approaches zero for a thermal atomic ensemble, as illustrated in figure 9.6. The birefringence originates from the hyperfine splitting of the excited states and different strengths of the dipole-allowed transitions for π- and σ-polarized light (Dideriksen (2021)). Typically, we observe a frequency shift of $\Delta\nu_\mathrm{res} \approx 32\,\mathrm{MHz}$. Instead of correcting the frequency difference by stepping the piezo between write and read step, we rather adjust the light frequencies between our write and read pulses to accommodate the resonance shifts. The frequency difference between write and read scattered photons comes at the price of additional experimental complexity. Due to their large frequency shift, we require two dedicated filtering and detection setups for write and read scattered photons.

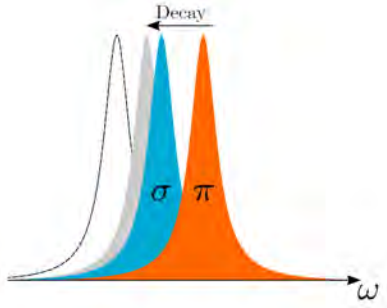

Figure 9.6: Illustration cell cavity birefringence. The atomic birefringence depends on the atomic population distribution. The resonances for the fully pumped ensemble are strongly split for horizontally polarized (π) and vertically polarized (σ) light. From here, the two resonances shift to the same frequency for the ensemble at thermal equilibrium (grey). The dashed lineshape illustrates the empty-cavity resonance. Figure and caption adapted from figure 3.17 (left) in Dideriksen (2021).

However, the frequency shift reduces while the atomic polarization degrades. The reduction in birefringence poses a problem when we wish to delay the readout of a heralded collective excitation. One way of remedying this would be to adjust the probe EOM modulation frequency, which determines the frequency the laser is locked to, and optimize the common resonance for each delay. We have tried this, and it is possible to do. However, this would mean that we cannot interleave measurements with different delays but would need to perform measurements after each other. Additionally, this optimization process of finding common resonances between scattered light fields and probe laser is time-consuming. It is a significant disadvantage to be unable to interleave measurements, as drifts, alignment degradation, and more would affect experimental runs with different delays between write and read pulses differently. Therefore, we want to interleave measurements with different write-read delays. To do so, we require a different approach to compensate for the change in the birefringence of the cell cavity. Another way to remedy the polarization-dependent birefringence is to include an additional, weak repump pulse into our experimental sequence (see section 9.5) when delaying the read pulse more than 100 µ sec after the write pulse. At the expense

of small repump-induced decoherence, we observe that the atoms transferred from $|F = 3, m_F = 3\rangle$ to $|F = 4, m_F = 4\rangle$ help us counteract the change in birefringence of the cell cavity. For a more thorough discussion of the cell cavity birefringence, the interested reader is advised to consult Dideriksen (2021).

9.4 Filtering and detection

In the following, we will discuss how we separate our desired scattered photons from a background of $>10^{12}$ classical photons in the same spatial mode. As seen in section 4.2, two traits differentiate the single-photons from their respective drive light. First, the scattered photons are of orthogonal polarization with respect to their drive light. For the write step, we expect the heralding scattered photon to be in σ_--polarization, while the write drive light is π-polarized. The roles are reversed during the retrieval process. The read drive light is σ-polarized for the read pulse, while the retrieved scattered photon is π-polarized. This orthogonality in both processes between drive and scattered light can be exploited by polarization filtering. As a first level of filtering, we use a Glan-Thompson polarizer that allows us to achieve suppression of $5 \cdot 10^{-5}$ of the respective undesired light polarization. However, this alone is not enough to suppress the drive light to filter out the desired scattered photons from the background of classical photons. Therefore, we must exploit spectral filtering to further suppress the residual drive light. Spectral filtering is possible since the scattered and drive light fields are separated by the Larmor frequency $\nu_L = 2.4\,\mathrm{MHz}$.

Due to the significant frequency difference between write and read scattered photons originating from the cell cavity birefringence (section 9.3), we require two dedicated filtering and detection setups for write and read. If this would not be the case, we could, in principle, exploit a single detection setup combined with an optical element that allows us to change the polarization of light before the Glan-Thompson polarizer for either write or read. For example, changing the polarization of one of the scattered light fields could be done using a Pockels cell. A Pockels cell controls the polarization rotation of light by changing the voltage applied to it.

In the following, we will discuss how we implemented the detection setups for write (subsection 9.4.1) and read (subsection 9.4.2) processes, as well as the single-photon detectors (subsection 9.4.3) used for recording the scattered photons.

9.4.1 Write detection setup

The write detection and filtering setup is the detection setup we use to filter out our desired heralding single-photons during the write pulse, separating them from the write drive light field. Since the initial polarization filtering using a Glan-Thompson polarizer (shown in figure 9.4) is insufficient,

we exploit spectral filtering to separate the remaining drive photons from the desired scattered light field.

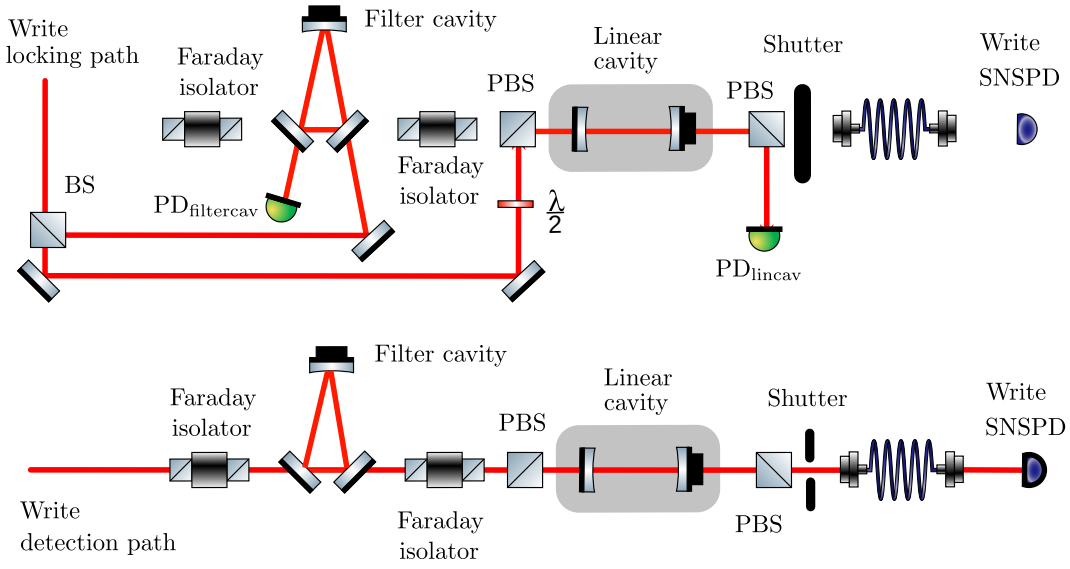

Figure 9.7: Write detection setup. Top: Beam paths for locking the write filtering and detection setup, the transmission signals recorded on the photodetectors are used to lock the two cavities. A shutter is blocking the path toward the SNSPD for its protection. Bottom: Beam path to detect the scattered write photon and suppress residual write drive light. The shutter is open during the write pulse. More details are provided in the text.

For the write filtering and detection setup, we use two cavities. One is a triangular cavity placed on the same spacer as the filtering cavity of the narrowed ECDL laser discussed in section 9.2. The piezo is attached to the curved mirror. The cavity has roughly a linewidth of 98 kHz. Since this cavity's extinction alone is insufficient, a second linear cavity is used to further spectrally filter the 2.4 MHz detuned drive light from the desired scattered heralding photon. This cavity has only a linewidth of 240 kHz. The two cavities combined have a total suppression of roughly 60 dB.

In figure 9.7, the beam paths used for locking are shown (top), as well as the path the scattered photon takes through the setup towards the detector, while the residual drive photons are rejected due to their frequency difference (bottom). During the locking window of our sequence (see section 9.5), we lock all cavities used in our experiment. Using the AOM generating the write pulse, we generate light at the scattered photon frequency to lock the cavities on resonance with the scattered photon. Further, we modulate the locking light with 3 kHz sidebands to lock the two cavities. The recorded transmission signal on the respective photodetector of each cavity is demodulated. Using an analog PID locking circuit, the respective error signal is used to lock the cavities (Zugenmaier et al. (2018); Dideriksen (2021)). During the locking period of our experimental sequence, we exploit a mechanical shutter to block the path toward the fiber leading to the single-photon detector to protect it

from stray light during the locking stage. The design of the shutters used in our experimental setups is heavily inspire by Zhang et al. (2015). The mechanical shutters lead to mechanical vibrations significantly disturbing our locking performance. Therefore we spent some time in optimizing the damping the shutters and isolating them from the optical table. Our choice ended up being multiple layers of thick rubber. Of course, this can be improved further but for our purposes this proved to be sufficient.

All locks are frozen during the experimental pulse sequence, and the locking beams are turned off. The shutter protecting the single-photon detector during the locking stage is opened. The scattered light propagates through the two write filter cavities (figure 9.7, lower part), while the undesired write drive light, off-resonance with the cavities, is reflected. To avoid back-reflection and cavity effects between the cavities, we introduced Faraday isolators between the cell cavity and the triangular lock cavity, as well as between the triangular and the linear cavity. As we will see later, the combination of polarization and spectral filtering suppresses the leakage of classical drive light to our detected scattered photons very efficiently.

9.4.2 Read detection setup

For the read step in our herald-retrieve scheme, we wish to detect the successful retrieval of a single-photon in the background of our read drive light field – we face the same challenges as for the write setup. Due to the frequency and polarization difference to the write step, we use a dedicated filtering and detection setup for the read. We use two high-finesse linear cavities for the read detection setup based on a design of an earlier generation of the filter cavities presented in Galinskiy et al. (2020). We have two distinct beam paths, one for locking, as indicated at the top of figure 9.8, and one for filtering the scattered light from the drive light, as shown in the lower part of figure 9.8.

We lock the cavities of the read detection setup using RedPitayas. These RedPitayas (STEMlab 125-14) are small, versatile, and affordable FPGA-powered boards with fast analog in- and outputs that come with a variety of tools on them, including PID modules. Together with the open source library *PyRPL* by Neuhaus and Deléglise (2017) that we modified to our needs, it is easy to automate and control the locking of the cavities. We generate the error signals and feedback using lock-in detection and dithering of the piezo of each cavity. We automated the locking and freezing of the active feedback using a home-written python interface using PyRPL. As opposed to the approach described in Schmieg (2019), we had to improve the locking routine and the lock's stability. Initially, we used only a single RedPitaya to lock both filtering cavities, as discussed in Schmieg (2019). However, this implied that we are limited by the bit-resolution of the RedPitayas arising from the digital-to-analog converter. In order to remedy this, we switched to a two PID locking scheme for each cavity, requiring a single RedPitaya for each cavity. Our locking scheme for each cavity is now based on two analog output channels,

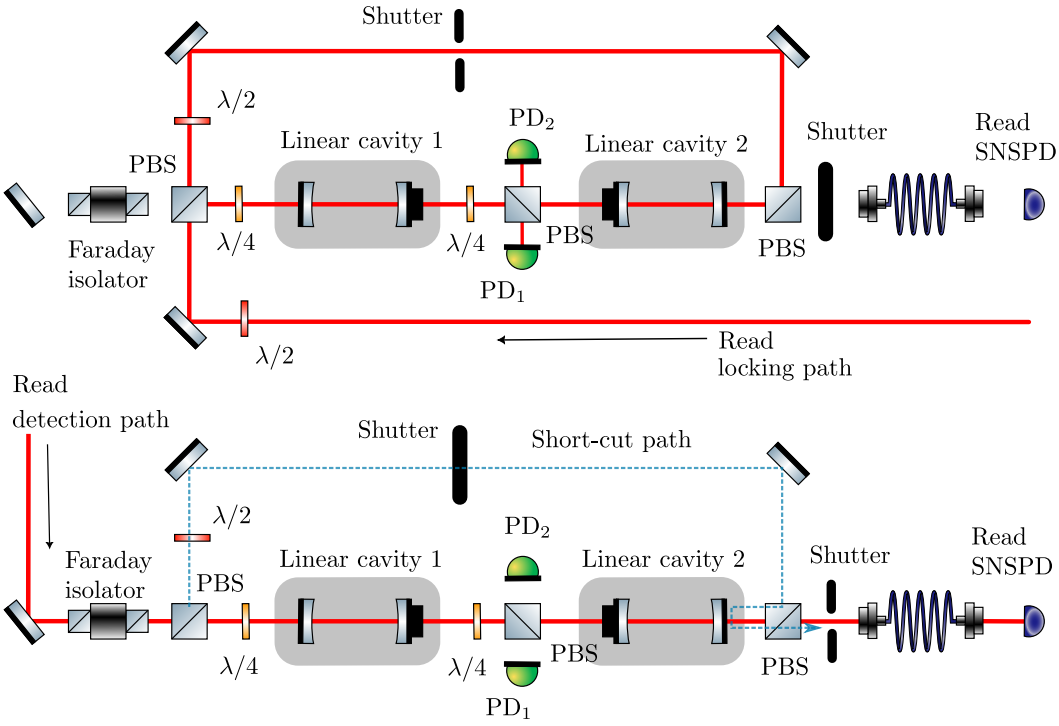

Figure 9.8: Read detection setup. Top: Beam paths for the locking of the read detection setup. Bottom: Beam path for the detection of the read scattered light field. The light blue path indicates a short-cut path part of the read drive light could take in the absence of the shutter. The respective shutter positions are indicated.

a coarse-gain and a fine-gain feedback channel. We amplify the course-gain output significantly to allow scanning over multiple FSRs of the cavity. Once we have found the initial locking position on the side of a fringe by scanning the coarse-gain channel, we freeze the feedback from this coarse-gain channel. Instead, the fine-gain channel takes over. This fine-gain channel has only a narrow range to ensure that the digital resolution does not limit us, and it controls the on-resonance locking of the cavity. The two outputs are combined using an analog summing circuit. The output of the amplifier is low-pass filtered to reduce the noise.

In our locking routine, we have implemented a "feed-forward" that adjusts the constant output of the coarse-gain channel. The feed-forward adjusting the coarse-gain channel's constant voltage output avoids that the fine-gain channel reaches the edge of its output range. Our feed-forward locking routines operate smoothly enough that after these improvements, the two cavities only unlock when the laser itself relocks. Otherwise, the lock is fully maintained or re-captures the peak without restarting the scanning part of the locking routine.

Overall, adding the new fine-gain channel for more precise on-resonance locking improved the average transmission during the total freeze window

by approximately five and six percent for InCav (Linear cavity 1) and AlCav (Linear cavity 2), respectively[1]. The read detection setup's improved stability and overall better transmission might initially seem minor. Considering that we are very sensitive to losses, even these minor improvements will prove vital when recording three-photon coincidences required for the conditional read auto-correlation $g^{(2)}_{\mathrm{RR}\,|\,\mathrm{W}=1}$.

	Single channel feedback	Two channel feedback
InCav (Linear cavity 1)	$89 \pm 12\,\%$	$94.2 \pm 6.9\,\%$
AlCav (Linear cavity 2)	$89 \pm 11\,\%$	$95.1 \pm 4.8\,\%$

Table 9.1: Comparison of average transmission during freeze window of 50 ms for old lock and the newly implemented two channel locking solution.

9.4.3 Single-photon detector

Throughout this thesis, we will mainly cover results obtained after we were fortunate enough to replace our old SPCMs (single photon counting modules). The SPCMs are based on single-photon avalanche detectors from LaserComponents, with only limited quantum efficiency ($\approx 30 - 50\,\%$). We replaced the SPCMs with two superconducting nanowire single-photon detectors (SNSPD) from *Photon Spot*. These SNSPDs are advantageous as they offer a higher intrinsic quantum efficiency ($> 90\,\%$). Exchanging our detectors came at the expense of some complications to our experimental setup, and our DLCZ experiment no longer being truly room-temperature-based.

The SPCMs were more straightforward in operation as we could use free space propagation of our scattered light fields. For the SNSPDs, however, we needed to couple the scattered light fields into fibers to guide and record the scattered photons with the SNSPDs. Overall, the reason for switching to the SNSPD was the significantly higher quantum efficiency and expected improvement of the detection efficiency. A higher detection efficiency decreases the time between single-photon detection events as more scattered photons are collected and not lost along the detection path. However, the actual gain of these detectors comes when looking for detection events with multiple photons, especially when measuring the conditional auto-correlation of the scattered light field during the readout. Since the conditional auto-correlation corresponds to multiple photon detection events – one write and two read photons – a factor of two in the overall detection efficiency leads to an eight-fold improvement in the overall measurement time required for sufficient statistics to estimate the conditional auto-correlation. A higher detection efficiency also allows us to reduce the write excitation probability. A lower write excitation probability reduces the probability of multiple collective excitations further.

Typically, we observe with the new detectors a dark-count rate of less than 1 Hz, as opposed to more than 10 Hz when we were using the SPCMs (see

[1] AlCav and InCav are the internal names of the cavities, linear cavity 1 and 2 is used in figure 9.8 for more generic description.

Schmieg (2019)). We can determine the detection efficiency of the two detection setups using calibrated neutral density filters to attenuate a beam with well-known optical power after the cell cavity[2]. For the read detection setup, we observe $\eta_{\text{det}}^{\text{R}} = (19 \pm 2)$ %. This value is an increase compared to previously determined values using the SPCM as a single-photon detector (see Schmieg (2019)). However, for the write detection setup, we only observe $\eta_{\text{det}}^{\text{W}} = (5.5 \pm 1.0)$ %. The value is significantly lower than that of the read detection efficiency. Part is related to the fact that we already previously observed low transmission through the write detection setup. The low transmission does not explain why we do not observe an improvement compared to the SPCM detector. We have had problems with the custom-ordered fiber used for the write detection setup, collecting the scattered light field, and coupling the light to the SNSPD. The fiber has some problems we could not remedy. We verified that the issue was not with the SNSPD channel or the connection spliced to it by switching between multiple detector channels. The result remained the same, indicating that the fiber connecting the write detection setup with the SNSPD is the limit. In the future, fixing or exchanging the compromised fiber causing the poor write detection efficiency can speed up our required measurement time. Given that our scheme operates "just" slower with a low detection efficiency, the problem caused by the low write detection efficiency is not a fundamental problem but rather an inconvenience.

9.5 Experimental control and sequence

Our experimental sequence is controlled using a field programmable gate array (FPGA) board, sending the trigger signals to our electronic controls, for example, the RedPitayas locking the read filter cavities. In addition, the FPGA board controls the trigger signals for the gating of the single-photon detectors (see section 9.4) and respective recording of the detection events, assigning each detection event with a time tag. It also records additional information, such as the transmission signals of the cavities.

For the write and read step, along with the locking frequencies for the filter cavities, we rely on precise frequency generation in the RF frequency range. To generate these desired frequencies controlling the AOMs in our experimental sequence, we employ a second DDS-FPGA controlling a DDS (direct digital synthesis technology) board. The DDS board generates the RF frequencies, allowing us to switch between the frequencies used for locking the cavities and the excitation light. The DDS-FPGA is controlled using our primary FPGA board and measurement interface.

Our total experimental control is synced to the 50 Hz line of the power grid. The overall repetition rate of the experimental pulse sequence is limited to a total duration of 120 ms. From this maximal duration of the experiment, only 65 ms can be exploited to run the desired DLCZ-type write-read sequence corresponding to a maximum of 75 repetitions. The remainder of the 120 ms is used to relock the cavities (see section 9.5). Each experimental sequence cycle,

[2] Later, we will also determine the detection efficiencies based on the correlation model (section 4.6) from fitting the model to our experimental data. Fitting the correlation model gives us an alternative estimate of the detection efficiency.

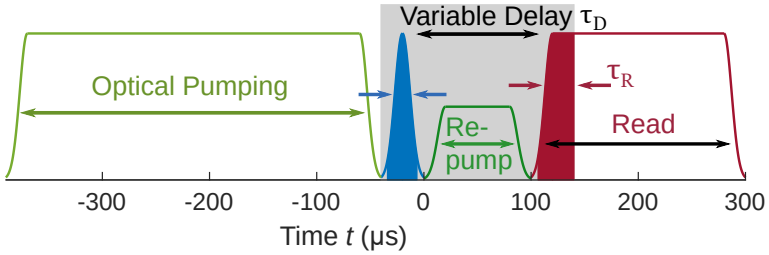

Figure 9.9: Pulse sequence. Pulse sequence including intermediate pumping, write and read pulse with optional, variable delay τ_D. Repump pulse for counteracting cavity birefringence effects is indicated along with shaded areas showing the integration of data in the experimental analysis. Figure from Dideriksen et al. (2021).

illustrated in figure 9.9 consists of the following:

1. **Locking window:**
   All filter cavities are locked to the respective scattered photon frequencies of the write and read steps. The cell cavity is locked using far-detuned probe light. At the end of this locking window, the active feedback to the cavity locks is frozen.
   Duration: 55 ms

2. **Optical pumping window:**
   Long optical pumping duration for atomic polarization preparation.
   Smooth turn-off of the optical pumping, pump turn-off is 40 μs delayed compared to repump.
   Duration: 6.5 ms

3. **DLCZ-type write-read scheme:**
   A variable number of repetitions, up to 75 depending on the delay τ_D between the write and read pulse, is performed.

   a) **Write window:**
   Horizontally polarized write drive light. The pulse is shaped to exhibit smooth turn-on and turn-off.
   Duration: 40 μs

   b) **Delay τ_D:**
   Variable delay τ_D between creation and retrieval of stored excitation. For delays exceeding 100 μs, a weak repump pulse is applied to counteract atomic polarization decay and resulting cell cavity resonance shift (see section 9.3).
   Duration: 10 μs - 1 ms

   c) **Read window:**
   Vertically polarized read drive light. The pulse is shaped to exhibit smooth turn-on and turn-off.
   Duration: 200 μs

d) **Intermediate optical pumping:**
Intermediate optical pumping to reinitialize atomic state before repeating another write-read sequence. Similar to the main optical pumping, the pulses are shaped to be smooth, pump turn-off delayed by 40 µs.
Duration: 350 µs

Figure 9.9 illustrates the core write-read sequence. While the duration of the pulses is fixed in the sequence, we can choose how long we integrate the pulse during the analysis. The integration of the pulses in the analysis is reflected by the shaded areas in figure 9.9. How we choose the timings will be discussed more thoroughly in the analysis presented in the next chapter, chapter 10.

Chapter 10

Cavity enhanced DLCZ

After discussing the experimental setup and the design choices in chapter 9, we will look at the experimental results of our DLCZ-type experiment. We will distinguish the impact of different parameters on our experimental performance regarding our generated single-photons and consider the intrinsic memory performance of our source.

Throughout this chapter, we will present the results published in Dideriksen et al. (2021), which were achieved as a group effort with Karsten Dideriksen and Michael Zugenmaier. We will elaborate on the results more thoroughly. Due to the close collaboration and overlap with another PhD project, the results have also been covered in Dideriksen (2021). This chapter has two main parts. First (section 10.1), we will quantify our source for immediate retrieval of stored excitations and analyze the statistics of write and read scattered light fields, along with the noise in the spectrum. We will introduce and identify the origin of different contributions to the scattered light fields. This information will be used as input for the correlation model introduced in section 4.6. Further, we will estimate the second-order correlation functions to quantify our herald-retrieve scheme. In the second part (section 10.2), we will quantify the memory capabilities of our experimental system by introducing delays between write and read drive light pulses. Considering different bounds of non-classicality, we define the memory time of our quantum memory.

A short note on our optimization

We have, throughout the years, spent much time improving the performance of our experimental scheme. A big part has been improving the optical pumping and coherent state preparation but likewise included optimizing the detection efficiencies (section 9.4) and more. These properties can be tested and improved without running the complete DLCZ-type experiment. Part of these efforts has been covered in this thesis as part of chapter 9. Other parameters, such as the read power used for the scheme or the pulse shapes of the optical pumping, write and read pulses, require running the experiment

with the entire experimental setup. These optimizations have been presented for the respective experimental increments in Zugenmaier (2018), Schmieg (2019), and Dideriksen (2021). For our most recent implementation, the following sections only include a subset of the optimizations going into it for the sake of the brevity of this thesis. Therefore, it is recommended that interested readers consult Zugenmaier (2018), Schmieg (2019), and Dideriksen (2021) for details on additional parameter optimization, for example, on optimization of the read power or the beam waist inside the cell cavity, or shaping of the optical pulses.

10.1 Observation of non-classical correlations

Following the introduction in section 4.6, we will consider the statistics of our scattered light fields. First, we will consider the individual statistics of pure write and read auto-correlations before estimating the conditional auto- and cross-correlation function characterizing the relationship between write and read scattered light fields. These will be our measure of success.

Throughout this section, we will consider ourselves only with minimal delay between write-in and retrieval of stored collective excitations and vary the write-excitation probability.

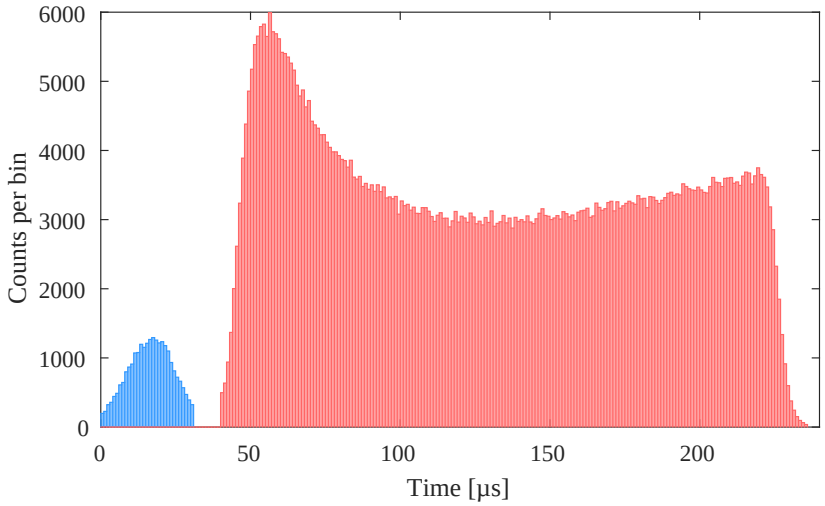

Figure 10.1: Histogram of time bins in sequence. Histogram of detection events during write and read pulses in bins of 1 μs. The write and read photon counts are shown in blue and red, respectively, and were measured with two separate detectors of the SNSPD. The histogram is obtained from 31 million sequence repetitions folded back onto each other of the combined data set covered in section 10.1.7.

Before diving into the analysis, we will consider the temporal shape of our recorded data. As introduced in section 9.5, each experimental sequence contains multiple repetitions of our write-read pulse sequence. Further, our recorded data files contain multiple of these sequences. Each count is recorded

in these with a time tag. The time tags allow us to analyze the data in various ways. The fundamental analysis is to fold all pulse sequences and detection events back onto a single write-read pulse sequence and consider the resulting histogram. In figure 10.1, the detection events are shown in 1 µs bins. These histograms give us an idea about how the detection events are distributed on average across write and read pulse. Both write and read exhibit slow rise and fall of the counts at the start and end of the respective pulse. This finite rise and fall are expected as we shape our pulses to have a rise and fall time of 10 µs (see section 9.5). We previously observed less noise when shaping all the pulses (Schmieg (2019); Dideriksen (2021)). Also, Bao et al. (2020) observed sensitivity to the turn-off shape of optical pumping.

The readout shape exhibits two distinct features in figure 10.1. We observe, in addition to the rise time related to the smooth shaping of the write and read drive pulses, an exponentially decaying component of the readout rate, ranging from 55 µs to 120 µs on the time axis in figure 10.1. This slope can be fitted with an exponential function $f(t) = a \cdot \exp(-\gamma_R t) + c$. Here, we define γ_R as the rate at which we read out the single-photons. We typically observe a readout rate of $\gamma_R = 40.2 \pm 1.6\,\text{kHz}$ for our optimal read drive power of $P_R = 200\,\mu\text{W}$ as estimated from figure 10.2. Towards the end of the read pulse, ranging from 120 µs to 220 µs in figure 10.1, the readout rate approaches a linear trend. We will discuss these observations more thoroughly in later sections of this chapter.

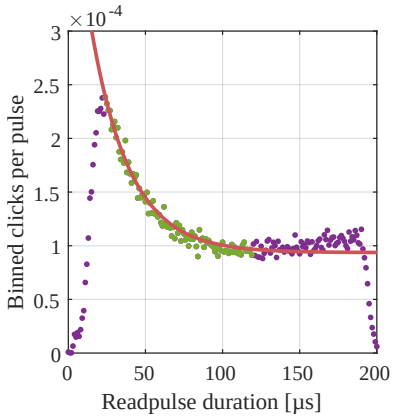

Figure 10.2: Readoutrate. We determine the coherent readout rate γ_R using the read data ranging from 55 µs to 120 µs, marked in green. The resulting exponential fit is shown in red, while purple shows the data of the complete read pulse.

10.1.1 Filter cavity scan

We use narrow filter cavities to filter out any residual excitation light leaving the cell cavity that remains in the same spatial mode after the polarization filtering. In order to quantify the spectral contributions to our scattered light fields, for example, noise arising from the broadband noise (see section 4.5) or residual drive light, we need to shift our filters with respect to the desired scattered photon frequency. Detuning the filters enables us to record a spectrum of the signal and noise constituting our detected photon counts of the SNSPDs during the write and read pulses. For this, let us motivate which contributions we expect to comprise our spectra during write and read pulses. For both cases, we expect a narrow and broadband contribution centered around the Larmor frequency ($\pm\nu_L$), constituting contributions from symmetric and asymmetric collective excitations. Further, residual drive light, detuned $\mp\nu_L$ from the scattered photon frequency for write (-) and read (+), is expected to contribute to our spectrum. We will refer to this residual drive light also as leakage. Last, we expect a spectrally flat background noise floor originating from detector dark counts or stray photons. Based on this, we set up a fitting model for the write scattered photon spectrum given as (Dideriksen et al., 2021):

$$\begin{aligned} S_W(\Delta_{FC}) =& a_{NB}\mathcal{L}_1(\Delta_{FC},0)\mathcal{L}_2(\Delta_{FC},0) + a_{BB}\mathcal{L}_{BB}(\Delta_{FC},0) \\ &+ a_{LKG}\mathcal{L}_1(\Delta_{FC},-\nu_{\mathcal{L}})\mathcal{L}_2(\Delta_{FC},-\nu_{\mathcal{L}}) + a_{BG} \end{aligned} \tag{10.1}$$

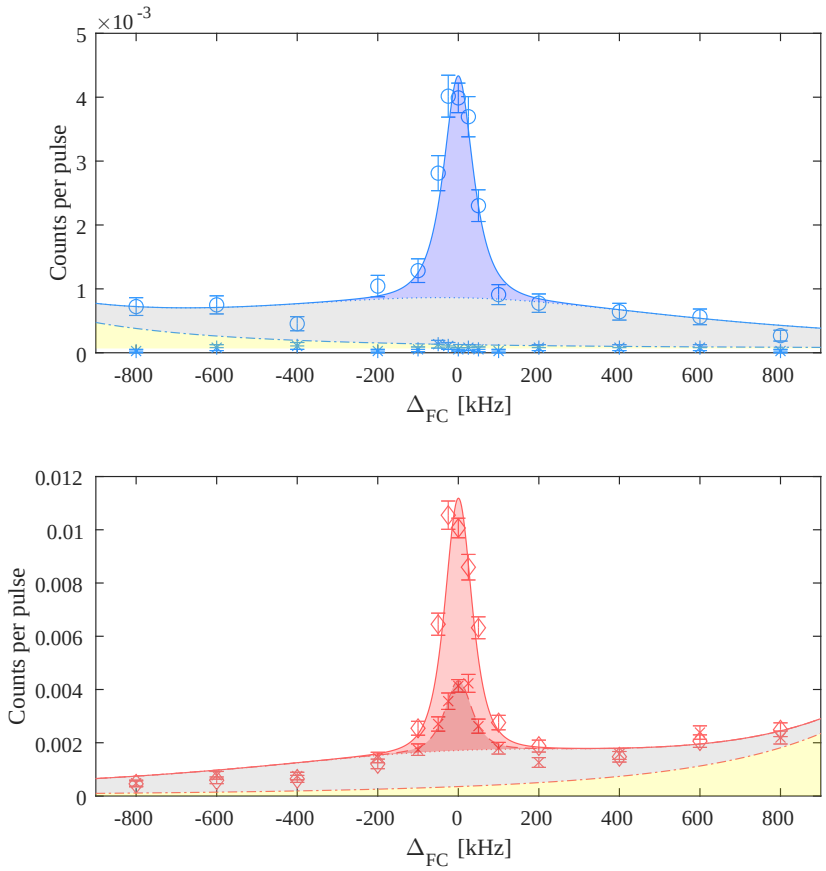

Figure 10.3: Spectrum of scattered write and read photons. Detected unconditional counts per pulse during write and read pulse. The read spectrum corresponds to $\tau_R = 40\,\mu s$, and minimal read delay $\tau_D = 10\,\mu s$. The choice of τ_R will be addressed in section 14.4.1. Each point corresponds to a different filter cavity detunings Δ_{FC}. For the read spectrum, circles illustrate measurements with a preceding write pulse, while crosses correspond to not sending a write pulse. The fits (lines) are shown with colored areas for narrowband (blue and red for write and read, respectively), broadband (gray), and leakage (yellow) contributions. Figure (replotted) and caption from Dideriksen et al. (2021).

where we have introduced the two cascaded filter cavities for the write detection setup (section 9.4.1) as a product of the transmission through the two Lorentzian filters $\mathcal{L}_1(\Delta_{FC}, 0)\mathcal{L}_2(\Delta_{FC}, 0)$ with FWHM linewidths of 98 kHz and 240 kHz. Scattered and drive light photons are both subjected to these filters. The drive light spectral component is detuned by $-\nu_L$. For the broadband response (BB), we have introduced a contribution with $\mathcal{L}_{BB}(\Delta_{FC}, 0)$ with a fixed width as motivated in section 4.5, as well as a spectrally flat contribution for the background counts. The fitting parameters for our write spectrum are the four factors a_i describing the four spectral contributions. The widths of the Lorentzian lines are not used as fitting parameters since we determine these by other means and observe good agreement of the model with the data. Us-

ing the line widths as parameters did not improve our model's reliability.

In the case of the readout, we expect a similarly structured spectrum but with two differences. First, the drive light is centered around $+\nu_L$. Second, we must account for an additional narrowband contribution recorded during the readout even without a preceding write pulse, as observed in Zugenmaier et al. (2018). For our read spectrum, we need to distinguish write and no-write cases indicated using the index $i = [\mathrm{W}, \mathrm{NW}]$ (Dideriksen et al. (2021)):

$$\begin{aligned} S^i_{\mathrm{W}}(\Delta_{\mathrm{FC}}) =& b^i_{\mathrm{NB}}\mathcal{L}_1(\Delta_{\mathrm{FC}}, 0)\mathcal{L}_2(\Delta_{\mathrm{FC}}, 0) + b_{\mathrm{BB}}\mathcal{L}_{\mathrm{BB}}(\Delta_{\mathrm{FC}}, 0) \\ &+ b_{\mathrm{LKG}}\mathcal{L}_1(\Delta_{\mathrm{FC}}, \nu_{\mathcal{L}})\mathcal{L}_2(\Delta_{\mathrm{FC}}, \nu_{\mathcal{L}}) + b_{\mathrm{BG}} \end{aligned} \tag{10.2}$$

with $i = [\mathrm{W,NW}]$ for the write and no write case. We note that we fit both cases as a combined fit where only the narrowband contributions for write and no write case are independent. This is expected since asymmetric collective excitations are created during the write pulse decay much faster than the symmetric mode. Therefore, uncorrelated broadband noise from the heralding process should not affect our readout. The broadband noise during the readout should only originate from the read process. This fits with our observation that the recorded count rates outside the narrowband feature coincide for the read with and without a preceding write pulse.

In figure 10.3, the resulting spectra were obtained with the two fit models described by equations (10.1) and (10.2). We note that the read spectrum corresponds to $\tau_{\mathrm{R}} = 40\,\mu\mathrm{s}$, we motivate this choice later in section 10.1.4 based on the trade-off between retrieval of excitations and signal-to-noise during the readout. Using this method of scanning the filter cavity resonances with respect to the scattered photon frequencies, we can estimate the different noise contributions at the desired scattered photon frequency from the obtained spectrum. Without the scan of the filter cavities and the obtained scattered photon spectra, we would be unable to estimate the write efficiency η_{W} or the coherent readout compared to the overall detected read clicks, for example. The drive light leakage on resonance with the respective scattered light field frequency is a vanishing component for write and read. Also, the background contribution is, in both cases, only minor. Coherent write and read – the good narrowband contribution in both spectra – is the largest contribution to the spectrum on resonance.

As discussed in section 4.6, the fitting model for the non-classical correlation relies on the auto-correlation $g^{(2)}_{\mathrm{BB}}$ of the read light field in the case without a preceding write pulse. The required data we acquire as part of the filter cavity scan allows us to determine $g^{(2)}_{\mathrm{BB}} = 1.33$ for our readout. Also, the same data allows us to find an estimate for the readout noise λ_{B}, which is given by the read detection level for the no-write case. It amounts to $\lambda_{\mathrm{B}} = 4.3 \cdot 10^{-3}$ which corresponds to the resonance point for the dark-red shaded area in figure 10.3.

10.1.2 Write

For our experimental runs, one parameter we change and try to find the optimum is the applied optical write drive power. It is directly related to the probability of writing an excitation into the ensemble. For the write pulse, we have multiple constraints. On the one hand, we do not want to use an excitation probability rendering our assumption that double excitations are negligible invalid. On the other hand, for a too-low excitation probability, we expect to reach a limit where background noise will become too predominant. A low excitation probability will likewise slow down the time between successful write-read events due to the higher number of trials required.

First, we will investigate the dependency of the observed write noise versus the observed mean write counts when varying the applied write drive light power. The mean number of noise counts during the write can be determined from a spectral scan of the filter cavities (see section 10.1.1). We estimate the mean number of coherent write counts by subtracting the narrow contribution in the spectrum from the overall write counts on resonance, as motivated in section 4.2.1. In figure 10.4, the respective mean noise counts are plotted versus the average number of write clicks. We observe a clear linear relationship. We fit a linear model $a \cdot \langle n_W \rangle + a_{BG}$, where the minor offset a_{BG} is only included phenomenological. It should be noted that physically speaking, we would expect $\langle n_W \rangle \geq \langle n_{W,noise} \rangle$ since $\langle n_W \rangle$ includes the noise already. The minor positive offset instead of the negative is an artifact of the finite error bars and statistics. Since it is such a minor contribution, we decided not to remove it from the model.

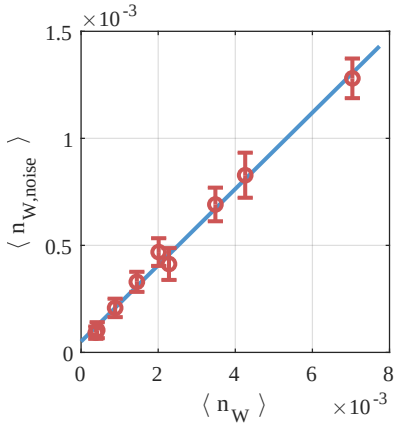

Figure 10.4: Mean write noise clicks versus mean write clicks. Observed write detection events versus the number of the total observed write detection events corresponding to changing the write drive power and hence excitation probability. Error bars reflect the Poissonian standard deviation. Figure replotted from Dideriksen et al. (2021).

From the slope a, we can determine the write efficiency as $\eta_W = 1 - a$, which tells us about the ratio of good to bad write detection events. We determine $\eta_W = 82 \pm 1\,\%$. As discussed previously, the write efficiency depends on the filling factor of the vapor cell with the beam intensity profile. Increasing η_W further would require a better filling factor of the cell cross-section with the beam profile of the drive light. Without altering the beam or cell, a narrower filter would aid the motional averaging for better write efficiency.

For the correlation model, we wish to express the write noise counts as $\lambda_A(\mu)$ where μ is the excitation probability. This requires us to find an expression relating the experimentally observed write counts to the excitation probability. Following (Dideriksen (2021)), we express the mean number of write counts in terms of the excitation probability as $\langle n_W \rangle(\mu) = \eta_X \mu / \eta_W + a_{BG}$, with $\eta_W = 0.82$ and $a_{BG} = 51 \cdot 10^{-6}$ from the fit in figure 10.4. This allows us to determine the model parameter λ_A as $\lambda_A(\mu) = \frac{1-\eta_W}{\eta_W}\eta_X \mu + a_{BG}$. Using this relation reduces the number of free parameters in the correlation model (section 4.6) by rewriting λ_A in terms of η_X. The remaining parameters going into λ_A can be determined using other experimental measurements.

10.1.3 Read

Similar to the write noise scaling with the applied write drive light power, we also wish to investigate the scaling of the mean count rate during the read pulse $\langle n_R \rangle$ for various mean write counts $\langle n_W \rangle$.

As part of the correlation model, we wish to determine the mean number of read counts $\langle n_R \rangle$ versus the mean write excitation probability μ. However, experimentally we have only $\langle n_W \rangle$ readily available. We use the relation introduced in the previous section to relate the model input μ to $\langle n_W \rangle$. In figure 10.5, we show our experimental obtained read counts versus the mean number of write counts. In addition, we show the linear fit obtained as part of the correlation model fit[1]. In general, we find a nice linear dependency of the observed mean number of read counts $\langle n_R \rangle$ from an increasing number of mean write counts $\langle n_W \rangle$. The finite offset of $\langle n_R \rangle$ for $\langle n_W \rangle = 0$ originates from the mean number of read noise counts in the absence of a write pulse. We can determine this noise level in the readout from a measurement without a write pulse preceding the read pulse. In the expressions for the correlation model, this read noise level is referred to as λ_B. We determine it to be $\lambda_B = 4.3 \cdot 10^{-3}$.

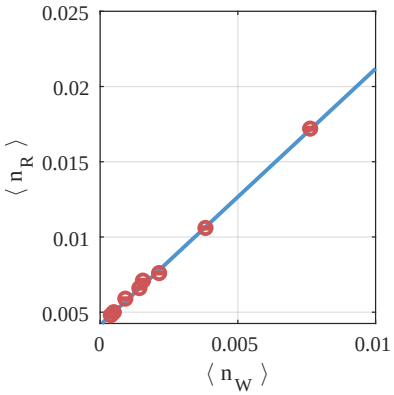

Figure 10.5: Mean read clicks versus mean write clicks. Observed mean number of read detection events $\langle n_R \rangle$ versus the mean number of write detection events $\langle n_W \rangle$ corresponding to different excitation probabilities during the write pulse. Figure replotted from Dideriksen et al. (2021).

10.1.4 Comparison conditional-unconditional readout

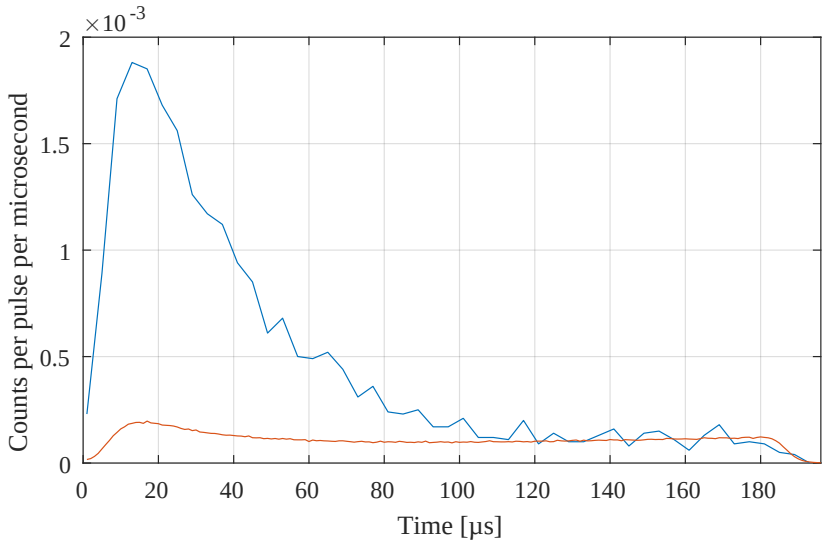

Figure 10.6: Comparison conditional - unconditional read counts. Shown are the average number of unconditional read counts per time bin (microsecond) per pulse (red). For comparison, the conditional readout considering only read counts with a single write click during read (blue), the mean number is significantly higher. Due to the lower statistics, the conditional read time bins are averaged over 4 µs and normalized accordingly.

After considering write and read detection events independently, we want to investigate conditional and unconditional readout. Sending a write and

[1] We reiterate here that for the correlation model, we do not fit individual properties, but perform a combined fit of the retrieval efficiency η_R, the mean number of read detection events $\langle n_R \rangle$ and the cross-correlation function $g^{(2)}_{WR}$.

read pulse after each other does not ensure we record a read photon during every read pulse. To quantify how many detection events during write and read pulses are correlated, we need to combine the information obtained in consecutive write and read pulses. Considering all readout, without regard to whether a write scattered photon was detected or not, is termed unconditional readout. However, the more interesting case is when we condition the readout on successfully detecting a single heralding click during the preceding write pulse. If our write-read scheme is successful, we expect a higher readout rate in the conditional case. At the same time, due to losses and the low excitation probability, we only expect a smaller subset of the total measurement recordings to fulfill this criterion. Hence, the statistics should be more limited for the conditional readout.

Figure 10.6 shows the read pulse count rates for different time bins. In the conditional case, we observe a significantly higher count rate at the beginning of the read pulse, verifying that it is more likely to record a scattered photon during the readout if we detect a heralding photon during write. Towards the end of the read pulse, the level of the unconditional readout and the conditional readout reaches the same plateau, indicating that the tail of the read pulse contains only noise.

From the shape of the conditional readout compared to the unconditional one, we see that there will be a trade-off in the analysis when considering the cumulative readout. For this purpose, we will consider the retrieval efficiency along with the data in figure 10.6. We consider the cumulative retrieval efficiency as follows:

$$\eta_R(\tau_R) = \langle n_{R\,|\,W=1} \rangle (\tau_R) - \langle n_{\text{noise}} \rangle (\tau_R) \tag{10.3}$$

We note that we refer to read noise counts here instead of write noise counts. The retrieval efficiency estimates how well we retrieve an excitation in the conditional readout. In figure 10.7, the retrieval efficiency is determined versus the cummulative readout duration. We see that the cumulative retrieval efficiency η_R approaches $\eta_R = 7.5 \pm 0.4\,\%$.

In our experiment, we chose a fixed duration of $\tau_R = 40\,\mu s$ as our preferred choice of the read pulse duration to use in the analysis. It offers a good retrieval efficiency $\eta_R\,(\tau_R = 40\,\mu s) = 5.3 \pm 0.3\,\%$ of the total attainable retrieval efficiency while maintaining a good signal-to-noise ratio. In the following we will automatically assume that $\tau_R = 40\,\mu s$, unless we specify otherwise. We will discuss the retrieval efficiency further in subsection 10.1.7, where we will investigate it in the framework of our correlation model, as well as how to account for losses and determine the intrinsic efficiency of our scheme.

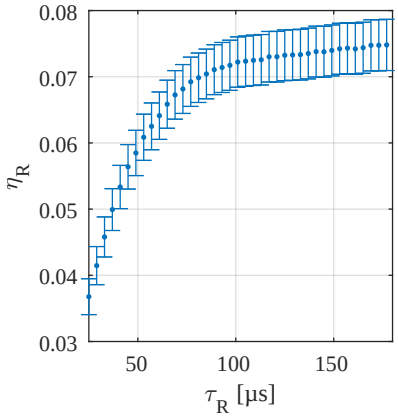

Figure 10.7: Retrieval efficiency. Determined retrieval efficiency versus the duration of the read pulse. It should be noted that points are integrated over the read pulse duration. Errors are estimated using Poissonian errors.

10.1.5 Cross-correlation between write and read

In the case of writing an excitation into an atomic ensemble during the write process and retrieving it successfully again during the retrieval process, we expect the two scattered photon fields to be non-classically correlated.

Consequently, we investigate the cross-correlation between the two scattered light fields. From figure 10.6, we already observed a significantly increased readout rate when considering read pulses with a successful heralding photon detection only. To quantify this further, we will consider the second-order

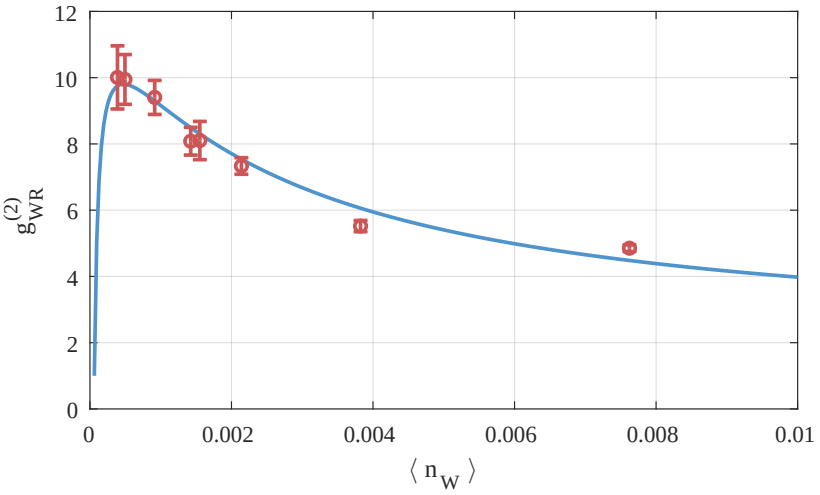

Figure 10.8: Cross-correlation versus mean write clicks. Observed cross-correlations between write and read versus the observed mean write clicks $\langle n_W \rangle$ corresponding to varying the excitation probability. Error bars are estimated from Poissonian statistics. Figure replotted from Dideriksen et al. (2021).

cross-correlation function between the recorded detection events during write and read. To do so, we consider the cross-correlation between mean write and mean read detection events as follows:

$$g^{(2)}_{WR} = \frac{\langle n_W n_R \rangle}{\langle n_W \rangle \langle n_R \rangle} \tag{10.4}$$

While not explicitly stated, we note that the expression has some dependency on the choice of excitation probability μ and the length of τ_R considered for the readout. In figure 10.8, the obtained cross-correlation versus the observed number of mean write clicks $\langle n_W \rangle$ is shown. The error bars are estimated from Poissonian statistics. We observe an explicit dependency of the cross-correlation between the applied excitation probability reflected in the observed mean write counts $\langle n_W \rangle$. The higher our excitation probability, the lower our cross-correlation. We can understand these dependencies based on our considerations in section 4.6. The more excitations we write into the ensemble on average, the more likely it becomes that two or even more collective excitations are written into the ensemble. Even in the case of number-resolving detection, this will compromise the attainable level of cross-correlation according to equation (4.27). Towards lower excitation probabilities, we can observe cross-correlations of up to $g^{(2)}_{WR} = (10 \pm 1)$ for $\langle n_W \rangle = 0.5 \cdot 10^{-3}$. From equation (4.27), we expect the cross-correlation to keep increasing for smaller and smaller mean excitation probabilities p_0. This is true even in the case of losses

and hence imperfect detection efficiency, as we are faced with in our experiment. The lower the excitation probability, the more trials and longer we need to measure for sufficient statistics to estimate our cross-correlation since the rate at which we will detect write and read scattered photons decreases. What puts a limit in the possible cross-correlation are noise counts, even if we would detect scattered photons with perfect detection efficiency. For sufficiently low write probability, uncorrelated noise counts will reach equal footing with the desired scattered photons. This illustrates why we have put much effort into reducing the number of dark counts due to external stray photons and intrinsic dark counts of our detectors to avoid degrading our cross-correlation. Due to the finite residual noise counts, we expect the cross-correlation to degrade for minuscule excitation probabilities p_0. For the experimental run presented here, we have not observed a reduction in cross-correlation for small write powers (yet). However, the model line in blue in figure 10.8 illustrates this expectation.

We observed non-classical correlations between the write and read scattered light fields for all excitation probabilities, exceeding the classical boundary $g^{(2)}_{\mathrm{WR}}(n_{\mathrm{W}}) > 2$. We consider this a significant improvement compared to the previous publication on this experiment performed on the D_2 line in our group (Zugenmaier et al. (2018)). We observed even higher cross-correlations reaching values of 12 and above when truncating the integrated read pulse duration earlier than for our choice of $\tau_{\mathrm{R}} = 40\,\mu\mathrm{s}$. However, this comes at the expense of reduced retrieval efficiency. Therefore, we decided to improve the retrieval efficiency at the expense of a slight loss in the observed cross-correlations.

Part of our model developed for fitting our data is the cross-correlation function. The cross-correlation versus mean write excitation is fitted in a combined fit with the mean read counts and the retrieval efficiency. In figure 10.8, the obtained fitted model result for the cross-correlation is shown along with the values obtained from our measurements. We observe good agreement between the measurements and the fitted model, which we will discuss further in section 10.1.7.

10.1.6 Conditional auto-correlation

The single-photon character of the retrieved scattered light field conditioned on the successful detection of a single heralding photon during write is quantified by the conditional auto-correlation $g^{(2)}_{\mathrm{RR}\,|\,\mathrm{W}=1}$. In the following, we will investigate how truncating the duration of the read pulse affects our conditional auto-correlation. This means that the different values shown versus the read pulse duration are not statistically independent since we consider the cumulative read pulse instead of the independent time bins of the read pulse. For the analysis, we combine multiple data sets into one to improve the statistics of our result - we will address this further in section 10.1.7.

To determine the conditional auto-correlation, we use the following ex-

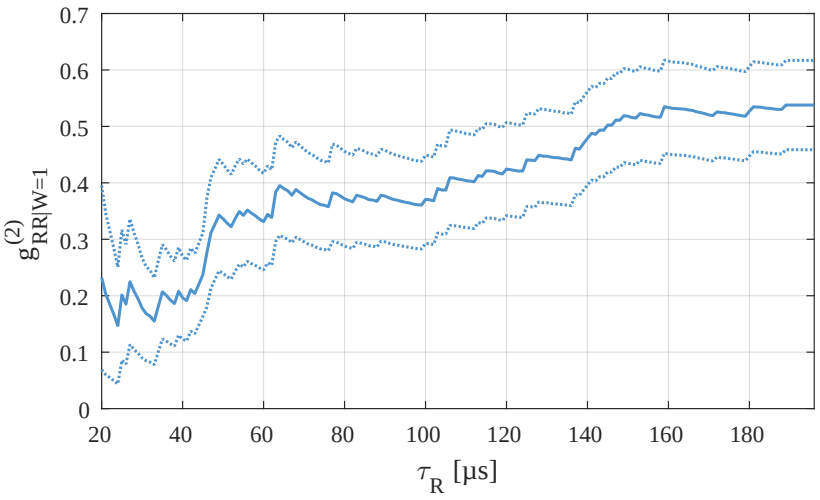

Figure 10.9: Conditional auto-correlation versus readout duration. Observed conditional auto-correlation when varying the length of the integrated readout duration τ_R. Dotted lines represent uncertainties estimated from Poissonian errors.

pression:

$$g^{(2)}_{RR\,|\,W=1}(\tau_R) = \frac{\langle n_{R\,|\,W=1}(\tau_R)(n_{R\,|\,W=1}(\tau_R)-1)\rangle}{\langle n_{R\,|\,W=1}(\tau_R)\rangle^2} \tag{10.5}$$

where we consider read pulses with precisely a single detected heralding photon during the preceding write pulse. Equation (10.5) can be understood as how likely it is to detect two or more photons after registering only a single heralding write click.

In figure 10.9, we plot the obtained values of the conditional auto-correlation versus the integration time of the readout τ_R. As expected, we observe a degradation of the conditional auto-correlation. The degradation can easily be understood. The longer we read out, the more noise will be included. At the same time, we know from the shape of the conditional readout (figure 10.6) that most of the "good" readout is fast and occurs during the first 100 μs. Considering more and more of the read pulse includes toward long read duration only additional noise, thus degrading the conditional auto-correlation as in relative terms, more bad counts are considered in the estimate of the conditional auto-correlation. Up to roughly 120 μs, the observed conditional auto-correlation remains at least one standard deviation below the expected auto-correlation of a two-photon Fock state. The "steps" in our conditional auto-correlation may seem a concern. To explain this, we have to consider what the conditional auto-correlation function experimentally reflects. It tells us the likelihood of detecting three photons - one during the write pulse and two during the read pulse. These triple-detection events are unlikely for an excellent on-demand single-photon source that generates single-photons with a high probability. Therefore, these only occur very rarely. However, each time we observe such a triple-detection event, it significantly alters the observed

conditional auto-correlation. We expect the shape in figure 10.9 to smooth if we measure for longer and obtain more statistics.

We will provide precise numbers for the observed double- and triple-detection events when discussing the results of the correlation model. We use our observed conditional auto-correlation to quantify the model fit by predicting the expected conditional auto-correlation for various excitation probabilities. To that end, we will also discuss the non-classical bounds of the conditional auto-correlation for the scattered read light field.

10.1.7 Discussion of correlation model

As part of section 4.6, we have introduced the expressions used to model the correlations derived in Dideriksen (2021). In the following, we will discuss the approach and the fit results of the correlation model. We will then proceed to compare our experimentally observed conditional auto-correlation $g^{(2)}_{\mathrm{RR}\,|\,\mathrm{W}=1}(\mu)$ versus the mean number of write counts $\langle n_{\mathrm{W}} \rangle$ with the prediction based on fitting our model to the experimental data.

The three experimental results are fitted using a combined fit for the three expressions for $g^{(2)}_{\mathrm{WR}}(\mu)$, $\eta_{\mathrm{R}}(\mu)$ and $\langle n_{\mathrm{R}} \rangle(\mu)$. Here, it is noteworthy that while we found the expressions for the excitation probability μ, experimentally, we only obtain the mean number of write counts $\langle n_{\mathrm{W}} \rangle$. We can relate the two using appropriate scaling, as introduced in section 10.1.2.

As part of optimizing the duration of the readout τ_{R}, we have introduced the retrieval efficiency in section 10.1.4. Now we will consider the retrieval efficiency versus the mean number of write clicks $\langle n_{\mathrm{W}} \rangle$. The result is shown in figure 10.10. The retrieval efficiency is the third experimental property used in the correlation model's combined fit. As discussed in section 4.6 and throughout this chapter, the model takes five different parameters into account. However, due to the different experimental runs we perform, it is possible to reduce the number of free parameters to the total write and read detection efficiencies η_{X} and η_{Y}.

For the fitting routine, the two free fitting parameters are optimized in a combined fit of $\langle n_{\mathrm{R}} \rangle(\mu)$, $g^{(2)}_{\mathrm{WR}}(\mu)$, and $\eta_{\mathrm{R}}(\mu)$. The data points for these three properties are shown in the figures 10.5, 10.8 and 10.10. The data points are weighted according to the inverse of their uncertainty. The resulting model lines obtained by fitting the data are shown along with the respective experimental data points in the respective figures.

From the fits, we obtain the total write and read detection efficiencies as $\eta_{\mathrm{X}} = (2.9 \pm 0.1)\,\%$ and $\eta_{\mathrm{Y}} = (6.0 \pm 0.2)\,\%$ where the uncertainty correspond to fit confidence intervals of one standard deviation. To put the model to the test, we use the obtained parameters from the fit with the other fixed parameters determined by independent measurements to predict the conditional auto-correlation $g^{(2)}_{\mathrm{RR}\,|\,\mathrm{W}=1}$ using equation (4.34). The model prediction is shown in figure 10.11, plotted together with our experimentally observed values. We observe good agreement between the measurement and the model prediction.

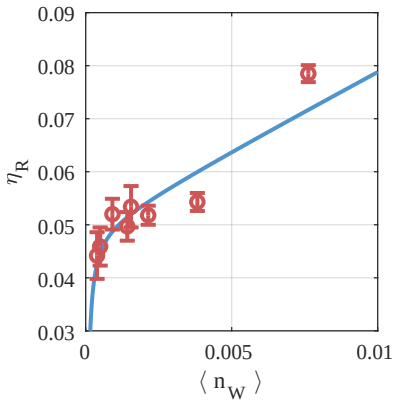

Figure 10.10: Retrieval efficiency versus mean write clicks. Measured retrieval efficiency η_{R} versus mean number of write clicks. Error bars reflect one standard deviation. The fitted correlation model is shown in blue. Data replotted from Dideriksen et al. (2021).

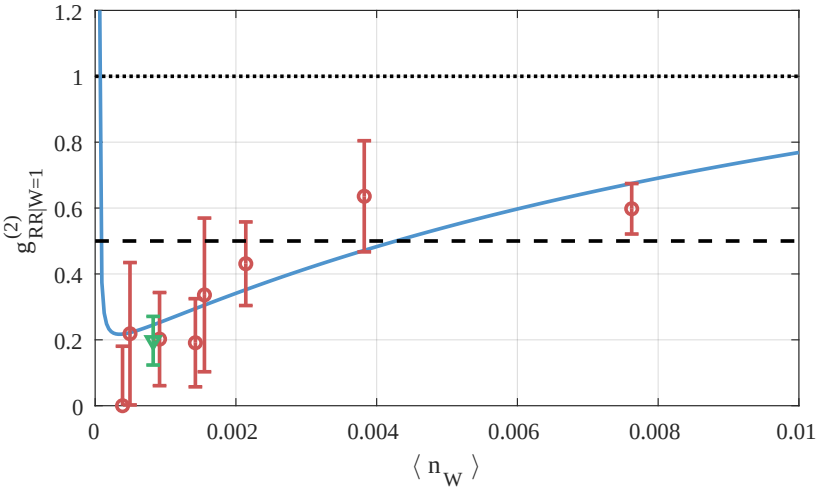

Figure 10.11: Conditional auto-correlation versus write probability. The experimentally observed conditional auto-correlation versus the mean number of write counts $\langle n_W \rangle$. The error bars are obtained using Poissonian errors, except for the point with zero conditional auto-correlation. There the error bar reflects the uncertainty if a single double-read detection event would have been observed. The green point is the conditional auto-correlation for analyzing the combined dataset of the lowest five mean write count values. The dashed line indicates the two-photon Fock state. The dashed-dotted line corresponds to the coherent state auto-correlation function. The blue line is the prediction of the conditional auto-correlation function using the correlation model. Figure replotted from Dideriksen et al. (2021).

Since the conditional auto-correlation function is one of the key factors for quantifying our single-photon source, we want to discuss the results in figure 10.11 illustrating the observed conditional read auto-correlation versus the observed mean write detection events. As expected, we observe that the conditional auto-correlation function increases and hence deviates more from our desired single-photon auto-correlation function for an increasing excitation probability. It degrades for higher excitation probabilities since double excitations of the ensemble become more probable. We can distinguish two limits for values of the conditional auto-correlation function. The classical limit of the conditional auto-correlation function is that of a coherent state, given as $g^{(2)}_{\text{coh}} = 1$. This value marks the limit between classical and non-classical correlations. All our experimental data points remain well below the classical bound of $g^{(2)}_{\text{coh}} = 1$. The more precise characterization for generating a non-classical read light field but truly a single-photon state is the comparison to the auto-correlation of a two-photon Fock state. For a two-photon Fock state, the auto-correlation function takes a value of $g^{(2)}_{\text{two-photon-FS}} = 0.5$. We can claim a single-photon character of our retrieval light field as long as we observe a conditional auto-correlation statistically significant below the conditional auto-correlation value of a two-photon Fock state. As indicated in figure 10.11, our error bars are rather large. The high uncertainties are connected to

the meager rate at which we observe one heralding and two retrieval detection events. For this reason, we combine the lowest five points into one big data set and perform the analysis on this extensive data set. We do this based on the experimental conditional auto-correlation values' low mean write count dependency, which the correlation model also predicts. Doing so improves the statistics significantly, and we obtain a common value for the conditional auto-correlation, shown in green in figure 10.11, with:

$$g^{(2)}_{\mathrm{RR}\,|\,\mathrm{W}=1} = 0.20 \pm 0.07 \tag{10.6}$$

This value is more than four standard deviations below the two-photon Fock state auto-correlation, assuring our retrieved single-photons' single-photon character. To motivate why we did not simply measure longer for each of the points but chose to combine them, we note that the green point corresponds to a cumulative measurement time of roughly 32 hours. During these 32 hours, we ran our experimental measurement sequence 31 million times, out of which we only recorded[2] 1321 times successfully a single write and a single read detection event in consecutive write-read pulses. A total of seven triple-coincidences have been recorded, meaning that we counted a single write detection event followed by detecting two photons during the read pulse, verifying that we have a high success rate for generating a single, on-demand photon. At the same time, the rarity of triple-detection evens requires a considerable number of measurements for sufficient statistics. The low detection efficiencies of our scattered light fields complicate and prolong this process further. Improving the detection efficiencies would allow us to reduce the write probability further or speed up our measurements when comparing equal excitation probabilities. Possible improvements will be discussed in the following chapter 11.

Using the fit result from the correlation model, we can predict the conditional auto-correlation of the read scattered light field and determine the intrinsic retrieval efficiency. For this, we use the fit model result for η_{Y} reflecting the overall read detection efficiency. We correct η_{Y} for the escape efficiency of the scattered light out of the cell cavity ($\eta_{\mathrm{esc}} = 45 \pm 2\,\%$) and the detection efficiency of the read detection setup ($\eta^{\mathrm{R}}_{\mathrm{det}} = 19 \pm 2\,\%$). We estimate the read detection efficiency independently with a light pulse of known optical power and attenuate it with calibrated neutral-density filters. Relating the count rate of the SNSPD with the number of photons in the attenuated beam gives us an independent measure of the detection efficiency. Combining these allows us to estimate the intrinsic retrieval efficiency - the retrieval efficiency corrected for losses - as:

$$\eta^{*}_{\mathrm{R}} = \frac{\eta_{\mathrm{Y}}}{\eta^{\mathrm{R}}_{\mathrm{det}}\eta_{\mathrm{esc}}} = 70 \pm 8\,\% \tag{10.7}$$

The high intrinsic retrieval efficiency confirms that we read out a lot of the heralded collective excitations despite truncating the read pulse. We achieve close to full retrieval if we consider the full read pulse duration. Due to the

[2] These numbers are only valid for $\tau_{\mathrm{R}} = 40\,\mu\mathrm{s}$.

cell cavity's low outcoupling efficiency and limited detection efficiency, our experimental retrieval efficiency is significantly lower than the intrinsic retrieval efficiency. Improving the outcoupling and detection efficiency would allow us to be closer to the intrinsic retrieval efficiency.

10.2 Delaying readout of single-photon

So far, we have only considered the immediate retrieval of a stored collective excitation. In order to allow for potential application in a quantum repeater scheme, our system should allow for a delayed on-demand retrieval of a stored excitation. This section will focus on combining the two properties of our system, allowing single-photon generation on-demand while exploiting the quantum memory capabilities of our system. For this, we investigate how different properties of our source change when sending the read pulse with a variable delay after the write pulse.

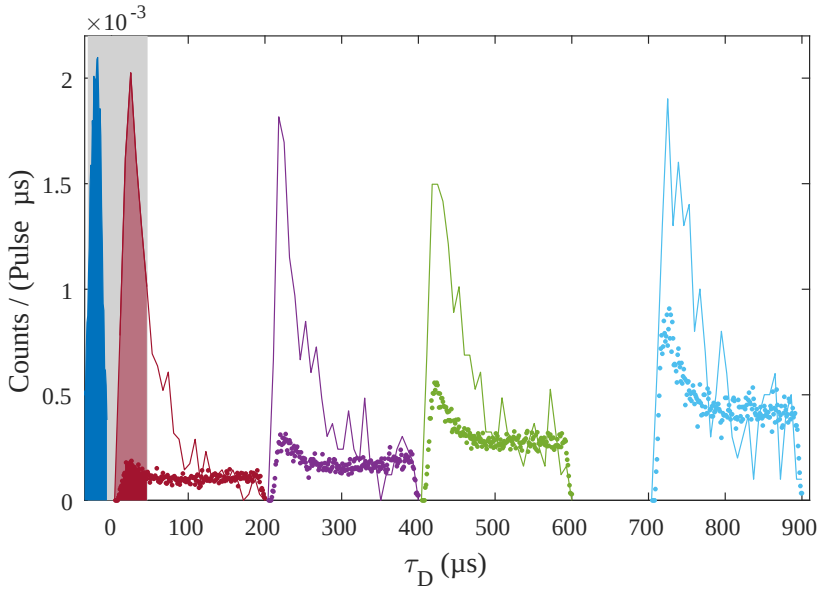

Figure 10.12: Write and Read pulse shapes. Temporal shape of detection events: Blue area - detected counts during heralding write pulses (31 µs, scaled 1/25). Solid curves - detected counts during read pulses (200 µs, delayed 10 to 710 µs) conditioned on the heralding write count (averaged over 7 µs bins). Dotted curves - the read noise level in the absence of write pulse (1 µs binning). Figure (replotted) and caption from Dideriksen et al. (2021).

Experimentally, we delay the readout for different delay times τ_D, ranging from 10 (minimal possible delay, choice of previous section) to 1010 µs. A subset of the delayed readout pulse shapes is shown in figure 10.12. The shaded areas in figure 10.12 indicate the integration time we typically found to be most beneficial for our analysis, i.e., for $\tau_R = 40$ µs. It should be noted

that the write pulse is scaled by a factor of 1/25 for better visibility of the read pulses in figure 10.12.

For the read pulses, we show two traces each. The lines correspond to the read conditioned on a single write detection event during the preceding write pulse. Due to the limited statistics, the data is averaged over 7 µs time bins. The dotted read pulse shapes correspond to the read noise for sequences without an optical write pulse. This differs from figure 10.6, where we compared conditional and unconditional readout, where both were with optical write pulse. Figure 10.12 illustrates nicely that the overall conditional retrieval during the read pulse is highest at the beginning of the pulse. The conditional readout degrades while we retrieve the stored excitation, as already seen in figure 10.6. However, the relative contribution of the conditional readout compared to the read noise is degrading towards higher delays. Secondly, the end of our read pulse is flat, and the noise level approaches the no-write noise level. Interestingly, the ratio between the narrow peak and base noise level for the read noise traces remains constant since both contributions grow equally towards higher delays.

The growth in the read noise and the degradation of the signal-to-noise when comparing read noise and conditional readout gives us a good idea that delaying the retrieval degrades our source performance when exploiting the memory capabilities. In the following sections, we will investigate the influence of delayed retrieval on the correlation functions and retrieval efficiency and how different noise contributions grow.

10.2.1 Decoherence of non-classicality

Intrinsic to our experimental design is that we generate a single-photon on demand using a two-step scheme. While the write generates a heralding photon, indicating that our source is loaded, the collective excitation is maintained in the atomic ensemble. The finite lifetime of collective excitations makes our source a quantum memory as we can delay the retrieval of the desired single-photon, allowing for on-demand readout. As discussed in 1.3, a quantum memory can be quantified by determining how long a non-classical state can be stored before the information has degraded.

In figure 10.13, we investigate the degradation of the Cauchy-Schwarz parameter $\mathcal{R}$ and the cross-correlation $g^{(2)}_{\mathrm{WR}}$ versus the delay time τ_{D}. To evaluate the decay rate of both, we fit the respective measurement values with a fit function. For the second-order cross-correlation function, we fit an exponential decay with an offset of one as follows:

$$g^{(2)}_{\mathrm{WR}}(\tau_{\mathrm{D}}) = B \cdot e^{-\tau_{\mathrm{D}}/\tau_{\mathrm{M}}} + 1 \tag{10.8}$$

Here, we have introduced the decay of the non-classical correlations as the inverse of the memory time $1/\tau_{\mathrm{M}}$. It should be noted that the parameter B in equation (10.8) is related to the cross-correlation for zero delay as $B = g^{(2)}_{\mathrm{WR}}(0) - 1$. In figure 10.13, the solid black line bordering the green area

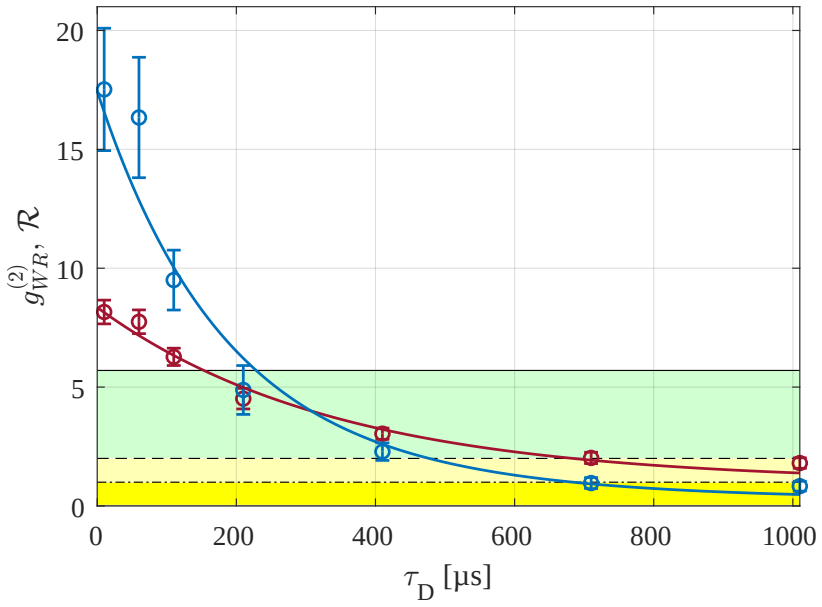

Figure 10.13: Decay of write-read cross-correlations. Decay of the cross-correlation function $g^{(2)}_{\mathrm{WR}}$ (red) and Cauchy-Schwarz parameter $\mathcal{R}$ (blue) versus the delay τ_{D} between write and read pulse. Figure replotted from Dideriksen et al. (2021).

marks the value 5.7 of the cross-correlation. This value marks the required cross-correlation between write and read scattered light fields to violate the Bell-inequality as motivated by Wallucks et al. (2020). For our experimental system, this bound for the non-classical correlations between write and read scattered light fields is violated for a duration of $\tau_{\mathrm{BI}} = (0.15 \pm 0.03)$ ms.

To find the expression for the Cauchy-Schwarz parameter $\mathcal{R}$, we scale the fit result of the cross-correlation according to equation (4.26). From section 4.6, we know that the non-classicality witness is defined as violating $\mathcal{R} \leq 1$. As long as our write and read scattered light fields exhibit cross-correlations violating this inequality, we have non-classicality. We define our quantum memory capabilities as the time until the observed cross-correlations no longer violate the non-classicality bound and denote it with τ_{NC}. This level is shown as the dash-dotted line in figure 10.13. For a total duration of $\tau_{\mathrm{NC}} = (0.68 \pm 0.08)$ ms our scattered light fields are non-classically correlated. Considering our optimal choice of readout pulse duration, together with the memory time τ_{NC}, we can estimate the simplified time-bandwidth product[3]. Considering our experimental values, the time-bandwidth is given by $\mathcal{B} = 17 \pm 2$.

10.2.2 Decay of retrieval efficiency

Following the discussion on the decay of the non-classicality of the retrieved single-photons during the readout, it is instructive to consider the re-

[3] Please note that we do not consider the time for re-initialization of the source and the like.

trieval efficiency. Considering the retrieval efficiency η_R in addition to the decay of the non-classical correlations is advantageous due to its definition. The retrieval efficiency is defined as the mean number of conditional read counts $\langle n_{R\,|\,W=1}\rangle$ corrected for the mean number of noise counts $\langle n_{noise}\rangle$ as introduced in equation (10.3). The latter is determined from a no-write sequence using the same respective delay τ_D. The retrieval efficiency is hence intrinsically corrected for noise counts. It means that we can understand the decay time of the retrieval efficiency as the expected decoherence time of non-classical correlations in the absence of detrimental noise processes speeding up their decay.

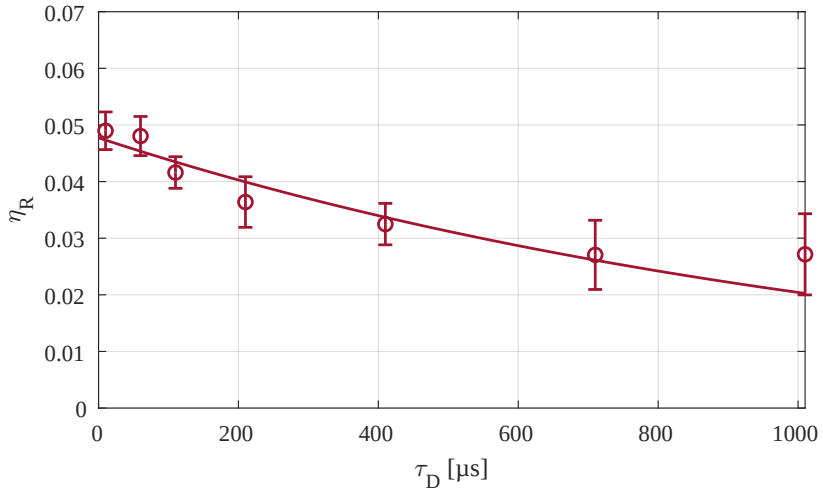

Figure 10.14: Retrieval efficiency η_R versus delay time τ_D. Shown is the retrieval efficiency η_R for various delay times and a fixed readout integration duration of $\tau_R = 40\,\mu s$. The uncertainty on the retrieval efficiency is calculated using Poissonian errors. An exponential function is fitted to obtain the intrinsic memory time. Figure (replotted) and caption from Dideriksen et al. (2021).

To find the decay time of the retrieval efficiency, an exponential model is fitted to the data:

$$\eta_R(\tau_D) = A \exp\left(-\tau_D/\tau_{\eta_R}\right) \tag{10.9}$$

From the fit, the decay time of the retrieval efficiency can be determined as the time until it is reduced to its $1/e$-value, it amounts to $\tau_{\eta_R} = 0.89^{+0.49}_{-0.23}$ ms. To put this number into perspective, we need to consider the limitations of the retrieval efficiency decay. While it is corrected for additional noise originating from false readout, for example, its ultimate limitation will be governed by the dephasing of the spin wave. Successful heralded readout, i.e., the detection of the on-demand single-photon, is given by $\langle \hat{a}^\dagger \hat{a}\rangle \propto \langle \hat{b}^\dagger \hat{b}\rangle(\tau_D)$. This expression is proportional to $\langle \hat{J}_+ \hat{J}_-\rangle(\tau_D) \approx \langle \hat{J}_+ \hat{J}_-\rangle(0) \exp(-2\tau_D/T_2)$ (see section 2.3). We expect the spin wave and retrieval efficiency to decay at twice the decay rate of the transverse spin coherence time T_2 (see 4.5). The decay time

of the retrieval efficiency τ_{η_R} fits within its uncertainty reasonably well with the observed $T_2 = 2\,\text{ms}$ estimated using the pMORS method (section 6.2).

We expect the decay time of our non-classical correlations to approach the decay time of the retrieval efficiency. However, due to the rise of detrimental readout noise due to atomic spin polarization decay while delaying the readout, visible in figure 10.12, the cross-correlation degrades more quickly. Using the fitted model for the cross-correlation $g^{(2)}_{\text{WR}}$ from the previous section, the $1/e$ value for it can be determined as $\tau_{1/e} = (0.44 \pm 0.04)$ ms. This means that the readout noise due to atomic decoherence speeds up the decay of non-classical correlations by a factor of two. Decreasing the growth of the atomic noise when delaying retrieval is an important factor in increasing the quantum memory capabilities of our source.

10.2.3 Noise evolution

As we have established in sections 2.3 and 6.2, decoherence effects lead to a redistribution of atoms from $|F = 4, m_F = 4\rangle$ to other Zeeman and the other hyperfine level. Therefore, we expect the overall conditional signal and the success rate at which we retrieve a heralded read photon to decay with increasing delay times τ_D. At the same time, false readout detection events become more dominant.

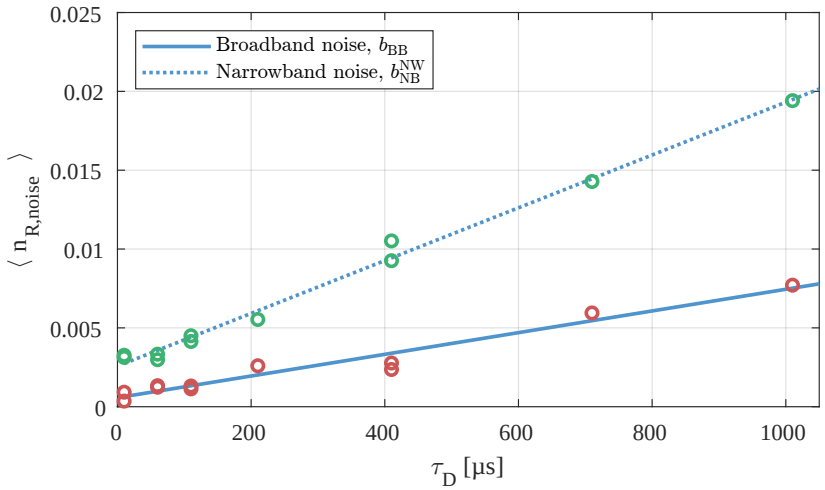

Figure 10.15: Noise contributions versus delay. Narrowband and broadband noise contribution during the read pulse for various delay times τ_D. The values are obtained from filter cavity scans following the procedure described in section 10.1.1.

In order to quantify the different noise contributions further, we require the spectrum to identify the magnitude of each noise contribution. To do so, we repeated the filter cavity scans. Figure 10.3 shows an example of such a spectrum for the minimal delay. We repeated a filter cavity for each delay time. We also perform the no-write measurement for each delay to gauge the narrowband noise in the readout.

In figure 10.15, the results of the narrowband and broadband noise, as described in section 10.1.1, are shown for various delays. Both noise contributions grow linearly with the delay time τ_D. We take this as an indication that both noise sources originate from the same source. It should be noted that we determined the noise contributions for $\tau_R = 40\,\mu s$ as we read out the narrowband noise much faster than the broadband noise (compare figure 10.6). The different speed of reading out the two noise sources originates from inefficiently addressing asymmetric modes when reading out collective excitations.

For the broadband noise, we have discussed in section 4.5 that insufficient motional averaging leads to asymmetric collective excitations. While the write process is related to atoms in $|4,4\rangle$, for the read, the asymmetric modes correspond to retrieval from $|4,3\rangle$ where the motional averaging is insufficient. At the same time, the narrowband noise contribution is also growing. This narrowband noise constitutes, in a sense, a false "coherent" readout. We attribute this narrowband noise to be originating from a residual population in $|4,3\rangle$ after the optical pumping. This hypothesis is supported by observing a significant reduction in the narrowband noise compared to Schmieg (2019), where the optical pumping led to a worse initial atomic state preparation. That both noise contributions grow with a linear trend leads us to believe that both originate primarily from the growing population in $|4,3\rangle$. The origin of the narrowband noise was further investigated in Dideriksen (2021) by varying the atomic spin polarization. The observations deepened our notion that both narrow- and broadband noise are related to residual atomic population in $|4,3\rangle$. This is good and bad news at once. It is good news for operating our source without delay. The residual population in $|4,3\rangle$ can be improved by improving our optical pumping to reach an even better initial atomic spin polarization of our ensemble. The bad news is that the redistribution of atoms into $|4,3\rangle$ will remain the same limitation, as the transverse spin decay time governs the redistribution of atoms. The transverse spin decay time does not change when the initial spin polarization is improved. This property is cell-specific. Only changing to another cell, possibly with a larger cross-section, will alter the redistribution rate.

In order to remedy at least part of this noise, one might consider narrower filters. We expect narrower filters to reduce the amount of broadband noise detected. However, since our desired scattered photons and the false coherent readout have the same spectral properties, narrower filters would not help eliminate that noise. How we can overcome these limitations will be discussed in the next chapter, chapter 11.

As a last, minor consideration, we determine the changes in the readout rate γ_R when delaying the read pulse. For this, we repeat the approach described at the beginning of this chapter (section 10.1) to determine the readout rate as $\gamma_R(\tau_D)$ using the unconditional readout. The fit of the readout rate and its respective value is shown versus the delay τ_D between write and read pulse in figure 10.16. The readout rate is fitted with a linear function, and the incline of γ_D is determined to be $a = 19 \pm 3\ \frac{\mathrm{kHz}}{\mathrm{ms}}$. In figure 10.15, we also

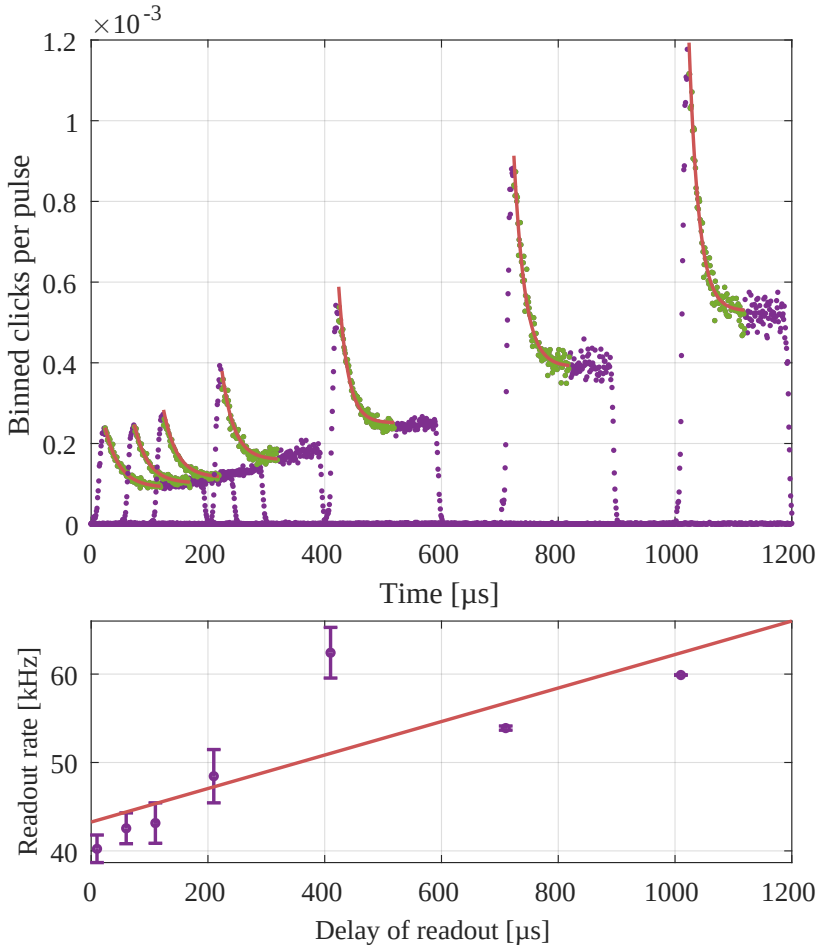

Figure 10.16: Readoutrate versus delay. Top: Various readout pulses sent at delays ranging between 10 and 1010 µs, shown in purple. We indicate the part of the readout used to fit the readout rate in green, while the respectively obtained fit is shown in red. Bottom: Obtained readout rate versus delay. Error bars reflect fit uncertainties of one standard deviation. The red line is a simple linear fit of $a \cdot \tau_D + c$

estimated the growth of the narrowband noise with the delay τ_D. However, this was based on the filter cavity scans and a fixed duration for the readout ($\tau_R = 40\,\mu s$), which reflects the number of symmetric excitations that we can efficiently address with our read pulse. We stress that not all of these symmetric excitations are good symmetric excitations due to the preceding write pulse, as those, of course, do not grow with the delay. The fit to the observed narrowband noise in the filter cavity spectrum in figure 10.15 has an incline, with a different relative scale, of $a = (17 \pm 2) \cdot 10^{-6}$ counts per pulse and microsecond. The relative incline between both analyses agrees well, considering their different scaling due to the analysis and measurements they originate from. We note that the filter cavity scan and the resulting estimate of the narrowband noise correspond in a sense to also determining the readout rate.

Therefore, we expect the two measurements to confirm each other.

Chapter 11

Outlook

We have presented the experimental results of our source-memory protocol using a room-temperature cesium atomic ensemble, as was presented in our joint publication in Dideriksen et al. (2021). In the following sections, we want to do two things. First, we want to provide a coarse benchmark compared to other experimental approaches. Second, we wish to provide an overview and elaborate on our current limitations. We have taken the first steps to implement changes to tackle some experimental challenges and limitations.

11.1 Benchmark

Our experimental system exploits a collective spin ensemble of cesium atoms for storage and retrieval of collective excitations for the on-demand generation of a single-photon following the proposal of the DLCZ protocol. In the following, we compare our experimental capabilities and put them into context with other people's work and performance parameters. The motivation here is that many different approaches have vastly different performances. Here, different performances will not necessarily be "good" or "bad" but rather be related to the suitability of systems for different practical applications.

In the preceding chapter, we successfully demonstrated a high single-photon purity of our retrieval single-photon with a conditional auto-correlation of the retrieval scattered light field more than four standard deviations below the expected auto-correlation of a two-photon Fock state. While the single-photon purity is relatively high, we must also consider our success rate. We successfully recorded consecutive write and read scattered photons 1321 times out of 31 million herald-retrieve attempts. To put these two numbers into perspective, only 0.04 ‰ of our attempts were successful. This relatively low success probability is mainly related to our high losses and low excitation probability to avoid double excitations within our atomic spin ensemble. We can compare our system to a single-photon source based on a quantum dot embedded in a planar nanophotonic waveguide circuit as done in Uppu et al. (2020).

Here, the authors achieve a single-photon purity of $g^{(2)} = 0.015 \pm 0.005$ while generating 122 million photons per second (Uppu et al., 2020). Our room-temperature source is far from the result presented in Uppu et al. (2020). However, the experiment presented in Uppu et al. (2020) comes with its own challenges. First, the experiment has to be operated on the few Kelvin level, requiring cryogenic cooling[1]. Further, these types of devices are not yet mass-producible. A general problem of quantum dot-based sources is low yield in their manufacturing process. Another example of a quantum dot-based source is Ding et al. (2016), suffering from the same experimental challenge arising from the required cryogenic operating temperatures. The authors in Ding et al. (2016) report $g^{(2)} = 0.009 \pm 0.001$ with a single-photon purity of 99.1 %. A thorough review of single-photon sources from semiconductor quantum dots can be found in Senellart et al. (2017). A different approach to semiconductor-based quantum dots is silicon carbide single-photon sources, discussed in an extensive review in Castelletto (2021), that do not require cryogenic cooling. Silicon carbide-based single-photon sources can be operated at room-temperature but have yet to achieve the same performance in the same single-photon purity and indistinguishably as cryogenic-operating quantum dots (Castelletto, 2021).

Atomic-based systems are an alternative approach. Our DLCZ-type on-demand source falls under this category. We can distinguish systems of cold atomic clouds or individual atoms that are optically cooled down to reduce the atoms' motion and systems at room-temperature or even elevated temperature ("hot" vapors). The authors of Mücke et al. (2013) have shown, for example, high single-photon generation efficiency using a single trapped atom inside a cavity – as opposed to the ensemble approach in our case. Generation efficiencies of 56 % on the D_2 line of rubidium with an outcoupling efficiency of 89 % of the photons out of the cavity have been reported Mücke et al. (2013). While cold atomic clouds or individually trapped atoms do not require cryogenic cooling, they still rely on a sophisticated cooling apparatus to slow the atomic motion. However, they also typically have a lower generation efficiency than sources operating at cryogenic temperatures, for example, in Uppu et al. (2020) and Ding et al. (2016). An atomic single-photon source based on a hot vapor employing a Rydberg blockade was presented in Ripka et al. (2018). The source presented in Ripka et al. (2018) exhibits a single-photon purity comparable to ours. However, it operates much faster with a total cycle repetition rate of tens of nanoseconds and sequence pulses on the nanosecond scale. Most of the previously mentioned single-photon sources have a higher repetition rate and generation efficiency than ours. Part of this is related to the operation of our system being intrinsically slow, while another part originates from the high losses, reducing the success rate significantly. Knowing this, we address these issues on the single-photon generation as part of our experimental limitations and present ideas on how to improve from section 11.2 onward.

The second cornerstone of our system is its memory capability. Therefore,

[1] We have to acknowledge here, while our source and memory are operated using a room-temperature system, our detection, however, is not. Our SNSPDs also require cryogenic operating temperatures. With our current choice of detectors, we cannot consider our experimental approach truly room-temperature.

we consider some other atomic ensemble-based quantum memories. Alternative atomic ensemble-based quantum memories capable of storing single excitations are ladder schemes exploiting D-shell storage as presented in Kaczmarek et al. (2018) and Finkelstein et al. (2018). These quantum memories exhibit highly favorable duty cycles compared to our quantum memory due to their fast reinitialization. Our memory requires 350 µs for reinitialization inbetween storage of excitations. At the same time, our memory time of 0.68 ms is significantly longer than the ones presented in Kaczmarek et al. (2018) and Finkelstein et al. (2018). We note that part of our comparably long reinitialization time of 350 µs is related to our read pulse and its comparably long duration of 200 µs. Reducing its length or testing the reinitialization in the absence of a read pulse would reduce the required time for the reinitialization pulse.

For comparison with an experiment combining quantum memory and single-photon generation within one physical system following the idea of the DLCZ protocol (Duan et al. (2001)), the room-temperature results obtained by Dou et al. (2018) in a buffer gas vapor cell can be considered. Similar to our approach, the authors of Dou et al. (2018) employ far off-resonance classical drive light pulses to store collective excitations. Dou et al. (2018) employ hyperfine storage and report a time-bandwidth product of up to 1400 with an intrinsic memory time of 6 µs. While their reported time-bandwidth product is two orders of magnitude larger than ours, the opposite is true for memory time. The time-bandwidth product Dou et al. (2018) states excludes reinitialization time. We would also need to know their reinitialization time for a better comparison to our time-bandwidth product. However, this reinitialization duration is unfortunately not provided in Dou et al. (2018).

With the long-distance entanglement generation in mind, combining a high time-bandwidth product with a long memory time will be beneficial. In our current setup, the time-bandwidth product is limited due to the speed of averaging our interaction (section 11.3.2), governing the duration of the optical pulses required. The current choice of cell geometry fundamentally limits memory time as atoms hit the glass walls quite frequently. Overall, for long-distance entanglement generation, a high success rate will also be essential, which in our case is mainly related to improving the losses present in our system (section 11.2). One way to improve this is to use a repeat-until-success scheme for the write pulse, similar to what the authors of Zhang et al. (2022) employ. We will discuss Zhang et al. (2022) later in this section.

Despite our single-photon source coming with its in-built memory, we can also imagine combining our source-memory system with another long-lived quantum memory. The combination with a distinct quantum memory extends its memory time at the expense of additional experimental complexity arising from interfacing and controlling two systems. However, an atomic single-photon source can be combined, for example, with a loop memory, as has been done by Pang et al. (2020). Since our in-built memory is already exhibiting a memory time of approximately 0.68 ms, interfacing our system with such a

loop memory is not reasonable due to the temporal length of our scattered photons. However, some systems mentioned above with memory times on the nanosecond or microsecond level could benefit from such a loop memory. Other experimental approaches where a single-photon source was successfully interfaced with a quantum memory at room-temperature was, for example, in Buser et al. (2022). The authors interfaced a spontaneous parametric downconversion single-photon source with an atomic ensemble as quantum memory exploiting electromagnetically induced transparency. In Buser et al. (2022), the memory time was limited to below a microsecond. Given that the repetition rate is significantly higher, the reported time-bandwidth product is $B = 250$ (Buser et al., 2022), making this type of memory more geared towards photon synchronization.

The origin of our experiment lies in the proposal for the DLCZ protocol for long-distance entanglement generation based on atomic ensembles. While we followed in these footsteps using an anti-relaxation coated cesium vapor cell operating close to room-temperature, we only realized a single quantum-repeater node. The minimum realization of the DLCZ protocol, containing only a single quantum repeater, requires four atomic ensembles. A more fundamental approach is to show the single-photon interference of two single-photon sources. Combining two or more of our current sources is possible. However, we have yet to do so. Other groups using similar experimental platforms have achieved this already. For example, Li et al. (2021) presented heralded quantum entanglement between two spatially separated room-temperature atomic ensembles. This heralded entanglement is an elementary step toward realizing proper quantum networks. The authors of Li et al. (2021) identify the memory time of 2.2 µs as one of the main limitations toward realizing large-scale quantum networks. The same group showed more recently in Zhang et al. (2022) that they can successfully demonstrate Hong-Ou-Mandel interference between two atomic ensembles exploiting hyperfine storage within their cesium ensembles. A fast repeat-until-success operation allows the authors of Zhang et al. (2022) to speed up the interference rate roughly 15 times, allowing for visibility of the interference to exceed the classical limit of 50 % statistically significant. The authors observe up to 75 % visibility of the quantum interference without correcting for background noise (Zhang et al., 2022). While the overall pulses are on the tens of nanoseconds scale, the memory time of the respective source is limited to a few microseconds in Zhang et al. (2022). While the presented result is impressive for room-temperature systems, the limited memory times will limit the extent of possible quantum networks. It should be noted that the single-photons generated from our source are relatively narrow, as we have seen in section 10.1.1 when scanning the filter cavity resonance frequency with respect to the scattered photon frequencies. Spectrally narrow photons are an advantage when imagining interference from two sources, as the temporal shape of the photon is in the range of multiple microseconds. A rather long single-photon wave package is less sensitive to small delays or path differences between interfer-

ometer arms[2]. Experimentally, the successful interference of a path difference above 100 meters has been shown in Rambach et al. (2018), where the delay between two single-photons was obtained by exploiting a cavity to delay one of them.

For quantum networks, ultimately, long-distance entanglement is of interest. Furthermore, how to connect different systems in the form of a quantum interface will be vital to connect communication channels to quantum computers. Such a hybrid interface could be between atoms and opto-mechanics, for example. Hybrid entanglement between atoms and opto-mechancis has been shown in Thomas et al. (2021). To enable interfacing on the single-excitation level, we require a scheme that allows similarly heralding a single-phonon as a scattered photon heralds our collective excitation. This has been, for example, shown in Galinskiy et al. (2020).

11.2 Experimental limitations

We have identified different limitations in our DLCZ-type experiment, and here we would like to shed some light on how to remedy these issues. Here we will give a short overview and present the consecutive steps taken to realize the improvements.

- **Losses:**
  Losses and limited (experimental) retrieval efficiency slow down the success rate of our protocol. When losses decrease the "good" detection event to the level where dark counts become significant, losses even reduce the fidelity of the retrievable on-demand single-photons. One of the main limitations is the outcoupling efficiency of scattered photons from the cell cavity, affecting write and read scattered photons to the same extent. Therefore, investigating a cavity-free scheme seems a promising path toward reducing losses and improving detection efficiency. Further, the losses due to limited transmission throughout our detection setups and towards the single-photon detectors can be improved. For the write detection setup, the attainable transmission through the fiber toward the detector limits us. Overall, enhancing detection efficiencies improves the success rate of our herald-retrieve scheme. Especially the rate at which triple-detection events will be recorded will gain from increased detection efficiencies.

- **Leakage and drive light suppression:**
  Currently, we are not limited by leakage from the drive light. The cell cavity escape efficiency reduces our drive light suppression requirements. For a cavity-free scheme, the leakage might return to be a limiting factor. Reducing the leakage can be achieved in two ways: by using narrower filters or by improving the magnetic field strength and homogeneity to allow for the scheme's operation at an even higher Larmor frequency. Both are more of an engineering challenge but can be solved.

[2] As a toy model, let us consider two single-photon wave packages we wish to interfere with each other. Considering 20 µs temporal lengths of the single-photons, a path difference corresponding to 10 µs would still allow for interference. In 10 µs, photons travel roughly three kilometers, a potentially long path difference illustrating the benefit of temporally long single-photons rather nicely.

- **Broadband noise:**
  One of our main challenges is broadband noise in both write and read scattered photon spectra. We attribute it during the write due to insufficient motional averaging. During the read, insufficient motional averaging is one of the reasons. However, another contributing factor is the residual population in $|4,3\rangle$ that becomes more pronounced when delaying the readout due to Zeeman level repopulation.

- **Narrowband noise:**
  We have seen that a significant part of the noise during the readout exhibits the same spectral shape as the desired scattered single-photons in the read scattered photon spectrum. To quantify its magnitude, we rely on an experimental sequence reading out the atomic ensemble without sending a preceding write pulse. This readout without preceding write-in of collective excitations corresponds to only a "false" coherent readout. Due to the observation that its contribution had decreased compared to previous iterations with worse optical pumping and its growth when delaying the readout, we attribute this contribution mainly to the population in $|4,3\rangle$. While we can (hopefully) push initial atomic spin polarization preparation further, the repopulation rate of $|4,3\rangle$ remains the same as it is determined by the spin coherence time. The decay of the atomic spin polarization is provided in appendix C. With the current cell geometry, noise contributions arising from $|4,3\rangle$ will remain the limiting factor for the memory time of our single-photon source. Alternatively, choosing a different excitation scheme not being limited by the repopulation of atoms to $|4,3\rangle$ can be considered. While hyperfine storage is not a suitable option in our case as determined in Borregaard et al. (2016), Zeeman level storage with $|4,2\rangle$ with $\Delta m_F = 2$ is a possibility. Choosing a $\Delta m_F = 2$ based excitation scheme comes with additional challenges, which we will discuss later in this chapter.

In the following, we will present a subset of our ideas for improving our experimental performance and some steps taken toward realizing them. However, we will exclude considerations regarding noise reduction due to improving the initial atomic spin polarization and the like and the expected impact on the correlations present in our system. This was discussed at length in Dideriksen (2021). The author considered the noise reduction and the atomic spin polarization improvement, focusing on the expected changes in the correlation functions. Based on the correlation model, also used for the analysis in chapter 10, the possible improvement arising from improved detection efficiency was considered. Dideriksen (2021) finds that a reduction of factor five in the readout noise roughly halves the conditional auto-correlation $g^{(2)}_{\mathrm{RR\,|\,W=1}} \approx 0.1$ according to the model. However, this comes at the expense that an atomic polarization of 99.86 % is required (Dideriksen (2021)). For more details, the reader is referred to Dideriksen (2021) for an in-depth discussion.

11.3 Where to go from here?

The following section will further present our efforts toward investigating our current limitations as presented in section 11.2. We will also present the first steps to finding remedies for the identified issues. As the following section is quite convoluted, and many of the investigated issues are interconnected, we will start with a rough overview. In table 11.1, we summarize some of the key points and motivate why and what we will be testing to improve our DLCZ-type experiment. It should be noted that throughout this chapter, we will not present any direct or verifying measurements using the DLCZ scheme and single-photon counting. Instead, more fundamental considerations and simplified tests will be presented.

What?	**Why?**
Comparison between cavity and no-cavity measurements.	Investigating the cavity enhancement during write and read step in the DLCZ protocol. Further, we test somewhat classical measurements as analogs to avoid running the full DLCZ experiment.
Spin noise measurement.	Classical analog for write step in DLCZ protocol. Tool for investigating reduction in broadband noise.
Homodyne-readout measurement.	Classical analog for read step in DLCZ protocol. The measurement relies on RF excitation instead of optical write-in of collective excitations.
Filling factor.	Influence on write efficiency and filter requirements. Motivation for the shaping of beam profiles.
Limitation excitation scheme.	Rethermalization of $\|F = 4, m_F = 3\rangle$ is limitation for delaying readout. Pro and contra about alternative excitation scheme relying on storage using $\Delta m_F = 2$ instead of $\Delta m_F = 1$.
Beam shaping.	Implementing a more homogeneous beam profile using a tophat profile toward implementing a better filling factor, thus enabling faster motional averaging and reduced broadband noise contribution to the scattered photon spectra.
Increasing cell channel diameter.	Enhance the potential memory time allowing for delaying the readout of stored excitations. Combined with improved filling factor and beam shaping, it can also aid in improving the time-bandwidth product of the DLCZ scheme.

Table 11.1: Overview investigation of limitation. This table aims to provide an overview of the investigations presented throughout this section and our motivation for doing so.

In the following parts of this section, we will address and present some of

the efforts we pursued. Due to the sheer extent, we refrain from presenting all details. As this section is extensive and many of the topics are interconnected, we will summarize the findings in section 11.4 and provide a condensed version of our efforts.

11.3.1 Cavity-free measurements

One of our major losses originates from the limited outcoupling efficiency of the scattered photons out of the cell cavity. While we benefit from the enhanced light-atom interaction due to the cell cavity, losses significantly reduce the speed of our protocol as more trials are required for successful heralding and retrieval in consecutive write and read pulses. Likewise, losses require us to ensure low excitation probability to avoid double excitations that could falsely be detected as single excitations. We reiterate that losses do not compromise the fidelity of our single-photon for negligible background counts (see section 4.6). Instead, they are inconvenient and limit the usability of the single-photon source as it slows down the rate at which the single-photons can be generated.

We performed spin noise and homodyne retrieval measurements with and without the cavity to see our experimental gains during the write and read process when utilizing a cavity around the vapor cell. We use these "classical" measurements because we do not have to adjust our filtering and detection setups to accommodate the different filter requirements between cavity and no-cavity measurements. A different way of thinking about cavity enhancement is that it reduces the filter requirements since fewer drive photons are required to generate the desired scattering process. In turn, this means that without the cell cavity surrounding the vapor cell, we must filter out more classical photons for the desired scattered photon. Hence, running the complete DLCZ scheme without a cell cavity would require new detection setups. We will compare the write and read steps for cavity and no-cavity cases using classical measurements as an analog for the DLCZ write and read step.

Write step: Spin noise measurement

We will use a so-called spin noise measurement to quantify the benefit of the cell cavity during the write step of our protocol. The idea is simple and not completely independent of what we exploit during the (pulsed) MORS technique. The difference is that instead of driving the spin with an RF pulse[3], we probe the thermal spins inside a bias magnetic field using a far-detuned probe laser and record their spectrum using homodyne detection. For the write, we expect the spectrum to consist of a shot noise level arising from the probabilistic nature of laser light, along with a narrowband and broadband contribution to the spectrum centered around the Larmor frequency. The narrow- and broadband contributions are expected to reflect the same ratio for the spectrum of the write scattered photon measured by scanning the filter cavity resonance. Figure 11.1 displays such spin noise spectra recordings.

[3]The measurement can also be performed using an RF pulse, but this is only used to get a more robust response of the spins and therefore "find" the Larmor peak and optimize the settings. The measurement is performed without driving the spins to get the spin noise signal.

For the measurement, we decided to perform the experiment using a Rohde-Schwarz spectrum analyzer and a balanced photodetector. The latter is limited in bandwidth, which required us to perform the measurement using a Larmor frequency of around 500 kHz, as shown in the spectra illustrated in figure 11.1. However, this proved advantageous over using a single output port of the PBS and the previously used APD with our usual choice of Larmor frequency. We suspect this is because the balanced PD is insensitive to common-mode noise. A simplified experimental setup indicating probing direction, polarization homodyne detection, and magnetic field orientation is portrayed in figure 11.2. For a successful spin noise measurement, we need to ensure two things. First, we need to be shot noise limited. We ensured this by recording the electronic noise traces and shot noise levels. All signal traces are corrected for electronic noise. The shot noise trace must be measured with the atoms being far-detuned to correctly estimate shot noise and broadband noise contributions. We ensure this by moving the atoms to our usual Larmor frequency of $\nu_L = 2.4\,\mathrm{MHz}$. Observing a linear dependency of the shot noise level from the probing power confirms that we are indeed shot noise limited. In order to compare the cavity and no-cavity spin noise measurements, we record the spin noise spectrum for various probing powers. As a reference, we use the optical power after the cell and calibrate the losses toward the detector. The calibration is necessary since the incoupling mirror reduces the optical power at the cell significantly. The power before the cell can not be used as a reference point.

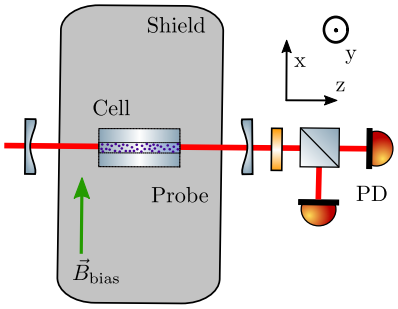

Figure 11.2: Experimental configuration spin noise measurements. Simplified experimental setup for the spin noise measurement. The desired Stokes component is recorded using a combination of a half-wave plate and a polarizing beamsplitter. The optics in front and behind the cell are either high-reflective mirrors (cavity measurement) or lenses (no cavity measurement).

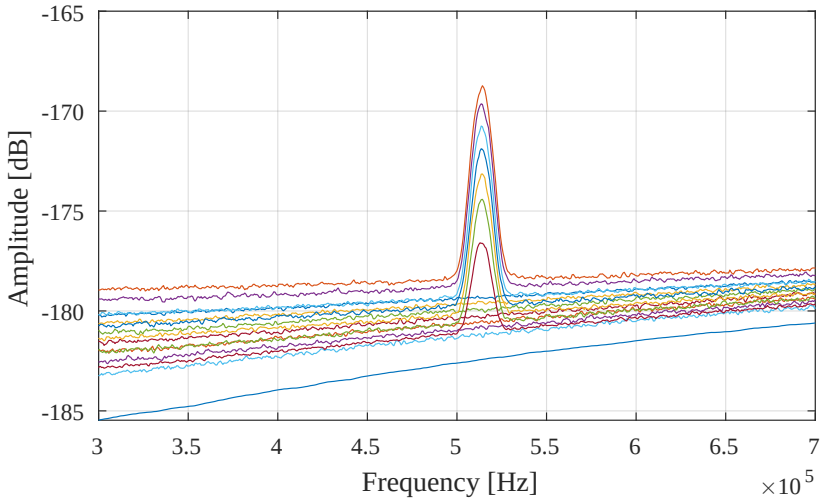

Figure 11.1: Spin noise spectra. The obtained spin noise spectra versus the frequency. The lowest trace is the recorded electronic noise floor, used to correct the signal traces for electronic noise. The peaks correspond to various spin noise spectra for different optical probing powers. We also plot the respective shot noise levels.

We can determine multiple things from the obtained spin noise measurements. First, we can plot the individual shot noise level versus the optical

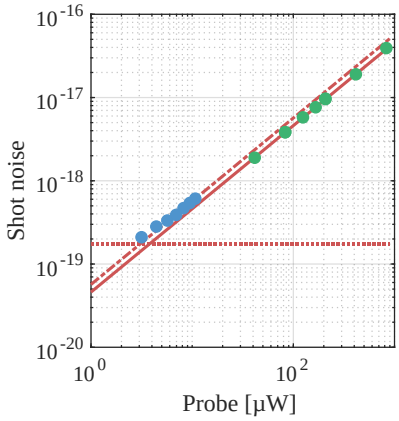

Figure 11.3: Shot noise versus probe power. Verification of linear growth of the shot noise level versus the probe power for the cavity (blue) and no-cavity (green) measurement. All traces are corrected for electronic noise. For reference, the electronic noise level is shown as a dotted line. A linear function $f(x) = a \cdot x$ is fitted to the data. The respective slopes are shown as a solid and dash-dotted line for the no-cavity and cavity cases, respectively.

power. Doing so allows us to verify that the shot noise level grows linearly with the probe power. In figure 11.3, the measured shot noise (arbitrary units) is plotted versus the probe power for the measurement with the cavity. A linear fit $f(x) = a \cdot x$ is fitted to the data for better visualization. We observe good agreement between fit and data. We observe a discrepancy in the slopes corresponding to 14 % despite our efforts in calibrating losses towards the detector. This discrepancy is related to multiple things. First, we are dealing with two different experimental setups. A thorough calibration of the losses is prone to errors. Further, there were multiple months of separation between the two measurements, and the changes to the setup were quite drastic. Despite our efforts to reproduce the cavity mode with lenses, this is a potential source of errors. We attribute this to different detection efficiencies and systematic errors in estimating the probe power between the two experimental configurations. Unfortunately, when we started performing the measurements, we did not plan to use them to estimate the cavity enhancement but only realized this opportunity afterward. Therefore, we should have more carefully calibrated and measured the losses through the paths in both cases. Repeating the measurements after realizing these issues was not straightforward, as replacing a lens with the incoupling mirror again is a tedious task and was, timewise, not an option.

The key for estimating how much we gain from the cavity is determined by the narrowband contribution to the spectrum with respect to the applied probing power. The difference in scaling between cavity and no-cavity cases provides information about the enhancement from placing the vapor cell inside a low-finesse cavity. In Thomas (2020), the dynamics of spin noise measurements for different measurement strengths, meaning probing powers, have been considered. It was found that the narrowband feature in the spin noise spectrum (figure 11.1) grows with the applied probe power – and so does the power broadening induced by it. As a simplification, we followed Thomas (2020) and considered only the peak height of the power spectral density at the Larmor frequency, corrected for the shot noise and the broadband noise. The latter is obtained from a fit to the spectral data using a broad Lorentzian. We expect the two competing effects of growth and broadening to follow different trends for the narrow feature in the spin noise spectrum. For high enough probing powers, the peak height will approach a plateau while the broadening of it will continue to increase. This effect allows us to express the probe power (P_{Probe}) dependency of the narrowband feature (NB) in the spectrum with a simple model as follows (Thomas, 2020):

$$\mathrm{NB}\left(P_{\mathrm{Probe}}\right) \propto \frac{a \cdot P_{\mathrm{Probe}}}{P_{\mathrm{Probe}} + b} \tag{11.1}$$

where the numerator describes the increase in the peak height of the narrowband feature with probe power. The denominator describes the broadening, which means that for large probe powers, a plateau is reached. This behavior is also clearly observable for the cavity-free measurement as sufficient probe

power was available (figure 11.4 bottom). For the measurement with the cavity surrounding the cell, we suffer from the low on-resonance transmission through the cell cavity, severely limiting the optical power after the cell. The trend towards a plateau is not as pronounced (figure 11.4 top).

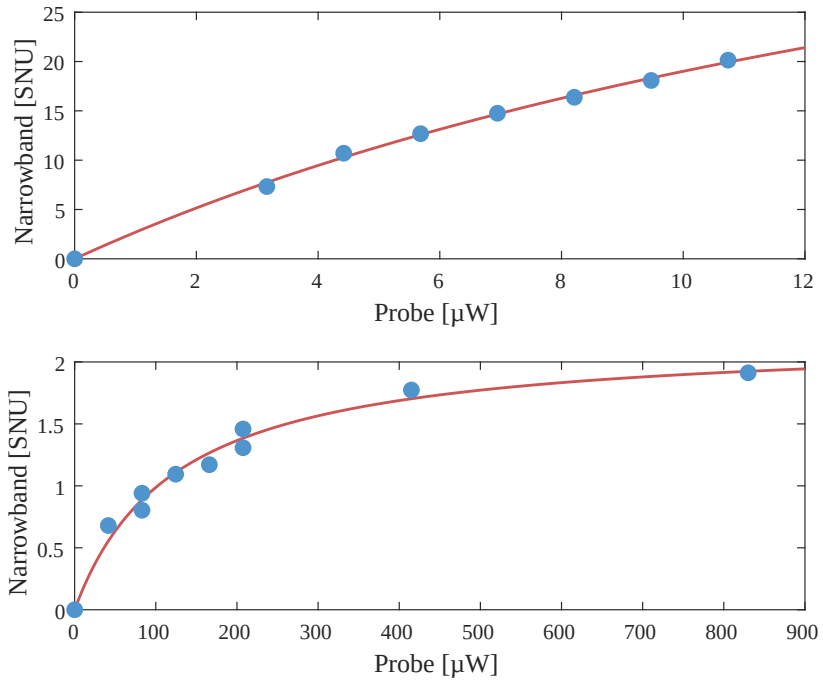

Figure 11.4: Narrowband contribution versus probe power. Experimental observed peak height of the narrowband peak versus the probe power for the cavity (top) and no-cavity (bottom) measurement. The data is accompanied by the obtained fit of $f(x) = a \cdot x/(b + x)$ for both measurements.

We fit the model from equation (11.1) to the recorded experimental data for both measurement series. As the parameter a describes the growth of the narrowband peak in the spin noise spectrum in the absence of broadening effects, we are only interested in the estimate of the cavity enhancement as $\xi_{\text{cav}} = \frac{a_{\text{cav}}}{a_{\text{nocav}}}$. The experimentally obtained values for the cavity enhance-

	Parameter a	Uncertainty Δa
Cavity	58.1	5.7
No cavity	2.2	0.1
Cavity enhancement	27	3

Table 11.2: Overview results spin noise measurement. Fit results with confidence intervals corresponding to one standard deviation for parameter a of the fit model in equation (11.1) for cavity and no-cavity measurements. We estimate the cavity enhancement between both measurements. The standard deviation for the cavity enhancement is calculated using the standard error-propagation formula.

ment are interesting results, but we have yet to make a comparison to what we would expect. Therefore, we wish to compare the values in table 11.2 with the value we would theoretically expect based on our experimental parameters. For this, we consider ξ_{Cav} as the ratio between scattered photons in the cavity and in the no-cavity case. For the cavity, the optical depth is increased by a factor $2\mathcal{F}/\pi$ as discussed in section 4.3. This alone is insufficient for consideration, as the (scattered) photons are subject to further losses in both cases. Common to both cases are the losses arising from the finite transmission through the cell and its windows ($\approx 87\,\%$). We are subjected to additional intra-cavity and outcoupling losses in the cavity case. Expressions accounting for these were already found in Dideriksen (2021) and simplified to $(2/T_{\mathrm{out}} - 1)P_{\mathrm{out}}$. Here, T_{out} indicates the transmission through the outcoupling mirror and P_{out} to the optical output power. We use this to determine the cavity enhancement as:

$$\xi_{\mathrm{cav}} = \left(\frac{2}{T_{\mathrm{out}}} - 1\right)\eta_{\mathrm{esc}}\frac{2\mathcal{F}}{\pi} \approx 34 \tag{11.2}$$

Even considering the associated uncertainties, the value is higher than we experimentally observed. While we tried to match the waist of the cavity by using a lens in front of the cell, changes and additional clipping losses could impact our results negatively, contributing to some of the discrepancies. Further, we use slightly different optical paths. Due to the time separation and different detection efficiencies (compare figure 11.3), we have to assume some underlying systematic errors that are not accounted for in the uncertainty. Considering our simple approach, the experiment and prediction of the cavity enhancement, nevertheless, agree fairly well. For the future, proper calibration and combination with a model that allows for accounting errors and losses, the reliability should improve further. In principle, repeating the measurement for both cases with this specific measurement in mind and gauging losses along optical paths more rigorously could allow for a more reliable value of the cavity enhancement.

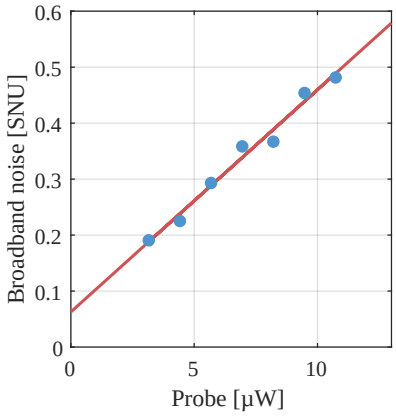

Figure 11.5: Broadband noise versus probe power. Obtained broadband contribution, normalized to units of shot noise versus the probe power at the cell cavity output. The fit is a linear fit of type $f(x) = a \cdot x + c$.

We further investigate the broadband noise level dependency from the optical probe powers. In figure 11.5, we plot the broadband noise, estimated from the spectrum in figure 11.1, converting it to shot noise units versus the probe power. Figure 11.5 exhibits a nice linear trend with an offset. This linear dependency matches our previous experimental observation when varying the optical write power used in the DLCZ sequence (see Zugenmaier (2018)). In figure 11.5, the broadband noise is a small contribution compared to the shot noise level. It will limit how well we can resolve further reductions in the broadband noise after improving the filling factor (see section 11.3.2). Nevertheless, this simple spin noise measurement is an easy and simple-to-implement technique allowing us to investigate and compare cells with different geometries without the challenges of matching filtering and detection setups for single-photon detection. The experimental simplicity of this method will be of particular interest when testing cells of different geometries in sec-

tion 11.3.2. Despite the limitations and sub-optimal conditions in the measurements presented here, we consider the test of this spin noise measurement a success for estimating the cavity enhancement, or in more general terms, the coupling strength to the collective mode.

Read step: Homodyne-readout measurement

In our write-read scheme, the classical analog to estimate the enhancement arising from the cell cavity for the readout proved slightly more complicated than for the write step. As the coherent readout follows the successful heralding of a collective excitation, we need an experimental sequence mimicking the optical pumping, excitation, and retrieval. We used an RF excitation instead of an optical write pulse, along with our usual optical pumping and readout for experimental simplification. The relevant pulse sequence for this measurement is illustrated in figure 11.7. A simplified experimental setup is shown in figure 11.6, illustrating the probing, detection, atomic state preparation, and the RF coils for exciting the collective spin. Here, we exploit that the interaction used to describe the interaction between the spins and the RF field used for the pMORS technique can be extended to ensemble interaction and shown to create symmetric collective excitations of the collective spin-oscillator. This property has been used in previous theses to create symmetric collective excitations inside the spin ensemble, and we refrain from introducing the theoretical description here (see Dideriksen (2021) and Zugenmaier (2018) for details).

For the homodyne-readout measurement, we need to use our D_1 laser tuned to the magical detuning instead of the probe laser we used for simplicity in the spin noise measurement.

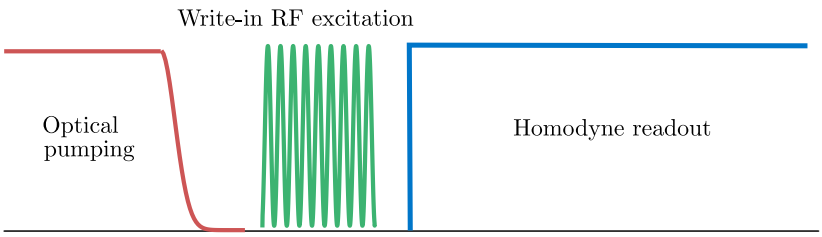

Figure 11.7: Sequence homodyne readout measurement. Simple experimental pulse sequence for the homodyne readout measurement. The coherent spin state is prepared using optical pumping. RF excitations are written into the spin ensemble using an RF pulse instead of an optical write-in. As usual, the excitation is optically read out, and the response is recorded using homodyne detection.

In the following, we vary the optical power of the read pulse and record the light-atom interaction using homodyne detection again. The resulting time recording is analyzed for the readout rate. The readout in the DLCZ is usually in the tens of kilohertz, as we have seen as part of our analysis in section 10.1 and figure 10.2 specifically. We again consider the power after the cell as a reference point for comparing the cavity and no-cavity cases. We record

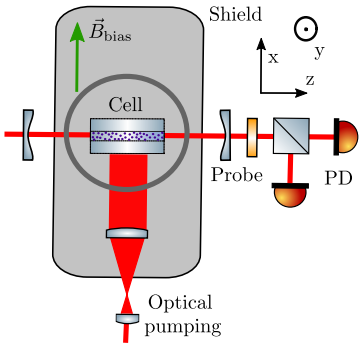

Figure 11.6: Experimental configuration homodyne-readout measurement. Simplified experimental setup for the read homodyne measurement. The desired Stokes component is recorded using a combination of a half-wave plate and a polarizing beamsplitter. The optics in front and behind the cell are either high-reflective mirrors (cavity measurement) or lenses (no cavity measurement). The spin state is prepared using optical pumping and excited using the RF coil.

the signal detected after the RF pulse for various optical powers. Similar to pMORS (section 6.2), we observe an exponential decay of the oscillations. The decay rate of the exponential is what will reflect our readout rate. We use the following fitting model to determine the readout rate:

$$f(t) = A\sin(2\pi(t - t_0)\nu_L) \cdot \exp\left(-\gamma_R \cdot t\right) \tag{11.3}$$

With the amplitude A, starting point t_0, the oscillation frequency – expected to be the Larmor frequency[4] – ν_L and the readout rate γ_R. Figure 11.8 displays an averaged time recording and the resulting fit using a function of the type presented in equation (11.3).

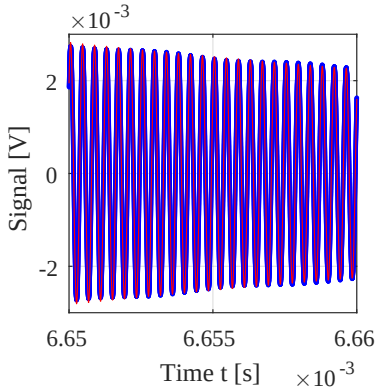

Figure 11.8: Readout signal fit. Data (blue dots) along with fit (red line) for the homodyne readout signal. The fitting model is given by $f(t) = A\sin(2\pi(t - t_0)\nu_L) \cdot \exp\left(-\gamma_R \cdot t\right)$. For better visualization, only a small time range is shown. The time trace was averaged 1000 times.

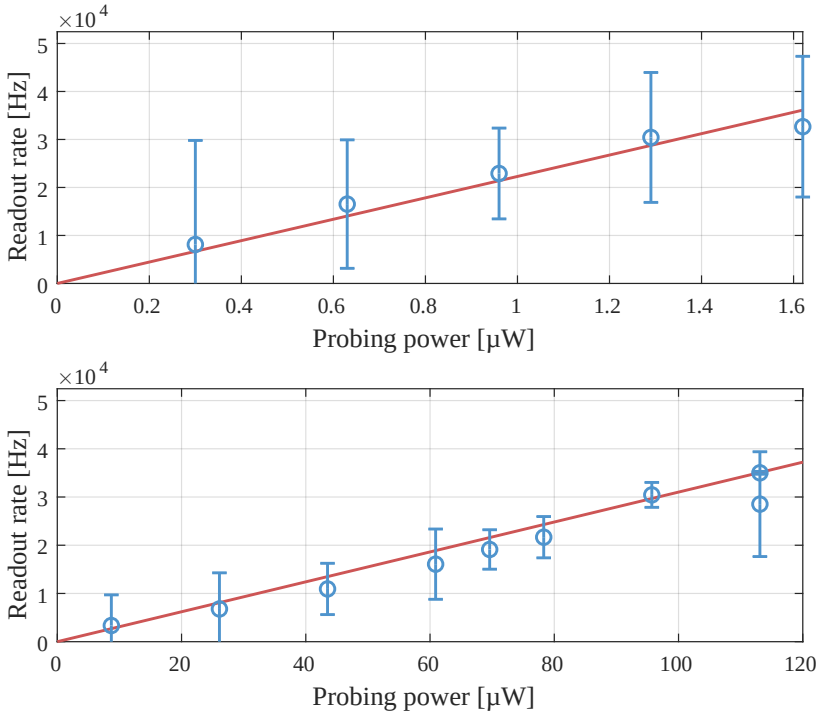

Figure 11.9: Readout rate versus probe power. The obtained readout rate γ_R versus the respective probing power for the cavity (top) and no-cavity (bottom) experiment. Due to the low optical powers, the fitting model is approximated as a linear function $f(x) = a \cdot x$. Error bars are estimated from confidence intervals for γ_R from the individual fits (see figure 11.8) corresponding to one standard deviation.

For both cases, with and without a cavity surrounding the cell, we determine the individual fitting result for the readout rate γ_R versus the optical power after the cell. The corresponding results for the various readout rates are shown in figure 11.9. As the values for the readout rate γ_R are obtained from fits, we use the confidence intervals from the fit corresponding to one standard deviation to estimate the uncertainty. These are reflected as error bars in figure 11.9. It should be noted that the uncertainties for many of the results seem to be rather large, while the points themselves seem to follow a

[4] In principle, we know the oscillation frequency, as it is our common Larmor frequency $\nu_L = 2.4\,\text{MHz}$ and fix it to reduce the number of parameters. We only observe small fluctuations in the fitting parameter for the frequency.

linear trend quite nicely. The nice linear trend with the seemingly too-large error bars could indicate that we overestimate the associated uncertainty of the readout rate here. It should be noted that the highest optical power used in the top part of figure 11.9 corresponds to the one used in the DLCZ-type experiment. With a readout rate of $\gamma_{\mathrm{DLCZ}} = 40.2 \pm 1.6\,\mathrm{kHz}$ in the DLCZ-type experiment, the observed readout rate using the homodyne-readout agrees well within their associated uncertainties (compare figure 11.9 top).

We are working with comparably low optical powers. Hence, we approximate the readout rate as depending linearly on the applied probing power to readout the RF excitations. Linear scaling of the readout rate is also the scaling we have experimentally observed when varying the read power, for example, presented in Schmieg (2019) and Dideriksen (2021). We fit a function $\gamma_{\mathrm{R}}(P_{\mathrm{Readout}}) = a \cdot P_{\mathrm{Readout}}$ to the data. The associated fits are shown in figure 11.9.

We can estimate the cavity enhancement as the ratio between the two slopes for the cavity and no-cavity homodyne-readout measurement from the obtained fits. Estimating the ratio between the slopes, we determine a cavity enhancement of $\xi_{\mathrm{cav}} = a_{\mathrm{cav}}/a_{\mathrm{nocav}} = 72 \pm 5$, where the uncertainty is estimated using the confidence intervals corresponding to one standard deviation and propagating them through the expression. This result should only be considered a very crude estimate for the cavity enhancement due to the simplifications we made.

Discussion

In order to investigate possibilities to test our experimental scheme for the DLCZ-type experiment without the need for a cell cavity, along with avoiding the requirement for detecting single-photons, we tested two more straightforward techniques as "classical" analogs for quantifying write and read processes. We presented a spin noise measurement for the write step to investigate its spectral composition. The advantage of this more straightforward measurement is that it provides an instant spectral response, allowing us to quantify the narrowband and broadband contributions to the write spectrum. The cavity enhancement was determined to be $\xi_{\mathrm{cav}} = 27 \pm 3$, but deviated from the theoretically expected value of $\xi_{\mathrm{theo}} = 34$. Further, we observed that the broadband contribution to the spin noise spectrum is small compared to the shot noise levels. The overall small broadband contribution poses a problem when comparing different cell geometries. Quantifying the reduction of broadband components for improved filling factors by changing the beam profiles could be limited by the resolution of the broadband noise level. The classical readout of RF excitations works nicely for the homodyne-readout technique. However, some things could be improved with the measurement technique. For now, we have only compared cavity and no-cavity measurements to estimate the cavity enhancement. We expect some issues with comparing the results to the entire DLCZ scheme for now. First, we have only used RF excitations instead of optical write. For now, we had no calibration of

the RF excitation compared to the optical write. The lack of calibration limits the comparability in absolute terms between the homodyne readout measurements to the DLCZ-type experiment. In order to estimate the read efficiency from this measurement, we require knowledge about how many collective excitations are created by an RF pulse. While this has not been done here, calibrating the number of collective excitations generated by an RF pulse can be done and has been used in the past to perform the DLCZ-scheme without optical write step in Zugenmaier et al. (2018). However, the homodyne readout measurement seems fine when we aim only for relative comparison, especially when considering repeating this measurement for vapor cells of larger cross-section diameters. Its simplicity and the lack of filtering and detection setups make this a promising approach for a simple test to quantify experimental performance across cell geometries in the future.

Spin noise and the homodyne-readout techniques are experimentally simple alternatives to quantify different processes in the write and read step without requiring a fully developed filtering and detection setup for detecting scattered single-photons. With a more thorough investigation and calibration of these measurements, they could, in principle, allow us to compare various cell geometries for their write efficiency and possible readout rates expected in the DLCZ scheme. So far, we have only used these experimental methods to quantify the cavity enhancement present in our DLCZ scheme. For write and read, we found factors of $\xi^{\mathrm{W}}_{\mathrm{cav}} = 27 \pm 3$ and $\xi^{\mathrm{R}}_{\mathrm{cav}} 72 \pm 5$ for the cavity enhancement, respectively. On the one hand, this confirms that we do benefit in our scheme a lot from placing the atomic ensemble in a low-finesse cavity. The significant reduction of required drive photons relaxes the requirements imposed on our filters, simplifying the filtering and detection setups. At the same time, since it is "only" an enhancement of fewer than two orders of magnitude, the optical power requirement and the gain in the experimental retrieval efficiency make a cavity-free scheme worth investigating. This also holds when considering the complete DLCZ scheme, including the single-photon detection, as a higher filtering requirement is not a fundamental limitation but rather a technical challenge. Using multiple cavities in our detection setup and the updated design presented in Galinskiy et al. (2020), the required suppression of drive photons combined with high transmission is viable. We will discuss the filter requirements further when considering cells with larger cross-sections to improve the memory time of our herald-retrieve scheme in section 11.3.3.

Overall, the two experimentally more straightforward methods of spin noise and homodyne-readout techniques are very convenient ways of quantitatively getting an estimate of a cell's performance. Even though the techniques are not (yet) allowing for an absolute reference and performance prediction, they appear as reasonable alternatives for judging relative changes.

11.3.2 Improving filling factor

We have seen in our filter cavity scans of the scattered photons in section 10.1.1 that one of our limitations in our herald-retrieve scheme is the broadband noise in the write and read spectra. For the write step, we have observed a write efficiency of $\eta_W = 0.82 \pm 0.01$ (section 10.1.2). We can also calculate the write efficiency based on the current filling factor of our cell for two cases: first, where we purely consider the filling factor of our cell, and second, considering the motional averaging arising from our filtering cavities. For both cases, we will consider the theoretical write efficiency as introduced in equation (4.16). For excluding the filter cavity contribution, we assume $\kappa_2 \to \infty$. Excluding the filter cavity reduces the expression to:

$$\eta_W^{\text{no filter}} = \frac{\pi\omega_0^2}{4L^2} \approx 0.28 \tag{11.4}$$

where we have used the parameters of our experimental setup given by the cavity mode, leading to a beam radius of $\omega_0 = 90\,\mu\text{m}$ and a channel cross-section diameter of $2L = 300\,\mu\text{m}$. Considering the narrow filter cavity during the write step of $\kappa_2 = 2\pi \cdot 98\,\text{kHz}$ together with the decay rate of the atom-atom correlations $\Gamma = 2\pi \cdot 456\,\text{kHz}$, we obtain the expected write efficiency η_W in the presence of the motional averaging facilitated by the filter cavity based on equation (4.16) to be:

$$\eta_W^{\text{filter}} \approx 0.80 \tag{11.5}$$

We can deduce two things from these two values for the write efficiency. First, our pure write efficiency from the filling factor is relatively low, but our write efficiency increases significantly due to the motional averaging facilitated by the filter cavity. Secondly, the write efficiency considering the filter cavity is within two standard deviations of our experimentally determined value. The slight discrepancy can originate either from overestimating the FWHM of the filter cavity or underestimating Γ, for example. Nevertheless, for this rather crude estimate, the agreement between estimated and observed write efficiency is verifying that we can use these expressions to investigate the expected improvements in the write efficiency when changing various parameters.

In the following, we want to improve the write efficiency further. One option to achieve this is to increase the waist of the Gaussian beam. Of course, this can easily lead to additional clipping losses, and as we have discussed in chapter 9, any losses inside the cell cavity are detrimental. Therefore, we want to avoid increasing the waist further than it already is. It should be noted that our choice of $\omega_0 = 90\,\mu\text{m}$ was already increased from the previous choice of $\omega_0 = 55\,\mu\text{m}$ presented in Borregaard et al. (2016), Zugenmaier et al. (2018), Zugenmaier (2018), Schmieg (2019), and Dideriksen (2021). While the write efficiency was worse for the smaller waist, the transmission through the cell was better. Due to the higher losses with the current waist, we did decide to refrain from increasing the waist further.

Figure 11.10: Illustration beam profiles. Simple illustration of the beam intensity and profile. The top illustrates a Gaussian beam, while the middle part reflects a super Gaussian beam with a round and flat intensity distribution. The bottom part illustrates a square tophat intensity profile.

An alternative is to increase the waist width as much as possible while using a more homogeneous intensity distribution across the cell channel. A homogeneous beam intensity profile should have steep edges and a flat top. Such a profile should introduce less losses than simply widening a Gaussian beam profile. A better filling factor reduces the broadband contribution from asymmetric modes to the spectrum and aids the motional averaging, as discussed in-depth in section 4.5. A beam intensity profile fulfilling this requirement is a super-Gaussian (round) or a flat tophat (square) profile. Given the experimental configuration presented in chapter 9 and chapter 10, a flat tophat (TH) profile will allow for the best filling factor considering a cell with a square cross-section. The different beam profiles are illustrated in figure 11.10. The blurriness of the edges is expected to be less pronounced for a super-Gaussian or a square tophat profile than for a normal Gaussian intensity profile.

For a crude estimate, let us consider replacing our circular waist ω_0 with the respective square cross-section. Following equations (4.11) and (4.12), the illuminated area increases by a factor two: $\omega_0^2 \rightarrow 2\omega_0^2$. The change in beam profile geometry increases the intrinsic write efficiency by a factor of two, excluding the motional averaging from the filter cavity. Including the motional averaging provided by the filter cavity still improves the write efficiency to $\eta_{\mathrm{W}}^{\mathrm{filter}} \approx 0.82$. The change might initially seem like a minor improvement, but this is not completely unexpected. The filling factor not only changes how well our beam illuminates the channel, but it also alters the spectral shape of the broadband contribution, which will become narrower for a higher filling factor. Therefore, improving the filling factor alone will not lead to the desired effect but has to be combined with narrower spectral filters to filter out more of the broadband contribution that is now more centered around the desired signal while overall being reduced. We will need to consider how to achieve and improve spectral filtering when improving the filling factor of our cell.

Before considering implementing a tophat beam, we have to ponder a second limitation in our experimental scheme - the memory time. This we will consider in the next section (11.3.3) before turning ourselves to putting our considerations towards the first steps of implementation of flat intensity profiles in section 11.3.4.

11.3.3 Improving the memory time

The advantages and disadvantages of our experimental scheme are that we have a quantum memory and a single-photon source combined within one physical system. We benefit from not requiring to combine two different systems, one for generating the single-photons with a system that acts as a quantum memory, allowing us to retrieve the single-photons on demand. At the same time, this also poses a disadvantage, as our scheme is intrinsically slow, and the repetition rate is limited. We have two figures of merit here. The first figure of merit is the memory time of the system. The memory time alone

does not provide us with the entire information when changing the performance of our system. We also want to consider the time-bandwidth product. Considering the time-bandwidth product allows us also to quantify if we improve on the relative speed of our scheme. Let us consider the following to motivate the latter as a valuable addition to the memory time alone. If we increase the memory time by a factor of ten, but all other time scales on the scheme increase by the same amount, then while the memory time has increased, the relative speed of our scheme remains unchanged. Considering the memory time alone can therefore be misleading.

In the following, we will first consider how to improve the memory property of our system. As seen in section 10.2, the successful retrieval of a single-photon and our system capability as a quantum memory is governed by the transverse spin-coherence time T_2. In our type of system, the T_2 time is mainly governed by wall collisions and consecutive loss of spin polarization. Our alkane coating remedies this to a certain extent, allowing us to reach a memory time of $\tau_{\mathrm{NC}} = (0.68 \pm 0.08)$ ms. For comparison, buffer gas cells, slowing down the atomic motion, have been shown to allow for storage of attenuated laser beams on the few-photon level to be limited to tens of microseconds (Namazi et al. (2017)) or even below that for single-photons or other non-classical light states (for example, Pang et al. (2020); Buser et al. (2022); Dou et al. (2018)). Alkane-based coatings do not offer the highest possible T_2 times of anti-relaxation coated vapor cells. Typically, alkene-based coatings allow for even more wall collisions before an atom loses its spin state. However, these coatings typically cannot endure our desired operating temperatures. Changing to an alkene-based anti-relaxation coating would mean a lower optical depth d available. A lower optical depth reduces the efficiency of our scheme as the interaction strength depends on the optical depth d. How much of an experimental challenge this poses has yet to be tested. Testing this could become easier with the simpler spin noise and homodyne-readout measurements. Due to time constraints, this has not been possible within this project.

Further, the spin coherence times T_1 and T_2 increase on average when increasing the cross-section diameter[5] of the channel, assuming that the length is much longer than its diameter. To use our experimental system for a quantum repeater scheme such as the DLCZ protocol, the distance over which such a network or connection can be employed depends on the memory time. In Borregaard et al. (2016), this was estimated for an experimental system similar to ours to be on the order of tens of kilometer[6]. To imagine a network of this size or even longer distances, we need to significantly improve our system's memory time. For starters, we will consider ourselves with cells of a diameter of 3 mm and 5 mm and a channel length of 80 mm. These should allow us for the desired factor of ten or more in the transverse spin coherence time. In principle, we could imagine an even longer cell, accommodating our need for a high optical depth and relaxing the disadvantages of the missing cavity enhancement in a cavity-free scheme. However, magnetic field homogeneity and attainable filling factor due to clipping losses will kick in and become

[5] In chapter 7, this is easily visible when comparing the T_1 times of cell geometries with variable cross-section. This can intuitively be understood since the mean free path of the atoms increases. A longer mean free path reduces the rate of wall collisions, effectively increasing the spin coherence times.

[6] It should be noted that they assumed for this estimation a higher level of detection efficiency and the like. It can only be considered a very crude and optimistic ballpark estimate.

problematic when extending the cell channel length. Therefore, the geometry of the cell remains a trade-off between losses, filling factor, and attainable optical depth.

Further improvements in memory time and issues arising due to repopulation of $|F = 4, m_F = 3\rangle$ during the delayed readout could also be remedied by switching to a different excitation scheme. While hyperfine storage in our setup has also been found to not suffice (Borregaard et al. (2016)) due to its lifetime, we have also seen that $|F = 3, m_F = 3\rangle$ repopulation is fast (see appendix C). The only reasonable alternative seems to be investigating a $\Delta m_F = 2$ scheme. The transitions involved are shown in a simplified level scheme in figure 11.11. Due to the separation from the main population $|F = 4, m_F = 4\rangle$, we expect the readout noise due to false coherent readout to grow slower than we have observed in figure 10.15 in section 10.2. For this, we would switch to a different experimental configuration where the bias magnetic field is oriented along the cell's channel for multiple reasons. First, only the $\Delta m_F = 2$ transition is driven in this colinear configuration. This has been shown in Fomin et al. (2020), where the authors investigated the spin noise signals for colinear and transverse magnetic field orientation.

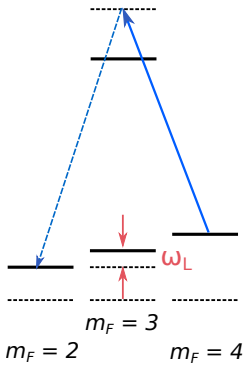

Figure 11.11: Illustration $\Delta m_F = 2$ scheme. Simplified excitation scheme employing $|4, 2\rangle$ instead of $|4, 3\rangle$ as storage state. This scheme implies a separation of the scattered photon of $2\nu_L$ to the drive light. The dotted lines in the lower part of the figure indicate the levels in the absence of the magnetic field.

Then we would need optical pumping along the channel. A colinear configuration can be a gain and a loss simultaneously. On the one hand, this adds complexity concerning the number of beams required to propagate colinear and overlap with each other. Additionally, we have yet to determine if we can accomplish the same level of atomic spin polarization using colinear optical pumping. On the other hand, optical pumping from the side with an 8 cm cell is also cumbersome when having only 2.5 cm holes in the magnetic shield. However, another experiment at Quantop has already successfully implemented this. Further, we need to redesign our magnetic field design.

One main concern is the weaker transition strengths for $\Delta m_F = 2$. Considering the excited states mediating the transition we are interested in, we estimate an additional factor of 50-100 in the optical power required compared to our current scheme when changing to $\Delta m_F = 2$. The higher optical power requirement is not a fundamental problem but rather a technical challenge for our experimental setup requiring some optimization in our optical paths and higher-powered laser diodes than the current ones. At the same time, the higher optical drive power leads to more classical background photons with which the scattered photons share the same spatial mode. More drive light leakage increases the requirement on our filtering and detection setups as a higher suppression of classical photons is required. A higher leakage suppression can be achieved by employing a narrower filter or cascading multiple cavities after each other, as in Galinskiy et al. (2020). At the same time, we benefit from the higher spectral separation between drive and scattered light, as the scattered light is detuned $|\Delta| = 2\nu_L$. The additional spectral separation aids the filtering compared to the transverse magnetic field configuration.

It should be noted that in any case, when dealing with the bigger cells compared to the microcell used in chapter 10, we will require a higher amount

of optical power present in the cell. Considering that we currently lose a lot of drive light on the incoupling mirror of the cell cavity, the absolute increase in optical power requirement for switching from $0.3 \times 0.3 \times 10\,\text{mm}$ to $3 \times 3 \times 80\,\text{mm}$ as severe. Compared to our current input power in front of the cell cavity, we conservatively estimate that a factor of five in each pulse is sufficient. This optical power is well within the capabilities of ECDLs, considering that we commonly work in the hundreds of micro-watt range and below.

11.3.4 Tophat beam profile generation

One way to improve the motional averaging is implementing a tophat beam profile for the drive light. Depending on the excitation scheme and choice of geometry, one might consider different experimental configurations. Sticking to our previous excitation scheme exploiting Zeeman level storage with $\Delta m_F = 1$, we expect to improve on the time-bandwidth product of our single-photon source. However, repopulation of $|4, 3\rangle$ will still be a limiting factor for the memory time. Due to the requirement of optical pumping from the side, a square channel is beneficial to avoid lensing effects from the curvature. Only the drive light must be shaped for this type of channel to have a flat intensity profile. A square flat tophat profile will most benefit the filling factor for a square channel. If we want to investigate $\Delta m_F = 2$, a round channel is sufficient together with a round tophat or super-Gaussian intensity profile. In terms of how easily the mode can be converted back from a tophat profile to the fundamental TEM_{00}-mode, a round tophat has the benefit that it can be achieved using fewer higher-order modes, and radial symmetry makes alignment more convenient.

There are different ways of generating a flat tophat beam profile with either a round or square profile. One field driving the demand for the development of tophat beam shaping optics is the field of laser material processing. For laser material processing, a high and very confined laser intensity is required at the focal plane. These are precisely the property a tophat beam profile exhibits compared to the usual TEM_{00}-mode with its Gaussian profile. At the same time, this also means that less work has been gone into converting the beams back to match a Gaussian and making them compatible with a fiber mode or trying to collimate them over a longer distance. Both will be important for the actual DLCZ scheme. Efficient back conversion will be vital for single-photon detection without significant losses.

Different approaches can be used to generate tophat beam profiles. For example, Powell lenses have been exploited in Willstrand (2013). Alternatives are, for example, aspheric lenses (Möhl et al., 2016), so-called beam integrators (Dickey and Holswade, 2000), or refractive field mapping beam shapers (Laskin et al. (2016)). Due to previous experience in other experiments at QUANTOP, together with their availability and low losses, we decided to use a diffractive optical element (DOE) (see, for example, Pal et al. (2019); Katz

et al. (2018); Buske et al. (2022); Dickey and Holswade (2000)).

After these considerations, we implemented a tophat beam profile with a new generation of cells in mind. In the following, we will consider how a tophat beam can be experimentally implemented in our setup. This effort was performed together with Isaac Roca Caritg, who extensively presented the results and experimental challenges in Caritg (2022). We will summarize the findings here.

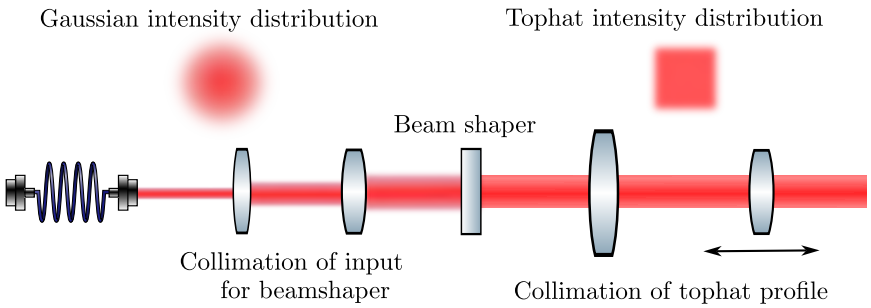

Figure 11.12: Tophat profile generation. We use a combination of two lenses to prepare a collimated beam of the desired waist (4 mm). This beam is incident on the beam shaper mounted on a 6-axis mount. We use a combination of two more lenses to collimate and size the beam to the desired waist. The last lens is mounted on a precision stage to optimize the collimation of the squared tophat beam profile.

Our experiment uses a *GTH-4-2.2* angular DOE manufactured by TOPAG lasertechnik. Angular means that the DOE has to be combined with a focusing lens to focus the desired tophat to a plane. The DOE exhibits a diffractive nanostructure, created through etching processes, that will generate a tophat beam when an appropriate input beam is provided. For our DOE, a waist diameter of $\omega = (4.00 \pm 0.15)$ mm and a divergence of less than 2.2 mrad is requried as input beam. We obtained the desired collimated Gaussian beam profile (Caritg, 2022) using a combination of three lenses after the fiber – one being the fiber coupler lens. Since the alignment of a beam shaper is very sensitive to angles of incidence and positioning, we placed the DOE on a 6-axis mount. The six degrees of freedom allow for rotation and translation of all three axes. The DOE must be combined with a collimation lens to obtain the tophat profile at an effective focal length (EFL) instead of an infinitely far-off plane. We use an achromatic doublet with a two-inch diameter and a focal length of $f = 100$ mm. In figure 11.13, we tested the alignment of the DOE for different tilting directions. We recorded the shape of the tophat profile with a simple camera at the focal plane.

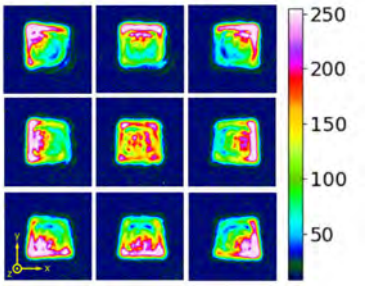

Figure 11.13: Influence of tilt on tophat intensity distribution. Effects of tilting the DOE with respect to the input beam. Pictures were recorded using a BFLY-BGE-12A2M-CS FLIR camera. The center picture corresponds to the proper alignment of DOE concerning the incident beam. All pictures are recorded at the effective focal length of the system. The waist of the tophat profile corresponds to 260 µm. Figure adapted from Caritg (2022).

We do not want a tophat profile in only one focal plane. Therefore we rely on a combination of lenses to collimate the beam and modify the waist diameter to the size. With a $3 \times 3\,\mathrm{mm}^2$ cross-section diameter, we aim for illuminating 2/3 of the channel. This is possible with a set of two lenses. Consider Caritg (2022) for a detailed approach. Using a precision translation stage, we varied the separation between the two lenses to find the best positioning al-

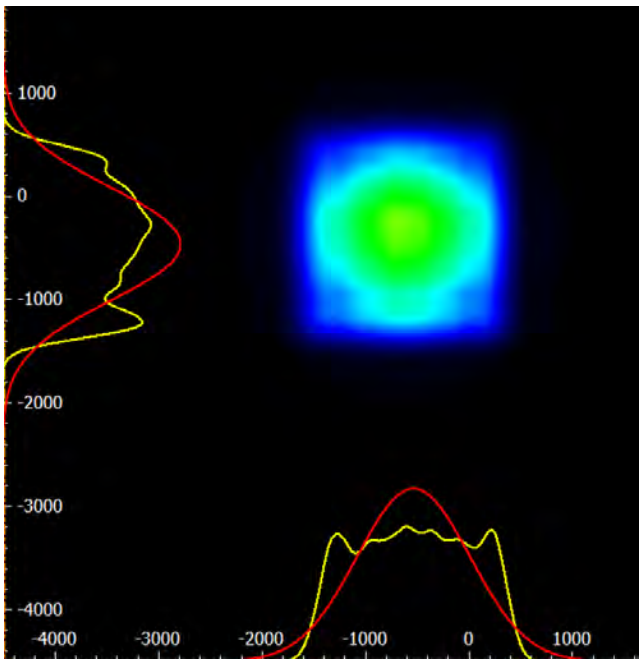

Figure 11.14: Beam profiler recording. Example recording of our efforts to collimate the tophat profile. The image is cropped and was recorded as bitmap data. Red and yellow lines indicate the intensity profile in x and y for a Gaussian and our observed profile, respectively.

lowing us to maintain a collimated beam for more than the required 80 mm. The combined set of lenses, including the beam shaper, is illustrated in figure 11.14.

For quantifying the beam profile along the light propagation direction, we used a scanning slit beam profiler from Thorlabs and placed it on top of a rail to move it with millimeter precision along the propagation direction. An exemplary recording is shown in figure 11.14. We see clearly a square shape. However, we are far from an optimal tophat profile. Compared to a Gaussian profile of the same waist, our observed beam profile exhibits sharper edges and a more homogeneous intensity distribution at the top. For the optimal position of the two lenses, we observe an overall waist diameter $\omega = (2.10 \pm 0.02)$ mm over a total length of 18 cm, which is more than twice of the length of the cells we have in mind. Further, the change in waist over those 18 cm corresponds to a very minor divergence of only $\theta = 0.24$ mrad. While this is not a perfect tophat profile, the observed beam shape should still benefit our goal of forming a Gaussian intensity profile towards a more homogeneous intensity distribution for application in the DLCZ-type experiment. The obtained profile should improve with more thorough alignment and further optimization of the input beam of the DOE, along with the lens positions, for collimating the tophat profile.

While we have – more or less successfully – implemented a collimated

tophat beam profile at the desired waist diameter, lack of time has prevented us from investigating the back conversion to a Gaussian beam profile or the implementation together with testing the spin noise of a vapor cell. While the latter is more of a simple time issue, the back conversion with high efficiency is one of the leading technical challenges if we want to implement a tophat profile together with single-photon detection. A low conversion efficiency would lead to additional losses and lower detection efficiency. Too many of these would render the improvement from removing the cell cavity in terms of detection efficiency void.

Modeling, calculating, and propagating a beam's amplitude and phase information is complex. The complexity of the task is why designing and manufacturing optics shaping a beam over an extensive length is tedious. The long-term future of our DLCZ-type experiment with a tophat beam profile will rely on efficient back conversion to a Gaussian beam. The back conversion to a Gaussian profile ensures compatibility with our filter cavities and fiber-coupled single-photon detectors (section 9.4.3). While we inquired with multiple companies about the possibility that they provide us with a custom DOE capable of the back conversion, this is a rather costly and non-trivial task. However, recently Buske et al. (2022) proposed neural network-assisted design of DOEs. This proposal could aid the availability of non-standard solutions such as ours for the back conversion of a tophat to a Gaussian beam profile in the future.

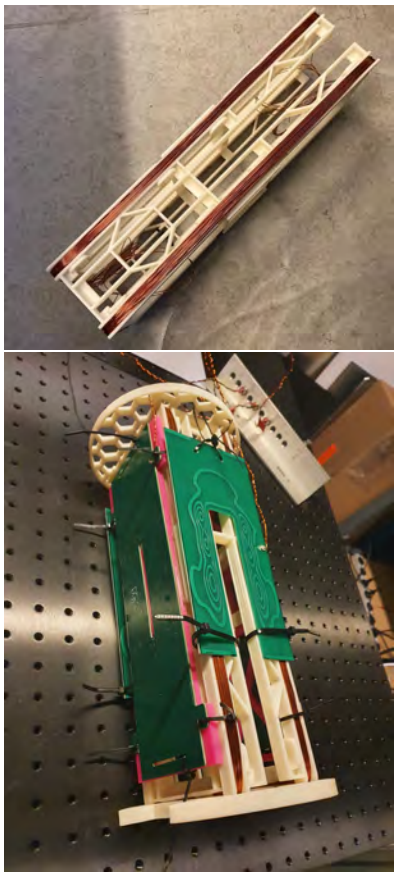

Figure 11.15: Coil frame for large cells Top: Rectangular coil wound on 3D-printed coil frame. Bottom: Attached are PCB coils as main and RF coil pairs.

11.3.5 Testing larger cells

As part of the considerations presented throughout this chapter, a subset of the cells manufactured as part of Generation O were designed with the desired dimensions. An overview of the characteristics is in a table in A.1, while the testing methods can be found in chapter 7. While we did not get all our desired cell geometries, we received cells with a round (4 mm diameter) and a square (3 mm diameter) channel.

Due to the sheer length of the cell (80 mm), we could not use the magnetic field configuration as discussed in section 9.1.1. In order to allow for a homogeneous field covering the whole extent of the cell channel, the magnetic shield had to be rotated. In contrast, the orientations of the bias magnetic field, RF field, and probing direction remained the same with respect to each other. Fortunately, previous work related to similarly-sized cells in one of the other experiments at QUANTOP allowed us to implement such a magnetic field relatively quickly instead of designing it ourselves. From a previous master thesis by Ryan Yde (Yde (2020)), PCB-based coils for generating a bias magnetic field and a transverse RF field had been designed. Further, a co-worker, Sergey Fedorov, had thought of large rectangular coils to act as a type of compensation coil for the bias magnetic field and had designed a 3D-printable coil frame where we can attach the two PCB coil pairs along with the rectangular coils. We wound the rectangular coils ourselves and attached the PCB coils to

the frame. The coil frame with the different coil pairs is illustrated in figure 11.15. Exploiting the method of a colinear MORS together with a small vapor cell of size 5 mm × 5 mm × 5 mm we optimized the current ratio between the two coil frame to obtain the best magnetic field homogeneity. When recording the Larmor frequency for different cell positions, we get a magnetic field profile since different magnetic field strengths will shift the observed Larmor frequency. We obtain the magnetic field profile by moving the cell in steps of 5 mm transverse to the bias magnetic field direction. First, we use this to find the best placement of the coils on the frame. Afterward, we optimize the current ratio between the rectangular and PCB coils for the best possible magnetic field homogeneity. A thorough description of the measurement technique and the results is presented in the appendix B since it is an integral approach for many of our experiments and a valuable tool for new students.

After optimizing the position of the coils and the current ratio, the best relative standard deviation of the magnetic field homogeneity over 10 cm is as low as $\sigma_{\text{rel}} = 1.3 \cdot 10^{-4}$. We deemed this homogeneity sufficient for performing the spin noise measurement with a cell of 80 mm channel length.

We started with a Gaussian beam profile for testing the larger cells with the spin noise measurement. Initially, we wanted to compare the two intensity profiles and verify the improvement using a tophat intensity distribution to the observed broadband contribution. However, time limitations prevented us from experimenting with the tophat beam profile. Further, initial tests using a Gaussian beam at room-temperature made it impossible for us to resolve any broadband contribution in the spectrum. We needed to implement some heating of the cell, allowing us to reach 40 °C to resolve any broadband noise in the spin noise spectrum.

For the final measurements of the spin noise using the larger vapor cells and elevated temperatures, I was joined by a project student, Veronika Kaminski (formerly Raschendorfer), who reported some of the findings in the respective project report (Raschendorfer, 2022). We chose a waist diameter of 2 mm for the Gaussian beam to match the width of our desired tophat profile. We then performed the spin noise measurement versus the applied probing power. The individual level of broadband noise is shown in figure 11.16. The overall level is smaller since we did not have more optical power available to compensate for the larger area illuminated by the beam. We note that the broadband noise level is only a very minor contribution to our overall signal compared to the shot noise level.

Further, we also determined the narrowband contribution to the spectrum for each of the two cell geometries used for testing, the round channel with 4 mm diameter (cell O17) and the square channel with 3 mm diameter (cell O19). The individual results and the fit based on the model previously introduced in section 11.3.1 are shown in figure 11.17. Due to the limitation in optical power, these measurements are not covering the entire range we are interested in and are only preliminary results. Due to the different interaction volumes but the same beam profiles, we observe a steeper incline for the

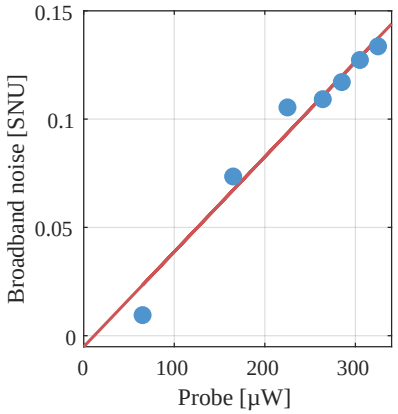

Figure 11.16: Broadband noise versus probe power. Measurement of broadband noise for cell O17 with 4 mm diameter and round channel cross-section.

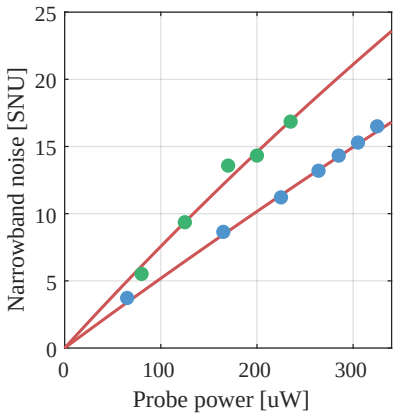

Figure 11.17: Narrowband noise versus probe power. Measurement of narrowband contribution for cell O17 with 4 mm round channel (blue) and cell O19 with 3 mm square channel (green), together with the respective fits of type $f(x) = a \cdot x/(b + x)$.

cell with a smaller channel and higher filling factor. We need more optical power for a more reliable measurement available for the cells. Additionally, we would need to adjust or even vary the beam diameters to thoroughly test and compare different cell geometries.

11.4 Summary

Throughout this chapter, we have discussed many possible improvements we have been considering following the results presented in Dideriksen et al. (2021) and have been the central results of the DLCZ-type experiment in chapter 10. Additionally, we have presented some steps to implement our ideas and proposals to remedy some of the current experimental issues.

We are limited in our experimental performance due to our low retrieval efficiency. A significant part arises from placing the vapor cell inside a low finesse cavity, which has only a limited outcoupling efficiency compromising our attainable detection efficiency of scattered photons. To investigate how much our light-atom interaction benefits from this cell cavity, we investigated the cavity enhancement for the write and read step. For experimental simplicity, we combined this with investigating the feasibility of spin noise and homodyne-readout measurements as somewhat classical measurement techniques not relying on single-photon detection. While we were limited due to somewhat sub-optimal conditions for these measurements, we stress that they are both useful tools, and the results should still be considered successful. We believe we could even start investigating expected retrieval efficiencies by properly calibrating the RF field for the homodyne readout measurement. We could observe the expected behavior and discriminate between different cell geometries when testing the spin noise measurement with larger vapor cells but different channel geometries. This is clearly in favor of using this technique as a tool before going full-on DLCZ scheme and the trouble arising from the drive light suppression coming with it. We also take it as a success that we could estimate the cavity enhancement for write and read step using these measurement techniques.

As part of this chapter, we have also addressed the issues and differences between improving solely on the memory time and how to, in addition, improve on the time-bandwidth product by speeding up the motional averaging of the light-atom interaction. We have considered increasing the transverse cell channel to enable longer transverse spin coherence times. This time fundamentally limits the memory time of our on-demand single-photon source. At the same time, memory time alone will only improve our scheme's performance significantly if we improve the relative speed as well. This means we need to improve on the time it takes for sufficient motional averaging. We have discussed that there are better options than increasing the Gaussian beam waist, as the increasing clipping losses will pose a problem. Introducing super-Gaussian or flat tophat intensity profiles could be the answer to our prayers. As part of this project, we decided to use a DOE to shape the beam

profile into a flat tophat profile. While we have obtained the profile and managed to collimate it, a lack of time resources prevented us from combining this with a spin noise measurement. Another important consideration for the future is how to implement efficient back-conversion of the tophat profile to a Gaussian profile to ensure the detection of the scattered photons using our fiber-coupled SNSPDs with high efficiency.

This chapter concludes all our efforts regarding the DLCZ-type experiment for implementing a deterministic single-photon source with built-in memory. We take it as a huge success that we could observe a conditional auto-correlation significantly below that of a two-photon Fock state auto-correlation function. We have identified how to potentially upscale our scheme's performance, especially in regard to memory capability, an essential step towards realizing networks for long-distance entanglement generation as proposed by the DLCZ protocol.

Part IV

Quantum-enhanced MIT

Chapter 12

Atomic ensembles for magnetic induction tomography

Magnetic induction tomography (MIT) is a non-invasive method to determine and image the electromagnetic properties of an object. It reveals material discontinuities and compositions without destroying the object of interest. This non-invasiveness makes MIT a sensing protocol with various applications ranging from usage in industrial material testing to geophysics and even biomedical applications.

MIT's traditional and fundamental working principle is the detection of eddy currents. The working principle relies on two coils that are moved past the sample of interest. The measurement configuration is illustrated in figure 12.1. One of the coils is driven with an RF current to generate an oscillating magnetic field, often referred to as the primary field. This primary field induces eddy currents in the conductive object. In return, the current loops induced in the sample generate a smaller, secondary field, oriented anti-parallel to the primary field. The secondary field from the eddy currents can then be recorded as the induction signal of the second coil, also referred to as the receiver or pick-up coil. Due to the eddy currents depending on the three passive electromagnetic properties permeability, conductivity, and permittivity (Griffiths (2001)), this non-invasive technique of MIT is a straightforward tool to investigate material properties.

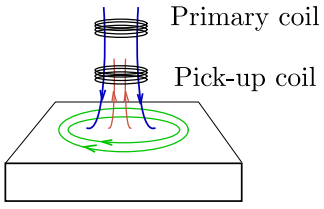

Figure 12.1: Illustration two coil MIT Graphic illustration of MIT measurement principle using two coils. The primary coil generates RF magnetic field (blue), inducing eddy currents in the objects (green). These eddy currents induce a secondary field (red) that is detected using the pick-up coil.

Atomic magnetometers exploit atomic spins to detect magnetic fields or their changes. The readout can be done optically, allowing for a comparatively simple experimental operation. Atomic magnetometers have been implemented in various forms. Ultracold and cold atoms have been one system of interest. These avoid issues arising from the thermal motion of the atoms and the finite spatial resolution due to the ensemble interaction volume. The suppression of atomic motion comes at the expense of additional experimental complexity due to the cooling of the atoms. Experimental implementations include spatially-selective magnetometry using ultracold atomic clouds in Elíasson et al. (2019), cold atoms in Cohen et al. (2019), and using a one-dimensional Bose-Einstein condensate in Wildermuth et al. (2006). At the ex-

pense of being subjected to atomic diffusion but benefiting from the lack of need for a sophisticated cooling apparatus for the atoms, warm atomic ensembles have been pursued as well. For example, their high sensitivity while operating at room-temperature was used for magnetocardiography (Jensen et al. (2018); Bison et al. (2009)). One specific application of such an atomic magnetometer is the use of the atomic ensemble for MIT measurements, where the atomic ensemble replaces the pick-up coil. Atomic magnetometers are of particular interest for frequencies below 50 MHz, as it has been shown that they intrinsically outperform the classical magnetometer with a pick-up coil of comparable size in Savukov et al. (2007). MIT measurements using rubidium atoms have been presented, for example, in Wickenbrock et al. (2014), Wickenbrock et al. (2016) and Deans et al. (2016), while for cesium Jensen et al. (2019) performed eddy current detection of low conductivity saltwater phantoms. The sensitivities attainable with atomic magnetometers for magnetic induction tomography have sparked interest in using them to image body tissue passively. For example, in Marmugi and Renzoni (2016), atomic MIT is proposed to map heart tissue.

The most advanced magnetometer from a commercial point of view, but also in terms of sensitivity, is the SQUID magnetometer - superconducting quantum interference devices (Degen et al. (2017)). As the name suggests, their working principle relies on superconductivity, requiring cryogenic temperatures for their operation. Given the experimental and operational complexity arising from cryogenic cooling, their application for material testing and imaging is rather costly. While their high sensitivity has driven SQUIDs to be the most advanced magnetometers, atomic magnetometers have been shown to approach the same level of sensitivity (Dang et al. (2010)). The progress made with atomic magnetometers makes them suitable for many applications. Due to their experimental simplicity and performance, large-scale application and production upscaling are within reach.

Advances and efforts in atomic magnetometry have also driven the evolution of the vapor cells, leading to miniaturization of the cells used, reducing their volume to a few cubic millimeters (Shah et al. (2007); Jensen et al. (2018)). The applications and operational regimes of atomic magnetometers are varied, ranging from DC magnetometer (Detlefsen (2021)) to applications aimed at operating at high magnetic field strength (Stærkind et al. (2022)). Here, in the frame of this thesis, we are mainly interested in how our atomic magnetometer can be operated as a type of RF magnetometer used for magnetic induction tomography combined with exploiting quantum mechanical effects – a quantum-enhanced magnetic induction tomography (QMIT). The goal is to achieve a quantum noise-limited sensor in a proof-of-principle experiment achieving an eddy current sensitivity exceeding the standard quantum limit for a continuously operating atomic magnetometer by exploiting spin-squeezing and back-action evasion.

In the following chapters, we will introduce the experimental details and results of our quantum-enhanced magnetic induction tomography experiment.

We exploit stroboscopic back-action evasion and conditional spin-squeezing of our atomic ensemble to achieve quantum enhancement. We will elaborate on the efforts and results that went into our experiment presented in our manuscript titled "*Entanglement-enhanced magnetic induction tomography*" (Zheng et al. (2022)), submitted for publication at the time of this thesis. Due to the close collaboration, the results presented here were obtained as a group effort with **Wenqiang Zheng** and **Hengyan Wang**. Also, the former master student **Alan Oesterle** helped build the experimental setup and presented a subset of results already in his master thesis (Oesterle (2022)).

Chapter 13

Experimental setup

This chapter will discuss the experimental specifics of the quantum-enhanced magnetic induction tomography (QMIT) experiment. Many techniques used to characterize vapor cells were already described in chapter 7. Here, we will address experimental subtleties that differ in the characterization used for this setup. The first two sections, section 13.1 and section 13.2, will cover the magnetic shield and vapor cell details. More importantly, we will introduce in this chapter the experimental setup and its control (section 13.3). There, we will present the outline of the physical experimental setup and discuss our choices in design and technical limitations arising from that. We present the setup used for the data acquisition used to acquire the data presented in the manuscript Zheng et al. (2022).

This chapter focuses mainly on the design and specifics of the setup rather than the physics and execution of experiments. The execution and optimization will then be covered in chapter 14 and chapter 15.

13.1 Magnetic field and shielding

For the QMIT experimental setup, we use a cylindrical magnetic shield consisting of multiple layers[1]. A frontal view of the shield without end caps is shown in figure 13.1, indicating the order of the layers. The outermost layer is made of iron. While this might initially seem counter-intuitive, the reasoning to use iron as part of the magnetic shield originates from the fact that it saturates at higher field strengths, acting in our case just as an initial "block" for strong fields. The inner layers are made of mu-metal and aluminum. Mu-metal has a very high magnetic permeability. This property allows magnetic fields to be guided along it rather than blocking them by providing a path of least resistance. A mu-metal layer, in a sense, "moves" or guides the magnetic field lines around the shield's center, removing stray magnetic fields at its center where the cell is placed. As mu-metal saturates more easily, multiple layers are used to reduce the strength of residual fields consecutively. The aluminum shield is employed to shield our vapor cell from external RF magnetic fields,

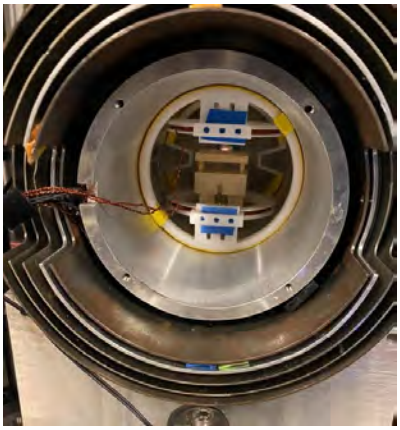

Figure 13.1: Photo magnetic shield layers. Magnetic shield showing all layers, with custom 3D printed RF coil and cell holder.

[1] Internally, this shield was formerly known as the "Test-setup shield".

as these compromise our signals as we rely on controlled RF signals for our measurements.

For this specific shield, we have two aluminum layers in the shield. The first aluminum layer is located between the second and third innermost mu-metal layer. The second, thicker aluminum layer forms our shield's innermost layer. The coil system that generates the homogeneous bias field is placed around the innermost aluminum layer. End caps can be attached to the ends of the cylinder to complete the magnetic shield. The shield has six holes centered on each axis of the shield, allowing access to the vapor cell with optical pumping and probing beams.

The bias magnetic field is generated using multiple sets of coils to improve the homogeneity over the spatial extent of the vapor cell. Here, we use a combination of *primary coils*, *saddle coils*, and *compensation coils*. The primary coils consist of three coil pairs (Figure 13.2). Since the cell channel is transverse to the bias field direction, the homogeneity of the primary coils is insufficient. Therefore, saddle coils are added to allow a radial gradient to improve the homogeneity along the cell channel. Further improvement of the magnetic field homogeneity can be obtained using an additional coil pair to further compensate for the magnetic field profile. The compensation coils are not included in figure 13.2. In order to find the optimal current ratio, a small cell is moved along the probe direction, mapping the field homogeneity of each coil configuration individually. The optimal ratio of the fields is found by minimizing the standard deviation of the magnetic field homogeneity. Appendix B presents this technique for optimizing the magnetic field homogeneity. However, it is presented for a different coil system. The optimization of the bias field for the coil frame used here can be found in Oesterle (2022). Experimental verification using the optimal ratio leads to a magnetic field homogeneity along the z-direction with only 0.3 ‰ relative standard deviation over 4 cm for field strengths ranging from 100 kHz to 1.5 MHz[2]. However, due to other experimental limitations discussed in subsection 13.3.1, a bias field allowing for $\nu_L = 725$ kHz Larmor splitting is sufficient for now.

Figure 13.2: Photo coil frame on the aluminum cylinder. Coil frame showing main and saddle coils. Compensation coils are not shown since they were added only after taking this picture. The small twisted wire is the heating wire.

Using additional coils that allow correcting for small tilts in y- and z-direction can allow for adjusting the magnetic field orientation and optical pumping direction. We optimize the magnetic fields to obtain a narrow linewidth in the pMORS spectrum, as a more narrow linewidth coincides with longer coherence times.

Figure 13.2 shows a tiny twisted wire. The twisted wire is a heating wire. It allows us to heat the vapor cell to 55 °C. Heating is necessary as the coils' heat dissipation alone is insufficient for high enough optical depth in the experiment. Twisting and locating the heating wire outside the aluminum layer should ensure that the currents flowing through the resistance wire cancel to a large extent and are shielded from the cell to avoid disturbances from the currents.

For determining the atomic polarization after optical pumping via pMORS or performing the MIT experiment, we need to drive radio-frequency (RF) os-

[2] An even more radical approach is changing the orientation of cell and magnetic field, which has initially been investigated using PCB coils in Yde (2020). This was done with high homogeneity over 10 cm with low Larmor frequencies in mind. However, they have also been proven suitable at high Larmor frequency when combined with a suitable wounded rectangular coil pair. This change in geometry would require substantial changes in the setup geometry. Therefore it was not implemented (yet).

cillations between the Zeeman levels. Therefore, an RF coil pair is necessary. In figure 13.1, they are visible as part of the 3D-printed cell holder. The coils have a radius of 40 mm, with ten windings each. They are close to being in a Helmholtz configuration, with a 48 mm separation between them. The RF field strength can be calibrated using a simple pick-up coil. Details on the calibration can be found in the appendix of Oesterle (2022). We have two options for connecting the RF coils, depending on which experimental technique we intend to perform. For pMORS, the coils are connected in parallel to have a mean field at the cell. For the quantum-enhanced MIT, we connect them anti-parallel to obtain a zero mean field at the cell without a conductive sample. Only in the presence of a conductive sample, the induced eddy currents will alter the mean RF field seen by the atomic spin-oscillator. Recording and detecting eddy currents with the anti-Helmholtz configuration of the RF coils will be discussed in chapter 15.

13.2 Cell J21

Vapor cells are the shared vital component for the experiments presented in this thesis. The common properties and manufacturing of vapor cells have already been described in chapter 7. Therefore, we will skip a thorough general description here and focus on the relevant experimental specifics of the cell used for the QMIT experiment[3].

The QMIT vapor cell is of encapsulated chip design (see chapter 7) and is internally known as cell J21. The side and frontal view of the cell are presented in figure 13.3. The channel inside the glass chip has a volume of $500\,\mu m \times 500\,\mu m \times 25\,mm$. The anti-relaxation coating is a C30-type[4], which allows operation of the experiment at an elevated temperature of approximately 55 °C. The cell's temperature can be monitored using a thermistor placed inside the shield close to the cell.

Figure 13.3: Cell J21. Side (top) and frontal (bottom) view of cell J21 used for QMIT experiment. The encapsulated chip with the channel is visible inside the glass cell body.

The same method described in 7.3 is used to determine the number of atoms here. However, the measurement itself is performed in the setup of the QMIT experiment, as well as with a different asymmetric MZI. Figure 13.5 depicts the fitted absorption spectrum (see section 7.3 for the model) and the residuals between the fit and normalized signal. While the fit reproduces the signal fairly nicely, we observe some high-frequency noise on our signal. Uncorrelated, high-frequency noise could be removed by averaging the signal when repeating the measurement. We can also see that the outermost parts of the wings are not fully recovered with the fit, indicating that we might have additional broadening effects or the like not included in the model. Alternatively, the measurement could be repeated with an even lower probe power to avoid broadening effects further. Nevertheless, the overall fit is reasonable enough to estimate the number of atoms order of magnitude-wise.

From the fit, and considering a temperature error of 1 °C, we obtain for the atomic density ρ and respective number of atoms N_{Atom} within the interaction

[3] The experimental details and techniques used for cell characterization can be found in chapter 7, discussed for a variety of cells.

[4] See section 7.1.1 for specifics about this type of coating.

volume to be the following at 55 °C:

$$\rho = (2.41 \pm 0.02) \cdot 10^{17} \, \frac{1}{\mathrm{m}^3} \tag{13.1}$$

$$N_{\mathrm{Atom}} = (1.51 \pm 0.01) \cdot 10^{9} \tag{13.2}$$

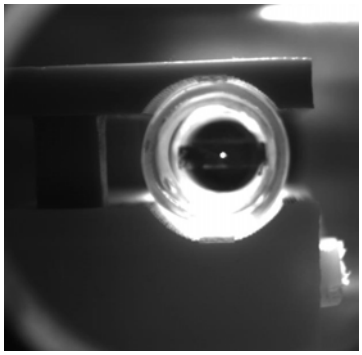

Figure 13.4: Probe alignment cell J21. Picture of the aligned cell J21 inside the magnetic shield, verified by observing the beam transmission through the channel using an attenuated light beam and a camera. We use a flashlight from the top of the shield to enhance the visibility of the vapor cell parts.

From the density ρ and the length of the cell $L_z = 25\,\mathrm{mm}$, we can determine the optical depth using equation (9.1) together with the wavelength of the D_2 line. Considering all atoms in the coherent spin state, the optical depth is estimated to be $d \approx 690$.

The standard transmission observed for this cell is only around 91 %, which might make it seem counter-intuitive to use an old cell when we had new cells of the same dimensions availableAs apparent from table A.1, the observed T_1 times for cells of Generation O are significantly worse than the one for J21. Additional tests[5] including repeated recuring and tests at elevated temperatures, did not improve their performance to reach the performance of cell J21. Recuring cells is a technique to recover cell performance if coherence times or transmission has dropped for unknown reasons. A short description of the newest approach to recuring vapor cells can be found in appendix A.1. It is hard to pinpoint the exact reason for their worse behavior. It is most likely related to the manufacturing process generating natural variation in the performance, either by worse glass blowing, different coating composition, or other causes. Therefore, we did continue with vapor cell J21 instead of using one of the newly fabricated vapor cells.

13.3 Experimental setup and control

The following section will describe the experimental setup and control used for the QMIT experiment. The experimental setup description has been clustered into five building blocks to guide the reader's understanding. The parts are described after each other and are shown as differently colored tiles in figure 13.6. All relevant optical paths for the experiment are indicated. The heart of the experiment is the cell and shield, which have already been described in detail in the previous sections 13.1 and 13.2. The remaining building blocks of our experimental setup are the optical pumping, indicated in orange and addressed in section 13.3.2. The probing is shown in blue and is covered in section 13.3.1. The specifics of our detection will be discussed in section 13.3.3. The polarization homodyne detection is marked green in figure 13.6. As precise experimental sequence control and data acquisition are essential, this will be the topic of section 13.3.4. Sequence control and data acquisition are illustrated in a purple rectangle in figure 13.6.

13.3.1 Stroboscopic probing pulses

[5] For the sake of brevity, not presented here or in chapter 7 about cell testing.

Essential for our approach towards a quantum-enhanced MIT sensor is the back-action evasion. To reduce the back-action introduced in our measure-

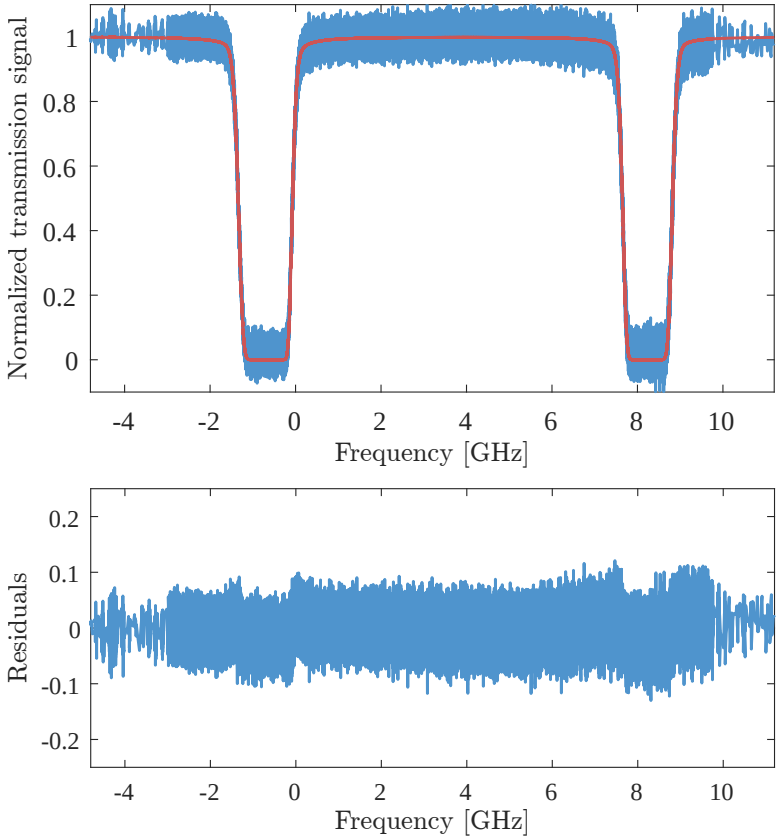

Figure 13.5: Atomic absorption spectrum for J21 at 55 °C**.** Top: Fit (red) and normalized transmission spectrum (blue) with absorption dips for cell J21 at 55 °C using the model presented in chapter 7.3. Bottom: Residuals obtained by subtracting fit from the signal.

ment, we require stroboscopic probe pulses at twice the Larmor frequency with a small duty cycle D to allow for a QND-type interaction (see chapter 3). The origin of this stroboscopic approach can be found, for example, in Braginskii et al. (1978), Caves et al. (1980), and Braginsky et al. (1980). Optimally, the pulse should be infinitely short, in a sense like a "δ-pulse"[6] Only for $D \to 0$ a QND-type interaction will be realized. For finite duty cycle D, the back-action noise will at least be reduced compared to a continuous measurement with $D = 1$.

We use a commercially available AOM and function generator, indicated in the blue tile in figure 13.6, to control the stroboscopic probing pulses. The experimental control ensuring precise timings of the generated pulses will be covered in section 13.3.4. The rise time of the AOM is limited by the speed of the sound wave inside its crystal, combined with the spot size of the probe laser. This manifests in a finite rise time of the probe pulses on the order of 50 ns. Due to the switching speed and shape of the probe pulses, we found that we cannot exceed Larmor frequencies of approximately $\nu_L = 725$ kHz

[6] This is, of course, a simplification based on equation (3.29). The dynamics will get more complicated for very short pulses, and our model will break down as we introduce many (undesired) frequency components to our system.

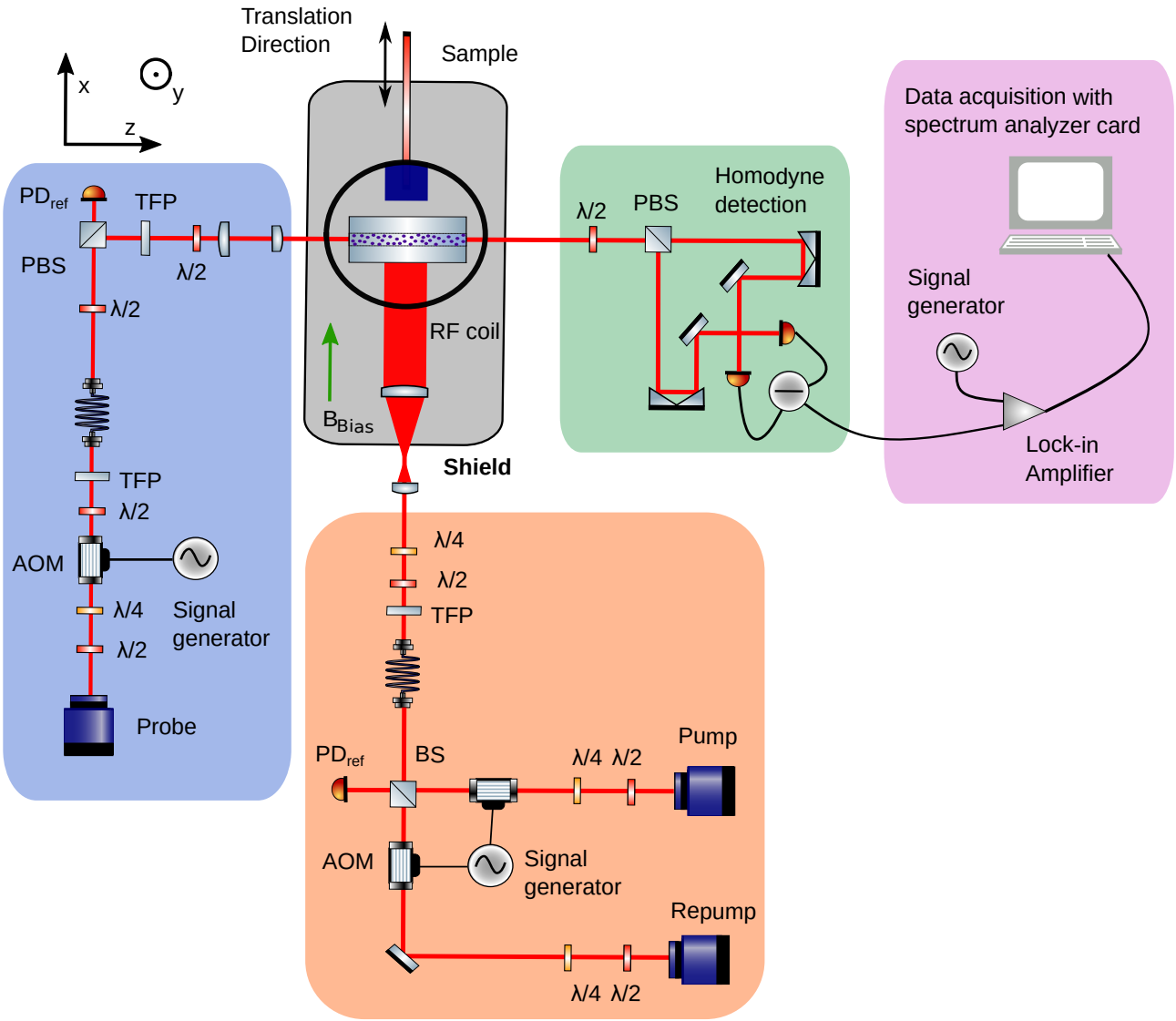

Figure 13.6: Simplified setup for QMIT experiment. Experimental setup containing all relevant optical paths. (P)BS indicates a (polarizing) beamsplitter, AOM indicates an acousto-optic modulator, and $\lambda/2$ and $\lambda/4$ represent half- and quarter-wave plates, respectively. Thin-film polarizers are indicated as TFP. Optical pumping and probe beam paths each have a reference detector, indicated by $\mathrm{PD}_{\mathrm{ref}}$. The colored areas are to distinguish parts of the setup relevant for the optical pumping (orange), probing (blue), polarization homodyne detection (green), and data acquisition and sequence control (purple). This figure is based on the experimental setup presented in the supplements of Zheng et al. (2022) but has been modified to aid the reader better.

with stroboscopic probing and reasonably low duty cycles. For this setting, we can send the stroboscopic probe pulses with a duty cycle as low as $D = 15\,\%$. Experimentally, this setting corresponds to a probe pulse width of approximately 100 ns per stroboscopic pulse. We verify the influence of different duty cycles on the back-action noise added to our system in section 14.3.

13.3.2 Optical pumping

For quantum-enhanced sensing, we want to be limited by quantum noise and minimize uncertainties in our measurement. Our spin-oscillator's intrinsic quantum noise is the spin state's projection noise. The projection noise is minimal for the coherent spin state (CSS). Therefore we exploit optical pumping to prepare the atoms in this desired coherent spin state or at least try to prepare our atomic ensemble as close as possible with perfect spin polarization. While we have already introduced the principle of optical pumping (section

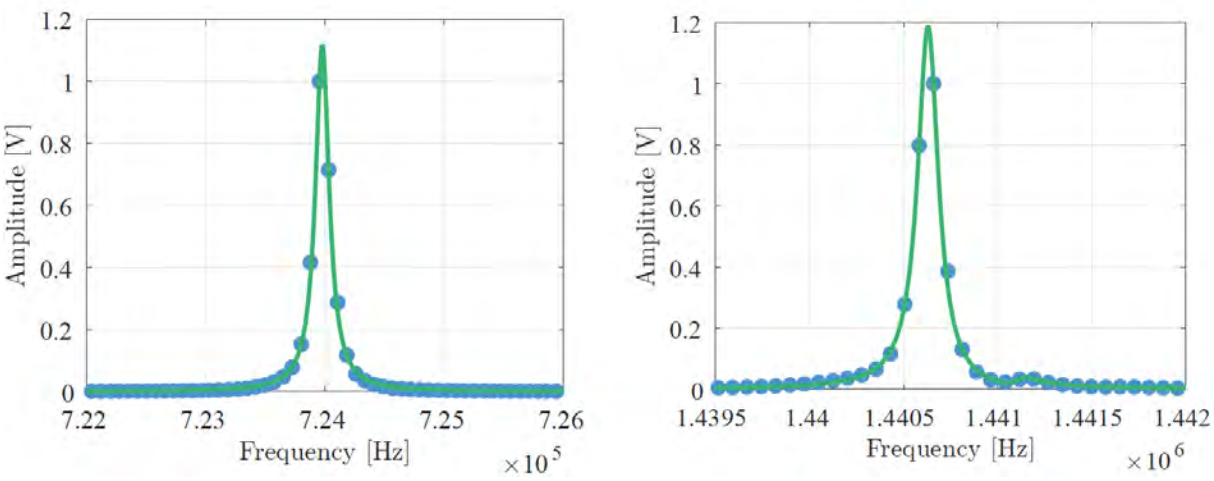

Figure 13.7: PMORS spectra. Left: Unresolved pMORS spectrum for 724 kHz. Right: Resolved pMORS spectrum for 1.44 MHz. Both spectra are shown with the respective fitting result. Figure adapted from Zheng et al. (2022).

5.2) for coherent spin state preparation and how we optimize it on the example of the DLCZ-type experiment (sections 6.2 and 9.1.2), there are some minor differences in the approach here. As indicated in the orange section marking the optical pumping in figure 13.6, the pump and repump laser are combined on a beamsplitter *before* they are sent through a fiber to the experimental setup. It comes with the advantage that only one optical beam path has to be aligned on the vapor cell, and no tedious overlapping of the two beams on the vapor cell is required. However, this experimental simplicity comes at the expense that we cannot control and optimize the circular polarizations of the two optical pumping beams individually[7]. Also, the pulse control is currently shared between the pump and repump laser, meaning that we cannot delay one with respect to the other. As we have seen in the discussion of CSS optimization for the DLCZ-type experiment (chapter 9), delaying the turn-off of the pump pulse can improve the attainable atomic polarization[8]. We mimic a smooth turn-off by low-pass filtering the square pulse sent to the AOMs controlling the pump and repump beams.

We quantify the atomic polarization through pMORS. The technique is presented in section 6.2. In the case here, a few differences should be noted. First, we quantify the atomic polarization after a gap of 220 µs[9]. Second, we

[7] While we use achromatic waveplates that should help with the wavelength dependency, we are still unable to reach the same polarization as in the DLCZ-type experiment (so far).

[8] Adjusting the sequence control in subsection 13.3.4 to allow for individual pump and repump control is not a fundamental problem. However, it requires setting up an additional control line, as separate AOMs already control the beams. However, it requires a lot of additional measurements and is a tedious process to optimize. Due to time constraints, it was not implemented yet.

[9] This particular choice is related to our optimization process. The time gap will become apparent in chapter 14.

have to increase the Larmor frequency to $\nu_L \approx 1.44\,\text{MHz}$ since we are unable to resolve the pMORS spectrum at our desired Larmor frequency due to the linewidth exceeding the quadratic splitting (left part in figure 13.7). Only with the increasing magnitude of the bias magnetic field can we resolve the pMORS spectrum (Right part in figure 13.7) and fit it more reliably to determine the atomic polarization. We infer the atomic polarization for our quantum-enhanced MIT at the lower Larmor frequency from the fit result of the resolved spectrum. Typically, we achieve for our settings an atomic polarization of 97.5 %.

As we have seen in chapter 6, optical pumping optimization is tedious. To further improve the CSS preparation, separate polarization control of the pump and repump could be achieved by combining the beams just before the cell. However, we would lose the advantage regarding the alignment. Also, from figure 13.7, we have a relatively low number of points for the spectrum. Improving the resolution of the spectrum by acquiring data for a longer time might make the fitting more reliable, and optimization might become more straightforward as changes are resolved better.

13.3.3 Signal detection

All optical measurements regarding the QMIT experiment are done using polarization homodyne detection. The detection part of the experimental setup is marked in green in figure 13.6. The combination of an HWP and a PBS allows us to record the $\hat{S}_y^{\text{out}}$ component of the light using a photodetector at each output port of the PBS. Subtracting the signals from each other, with the HWP oriented at $\pi/8$, corresponds to measuring the Stokes component $\langle \hat{S}_y \rangle$ (Hammerer et al., 2010).

All our desired signals are encoded in a sideband centered around the Larmor frequency[10] ν_L with respect to the carrier frequency determined by the probe light frequency ν_0 (Hammerer et al. (2010), Krauter (2011)). The balanced photo detector signal is modulated with a reference signal oscillating at the Larmor frequency. We optimize the relative phases of the signals used for lock-in detection to maximize our recorded signals. Further, the sinusoidal reference signal for the lock-in amplifier (LIA) has to match the Larmor frequency, which we generate using a simple function generator (RIGOL DG1032). The modulation of the recorded balanced photo detector signal with the reference signal leads to frequency components at twice the Larmor frequency and the difference between the two signals (DC signal). The LIA internally low-passes the signal, such that the output signal of the lock-in amplifier is close to DC. We effectively only obtain the detector response centered around our frequency of interest – the Larmor frequency ν_L. In principle, the lock-in amplifier provides us with two outputs, the demodulated sine and cosine components of the recorded balanced photo detector at the Larmor fre-

[10] While we are careful throughout this thesis to always state in the expressions whether we refer to ν_L or ω_L, the unfamiliar reader is advised to consider Julsgaard (2003) to get a more thorough understanding about when and why to use ω_L and ν_L, respectively.

quency integrated over an entire period (Hammerer et al., 2010):

$$\hat{S}_y^{\text{out},c} = \sqrt{\frac{2}{T}} \int_0^T \mathrm{d}t \hat{S}_y^{\text{out}}(t) \cos\left(2\pi\nu_{\text{L}} t\right) \tag{13.3a}$$

$$\hat{S}_y^{\text{out},s} = \sqrt{\frac{2}{T}} \int_0^T \mathrm{d}t \hat{S}_y^{\text{out}}(t) \sin\left(2\pi\nu_{\text{L}} t\right) \tag{13.3b}$$

For our purpose, it is sufficient only to record the cosine component $\hat{S}_y^{\text{out},c}$. The same method is exploited to record the noise contributions arising from the imprecision shot noise of light and the thermal atomic noise, which form the basis of our analysis later and is discussed further in chapter 14. We identify that we can recover the expressions presented in the theory part of the thesis with appropriate normalization in equation (13.3).

When subtracting the two signals, we have observed that even tiny path length differences or delays between the two signals can tremendously impact the balancing of our combined detector signal. To remedy any response mismatch in time, either by the two detectors responding not at the same time or actual path length mismatch, we ultimately settled on using square retro-reflecting hollow roof prism mirrors ("cat-eyes") together with precision x, y-stages[11]. These allow us to move each cat-eye parallel to the optical table with sub-mm precision. Therefore, we can correct for slight changes in the path or response time differences. We added these in both paths to maintain the same number of beam reflections. Through this, we could better match the two detector responses by reducing the overshooting of our balanced signals for the stroboscopic pulse edges in the time trace.

13.3.4 Sequence control & data acquisition

Unlike the DLCZ-type experiment, where a single FPGA ultimately controlled the whole experiment, data acquisition, and experimental pulse control are two different devices for the QMIT experiment. However, they are closely connected since precise experimental timings and triggering of the data acquisition are required.

Sequence control

Experimental timings with sub-microsecond precision are essential when dealing with stroboscopic pulses and phase-sensitive signals detected in the low megahertz range. Therefore, we use a *Quantum Composer 9518 plus* to control the electronic trigger and pulse generation with very high precision to an absolute reference. It allows the definition of up to eight independent pulses that can be conditioned on each other. In our case, we define one fundamental trigger reference that sets the maximal duration of our experimental sequence to 24 milliseconds. This absolute reference has to exceed our experimental pulse sequence to ensure that the experimental timings fit within the reference to avoid overlapping pulses from consecutive measurements. Ultimately, our experimental sequence is optimized to allow for sufficient optical

[11] Please note that x, y is not referring to our choice of the coordinate system here and instead to the common convention of x, y forming a horizontal plane.

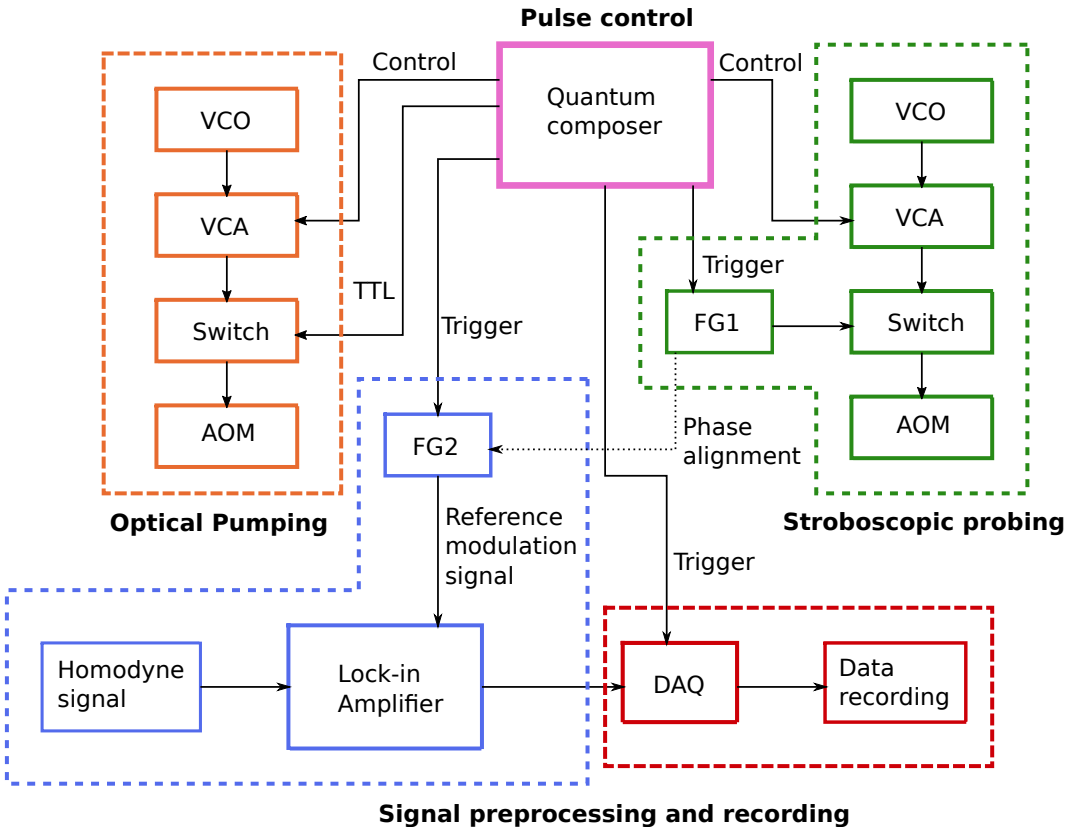

Figure 13.8: Diagram of pulse and acquisition control. The Quantum composer allows defining pulses to an absolute timing reference and between different pulses. The orange parts refer to the optical pumping (exists twice in the experimental setup), and the green parts illustrate the control for stroboscopic probe pulses generated using function generate FG1. Blue parts refer to the lock-in detection of our experiment. The reference modulation signal is a sinusoidal signal generated with the function generator FG2, and the phase is optimized that the signal amplitude overlaps with the stroboscopic pulses. The acquisition and recording using a spectrum analyzer card (DAQ) are indicated in red. For simplicity, additional control for the optional delay and RF pulse generation is not shown. The abbreviations in the figure are VCO: voltage-controlled oscillator, VCA: voltage-controlled attenuator, AOM: acousto-optical modulator, and TTL: transistor-transistor-logic trigger line. We labeled the lines of the Quantum Composer to match the labels of the control, TTL, and trigger ports of VCA, Switch, and function generators, respectively. They can all be understood as trigger signals nonetheless.

pumping and measurement time. We derive all relevant other pulses from this main trigger by defining our desired pulses using absolute delays from the fundamental reference. An illustration of the electronic control for the spin-squeezing experiment presented in chapter 14 is shown in figure 13.8. When performing the quantum-enhanced MIT, the control has to be extended with two additional control lines. A sequence of the trigger signals is illustrated in figure 13.9. First, the signal for the optical pumping is derived, and we set a pulse width of 12 ms exceeding the T_2 time of the vapor cell multi-

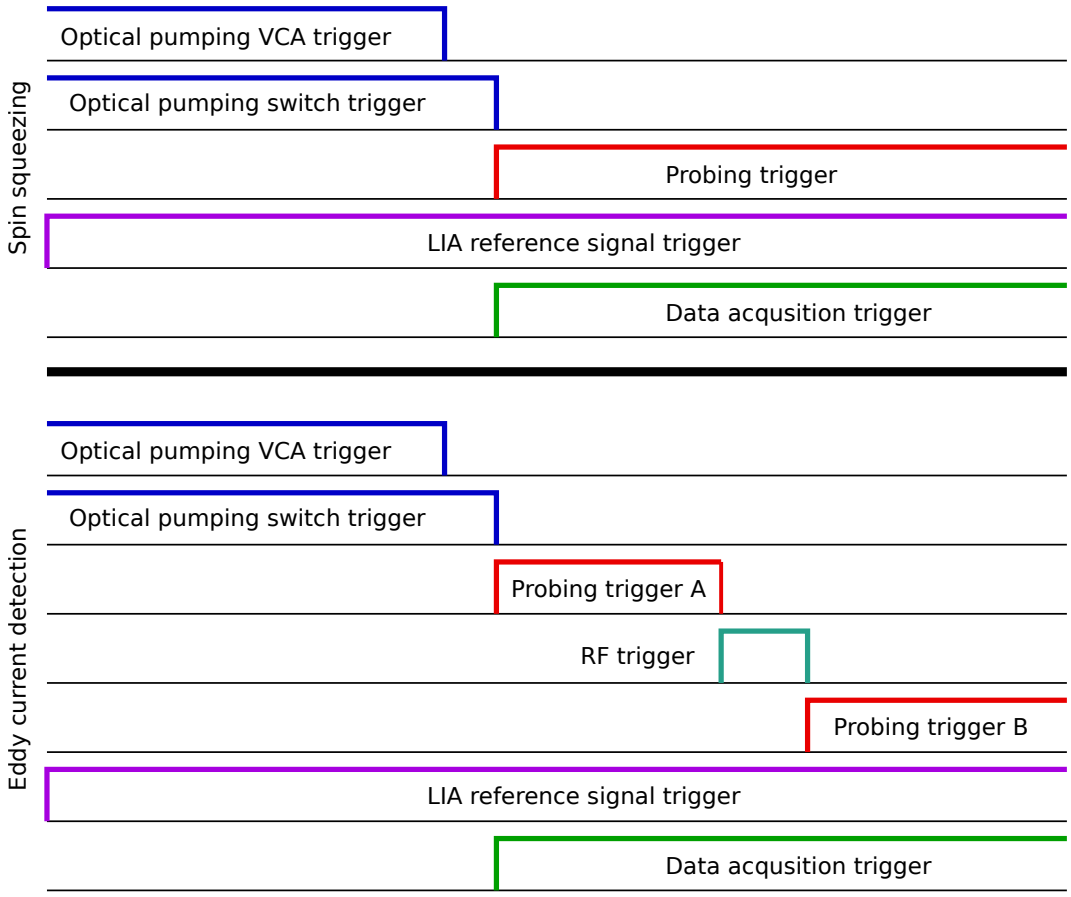

Figure 13.9: Order of trigger pulses. Sequence of trigger pulses generated by the quantum composer to generate signals described in the text and used for the pulse control shown in figure 13.8. The top part illustrates the trigger signals required for the spin-squeezing experiment, while the lower part indicates the sequence required for the quantum-enhanced eddy current detection. Pulse durations are not to scale. Timings are provided in the text.

ple times for proper atomic polarization preparation. The signal controls the VCAs[12] for the optical pumping AOMs. A second pulse of the same width is derived for the switch controlling the AOMs for the pump and repump laser of the optical pumping. We use the absolute reference to delay the turn-off of the switch by 50 µs to allow a smooth turn-off of the optical pumping pulses. We achieve the smooth turn-off by low-pass filtering the square pulse controlling the VCAs. Experimentally, the components in the dashed orange box in figure 13.8 exist twice. One for the pump laser and one for repump laser, but the components are controlled in parallel by the same pulse split into two signal lines.

The reference signal for the LIA is derived next. The delay to the initial trigger is given by 8 ms, which overlaps with the optical pumping. The trigger is sent to a function generator that generates a sinusoidal function with

[12]VCA = Voltage controlled attenuator.

a period corresponding to $1/\nu_L$. It sends a fixed number of oscillations exceeding the duration for recording the signal. This sinusoidal function is the reference signal for the LIA.

A single stroboscopic probe pulse train is required for the experimental demonstration of spin-squeezing, discussed in chapter 14. We use a single pulse signal from the Quantum Composer synced to the trigger of the optical pumping pulse. It triggers a function generator in burst mode, sending square pulses with adjustable duty cycle at twice the Larmor frequency and a fixed number of periods. From this, we get a fixed number of stroboscopic probing pulses. The same function generator provides the LIA reference signal. This has the advantage of easily adjusting the phases between the two signals to maximize the overlap with the cosine quadrature of the LIA. More details on optimizing the system's various phases will be described more thoroughly in section 14.2.

The data acquisition is controlled using another channel of the Quantum Composer. We sync it to the trigger of the stroboscopic probing. We only determine the acquisition start using the trigger from the Quantum Composer. The duration of the data acquisition has to be set in the interface for our *Spectrum M3i.4831-exp series digitizer card*.

In the case of the eddy current detection sequence or the pMORS sequence, we require additional trigger lines, which are not illustrated in figure 13.8, to be defined using the Quantum Composer. For these sequences, the function generator creating the stroboscopic probing pulses is operated in a gated fashion. We must carefully adjust the two pulse widths for the squeezing creation and verification times in the Quantum Composer settings to have an integer number of cycles. We use the burst mode of an additional function generator to create the RF pulse. The number of cycles has to be an integer and fit into the gap between the two stroboscopic probe pulse trains. The trigger for that is carefully defined using the sync function of the Quantum composer. While we use a RIGOL DG1032 for the stroboscopic pulses, the LIA reference signal, and the optical pumping reference signal, we require a better noise performance for the RF signal. Due to its reduced output noise, we switched to a RIGOL DG952 SiFi II for the RF signal generation. The respective required trigger lines for operating our experiment as a quantum-enhanced MIT sensor and their timely order are illustrated in the lower part of figure 13.9.

Data acquisition

The data is analyzed with a Zurich instruments lock-in amplifier of the type *HF2LI Lock-in Amplifier*, and the respective demodulated signals are then recorded with a spectrum analyzer card. We typically use a sampling rate of 10 MHz. We acquire 10 000 data points per measurement repetition, covering a total measurement duration of 1 ms. The data is binned into groups of 25, such that every data file contains 400 values for the 1 ms measurement duration. Often, each data file contains not a single measurement but many

repetitions. Instead of averaging them directly, they are stored together within one file to allow more flexibility during the data analysis.

In the particular case of recording a pMORS using this setup, the acquisition is extended to collect 12 0000 samples with a sampling rate of 20 MHz, covering 6 ms to have a long enough readout of the atomic spin state extending beyond the transverse spin coherence time T_2.

Chapter 14

Implementing back-action evasion and spin-squeezing

After introducing the experimental setup in the previous chapter, this chapter will focus on how we implement and optimize the back-action evasion and prepare a spin-squeezed state in our atomic ensemble. This chapter should be understood as a practical manual on how we optimize the experimental setup before turning ourselves to the goal of performing a quantum-enhanced magnetic induction tomography in chapter 15. A subset of the data presented throughout this chapter has also been part of the manuscript, submitted for publication, Zheng et al. (2022). We present and extend the information presented in the manuscript with additional explanations and experimental data.

This chapter is divided into multiple parts. First, we will shortly describe the signal contributions to be expected in our experimental signals and how we characterize them (section 14.1). Afterward, we will address the stroboscopic protocol and experimental optimization, described in section 14.2, focusing on optimizing the phases between different signals. The phase optimization will be followed by verifying the back-action evasion by recording signals for different duty cycles D in section 14.3. The last and most important part of this chapter, building up on the three preceding sections, will cover the topic of conditional spin-squeezing in section 14.4. We will investigate the attainable level of spin-squeezing for different parameters and how fast the spin-squeezing degrades.

Throughout this chapter, all measurements share the same basic pulse sequence. First, we minimize the atomic projection noise using a long pulse of optical pumping to prepare the atomic spin ensemble as close as possible to a coherent spin state (red in figure 14.1). Following this coherent spin state preparation, the basic sequence consists of a train of stroboscopic probe pulses. Throughout this chapter, we will keep the stroboscopic frequency constant at twice our Larmor frequency ν_L of approximately[1] 725 kHz, but we will vary the duty cycle D of the stroboscopic pulses (blue in figure 14.1). Figure 14.1 can be understood as a simple visualization of our probe intensity modulation function $\phi(t)$ as introduced in equation (3.16) with a fixed choice of

[1] Due to small changes in the lab environment, we need to tweak the currents generating the bias magnetic field. Therefore, the exact frequency of the Larmor frequency varies between 720 and 730 kHz.

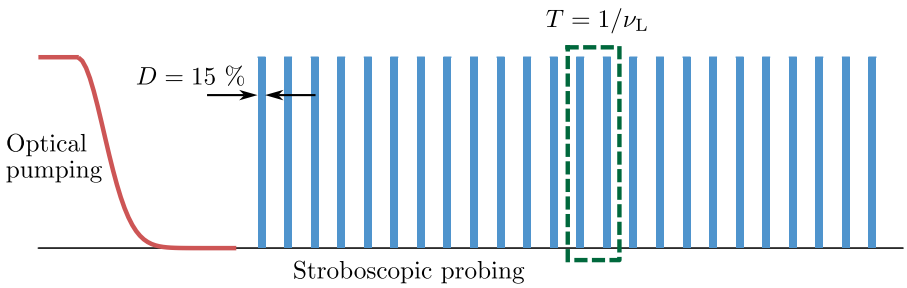

Figure 14.1: Simple stroboscopic pulse sequence. The sequence starts with the smooth turn-off of the optical pumping (red). Then, a sequence of stroboscopic probing pulses at twice the Larmor frequency ν_{L} are sent (green box). Here, the duty cycle of the stroboscopic probing pulses is $D = 15\,\%$.

duty cycle D.

14.1 (Un)wanted signal contributions

Our measurements rely on light interacting with a highly-polarized atomic ensemble, exploiting the Faraday interaction as introduced in chapters 2 and 3. In the following, we will discuss different contributions to our recorded signals. Ultimately, we want to be limited by quantum noise for our atomic eddy-current sensor. Quantum noise limited means that noise sources of quantum nature dominate our system rather than classical or technical noise sources. We can exploit quantum phenomena in this regime to modify and alter these. For example, we will try to circumvent the back-action noise or squeeze the noise variance of one of the transverse spin components. Suppose we are operating in a quantum noise-limited regime. In that case, our signal and noise should be comprised of contributions arising from the photon shot noise (SN), atomic spin projection noise (PN), and quantum back-action noise (BAN), as discussed in chapter 3.

14.1.1 Electronic noise

When performing our measurements, we are always subjected to the electronic noise originating from the detection and the devices used for recording our data. We measure the amount of electronic noise using identical experimental sequences used for the spin-squeezing measurement in 14.4. It is recorded in the same fashion as our signals, just that all light sources, probing and optical pumping beams, are blocked. Typically, we observe just below 30 % of electronic noise compared to the shot noise level considering our preferred choice of 5 µW probe power throughout most measurements presented here. We wish the electronic noise level to be as low as possible and not limited by this classical noise source. Since any of our signals are suffering from electronic noise, we correct for the electronic noise and refer to it as $\mathrm{EN} = \mathrm{Var}\left(\hat{S}_y^{c,\text{no light}}\right)$.

14.1.2 Photon shot noise

Due to the statistical nature of laser light, any measurement that we perform will suffer from intrinsic noise due to the light we use to perform the measurement. The statistical distribution of arrival times of photons in coherent laser light means that the corresponding noise spectrum is "white", leading to a constant noise level evenly distributed across the spectrum[2]. On the one hand, we want to ensure that we measure strong enough, such that there is a significant enough number of photons for the interaction and hence recorded signal. On the other hand, too much probe power – too many photons – will introduce additional decoherence effects. Optimizing the probe power and hence photon number is a balance.

Commonly, we scale all our obtained measurement signals concerning the photons' shot noise level. For this, we record $\hat{S}_y^{\text{out},c}$ while detuning the atoms by changing the bias magnetic field. Altering the bias magnetic field changes the Larmor frequency of the atoms. If they are far-detuned enough[3], we effectively get a measure of the light noise at the usual Larmor frequency without any atomic contribution to the signal. The recorded signal is proportional to the number of photons and given by (compare equation 2.10):

$$\text{Var}\left(\hat{S}_y^{c,\text{out}}\right) = \eta(D)\frac{N_{\text{Ph}}}{4} \equiv \text{SN}_0 \tag{14.1}$$

Here, $\eta(D)$ is defined as before, accounting for the variable duty cycle D. We will use SN as a short notation in extensive equations when referring to the noise variance that originates from the shot noise of light. Due to the electronic noise of our system, we define our actual shot noise variance corrected for electronic noise as $\text{SN} \equiv \text{SN}_0 - \text{EN}$.

We ensure that we are shot noise limited by varying the probe power and recording the observed signal level, similar to chapter 11. If we can neglect classical noise sources such as electronic noise, the observed signal level should follow a linear trend with the probe power. It should be noted that the combined signal of the two detectors can be shot noise limited while the individual ones are not (Krauter, 2011). For the detector in use, we can only monitor the combined output of our detector and confirm that the combined signal is indeed shot noise limited.

[2]For the unfamiliar reader: Think of photons that are released in a continuous stream, however at random timings. Since each detection event is randomly separated in time, thinking of it in terms of frequency of events, we expect each frequency to have the same probability.

14.1.3 Projection noise

Another intrinsic noise source of our system is the contribution arising from the spin projection noise. As covered in chapter 2, we will suffer from atomic spin projection noise even for a fully polarized atomic ensemble due to the non-commuting transverse spin operators. However, in the case of a fully polarized atomic spin ensemble, i.e., the coherent spin state, the atomic spin projection noise will be minimal.

Experimentally, we distinguish the atomic spin projection noise, which refers to the uncertainty associated with the polarized ensemble. In contrast,

[3]Multiple bandwidths away from our center frequency set at the LIA will ensure that there will be no atomic contributions to the recorded light signal.

the thermal spin projection noise refers to the spin projection noise of a thermal - corresponding to an unpolarized - ensemble. For a polarized atomic ensemble, $\langle \hat{J}_x \rangle$ is non-vanishing. Therefore, our recorded atomic signals suffer from back-action noise (compare equation 3.3). However, this is not the case for the thermal spin state. There, the back-action should vanish as $\langle J_x \rangle = 0$ since our ensemble has no mean atomic spin polarization. In this unpolarized ensemble, all magnetic sublevels are equally populated, leading to the following symmetry for atoms in the 4-manifold of the ground state:

$$\hat{j}_x^2 = \hat{J}_y^2 = \hat{J}_z^2 = \frac{F(F+1)}{3} = \frac{20}{3} \tag{14.2}$$

Due to the equilibrium distribution of the atoms between both ground states, only 9/16-th of the atoms contribute to the signal[4]. Hence, the projection $\mathrm{Var}\left(\hat{J}_z\right)_{\mathrm{TSS}} = \frac{20}{3} \cdot \frac{9}{16} N_{\mathrm{A}} = \frac{15}{4} N_{\mathrm{A}}$. For the coherent spin state, the projection noise is given by $\mathrm{Var}\left(\hat{J}_z\right)_{\mathrm{CSS}} = F N_{\mathrm{A}}/2 = 2 N_{\mathrm{A}}$. Comparing the projection noise for the thermal state to the CSS projection noise, we find a factor of 8/15. Experimentally, we hence estimate the projection noise of the coherent spin state using the observed noise of the thermal spin state (TSS) and correct it with this factor of 8/15 as:

$$\mathrm{Var}\left(\hat{J}_z\right)_{\mathrm{CSS}} = \frac{8}{15} \mathrm{Var}\left(\hat{J}_z\right)_{\mathrm{TSS}} \tag{14.3}$$

The indices CSS and TSS indicate the coherent and thermal spin states, respectively. As we have seen in subsection 13.3.2, we only achieve an atomic polarization of 97.5 %. In the discussion later on, we will therefore need to investigate the impact arising from residual atoms in $m_{F=4} = 3$.

Experimentally, we record this thermal projection noise by blocking the optical pumping but keeping our usual bias magnetic field and stroboscopic probing turned on. Our recorded signal for the thermal spin state is, of course, also suffering from electronic noise, which we need to correct for:

$$\mathrm{TN} \equiv \mathrm{Var}\left(\hat{S}_y^{c,\mathrm{out}}\right) - \mathrm{EN} \tag{14.4}$$

The thermal spin noise is insensitive to back-action noise even when the measurement time or the photon number increases, as long as the pumping effects of the probing remain negligible. Therefore, we estimate our projection noise for the coherent spin state based on our observed thermal spin state projection noise as:

$$\mathrm{PN} \equiv \frac{8}{15} \mathrm{TN} \tag{14.5}$$

We will later see that we can exploit this relation to get an estimate for the back-action-free measurement.

[4] In total, the ground state of cesium has 16 Zeeman levels, out of which nine are in the ground state with $F = 4$ and seven belong to the ground state with $F = 3$.

14.2 Stroboscopic protocol: Signal and Phase optimization

A crucial part of our quantum-enhanced atomic magnetometer is the ability to achieve quantum noise-limited sensitivity and even further circumvent

the back-action noise introduced to our system when measuring. This section will cover how we implement stroboscopic probe pulses and optimize frequencies and relative phases to fulfill the requirements for a back-action evaded measurement as introduced in section 3.1. Experimentally, we are unable to realize infinitely short pulses. For a Larmor frequency of $\nu_L = 725\,\text{kHz}$, we are limited to a minimum duty cycle of 15 % due to our finite rise and fall time of the VCA. To realize back-action evasion, we must align our signal phases and frequencies to maximize our recorded signals and fulfill the criteria imposed from equation (3.10). Optimizing the frequencies and precise timings of when pulses are sent is crucial.

As discussed in 13.3.4 and 13.3.4, we use a combination of trigger reference signals to send our experimental pulses and record the signals using lock-in detection and a spectrum analyzer card. For starters, we usually need to optimize the atomic spectrum with the stroboscopic frequency of the probe pulses. Daily optimization is required because magnetic field drifts shift the center Larmor frequency. For this, we use a picoscope to record the atomic signal[5]. When the stroboscopic frequency does not match twice the Larmor frequency, we observe two slightly separated and mirrored atomic signals (green in figure 14.2) in the spectrum. A single symmetric atomic response can be observed when matching the stroboscopic frequency to the Larmor frequency (blue in figure 14.2). This frequency is also used as the lock-in amplifier (LIA) demodulation frequency.

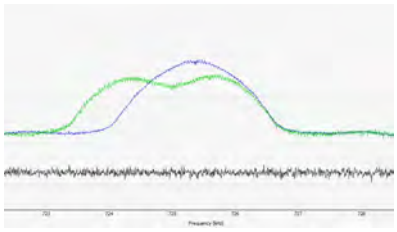

Figure 14.2: Illustrative snapshot of the atomic signal. Picture of atomic spectra observed before (green) and after (blue) optimizing the stroboscopic probing frequency. The black line corresponds to the electronic noise level.

Afterward, when recording the signal with the lock-in amplifier (LIA), we start with optimizing the demodulation phase of the signal to maximize the recorded signal. For this, we record the shot noise signal for both components of the LIA and vary the demodulation phase. Changing the relative demodulation phase of the LIA corresponds to varying the overlap of the signal from the stroboscopic probe pulse sequence with the cosine quadrature of the detection. Since we balance the signal recorded with polarization homodyning, considering the X- and Y-component for the shot noise will not give us any average signal. Therefore, we investigate the variance of the recorded shot noise traces for different LIA demodulation phases. While the phase difference between the two quadrature signals is expected to be 90 degrees, the variances should behave slightly differently. Since no overlap of the probe pulses with the Y-component means no signal, this should be reflected in a vanishing variance of the Y-component. At the same time, the maximal overlap of the probe is obtained for the X-component, which is 90 ° out of phase compared to the Y-component. We expect the variance for the maximal signal also to be maximal. Therefore we expect the variances to be 180 ° out of phase.In figure 14.3, the X-component reflects the cosine quadrature (blue), and the Y-component is the sine quadrature (red). We fit a sine to the observed shot noise variance. The optimal detection is then given by the phase angle for the minimum Y-component, while it is the maximum for the X-component. The obtained phases from the fits are:

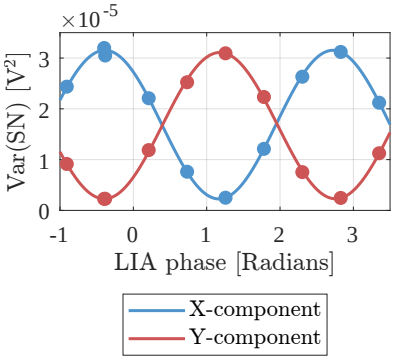

Figure 14.3: LIA phase optimization. X-component (blue) and Y-component (red) of the lock-in amplifier signal variance of the shot noise (SN) versus the phase.

We choose the average and set our lock-in amplifier demodulation phase

[5] I would like to acknowledge the excellent work done by Jonas Mathiasen in making the spectrum analyzer feature and interface for the picoscope and the convenient option to save the spectral data.

X-component	-22.3 °
Y-component	-22.7 °

to 22.5°.

The final optimization overlaps the stroboscopic probe pulses with the signal reference sent to the lock-in amplifier. For this, the LIA's sinusoidal reference signal phase is adjusted with the function generator such that the maximum amplitude coincides with the stroboscopic probe pulse. This has to be done whenever the Larmor frequency is adjusted.

14.3 Back-action evasion

One of our two fundamental building blocks is verifying the back-action evasion due to our stroboscopic probe pulses. We can avoid introducing extraneous back-action noise into our system by probing our spin-oscillator with twice its precession frequency with a duty cycle $D \to 0$ and singling out the cosine component of our observable. Then, the "bad" back-action noise compromises only the quadrature we are not optically probing. This allows us to realize a stroboscopic quasi-QND measurement described in chapter 3. Realistically speaking, our finite duty cycle does only allow us to reduce the back-action noise introduced to our system. However, we expect a significant reduction in that back-action noise and wish to quantify this. As we have seen in section 3.2, the noise variance can be expressed in terms of[6] (equation (3.29)):

$$\mathrm{Var}\left[\hat{S}^{\mathrm{out},c}_{y,\tau}\right] \approx \frac{\Phi\tau}{4}\left[1+\mathrm{sinc}\left(\pi D\right)\right]\left[1+\frac{\tilde{\kappa}^2}{2}+\frac{\tilde{\kappa}^4}{12}\frac{1-\mathrm{sinc}\left(\pi D\right)}{1+\mathrm{sinc}\left(\pi D\right)}\right], \qquad (14.6)$$

where the third contribution determines the amount of back-action noise compromising our measurement. As seen in section 3.2, the fraction approaches zero for a duty cycle $D \to 0$ and is maximal for continuous probing. We tested this by considering the observed noise for three different duty cycles: 15, 50, and 90 %. At the same time, we keep the number of photons per cycle constant, meaning that altering the duty cycle only alters the temporal distributions of the photons interacting with the spins, not their total number. To illustrate this, we can consider the simplified drawing in figure 14.4. This figure shows the relative intensity over a single period. By measuring only average powers over many cycles experimentally, we can keep the number of photons per period constant, corresponding to the area under the curve. Keeping the average number of photons constant means that the intensity during the time of the pulse increases towards shorter duty cycles D. For example, the intensity during the pulse has to double when halving the duty cycle from one measurement to another if the number of photons should remain the same. As long as we ensure that the average optical power is estimated over multiple stroboscopic probing pulses, we thus can ensure that the same number

[6] There are two commonly used definitions of the sinc-function, we use

$$\mathrm{sinc}\left(x\right) = \frac{\sin(x)}{x},$$

which differs in the scaling on the x-axis from the other definition, exhibiting an additional factor of π.

of photons interacts with our collective spin-oscillator and only when in time they interact with it changes. Only then can it be directly compared how the duty cycle used for our probing alters the back-action noise introduced to our system.

The overlap of the signal with the LIA cosine quadrature depends on the duty cycle. Therefore, we have to correct the noise variances by a factor of $[1 + \mathrm{sinc}\,(\pi D)]$. Doing so allows us to correct the different detection efficiencies arising from the differing overlap with the LIA demodulation. For a better comparison, we normalize all signals to shot noise units. The noise variance is expected to follow a second-order polynomial. From equation (14.6), we expect the quadratic contribution to reflect the back-action noise introduced to our system. It depends on the duty cycle D. The constant and first-order contribution should be independent of the duty cycle D when we correct for the different overlaps with the cosine quadrature of the LIA.

Figure 14.5 shows the noise variance for three duty cycles versus the probing duration. It is scaled to units of shot noise before it is corrected for the different overlap with the detection mode of the LIA by a factor of $1/\eta$, with the previously introduced η as $\eta = (1 + \mathrm{sinc}\,(\pi D))$. Fitting a second-order polynomial to the data, we observe excellent agreement between the fit and the data. As expected, the lower the duty cycle, the smaller the quadratic contribution to the overall noise. We also witness good agreement of the linear part for 50 and 90 percent duty cycle. The linear part for the 15 % duty cycle is slightly higher. This discrepancy is most likely related to the pulse shape of the stroboscopic pulses. For this setting, the pulses generated by the AOM are not nicely square-shaped as assumed for the calculation used in the toy

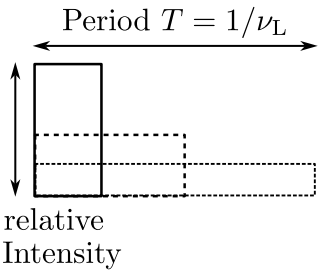

Figure 14.4: Varying duty cycle. Illustration of variable duty cycles while the intensity during the pulse varies, but the "area" under the curve remains constant such that the same average number of photons is used while only their temporal distribution changes for the measurement shown in figure 14.5.

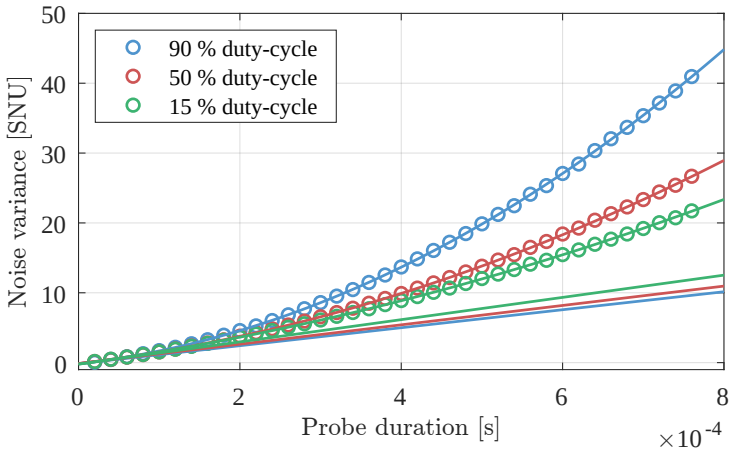

Figure 14.5: Verifying back-action evasion. Measured overall noise variance versus the probing duration, corrected for different detection efficiencies arising from the different duty cycles (15 (green), 50 (red), and 90 % (blue) duty cycle) and normalized to shot noise units (SNU). The fits for the second-order polynomial are shown, along with the linear parts obtained from the fits. The figure is adapted from Zheng et al. (2022) (replotted). [8]

[8] In principle, the probing duration in figure 14.5 could also be expressed in terms of the number of photons.

model. Therefore, the prefactor might not be reflecting the effective duty cycle leading to a slight change in the linear incline.

Overall, we still observe a relatively good agreement on the linear part, allowing us to use these corrected noise variances to judge the reduction in back-action noise introduced to our system. Comparing the quadratic parts for the green and blue data, we observe a reduction of more than a factor of two in the quadratic contribution corresponding to the back-action noise. The reduction of duty cycle and the stroboscopic probing at twice the Larmor frequency reliably reduces the back-action noise introduced to our measurement. With improvements in our pulse shaping capabilities, we should enable a higher stroboscopic probing frequency and hence allow for a higher Larmor frequency. This would benefit us overall as technical noise sources decrease at higher frequencies. Alternatively, faster switching of the pulsing enables reducing the duty cycle further. A lower duty cycle could further reduce the back-action noise added by our measurement as long as we do not become Fourier limited with our stroboscopic probe pulses and start introducing unintended physical effects due to the spectral width of the temporally short pulse.

14.4 Conditional spin-squeezing

After investigating the impact of the stroboscopic probing and reducing the duty cycle of the pulses, we now want to investigate the attainable level of spin-squeezing. We will start by comparing the conditional and unconditional noise in subsection 14.4.1, which forms the basis for determining the level of squeezing later on in subsection 14.4.2. Here, we will examine how experimental timings and other parameters influence our attainable level of spin-squeezing.

14.4.1 Conditional vs. unconditional measurement

Essential for squeezing is the noise reduction in a measurement when conditioning a consecutive measurement on a preceding one. This means that instead of purely estimating the noise during the stroboscopic pulse as in the verification of back-action evasion in 14.3, the probe pulse train is split into two for the analysis. We will refer to the two pulse trains as τ_A and τ_B, where the signal obtained during τ_B can be conditioned on the measurement during τ_A. Comparing both cases – conditional and unconditional – will tell us how much we can "learn" when performing conditional measurements. This splitting of our most basic pulse sequence is illustrated in figure 14.6, where we indicate the (relative) choices of τ_A and τ_B using dashed boxes.

First, we must find a way to describe and analyze our measurement data. We have already described in a previous section how we determine the contributions to our overall noise arising from electronic noise (EN), projection noise (PN), and shot noise (SN). However, we are missing how to describe the

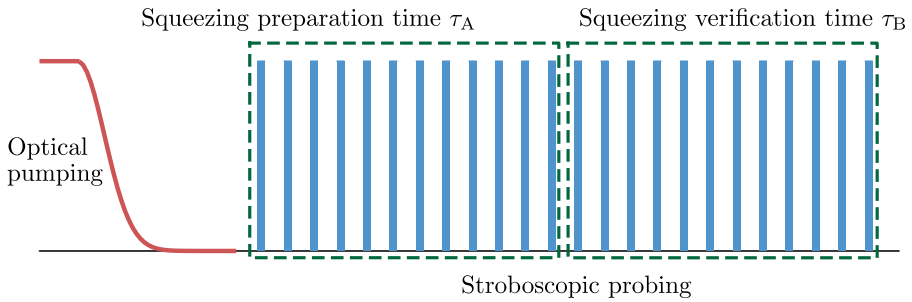

Figure 14.6: Simple stroboscopic pulse sequence. Illustration of the stroboscopic pulse sequence used for testing the back-action evasion and conditional spin-squeezing. The smooth turn-off of the optical pumping is indicated in red, while the stroboscopic probe pulses are indicated in blue. Here, $D = 15\,\%$. The squeezing preparation and verification times τ_A and τ_B are indicated using green dashed boxes and can be chosen in the analysis. See text for more details.

observed signals and convert them into shot noise units before finding an expression for the conditional observed noise. In the following, we refer to the signal obtained during τ_A as $\hat{X}_A$, and τ_B as $\hat{X}_B$, corresponding to the cosine component of the LIA for the recorded signal (compare equations 2.10):

$$\hat{X}_A = \int_0^{\tau_A} \mathrm{d}t \hat{S}_y^{\mathrm{out}}(t) \cos(\omega_L t) \tag{14.7a}$$

$$\hat{X}_B = \int_{\tau_A}^{\tau_A+\tau_B} \mathrm{d}t \hat{S}_y^{\mathrm{out}}(t) \cos(\omega_L t) \tag{14.7b}$$

indices A and B indicate the stroboscopic pulses used for the squeezing preparation (A) and verification (B). As before, we are interested in the associated noise, which we, for comparability, wish to express in shot noise units as follows:

$$\mathrm{Var}(\hat{x}_A) = \frac{\mathrm{Var}(\hat{X}_A) - \mathrm{EN}_A}{\mathrm{SN}_A} - 1 \tag{14.8a}$$

$$\mathrm{Var}(\hat{x}_B) = \frac{\mathrm{Var}(\hat{X}_B) - \mathrm{EN}_B}{\mathrm{SN}_B} - 1 \tag{14.8b}$$

Here, we need to correct our recorded atomic signals by the electronic noise of the respective time window. We express our recorded noise variance in shot noise units (SNU) by normalizing it to the shot noise SN and subtracting one. In the following, we will not explicitly state the correction for the electronic noise. However, we still correct for it throughout our analysis for contributions arising from this.

In order to determine the degree of spin-squeezing later, we need to estimate the conditional noise variance during τ_B first, when conditioning it on the preceding measurement during τ_A as (Zheng et al., 2022):

$$\mathrm{Var}(\hat{x}_{B|A}) = \frac{\mathrm{Var}(\hat{X}_{B|A})}{\mathrm{SN}_B} - 1 \tag{14.9}$$

with

$$\begin{aligned}\mathrm{Var}\left(\hat{X}_{\mathrm{B}\,|\,\mathrm{A}}\right) &= \min(\mathrm{Var}\left(\hat{X}_{\mathrm{B}} - \alpha\hat{X}_{\mathrm{A}}\right)) \\ &= \mathrm{Var}\left(\hat{X}_{\mathrm{B}} - \alpha_{\mathrm{opt}}\hat{X}_{\mathrm{A}}\right)\end{aligned} \tag{14.10}$$

Here, α_{opt} describes the value that minimizes the expression. This is the case for $\alpha_{\mathrm{opt}} = \frac{\mathrm{Cov}^2\left(\hat{X}_{\mathrm{B}},\hat{X}_{\mathrm{A}}\right)}{\mathrm{Var}\left(\hat{X}_{\mathrm{A}}\right)}$, which allows us to rewrite equation (14.9) as follows:

$$\mathrm{Var}\left(\hat{x}_{\mathrm{B}\,|\,\mathrm{A}}\right) = \frac{\mathrm{Var}\left(\hat{X}_{\mathrm{B}}\right)}{\mathrm{SN}_{\mathrm{B}}} - \frac{\mathrm{Cov}^2\left(\hat{X}_{\mathrm{B}},\hat{X}_{\mathrm{A}}\right)}{\mathrm{SN}_{\mathrm{B}}\cdot\mathrm{Var}\left(\hat{X}_{\mathrm{A}}\right)} - 1 \tag{14.11}$$

All contributions in this equation can easily be determined from our experimental recordings. From equation (14.11), we see that we expect to observe a reduction in the conditional variance, meaning a reduction in noise, if there is a correlation between the observations of the two stroboscopic measurements[9].

With these expressions at hand, we can investigate how the unconditional and conditional variances behave, along with the contribution of our noise originating from the projection noise of the atoms. We have multiple parameters that we will vary. For convenience, we will first consider the different duty cycles D and vary the length of τ_{A} of our measurement for a fixed duration of $\tau_{\mathrm{B}} = 40\,\mu\mathrm{s}$ and compare the projection noise level with the conditional and unconditional noise. Figure 14.7 shows the respective contribution of the noise variances. The data is scaled and corrected for the shot noise level. One common feature in figure 14.7 is that the contribution arising from the coherent spin state projection noise is roughly constant for each measurement for different values of τ_{A}. While this might be confusing initially, it should be noted that the identical duration $\tau_{\mathrm{B}} = 40\,\mu\mathrm{s}$ was used for each point. In addition, we do not correct for the expected decay of the atomic spin and hence increase in the expected projection noise compared to a coherent spin state. We do not incorporate the decay of the collective spin coherence because our experiments' time scales are much shorter than T_1 and T_2 times. For example, compare figure D.1 in appendix D.1. In figure 14.7, the unconditional noise grows faster for larger duty cycles. This behavior is not unexpected, given the more significant back-action noise introduced to the system. At the same time, conditioning the second probe pulse train on the first one results in a much more substantial noise reduction. For the two lower duty cycles, we observe a conditional noise variance below the expected contribution to the overall noise arising the contribution due to the projection noise of the atoms. The lower the duty cycle, the smaller the minimal conditional noise variance and the longer its preparation.

For figure 14.7, we kept $\tau_{\mathrm{B}} = 40\,\mu\mathrm{s}$ constant and only varied how long we integrated the signals during τ_{A}. To investigate the dependency of the conditional noise from the duration of τ_{B}as shown in figure 14.8, we need to fix τ_{A}. We present the data for $\tau_{\mathrm{A}} = 220\,\mu\mathrm{s}$. This choice depends on our

[9] For a more rigorous mathematical description in terms of light and atomic operators, the derivations are shown in the supplements of Vasilakis et al. (2015) and also throughout Shen (2014).

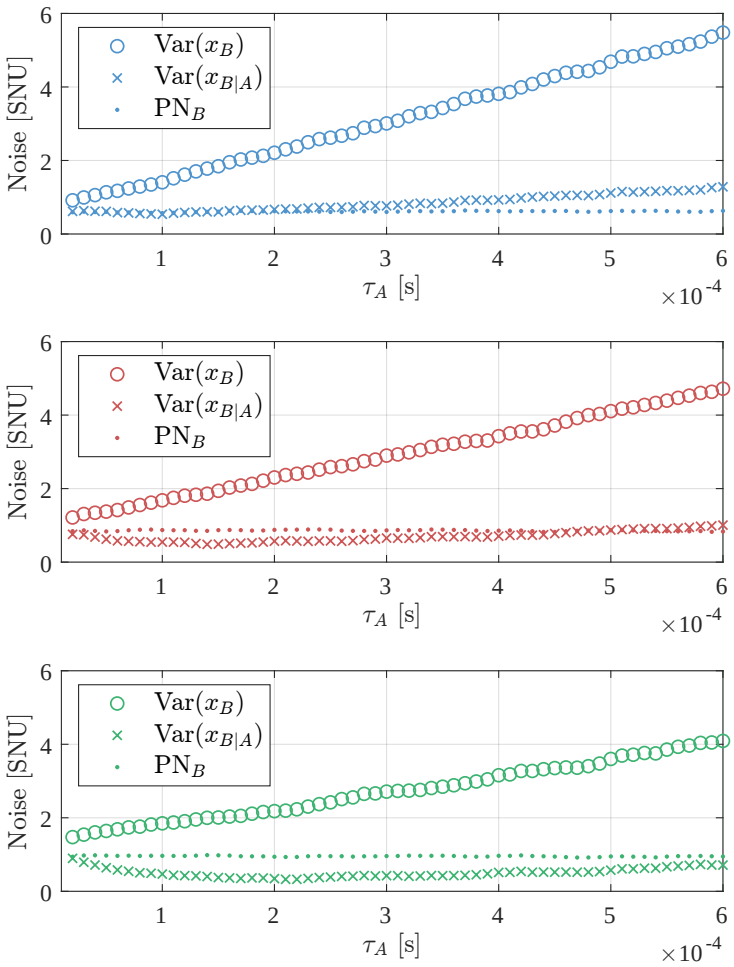

Figure 14.7: Conditional and unconditional variance. Comparison of conditional and unconditional variance during readout pulse $\tau_B$for three different duty cycles with 15 % (green), 50 % (red), and 90 % (blue) versus the duration of τ_A. All duty cycles have an average probe power of 5 µW.

optimization of the level of spin-squeezing, which will be presented later in this section.

Here, our noise, of course, grows as the cumulative integration time of the points increases. It should also be noted that the points are not statistically independent. As before, we observe that the conditional noise is significantly lower than the unconditional one. We note that the conditional noise variance reaches the shot noise level only for $\tau_B$exceeding 100 µs. Also, for $\tau_B$shorter than 50 µs, the shot noise level is equal to or even more significant than the expected contribution to our noise arising from the coupling to the projection noise of the atoms, making shot noise a substantial noise contribution to our overall recorded signal and noise variance.

The conditional noise level below the contributions arising from the pro-

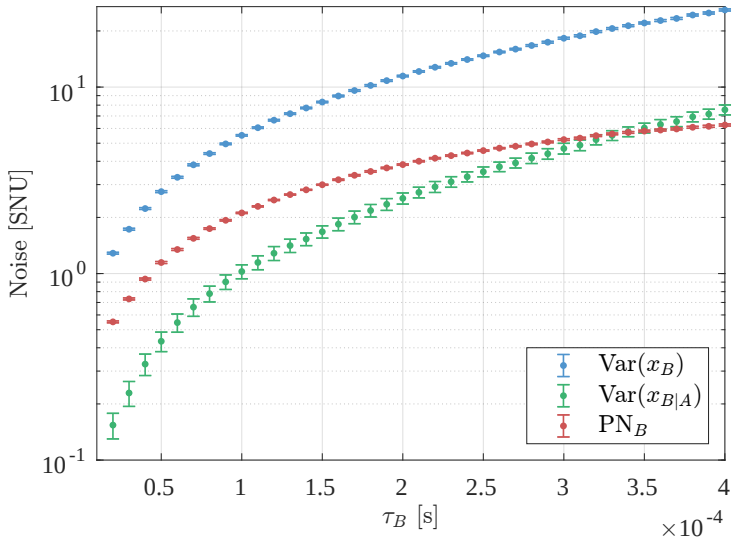

Figure 14.8: Conditional and unconditional noise variance. Comparison of conditional (green) and unconditional (blue) noise variance during readout pulse $\tau_B$for 15 % duty cycle and 5 µW probe power versus the duration of τ_B for a fixed squeezing preparation time $\tau_A = 220\,\mu s$. In addition, we plot the expected noise contribution arising from the atomic projection noise in red. Errors reflect standard errors obtained from 8 data sets containing 4000 measurements each. This figure is adapted (replotted) from figure 2 (d) in Zheng et al. (2022).

jection noise in figures 14.7 and 14.8 is a robust sign that we observe spin-squeezing. Verifying and estimating the degree of spin-squeezing within our collective spin ensemble will be the topic of the following subsection.

14.4.2 Squeezing verification

Following the introduction of back-action evasion and conditional measurements in the previous subsections, the last step is to estimate the attainable level of spin-squeezing. To estimate the level of spin-squeezing, we define the parameter ξ^2 as the ratio between the conditional and unconditional noise variances during the second stroboscopic probe pulse of duration τ_B, corrected for the shot and electronic noise:

$$\xi^2 = \frac{\mathrm{Var}\left(X_{\mathrm{B|A}}\right) - \mathrm{SN_B} - \mathrm{EN_B}}{\mathrm{Var}\left(X_{\mathrm{B}}\right) - \mathrm{SN_B} - \mathrm{EN_B}} \tag{14.12}$$

As before, SN and EN refer to the shot noise of light and the electronic noise. The squeezing parameter ξ^2 as defined in equation (14.12) hence tells us how much reduction in noise between the conditional and unconditional case is observed. We can interpret it as how much we learn about our spin oscillator during the first stroboscopic pulse during τ_A that can be used to perform a more precise measurement during τ_B.

Now it is also becoming evident why we previously referred to τ_A as squeezing preparation and τ_B as squeezing verification time windows and

pulses. Often, it is more convenient to express the degree of spin-squeezing in the dB scale. Throughout this thesis, we will often state and compare $10\log(\xi^2)$ to quantify the level of conditional spin-squeezing. In figure 14.9 we conceptualize what happens when probing the spin-oscillator stroboscopically and compare it to the conditional spin-squeezing. We do not introduce any back-action noise to the transverse spin component of interest for a back-action evaded measurement. This is illustrated by the fixed width of the horizontal component of the left side in figure 14.9. If we, in addition, exploit conditional spin-squeezing, the more information we gain about our spin component of interest and the associated uncertainty, the more it is squeezed. This is illustrated on the right side of figure 14.9. We note that this is more a phenomenological simplification in the illustration, and a thorough description of how the back-action can be evaded was discussed and provided in the theory section (section 14.3). We note that the conditional spin-squeezing improves beyond what we can expect from evading the back-action alone and that from experimental point of view it is of course not smart to not exploit knowledge from consecutive measurements. The left side of figure 14.9 is therefore just an illustration and the knowledge gain from consecutive measurements should always be exploited and will then allow us to squeeze the expected noise variance.

As part of the analysis, we will vary and map out the attainable level of spin-squeezing as a parameter of the duration of the two stroboscopic pulse trains τ_A and τ_B, the duty cycle D of the stroboscopic pulses, and the optical probing power corresponding to the number of photons interacting with our system.

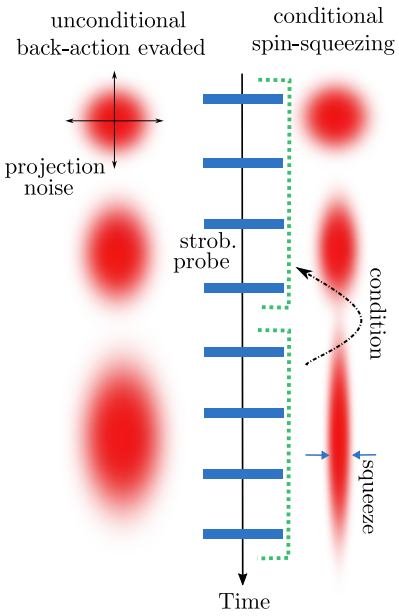

Figure 14.9: Concept illustration squeezing. Simplified illustration of back-action evaded measurement (left) and comparison to the projection noise contribution subjected to conditional spin-squeezing. The areas illustrate the variance of the expected value when repeating a measurement many times.

Squeezing versus duty cycle

As seen in section 14.3, how well we evade the back-action noise depends highly on the duty cycle used for the stroboscopic probing pulses as predicted by the theory presented in chapter 3. For the same reason, we will investigate the duty cycle dependency of the spin-squeezing. It should be noted that conditional spin-squeezing and back-action evasion are two separate things. However, they are highly connected. While back-action evasion aids us in not adding additional noise to our system by interrogating it with our optical probing beams, conditional spin-squeezing relies on the fact that we condition a measurement on a preceding one. As one can easily imagine, the gain from this conditioning is better the closer we are to a QND-type measurement interaction. Therefore, we also expect the degree of conditional spin-squeezing to benefit from lower duty cycles D of our stroboscopic probing pulses.

In figure 14.10, the attainable level of conditional spin-squeezing is shown versus the duration of the squeezing preparation pulse τ_A. For all three duty cycles (15, 50 and 90 %), the same average probing power of 5 µW and squeezing verification time $\tau_B = 40$ µs is used. We measured for each duty cycle 8 data sets containing 4000 measurement sequence repetitions each. We did this for the electronic noise, photon shot noise, thermal atomic noise, and our

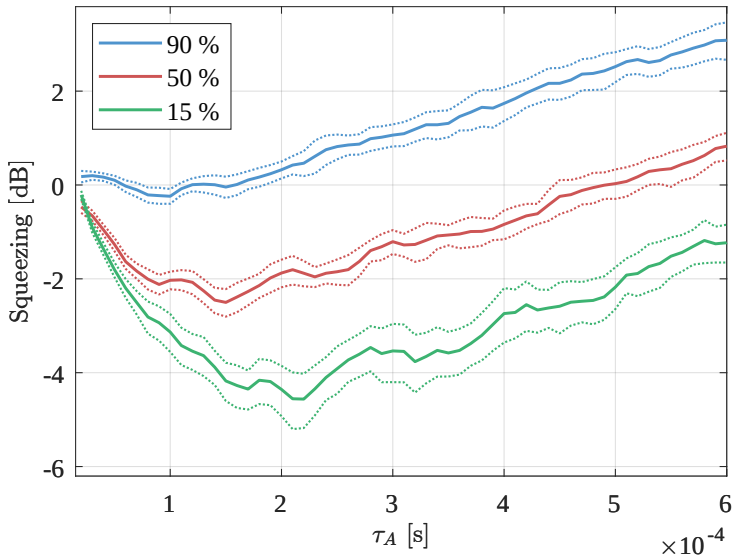

Figure 14.10: Duty cycle dependency of spin-squeezing. Impact of the duty cycle D on the achievable spin-squeezing level for fixed $\tau_B = 40\,\mu s$ versus the squeezing preparation duration τ_A(solid lines). Dashed lines correspond to standard errors estimated from 8 data sets containing 4 000 measurement sequence repetitions each. This graph contains the same data as presented in figure 2 (c) in Zheng et al. (2022) but with smaller time steps and a larger range of τ_A.

atomic signal, respectively. This is relevant to estimate the squeezing as stated in equation (14.12). From these statistics, we estimate the uncertainties associated with each contribution and propagate the errors to estimate the uncertainty associated with the level of conditional spin-squeezing.

As expected, the attainable degree of conditional spin-squeezing is highly dependent on the duty cycle[10]. Also, the degradation of the conditional spin-squeezing is faster for larger duty cycles, indicating that the more significant and faster increasing back-action noise not only decreases the attainable level of conditional spin-squeezing but also accelerates its degradation.

Probe power dependency

While it is apparent that the degree of conditional spin-squeezing improves for lower duty cycles D since the back-action introduced to the system is smaller compared to higher duty cycles, the probe power dependency is more complex. On the one hand, we would expect that the lower the probe power, the lower the number the photons and hence the smaller the shot noise level. At the same time, the conditional spin-squeezing only acts on the projection noise. However, its contribution to our signal depends on the coupling constant, which is proportional to the number of atoms and photons. Therefore, it is not intuitive which probe power dependency of the conditional spin-squeezing to expect. In figure 14.11, we plot the obtained level of conditional spin-squeezing for three different probe powers of 2.5, 5.0, and 8.5 µW versus

[10] To reiterate once more: The overall number of photons interacting with the spin-oscillator was the same in all three cases as we determined the probe power as the average over many oscillation periods.

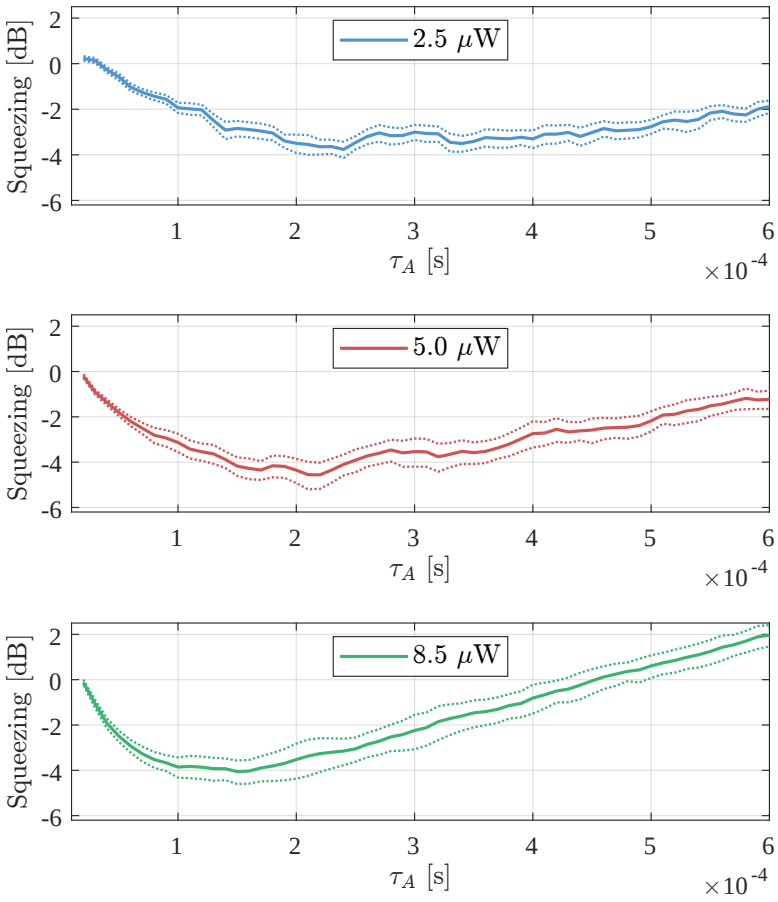

Figure 14.11: Probe power dependency of spin-squeezing. The degree of spin-squeezing observed for three different probing powers versus the squeezing preparation duration τ_A, calculated for steps of 10 µs. The squeezing verification duration was fixed to $\tau_B = 40$ µs. Dotted lines represent standard errors obtained from 8 data sets containing 4 000 measurements each. The center part of this figure shows the same data as figure 2 (c) in figure Zheng et al. (2022). However, it is recalculated with smaller time bins.

the squeezing preparation time τ_A. In all cases, the squeezing verification time was fixed to $\tau_B = 40$ µs, and a minimum duty cycle D of 15 % was used.

We observe that the probe power determines how fast the maximum level of spin-squeezing is reached. The higher the probe power, the faster the maximum level of conditional spin-squeezing. Interestingly, we observe the best spin-squeezing for the intermediate probing power. This could have different reasons. A possible explanation is that we are starting to get limited by electronic noise for the lowest probe power. This would explain why we do not observe better conditional spin-squeezing despite introducing less probe-induced decoherence. At the same time, we do not interrogate our system strongly enough to gain sufficient information during the squeezing preparation to compensate for other decoherence effects degrading the system's state

that we are probing. We also observe a slightly worse spin-squeezing when probing our system more vigorously using higher probing power. Given that in the absence of conditional spin-squeezing, the coupling constant has a clear optimum, one explanation could also be that the higher number of photons supersedes the one for the optimal coupling constant, and the back-action is more severe and exceeds the gains from the conditional measurement. However, we have not quantified the coupling constant κ beyond this passive optimization by optimizing the conditional spin-squeezing presented in this section. Another more technical point is that the highest probe power used here was the largest one we could use while maintaining the same settings for the input range of the LIA. From time to time, fluctuations in the setup could have led to short overshooting of the signals leading to punctual saturation of the LIA. Saturation would pose a limitation to our detection here. For this reason, we did not go to higher powers for the probe power. In order to do so, we would have been required to switch the input range of the LIA. However, this would lead to a different noise floor. This limits the comparability of different data sets when switching between settings. In order to ensure comparability, additional efforts are required. We have yet to do this, and the investigation is ongoing.

Optimizing the attainable level of spin-squeezing

In order to maximize the overall level of conditional spin-squeezing, we vary τ_A and τ_B for the duty cycle of 15 % and a probe power of 5 µW. In the previous subsections, we have seen that this duty cycle and probe power lead to the best results. We have already used the optimal squeezing preparation duration $\tau_A = 220\,\mu s$ and verification duration $\tau_B = 40\,\mu s$ in the previous figures since we could only vary one parameter at a time. However, now we will explain how we managed to find these optimal pulse durations. Since we use a sequence without a time gap between the two stroboscopic probe pulse trains, we can vary the time windows used for τ_A and τ_B during the analysis. Instead of calculating the conditional spin-squeezing for only a single value, we vary both parameters in steps of 5 µs during the analysis, allowing us to plot a two-dimensional parameter sweep. Instead of a 3D plot, we have chosen a heat map to illustrate the degree of spin-squeezing as it served clarity better. It is shown in figure 14.12. We expect two trends to be apparent when varying the squeezing preparation time τ_A and squeezing verification time τ_B. First, we expect a trade-off between the conditional spin-squeezing present in our collective spin ensemble and the duration of τ_A. We expect it to increase for the increased duration of τ_A due to the "knowledge" gained when extending the primary measurement that the second measurement is conditioned on during τ_B. At the same time, decoherence should degrade our spin-squeezing for extending $\tau_A$too long. This effect should also be reflected in the duration of τ_B. We can explain the degradation due to the decoherence as follows. We will see improvement if the information we learned during the first pulse is still maintained in the ensemble during our second

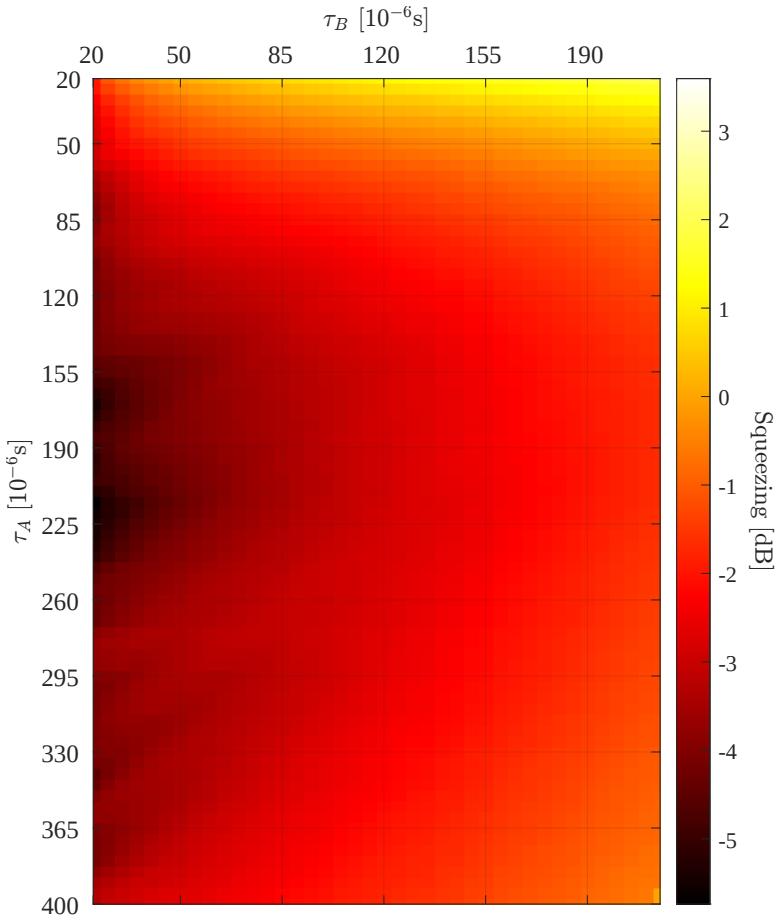

Figure 14.12: Squeezing heatmap. Obtained level of conditional spin-squeezing in dB for varying the squeezing preparation duration τ_A and squeezing retrieval duration τ_B, both in steps of 5 µs for the data set of 15 % duty cycle from figure 14.11 (center). The figure is replotted using smaller time bins using the same data as presented in figure 2 (b) from Zheng et al. (2022).

pulse. However, if decoherence affects the state, meaning that the state or information in our state changes during our measurement sequence, what we learned about our ensemble at the beginning of our pulse will have been altered by the end of the sequence. Conditioning on this information does not lead to further improvement and will even degrade our conditional spin-squeezing towards longer pulse durations. We hence expect a clear optimum of τ_A. This expectation is quickly confirmed in figure 14.12 and amounts to $\tau_A = 220\,\mu s$. At the same time, we also vary τ_B. Generally, the best conditional spin-squeezing is observed with short time windows for the squeezing verification, close to the minimum possible duration. From the data in figure 14.12 and the same approach for data sets with different probe powers and duty cycles, we determined our best degree of conditional spin-squeezing to be $10\log(\xi^2) = -4.6 \pm 0.6$ dB, obtained for the data set with the parameters

as stated in table 14.1. Especially the squeezing preparation time τ_A is an experimental timing of importance to us since we need to fix it as soon as we start introducing a gap between both stroboscopic pulse trains. For τ_B, the requirement is less stringent as we can always record a longer duration of $\tau_B$and truncate its length during the analysis. This degree of conditional spin-squeezing $10\log(\xi^2) = -4.6 \pm 0.6$ dB is the best we have observed throughout all data sets presented in this thesis. Using Sørensen and Mølmer (2001), the degree of conditional spin-squeezing together with the atomic polarization of >97 % can be used to estimate that our squeezing corresponds to groups of up to ten entangled atoms (compare Zheng et al. (2022)).

Probe power	5 µW
Duty cycle	15 %
Squeezing preparation time τ_A	220 µs
Squeezing verification time τ_B	40 µs
Degree of squeezing ($10\log(\xi^2)$)	-4.6 ± 0.6 dB

Table 14.1: Optimal parameters for squeezing preparation. Summary table of the relevant parameters to prepare and obtain the best level of conditional spin-squeezing in our collective spin state.

While a high level of conditional spin-squeezing for $\tau_B = 40\,\mu s$ naively seems to be the best possible choice for conducting our measurements, we must consider how our total quantum noise is comprised. The conditional spin-squeezing only affects the noise contribution arising from the atomic projection noise, not the shot and residual back-action noise. In figure 14.8, we have noted that for τ_B smaller than 50 µs, the projection noise is smaller than the contribution arising from the shot noise of light. However, conditional spin-squeezing impacts the atomic projection noise only. The maximal level of conditional spin-squeezing might not be the most beneficial choice regarding overall noise reduction, which will be investigated further in the next section (section 14.5).

14.5 Noise reduction vs. spin-squeezing

Naively, one would expect the best noise reduction for the highest degree of conditional spin-squeezing. However, when considering figure 14.8, it becomes apparent that for short τ_B, the contribution of shot noise to the overall quantum noise exceeds the contribution originating from the atomic projection noise. However, shot noise is not affected by conditional spin-squeezing. Only the projection noise of the atoms is. Therefore, our observed conditional quantum noise exploiting conditional spin-squeezing is still governed by shot noise, and the overall improvement of the noise reduction from the spin-squeezing is limited. When increasing the duration of τ_B, projection noise con-

tribution and shot noise are more on equal footing. In figure 14.8, we see that for $\tau_B = 100\,\mu s$, the contribution originating from the atomic projection noise is roughly two times the level of shot noise. This is more of a hand-waving argument regarding noise reduction for our preferred choice of $\tau_B = 100\,\mu s$. Following the observation in figure 14.8, it can be verified from the data that our choice is better for noise reduction than using $\tau_B = 40\,\mu s$ with the highest degree of conditional spin-squeezing in our ensemble. For quantifying the

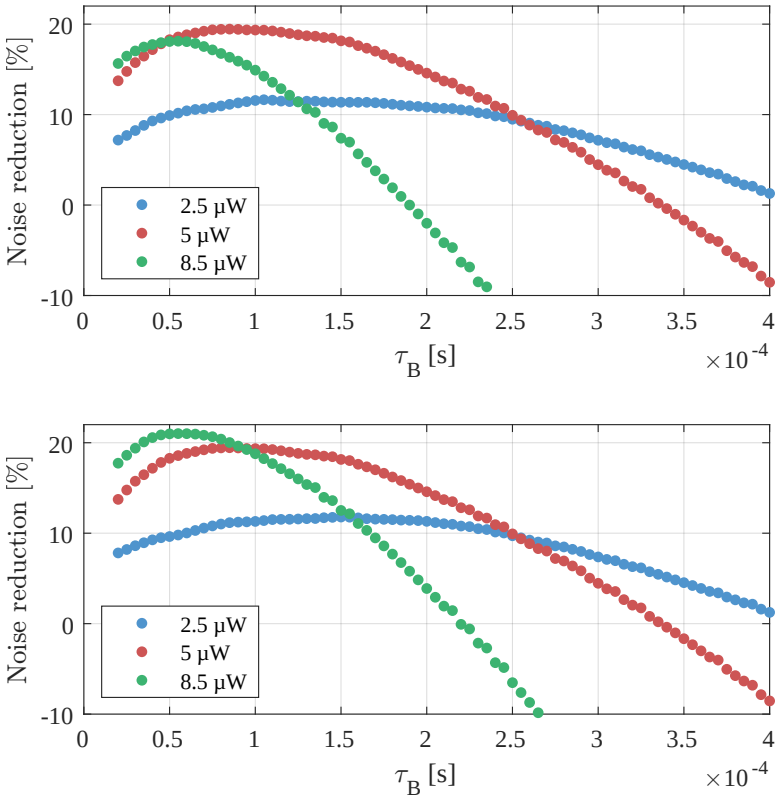

Figure 14.13: Conditional spin-squeezing versus gap duration. Calculated noise reduction for a fixed $\tau_A = 220\,\mu s$ for 15 % duty cycle and three different probing powers (top) and for respective individually optimized τ_A(bottom) using the values stated in table 14.2. The length of τ_B is varied, and the observed conditional quantum noise compared to the expected noise of a back-action-free measurement exhibiting quantum noise given by $\sqrt{SN_B + PN_B}$. Positive values indicate the reduction in percent compared to $\sqrt{SN_B + PN_B}$, while negative values mean our observed quantum noise exceeds it.

noise reduction, we calculate the reduction in quantum noise for the conditional signal and compare it with the combined shot and projection noise. The latter corresponds to the quantum noise in the absence of back-action noise. Moreover, scaling it with the total observed noise allows us to compare the reduction in noise in our measurement due to conditional spin-squeezing. In figure 14.13, the relative noise reduction is shown for a variable duration of τ_B. The observed noise is determined as the square root of the noise vari-

ance. We denote the shot noise and estimated contribution arising from the CSS projection noise over the duration τ_B as SN_B and PN_B to illustrate their origin. The best noise reduction is obtained for a choice of τ_B= 85 µs, corresponding to 19.4 %. However, the maximum is rather flat, and our intuitive choice used in Zheng et al. (2022) of τ_B = 100 µs is not far off of that optimum with 19.3 %. Using the best conditional spin-squeezing observed for τ_B = 40 µs, we observe only 17.1 % noise reduction for this shorter squeezing verification duration. Extending the readout duration for the squeezing verification pulse to τ_B = 100 µs leads to a sacrifice of the degree of spin-squeezing (-3.1 ± 0.3 dB), but we gain in the observed noise reduction due to the increasing contribution from the atomic projection noise to our overall noise. This comparison between optimal conditional spin-squeezing and overall noise reduction illustrates nicely that the highest degree of spin-squeezing not necessarily coincides with the maximal gain in noise reduction due to conditional spin-squeezing.

Probe power [µW]	τ_A [µs]	τ_B [µs]	Noise reduction [%]
2.5	220	130	11.5
5.0	220	85	19.4
8.5	220	55	18.1
Probe power [µW]	τ_A [µs]	τ_B [µs]	Noise reduction [%]
2.5	240	150	11.8
5.0	220	85	19.4
8.5	150	55	21.0

Table 14.2: Noise reduction for various settings. Comparison of obtained values for the best noise reduction. Upper part reflects the result when using optimal τ_A for squeezing for 5 µW setting, while lower values are individually optimized.

From the observation that maximal conditional spin-squeezing does not necessarily correspond to the best noise reduction, the different probing powers are revisited and analyzed for their noise reduction versus duration τ_B. This noise reduction is shown in the upper part of figure 14.13 with a fixed τ_A = 220 µs versus the duration of τ_B. Since the choice for τ_A stems from the optimized parameters for the 5 µW setting, it is not surprising that we also observe the best noise reduction for this probe power. However, this observation does not hold when re-running the optimization of the experimental timings for the other two probing powers. We can get an even better noise reduction with the higher probe power of 8.5 µW while simultaneously speeding up the overall measurement time. The noise reduction of 21.0 % compared to 19.4 % seems like a slight improvement but needs to be kept in mind for future optimization. This observation could indicate that even higher probe powers could benefit our scheme and need to be considered in the future.

It should be noted that we chose 5 µW probe power, along with a duty cycle of 15 %, as well as $\tau_B = 100\,\mu s$ for all quantum-enhance MIT measurements presented in Zheng et al. (2022). This more thorough analysis performed in the framework of this thesis hints that this choice could have been suboptimal. Partially, this optimization can be done in the analysis script, like the precise duration of τ_B. Other parameters, such as the probe power, would require entirely new experimental data acquisition as we acquired data for chapter 15 with a probe power of 5 µW. Therefore, all consecutive measurements presented in the following section and chapter will use this probe power only – due to lack of time, these measurements could not be optimized further and tested with other settings.

14.6 Decay of squeezing

For the operation of our collective spin-oscillator as a magnetometer, we need to be able to send an RF pulse to induce eddy currents in a conductive sample. A gap must be introduced between the squeezing preparation and verification pulse time windows to do so. We will delay the squeezing verification pulse to find a suitable gap duration τ_{gap} as indicated in figure 14.14. For now, the pulse sequence will not contain an RF pulse as this will be part of the chapter concerned with the eddy current detection in chapter 15.

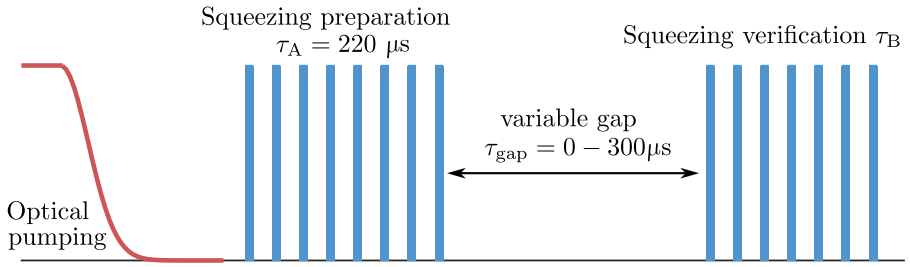

Figure 14.14: Pulse sequence with gap. Illustration of the pulse sequence with a gap using stroboscopic pulses with $D = 15\,\%$ (blue). The smooth turn-off of the optical pumping is indicated in red. For this sequence, the duration of the squeezing preparation is fixed to $\tau_A = 220\,\mu s$. The gap τ_{gap} can take values ranging between 0 µs and 300 µs. The duration of τ_B is optimized in the analysis.

We leave the RF coils disconnected from a function generator for this test. In figure 14.15, the observed levels of conditional spin-squeezing for gaps τ_{gap} ranging between 0 µs and 300 µs are shown. The measurement points are obtained using the previously determined optimal settings for the squeezing preparation time $\tau_A = 220\,\mu s$ and squeezing verification time $\tau_B = 100\,\mu s$. We again had to perform shot, electronic, thermal, and atomic noise measurements for each measurement setting. Each point in figure 14.15 corresponds to 36 000 individual measurement sequence repetitions. We expect shot and electronic noise not to depend on the choice of the gap τ_{gap}. These noise sources should only require a single measurement setting. Unfortunately, we

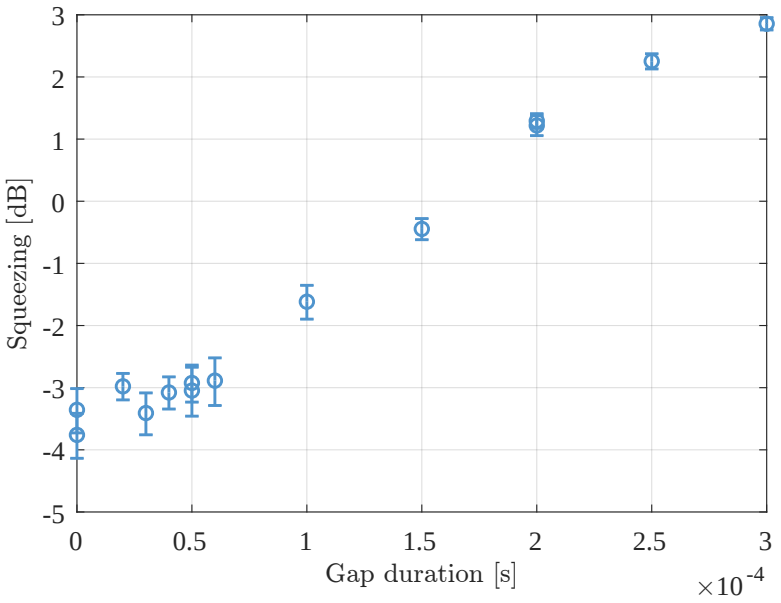

Figure 14.15: Spin-squeezing versus gap duration. This figure shows the observed level of spin-squeezing versus the gap width τ_{gap} between squeezing preparation ($\tau_A = 220\,\mu s$) and squeezing verification ($\tau_B = 100\,\mu s$). For the points at 0, 50, and 200 µs delay, two measurements originating from different days verify the repeatability of our experiment. Each point represents nine measurements containing 4 000 repetitions. Figure replotted from Zheng et al. (2022).

Gap τ_{gap} [µs]	Squeezing [dB]
0	-3.4 ± 0.4
	-3.8 ± 0.4
20	-3.0 ± 0.2
30	-3.4 ± 0.4
40	-3.1 ± 0.3
50	-3.0 ± 0.4
	-2.9 ± 0.3
60	-2.9 ± 0.4
100	-1.6 ± 0.3
150	-0.4 ± 0.2
200	1.2 ± 0.2
	1.3 ± 0.1
250	2.3 ± 0.1
300	2.9 ± 0.1

Table 14.3: Obtained values of spin-squeezing as plotted in figure 14.15 for $\tau_A = 220\,\mu s$ and $\tau_B = 100\,\mu s$. Data points that were measured twice were obtained on different days for repeatability.

observed a dependency of the shot noise from the gap duration τ_{gap}. This is most likely related to the detector response, which is missing for the shot noise trace when the gap τ_{gap} is not included in the time window. We, for simplicity, also measured shot noise traces with respective gaps between the stroboscopic pulse trains to obtain the same detector response as for the atomic signals.

In figure 14.15 and respective data in table 14.3, we note that the conditional spin-squeezing[11] degradation is only minuscule for values of τ_{gap} below 60 µs. However, decoherence has degraded the conditional spin-squeezing completely after only 200 µs gap between both stroboscopic pulse trains. Hence, we chose a gap τ_{gap} of 50 µs for the RF pulse when operating the spin-oscillator as a quantum-enhanced MIT sensor in chapter 15. This section concludes all our efforts in preparing and verifying the back-action evasion and conditional spin-squeezing. In the next chapter, we will put things to the test and operate our system with the here-found optimal parameters as a quantum-enhanced sensor detecting the presence of a conductive sample.

[11] Please note that the overall levels of squeezing are lower since we chose to perform the analysis with $\tau_B = 100\,\mu s$ instead of $\tau_B = 40\,\mu s$. This is why for a delay of zero microseconds, we have a different value of the conditional spin-squeezing as in figure 14.10.

Chapter 15

Proof-of-principle: Quantum-enhanced MIT

After preparing the conditional squeezing of the spins and evading the back-action noise to a large extent in the previous chapter 14, this chapter will focus on quantum-enhanced magnetic induction tomography (MIT). As introduced in chapter 12, MIT relies on induced eddy currents in a sample that can be recorded. In a proof-of-principle experiment, we wish to combine the well-known technique of magnetic induction tomography using an atomic magnetometer with the technique of conditional spin-squeezing and back-action evasion. Combining these two well-known techniques, we aim to add quantum-enhanced MIT (QMIT) to the variety of existing quantum protocols. Our manuscript submitted for publication, Zheng et al. (2022), has already established the results. Here, we present them and elaborate on the findings in more in-depth. Throughout this chapter, we will shortly address the operating principle of the quantum-enhanced MIT before turning to the proof-of-principle demonstration. Our sample measurement will focus on two parts. First, we will consider a static sample, which we will use to optimize the measured signal. In the second step, we will move the sample to present the 1D tomography of a small conductive sample.

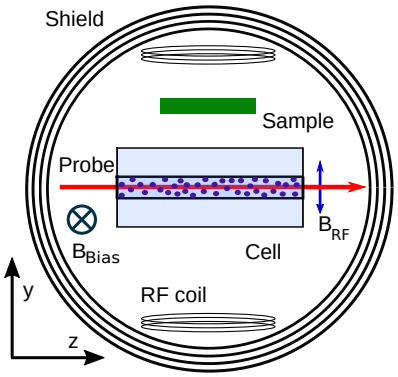

Figure 15.1: Sample and cell configuration. Transverse view of the cell and RF coil configuration inside the shield. The conductive sample (green) is placed in-between the cell and one RF coil, distorting the zero mean field seen by the collective spin-oscillator from the anti-parallel connected RF coils (40 mm radius, ten windings). The response with and without the sample is optically read out with the probing beam (red). Figure adapted from Figure 1 (a) in Zheng et al. (2022).

15.1 QMIT operating principle

For the quantum-enhanced MIT, we extend our experimental configuration used in the previous chapter by a small titanium sample of 10 mm × 10 mm × 1 mm size, placed in between one of the RF coils and the vapor cell. An illustration of the sample, cell, and coil configuration is shown in figure 15.1.

The previous chapter introduced a gap between the squeezing preparation and verification pulses. The gap is necessary for sending an optional RF pulse. Including this RF pulse into the sequence, the pulse sequence is changed to the one shown in figure 15.2. Introducing an RF pulse into the gap is required as this pulse is our only way to induce eddy currents in a conductive sample we

wish to detect. The RF pulse can be sent using a pair of RF coils, generating a field transverse to the bias magnetic field and our probing beam propagation direction (figure 15.1). Noteworthy in our case is that we connect the RF coils for our quantum-enhanced MIT in an anti-parallel configuration. This anti-parallel configuration serves the purpose that we do not record any signal in the absence of a conductive sample. The collective spin-oscillator is only disturbed in the presence of a conductive sample. The induced eddy currents in the conductive sample unbalance the RF field seen by the collective spin-oscillator. Only then a mean transverse spin component will be created. The resulting signal can then be recorded when optically probing the atoms.

Before considering the experiment in more detail, we want to illustrate what happens when the conductive sample is placed inside the RF magnetic field. The generated field is attenuated within the sample. The frequency-dependent skin depth characterizes the penetration depth of a magnetic field oscillating at a given frequency ω as

$$d(\omega) \approx \sqrt{2/(\omega \mu_0 \sigma)} \tag{15.1}$$

Here, μ_0 is the vacuum permeability, and σ is the conductivity of a sample in S/m (Jensen et al. (2019)), assuming an object is non-magnetic. The skin depth describes how the primary field from our RF coil is exponentially decaying inside the conductive sample. The higher the conductivity σ of a sample, the smaller the skin depth. In a sense, the skin depth determines where the currents are located in a sample and how far they "reach" into a conductive sample. For our experiment, we use a small piece of titanium of 1 mm thickness and conductivity of $\sigma = 1.8 \cdot 10^6$ S/m. At our choice of $\omega_{\mathrm{RF}} = 2\pi \cdot 725\,\mathrm{kHz}$, the skin depth is $\delta \approx 0.4\,\mathrm{mm}$.

As previously introduced, the RF coils are connected in an anti-parallel Helmholtz configuration, and the field at the center between them at the vapor cell is effectively zero. The collective spin-oscillator will not be disturbed for a zero mean field, and the mean transverse spin projections will remain zero. Placing a conductive sample between one of the RF coils and the cell, i.e., the sample is located closer to one of the RF coils (compare figure 15.1), the eddy currents create an additional magnetic field. This magnetic field originating from the eddy currents distorts the cancellation of the RF magnetic field at the vapor cell, and the collective spin is now subjected to a finite mean field. Hence, the presence of a conductive sample will affect our collective spin-oscillator. For a finite duration τ of the RF pulse starting at time $t = 0$, a finite transverse spin component will be created (Jensen and Polzik, 2013):

$$\langle J_\perp \rangle = \frac{\gamma B_{\mathrm{ec}} J_x T_2}{2} \left[1 - \exp\left(-\tau / T_2\right)\right] \tag{15.2}$$

Here, $\gamma = \frac{g_F \mu_B}{\hbar}$ is the gyromagnetic ratio, T_2 the transverse spin coherence time, J_x the macroscopic spin, and B_{ec} the magnetic fields arising from the eddy currents. Following the previous chapter, the probing signal is recorded

by probing the spin-oscillator optically. As before, we use polarization homodyne detection to record the signal. During the analysis, we optionally condition the measurement after the RF pulse on the measurement preceding the RF pulse inducing eddy currents in the sample (figure 15.2). In the following, we will concern ourselves with two types of measurements. First, a static sample measurement where we only detect the presence of a sample (section 15.2). We will use this measurement to optimize the obtained signals. Following this, we will perform a 1D tomography using our quantum-enhanced measurement protocol, where we try to map our atomic response versus the sample location (section 15.3).

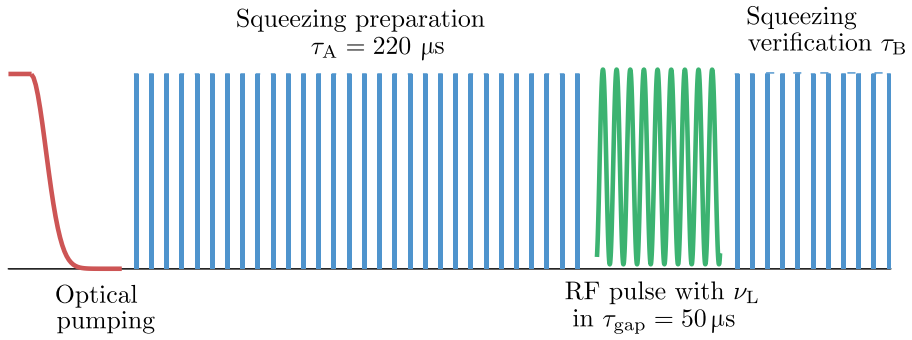

Figure 15.2: Pulse sequence with gap and RF pulse. Stroboscopic pulses for squeezing preparation $\tau_A = 220\,\mu s$ and verification $\tau_B = 100\,\mu s$ (blue) with an RF pulse (green) in-between them to induce eddy currents in a sample for the quantum-enhanced MIT. The duty cycle of the stroboscopic probe trains is 15 %.

15.2 Quantum-enhanced sample measurement

Having illustrated the fundamentals and the approach towards performing the quantum-enhanced MIT, we can start putting the parts together to perform our proof-of-principle measurement. To do so, we will use the previously found suitable parameters for the optical probing power of 5 µW, a duty cycle of 15 %, and the stroboscopic pulse train durations of $\tau_A = 220\,\mu s$ and $\tau_B = 100\,\mu s$ (see section 14.5 and table 14.2). In the first step, we introduce an RF pulse between the two stroboscopic pulse trains, as indicated in figure 15.2, to enable the induction of eddy currents in a conductive sample. The previous chapter shows that a gap of approximately 50 µs should not degrade the spin-squeezing too much. The RF pulse has to match the Larmor frequency of the macroscopic spin precession. We adjust the exact span of the gap to fit an integer number of RF oscillations between the two stroboscopic probing pulses. Since we experimentally observed technical noise compromising our measurements using our standard function generators, we use a low noise function generator of the type RIGOL DG952 SiFi II for the RF pulse generation.

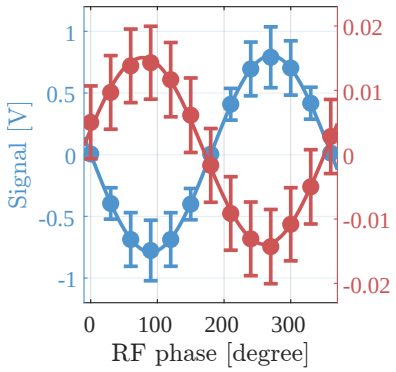

Figure 15.3: Eddy-current phase optimization. Recorded signal detected with the lock-in amplifier versus the RF phase setting of our function generator for the RF coils connected in parallel (blue) and the detected eddy current signal of the sample (red), obtained for the RF coils in the anti-parallel configuration. The eddy current signal (red) is the difference between the recording with and without the sample. Each point is the average of 2 000 measurements, while error bars reflect the statistical deviation across the measurements.

	Phase [°]
RF max.	270
Signal max.	78
Phase difference	-192

Table 15.1: Phase optimization. Values for the phase as obtained from the fits as shown in figure 15.3 and the respective phase shift of the signal recording compared to the RF signal.

We expect the signal strength to vary depending on the phase of the RF pulse concerning the stroboscopic pulses and macroscopic spin precession. Similar to the phase optimization between the lock-in amplifier and the stroboscopic probing in 14.2, we need to optimize the phase of the RF signal to our other signals. To do so, we optimize the phase of the RF field to maximize the recorded eddy current signal. We perform two steps to find the optimal settings. First, we connect the RF coils in parallel to get a mean field at the cell without any conducting sample. Only then will we have a transverse spin component of our collective spin-oscillator without the conductive sample. Then we record the signal in steps of 30 degrees for the RF phase set on the function generator. The RF strength is 100 mV, and the result is shown in blue in figure 15.3. Then, we connect the RF coils in an anti-parallel configuration and repeat the measurement versus the RF phase for two arrangements, once in the presence of a conductive sample and once without the sample. The latter is used as a background trace which we subtract from the measurement with the sample (Titanium 10 x 10 x 1 mm^3, approximately 10^6 S/m). The resulting signals are shown in figure 15.3. The blue points indicate the recordings of the transverse spin component when driving the RF coils in parallel without the conductive sample. The red points correspond to the difference between the sample and no-sample measurements when connecting the RF coils in an anti-parallel configuration. We subtract the sample and no-sample measurements to get the pure response of the transverse spin component arising from the induced eddy currents. These eddy current signals are, of course, significantly smaller. Therefore a second scale is used for the red points in figure 15.3. We fit sinusoidal functions to both measurements to determine the best phase for eddy current detection. The phase difference between both tells us about the phase delay between the applied RF magnetic field and the phase of the magnetic field response in the sample.

The expected phase difference between the recorded eddy current signal and the RF oscillation can be modeled. As part of his Master Thesis, Alan Oesterle (Oesterle (2022)) modeled the expected response of our atomic spin-oscillator at different Larmor frequencies in the presence of the weakly magnetic titanium sample. He determined the expected phase difference to be -170 degrees at our Larmor frequency of 725 kHz. This value differs 22 degrees from the experimentally observed value (table 15.1). We have some suspicions about where the discrepancy could originate. For once, our inner aluminum shield could also be subjected to eddy currents which are only recorded in the presence of another sample as we balance the signal in the absence of the titanium sample. Another reason could be the differeing impedances of our two RF coils depending on the orientation we connect them with respect to each other. To this end, we have not found the reason for the discrepancy between model prediction and our experimentally observed phase difference.

In addition to the RF phase-dependent signal, we also investigate the influence of the RF phase on the degree of spin-squeezing. We do this for both cases, with and without the titanium sample present. The results are shown

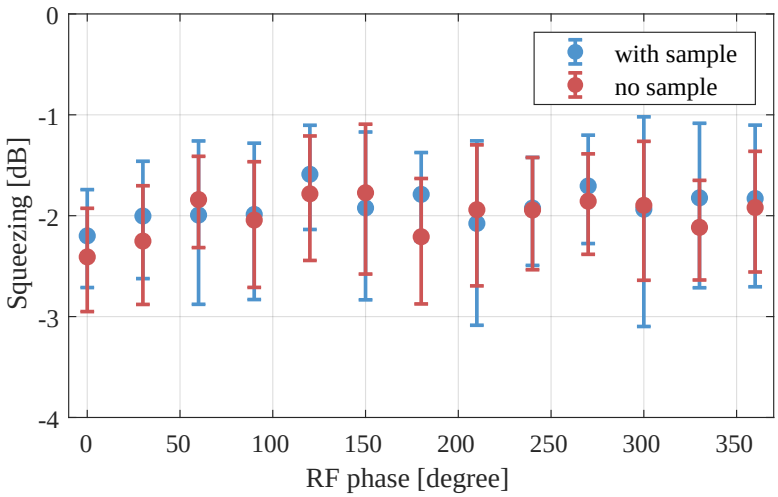

Figure 15.4: Squeezing versus RF phase. Shown are the obtained values of squeezing when varying the RF phase with (blue) and without (red) sample. Error bars are estimated from 4 datasets containing 4 000 measurements each.

in figure 15.4. There are three observations worth noting. First, the degree of spin-squeezing $10\log(\xi^2)$, determined according to equation (14.12), does not seem to depend on whether the sample is present. Secondly, there does not seem to be an explicit RF phase dependency. The third observation is the most important one. While we expected a slight reduction in the observed spin-squeezing due to the disturbance of our system when applying an RF pulse, we observed a significant degradation of the conditional spin-squeezing:

$$10\log\left(\xi^2\right) = (1.8 \pm 0.2)\ \text{dB}$$

The degradation is despite using the optimal parameters obtained in the previous chapter of $\tau_A = 220\,\mu\text{s}$ and $\tau_B = 100\,\mu\text{s}$ with 15 % of duty cycle and $5\,\mu\text{W}$ of average optical probing power. For the same setting, but without the RF coils connected to any function generator, we obtained using the same gap between squeezing preparation and verification pulses roughly -3 dB of conditional spin-squeezing (compare table 14.3). We have yet to pinpoint the reason for the drop in the degree of conditional spin-squeezing. From the observation that we have this degradation once the coils are connected to a function generator, but there is hardly a difference in whether we send a signal or not, we believe that we possibly have a problem with ground loops or unwanted induced currents adding to or increasing the speed of the decoherence of our level of conditional spin-squeezing. We have yet to identify the reason, and the investigations are ongoing.

While we are not as good in the degree of spin-squeezing as we hoped for the eddy current detection based on the results from the previous chapter, we still tried to investigate the improvement arising from our stroboscopic probing and conditional spin-squeezed measurements. For this purpose, we

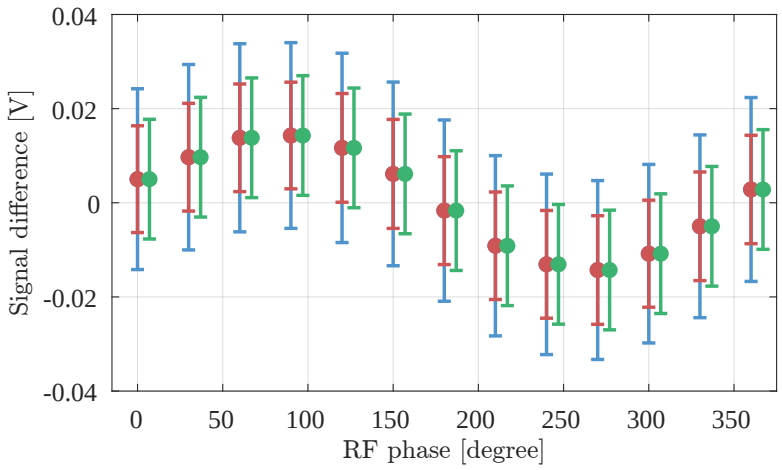

Figure 15.5: Quantum-enhanced MIT signal versus RF phase. Eddy current signals, as a function of the RF phase, are obtained by subtracting the background signal from the sample signal. Each point reflects the average value of 16 000 measurements. The standard deviation corresponds to the single-shot uncertainty, with blue and red representing unconditional and conditional (squeezed) results, respectively. The green error bars represent the quantum noise $\sqrt{\mathrm{SN_B} + \mathrm{PN_B}}$, which corresponds to the back-action evaded measurement without squeezing and are horizontally shifted for clarity. Figure (replotted) and caption from figure 3 (b) in Zheng et al. (2022).

determined the conditional and unconditional noise for the eddy current signal for single-shot measurements. This means we determine the signal per measurement sequence and subtract the sample signal from the no-sample (background) signal. We repeat the measurement sequence for each parameter setting 16 000 times. We can determine the average single-shot measurement value and the spread of the values from this. For the statistical spread of the measurements, we can distinguish three cases. First, we can consider the unconditional uncertainty based solely on the obtained measurement during $\tau_\mathrm{B} = 100\,\mu\mathrm{s}$. The unconditional measurements are shown in figure 15.5 in blue. Further, we can determine the conditional uncertainty, which should be reduced due to the spin-squeezing present in our system, and is shown in red in figure 15.5. As a last step, we wish to compare the uncertainty of our measurements with the expected uncertainty for a back-action-free measurement. From equation (3.29), we know that the quantum noise variance for a measurement in the absence of back-action is given by evaluating the equation with $C \to 0$. The sum of the contributions arising from the shot noise of light and the atomic projection noise provides us with an estimate of the quantum noise in a completely back-action-free measurement. To estimate this, we estimate the contribution originating from the projection noise as discussed in section 14.1.3 from our thermal noise measurement. The standard deviation of the back-action-free measurement is then determined as $\sqrt{\mathrm{SN_B} + \mathrm{PN_B}}$, based on the theoretical motivation in section 3.2 and equation (3.30). We do not consider the spin-squeezing in this expression as we want to compare our ob-

served noise to a purely back-action-free measurement. This back-action-free quantum noise is shown as green error bars in figure 15.5, shifted for better visibility.

	Noise [mV]
Unconditional	19.7
Back-action-free	14.3
Conditional	11.3
	Noise reduction [%]
Conditional to unconditional	42.5
Conditional to back-action-free	10.9
	Signal-to-noise ratio
Unconditional	0.72
Back-action-free	1.11
Conditional	1.26

Table 15.2: Overview quantum noise reduction and SNR improvement. Experimentally observed quantum noise reductions and changes in signal-to-noise ratio for optimal relative output phase in figure 15.5. We compare conditional, unconditional, and back-action-free ($\sqrt{\mathrm{SN_B} + \mathrm{PN_B}}$) single-shot quantum noise estimates with each other.

We determine the best setting for the RF phase to be 90 degrees since we observe the maximal signal for this RF phase setting using the figures 15.3 and 15.5. Therefore, we determine the signal-to-noise ratio and noise reduction for this phase setting. Table 15.2 shows an overview of the values. For the 16 000 measurement repetitions for the sample and no-sample measurements, we determine the single-shot measurement uncertainty to change by $(41 \pm 1)\%$ from the unconditional to conditional measurement considering all 13 measured phases. The noise reduction is 42.5 % for the optimal phase. With this level of noise reduction, we observe a signal-to-noise improvement from 0.72 to 1.26 by exploiting the conditional spin-squeezing, which corresponds to roughly 75 %. This improvement is significant despite the drop in the degree of spin-squeezing present for the QMIT measurement.

In addition to the comparison between conditional and unconditional measurement, we wish to compare our squeezing-enhanced measurement with the expected quantum noise for a measurement without back-action and spin-squeezing governed purely by $\sqrt{\mathrm{SN_B} + \mathrm{PN_B}}$. For this, we estimate the projection noise of a coherent spin state based on the thermal spin state measurement (see section 14.1.3). We see in figure 15.5 that we gain in signal-to-noise ratio and observe 10.9 % noise reduction. We should note that this is a significant result since our practical reality is somewhat slightly different. First, in

the previous section, we observed, as expected, some finite back-action noise for a duty cycle of 15 % for the stroboscopic probing pulses. Of course, it is significantly reduced compared to a continuous probing pulse. Also, as mentioned in section 13.3, our atomic ensemble is not prepared in a perfect coherent state. The estimate for the quantum noise of a back-action-free measurement as stated in table 15.2 underestimates the actual projection noise of our spin-oscillator due to the assumption of a coherent spin state which prominently features the minimal projection noise. Hence, our estimate for the projection noise underestimates the one present in our system. Without correcting for this, the value stated in 15.2 puts more of a lower limit on the actual noise reduction. Further, we also have additional noise arising from the finite back-action noise introduced by our measurement. We will address this issue in the discussion and outlook chapter for the quantum-enhanced MIT experiment (chapter 16).

For comparison, we also estimate the expected noise reduction r between conditional spin-squeezing and without it for the back-action-free case:

$$\mathrm{r} = 1 - \frac{\sqrt{\mathrm{SN_B} + \xi^2 \mathrm{PN_B}}}{\sqrt{\mathrm{SN_B} + \mathrm{PN_B}}} \approx 11\,\% \tag{15.3}$$

This value is on par with what we experimentally observe using conditional measurement. That it is on par with the value stated in table 15.2 is more of a coincidence considering the previously mentioned issues with the finite back-action in our conditional measurement as well as underestimating the true projection noise.

Considering single-shot measurements between the sample and no-sample measurements, we observe an apparent reduction in quantum noise exploiting conditional spin-squeezing below the expected quantum noise in a back-action-free measurement. A second comparison we would like to address is the one to a classical measurement's standard quantum limit (SQL). We introduced the SQL in equation (3.15). It is $1 + 2/\sqrt{3}$ times larger than the contribution arising from the projection noise variance, previously introduced as PN. For the standard deviation, this corresponds to a factor of $\sqrt{1 + 2/\sqrt{3}} \approx 1.47$. For comparison, our observed quantum noise in units of projection noise contribution $\sqrt{\mathrm{PN_B}}$ for the conditional measurement amounts to $1.11\sqrt{\mathrm{PN_B}}$. We use this to compare our experimentally observed single-shot measurement noise with the expected SQL of a classical measurement. We observe a noise reduction of $1.11/1.47 = 0.76$ compared to the SQL of a classical measurement. The observed standard deviation verifies that we can improve the sensitivity beyond the SQL by reducing the back-action introduced to our system and exploiting conditional spin-squeezing. We will revisit these results and put them into context as part of the outlook in the next chapter (chapter 16). With this tool set at hand, we can finally combine all our efforts in finding the optimal settings to perform our desired proof-of-principle experiment where the sample is moved past the cell to perform a quantum-enhanced 1D magnetic induction tomography.

15.3 1D quantum-enhanced magnetic induction tomography

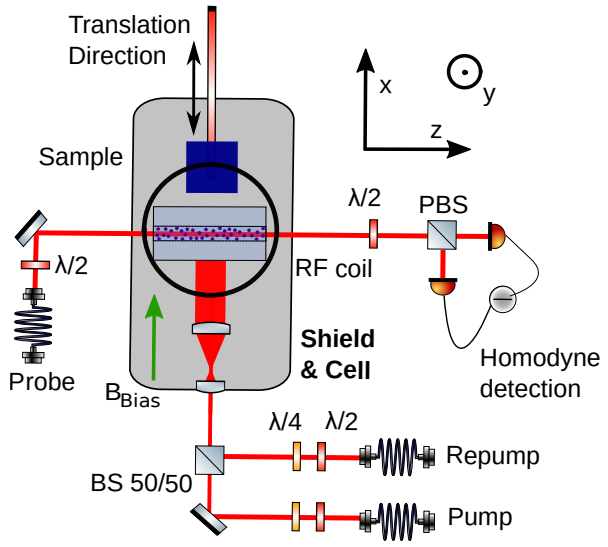

Figure 15.6: Setup for 1D tomography. The top view of the experimental setup illustrates relevant optics, including magnetic field direction, beam propagation directions, and the sample translation direction. As before, we indicate (polarizing) beamsplitter as (P)BS, while half and quarter waveplates are indicated as $\lambda/2$ and $\lambda/4$. Figure adapted from figure 1 (b) in Zheng et al. (2022).

Typically, tomography is a technique that maps out the properties of a sample non-invasively. We also want to test our system's response depending on the position of the sample. For this purpose, we move our sample using a precision stage in steps of 1 mm transverse to the cell channel. In principle, we could also move the cell past the sample, which will be required when thinking about a working prototype with potential industrial or medical applications. However, this would add complexity to the optical probing in our current experimental setup. Therefore, we move the sample instead. Figure 15.6 illustrates a simplified experimental setup, indicating relevant optics and beam paths, along with the translation direction of the sample. At each position, we record the atomic and thermal spin noise signals. For shot and electronic noise, we record only one measurement trace each since the sample's position does not influence those signals.

We record a total of 51 positions of the sample. We recorded 4 000 measurement sequences for each setting. Each sequence contains optical pumping, squeezing preparation, RF pulse, and optical readout. As before, we determine the signal as the difference between the measurement with the sample and the no-sample signal. As before, we first concern ourselves with the single-shot measurements comparing a single measurement sequence with and without a sample and determining their average and distribution. The result is shown in the upper part of figure 15.7, where we distinguish unconditional (blue) and conditional (red) results. We recover the same improvement

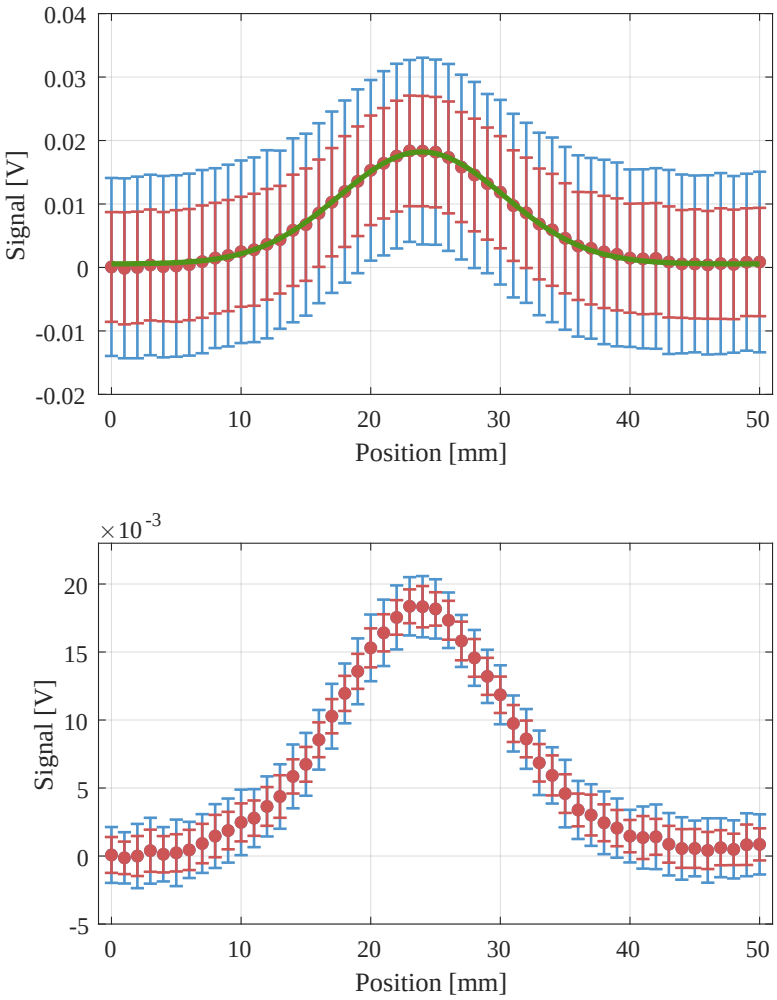

Figure 15.7: 1D tomography of a sample. Eddy current signal (sample − no sample signal) versus sample position. Top: Error bars reflect conditional (red) and unconditional (blue) uncertainty for the average single-shot measurement from 4 000 measurement repetitions. To the mean response of the single-shot measurements, we fit a Gaussian response function (equation (15.4)), and the result is plotted as a green line. Bottom: Error bars reflect the conditional (red) and unconditional (blue) uncertainty corresponding to the spread of 100 measurements containing 40 measurement repetitions each. The top part of this figure is replotted from figure 3 (b) in Zheng et al. (2022).

between the two cases as in the previous section ($r \approx 42\,\%$). To determine the maximal response, we fit the 1D tomography trace to a fitting model consisting of a Gaussian function as given by:

$$f(x) = A \exp\left(-\frac{(x-b)^2}{2c^2}\right) + d \tag{15.4}$$

Fitting the average of our single-shot measurements to this function, we ob-

tain the line shown in green in the top part of figure 15.7. We observe good agreement with the model. One thing to note is that the mean number is higher towards higher position values. Time-wise, these measurements were also recorded towards the end of the sweep. Hence, we attribute this slightly different base level to drifts in our experimental setup. To this end, we have not investigated this behavior further and extended, for example, this measurement to a forward and backward sweep[1].

However, we get an estimate for the sample center position from this fit. This can be investigated further by clustering the 4 000 measurement points at each sample position into sets of 40 measurements. For each of these 100 averaged measurements, we can individually fit the sweep as done for the top part in figure 15.7. Each of these 100 fits gives an estimate for the center position of the sample response. We get a distribution of results due to the fluctuation of the measurement results. We compare the results obtained for conditional and unconditional measurements. The average and standard deviation of the clustered measurements are shown in the lower part of figure 15.7. In contrast, the spread of the center distribution of the sample is shown in figure 15.8. As expected, clustering the data into more extensive data sets improves the signal-to-noise ratio when comparing the top and bottom parts in figure 15.7. In table 15.3, we state the values of the mean, the conditional and unconditional uncertainty for the maximum point in figure 15.7. As expected, the conditional measurements exhibit a lower uncertainty than the unconditional ones, leading to a higher signal-to-noise ratio. Averaging the measurement 40 times and considering the spread when comparing 100 such sets, we expect an improvement of $\sqrt{40} \approx 6.3$ in both cases. For our experimental data, we even observe an improvement of 6.8 and 7.1 for unconditional and conditional measurement, respectively. This is even slightly better than expected.

	Single-shot	**40 averages**
Mean [mV]	18.4	18.4
Unconditional std [mV]	14.3	2.1
Conditional std [mV]	8.7	1.2
Unconditional SNR	1.3	8.6
Conditional SNR	2.1	14.8

Table 15.3: Comparison SNR 1D tomography. Estimated mean, uncertainty, and respective SNR as estimated from the data presented in figure 15.7 for the 4 000 single-shot measurements and considering the spread when considering 100 measurements containing 40 measurement repetitions each.

In figure 15.8, we plot the spread of the center positions of the sample obtained for the 100 measurements, containing 40 measurement repetitions each, using the fit model from equation (15.4) from their mean value. We consider, as before, conditional (red) and unconditional (blue) measurements. Using the

[1] The cautious reader might also observe that the signal-to-noise ratio is slightly better here when comparing to figure 15.5. We attribute the difference to the two different ways of positioning the sample with respect to the cell. In the optimization process, we had the sample attached to a 3D-printed holder sliding it in through a hole in the top of the shield. This holder was used to ensure precise and repeatable placement of the sample concerning the vapor cell. For the 1D tomography, we had to slide the sample past the cell. Hence, a holder resembling a long stick had to be used to slide the titanium sample in from the side. The most likely explanation is that the sample distance and precise location are different between the two measurements. Furthermore, the two measurements were performed with a separation of a few weeks.

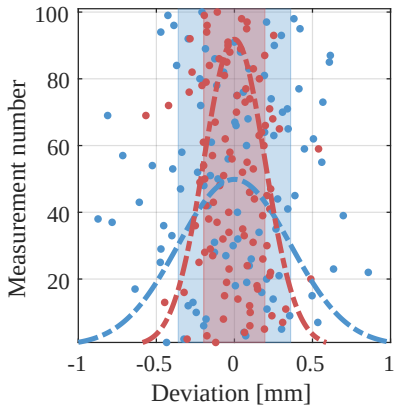

Figure 15.8: Sample center distribution. Fitting a Gaussian to the 100 data sets containing 40 measurements for each sweep shown in figure 15.7, the center values from the fit are shown for the conditional (red) and unconditional (blue) measurements. The dashed-dotted lines represent scaled normal distributions from the conditional and unconditional measurements, along with colored areas reflecting one standard deviation for the conditional (red) and unconditional (blue) distributions from their mean. Figure replotted from figure 4 in Zheng et al. (2022).

respective 100 individual results, we can determine the standard deviation for conditional and unconditional measurements. For illustration, we shade the area red and blue to illustrate the spread of one standard deviation. We plot scaled Gaussian distributions with the respective standard deviation as a visual guide to aid the reader. We recover the same behavior as in the previous section: The conditional measurement exploiting spin-squeezing has a significantly lower spread in the values than the unconditional measurement. The spread of the results for the center of the response signal is centered around 23.93 mm. The spread across the 100 measurement sets is 0.36 mm for the unconditional measurements. At the same time, the distribution is significantly narrower for the conditional measurements, amounting to only 0.20 mm.

When we perform our measurements, a single pulse sequence, including optical pumping and the stroboscopic probing sequence with the RF pulse, the total duration is 13 ms. With this measurement duration, a single sample position with 40 sequence repetitions can be recorded within 520 ms. For a full sweep of 51 positions, we then would need 26 s to get an estimate of the center of the sample within 0.20 mm.

To summarize the findings within this chapter, we have successfully combined the well-known techniques of conditional spin-squeezing and magnetic induction tomography and introduced a new quantum sensing protocol called quantum-enhanced MIT. In this proof-of-principle experiment, we have detected a conductive sample made of titanium and shown a single-shot measurement uncertainty below the SQL of a classical measurement. Further, with the spin-squeezing present in our system, we have observed a conditional uncertainty below that of a back-action-free measurement. We could observe a signal by performing a 1D scan of our sample past the vapor cell and determine its central location with a small uncertainty. In the outlook and discussion of this QMIT experiment, chapter 16, we will put the results of this chapter into the context of possible applications and other experimental approaches. Further, we will address some of the current limitations and possible remedies.

Chapter 16

Discussion and next steps

We have successfully implemented conditional spin-squeezing and reduced the back-action noise introduced into our system when probing the spin-oscillator. The conditional spin-squeezing allowed us to reduce the contribution to our noise originating from the atomic projection noise. We verified in a proof-of-principle measurement the possibility of combining the well-known technique of magnetic induction tomography with stroboscopic back-action evasion and conditional spin-squeezing to enhance it using these quantum mechanical resources. In the following, we will try to put our results into perspective with different experimental approaches, the focus point of section 16.1. Additionally, we will discuss some of our previously addressed limitations and address how to possibly overcome them in section 16.2. At last, we wish to address some possible future pathways of our experiment in section 16.3.

16.1 Benchmark

To the best of our knowledge, we added quantum-enhanced MIT to the variety of quantum sensing protocols as presented in our manuscript Zheng et al. (2022). Of course, magnetic induction tomography is a well-established measurement protocol and has also been widely used with atomic magnetometers. The other components, conditional spin-squeezing and back-action evasion, have previously been exploited in other experimental configurations. Therefore, we will provide some context to our approach and other experimental approaches.

Magnetic induction tomography

Magnetic induction tomography is a convenient method of performing non-invasive and non-destructive scans of materials by analyzing their response to magnetic fields. Atomic ensembles have been a popular choice as a sensor for recording the response of conductive materials, and many experimental implementations using room-temperature atomic systems have been

pursued. Similar to our choice, a common feature is to test the working principle using metallic samples that are non or only weakly magnetic. For example, the authors of Wickenbrock et al. (2014) imaged the phase and amplitude of differently shaped aluminum pieces using a Rubidium vapor cell. Using 2D scans, the authors in Wickenbrock et al. (2014) obtain conductivity maps of the surface of their samples. The same group extended their efforts to different non-magnetic metals using an atomic magnetometer as presented in Wickenbrock et al. (2016). There, the authors exploit the RF frequency-dependent amplitude and phase response for different conducting metals to distinguish the materials from each other. Using 2D scans of their samples, Wickenbrock et al. (2016) obtain a spatial resolution of the eddy currents in the sub-mm range. It should be noted that their RF coil has only a diameter of 0.5 mm (Wickenbrock et al., 2016), and their experimental geometry is slightly different. In our experiment, we use a larger RF coil which limits the attainable spatial resolution of our image since it "washes" the edges out. However, in our 1D scan, we could also determine the sample's center with a sub-mm precision. Fundamentally, our approach should allow for similar measurements as presented in Wickenbrock et al. (2016) when adapting the RF coil design and extending our 1D to a 2D scan. While we did not present it in this thesis, we have the technical ability to change the bias magnetic field and hence Zeeman level splitting to perform the measurements using different RF frequencies. In both papers by this group (Wickenbrock et al. (2014, 2016)), the group exploited RF frequencies of up to 250 kHz. Our experimental configuration is operating at roughly three times that.

The same group has also pursued a different approach towards the free-space operation of an RF magnetometer and performing MIT of metallic objects without needing a magnetic shield. Shield-free experimental approaches are an advantage to our current and previous approaches at Quantop. Here, and also previous experiments (for example, Jensen et al. (2019)), rely on shielding our vapor cell from external magnetic fields. With proper design and control of free space coils, pursuing such an approach in the future seems realistic. We emphasize that while it is possible, the requirements and changes to implement free-space operation using our choice of magnetic field configuration are not trivial. In Deans et al. (2016), the authors show free-space measurements at an RF frequency of only 10 kHz. Using a 2D scan, they record and resolve discontinuation in an aluminum ring. The same group extended their free-space approach by performing measurements of a sample that is shielded from the vapor cell in Deans et al. (2017) using a small ferromagnetic shield. When imaging an object, the authors successfully demonstrated effective compensation of DC magnetic field contributions due to such ferromagnetic shields. An alternative approach of unshielded measurements focusing on the detection of conductive disks using a portable optically pumped magnetometer also operating in the 10 kHz regime is presented in Rushton et al. (2022). The authors of Rushton et al. (2022) show successfully that their system allows for the detection of aluminum discs for distances of up to 25 cm.

This publication is a rather considerable improvement and step towards the true scalability and portability of an optically pumped atomic magnetometer operating at room-temperature.

Many of the beforementioned approaches employ samples of a similar conductivity as we did throughout chapter 15. A direct comparison of the results for the signal-to-noise ratio and corresponding measurement duration is not possible. Herefore, it is hard to quantify the precise improvement of our measurements by exploiting quantum enhancement with the reported results and comparing relevant parameters like measurement duration. Our results verify that we can use a quantum-enhanced MIT to detect a conductive sample and its center location when performing a 1D tomography. For future reference and better benchmark with continuously operating MIT using atomic magnetometers, we need to implement 2D scans and also vary the Larmor frequency of our atomic magnetometer to benchmark our current approach more thoroughly against existing approaches.

We have to acknowledge that in our current experimental setup and proof-of-principle measurements using a titanium sample with conductivity on the order of 10^6 S/m is not yet operating at a level where we can compare ourselves to the results presented in, for example, Jensen et al. (2019). There, a saltwater phantom with a conductivity of five orders of magnitude lower than our choice of titanium could be detected. With an application of sensing within the field of biomedical imaging in mind, the quantum enhancement will only prove to be a viable addition if we reach at least the sensitivity of 1 S/m in a reasonable measurement time. The requirements will be addressed in section 16.3. Further, we will comment on the issue from the low measurement duration to overall preparation time in our protocol compared to the continuous operating MIT protocols (section 16.3.2).

Spin-squeezing

Many experimental approaches employ conditional spin-squeezing and back-action evasion. These include room-temperature systems as presented here and have also been realized in cold atomic clouds. For example, the authors in Sewell et al. (2012) present successful spin-squeezing using stroboscopic probing and demonstrated magnetic sensitivity beyond the projection noise limit exploiting a cloud of cooled Rubidium atoms containing more than 10^5 atoms. The authors observed a noise reduction of 3.2 dB exploiting spin-squeezing of 2.0 dB according to the Wineland criterion (Sewell et al., 2012). Another example of quantum-enhanced magnetometry was presented in Muessel et al. (2014), where the authors prepared Bose-Einstein-condensates (BECs) in a spin-squeezed state. This allowed the authors to report a single-shot sensitivity of 310 pT using a probe volume of only 90 μm^3 (Muessel et al., 2014).

One of the stepping stones of the quantum-enhanced MIT exploiting stroboscopic back-action evasion and conditional spin-squeezing follows the results from a previous experiment at Quantop, presented in Vasilakis et al.

(2015). The authors successfully prepared the collective spin-oscillator inside a low finesse cavity in a spin-squeezed state using a stroboscopic back-action evading measurement (Vasilakis et al., 2015). Vasilakis et al. (2015) presents a maximum of $-2.2\,\mathrm{dB}$ of conditional spin-squeezing. Unlike our approach, where each stroboscopic probing pulse is weighted equally, in Vasilakis et al. (2015) exploits exponential mode functions to weigh the stroboscopic pulses in the squeezing preparation and verification time windows. This can be interpreted as weighing the information obtained from the stroboscopic probing more strongly towards the end of the preparation pulse and the beginning of the verification pulse. Weighing the information of the pulses like this allows compensating to a certain extent for the decoherence of information. In our current analysis, we have yet to implement that.

Further, the protocol of stroboscopic back-action evasion and conditional spin-squeezing can be extended to not only using prediction and retrodiction measurement – what we refer to as squeezing preparation and verification – but can even be extended further. In Bao et al. (2020)[1], the authors show that splitting the squeezing protocol into three instead of two pulse sequences can be beneficial to the overall degree of squeezing and maintaining it for longer. The authors use the third pulse as a backward reference. The information from the third pulse is used to obtain more information about the squeezing verification pulse (2nd pulse). The authors of Bao et al. (2020) observe that keeping the total sequence duration the same but splitting the stroboscopic sequence into the beforementioned three pulses leads to a better and longer maintained level of conditional spin-squeezing in the post-processing using past quantum states (Bao et al. (2020)). They test their approach by determining the sensitivity of both pulse sequences to an RF field applied during the second stroboscopic probe pulse train. Since our current approach only tests the passive response to the eddy currents in a sample, another method of quantifying our system's capabilities would be to test their pulse scheme without a sample and use it to benchmark our system against theirs. We acknowledge that we have no calibration of the absolute sensitivity for our quantum-enhanced measurement protocol as part of the proof-of-principle experiment introducing the QMIT protocol. Considering that we can only detect a highly conductive sample, there is reasonable doubt that our current sensitivity exceeds previously reported sensitivities. We are currently investigating how to calibrate our current measurement apparatus. One idea, also allowing for a direct benchmark to another group's result, is the method used in Bao et al. (2020).

Many of the above-mentioned experimental results exploit, in addition to stating the overall observed reduction in noise, the Wineland criterion (see Wineland et al. (1992)) to estimate the metrologically relevant improvement of the sensitivity from the quantum enhancement. For better comparison with other groups, quantifying this in the future will be relevant, especially when improving the current performance and when calibrating our absolute sensitivity.

As a final remark, at the current status and with the extent of the per-

[1] Coincidentally, this paper also observes the dependency of the noise introduced into the system for sharp turn-off of optical pumping and uses smooth turn-off of the optical pumping as we do throughout this thesis.

formed measurements, a complete benchmark against other existing protocols and experimental platforms can only be done rudimentary, as done here. Additional measurements and more thorough literary research and data analysis are required for a more thorough discussion. This was not sufficiently possible within the time frame of the thesis here. Therefore, in the following section, we will address experimental challenges and some of the required calibrations for better comparison to other people's work.

16.2 Current limitations and issues

We observed some experimental limitations and technical issues throughout chapters 14 and 15. We will summarize these in the following and provide some considerations for tackling the current experimental challenges.

- **Preparation-measurement duration**
  Our intrinsic repetition time is mainly limited by the time it takes to prepare the coherent spin state using optical pumping. Careful optimization of the timings could shave off a few milliseconds of the overall sequence time, but it will not be on the order of factor two or more.

- **Duty cycle:**
  The finite rising and falling edges of the AOM-generated stroboscopic probing pulses mainly govern our experimental sequence speed. The stroboscopic frequency for back-action evasion must be at twice the Larmor frequency, along with well-defined edges for maintaining a low duty cycle. We also note that while the model $D \to 0$ predicts a QND-type interaction, the simplification breaks down experimentally. For infinitely sharp and/or short pulses, the Fourier spectrum of our stroboscopic pulses will contain more and more frequencies, potentially driving undesired transitions in cesium atoms due to their multi-level structure. Hence, the toy model used to describe our system will eventually break down.

- **Bias magnetic field:**
  While the switching speed of the AOM is limiting the speed of the stroboscopic frequency available, we are currently not limited as such by the bias magnetic field. However, if we wish to reduce classical noise further, we want to operate the experiment at a higher bias magnetic field. Typically, classical noise sources decrease towards higher frequencies, making larger magnetic field splittings more desirable as the Larmor frequency ν_{L} determines the sideband frequency we encode our signal in compared to the carrier frequency.

- **Calibrations:**
  While we introduce the coupling parameter κ in our description, we do not currently estimate and calibrate it. Further, we do not calibrate the losses and determine the quantum efficiency of our detector. These

calibrations could help us quantify losses, identify where technical improvements are necessary, or support us in optimizing the light-atom interaction. Further, our projection noise calibration is based on probing the thermal spin state. While we are in a regime where we do not observe probe-induced decoherence, if we do follow indications from the analysis on the noise reduction (section 14.5) that increased optical probe powers could lead to better results, alternative calibrations might become relevant.

- **Drop in the level of spin-squeezing for QMIT measurement:**
  Whenever the RF coils are connected to a function generator, we observe a sudden drop in the attainable level of conditional spin-squeezing (see section 15.2). The investigation to pinpoint the reason and potential remedy are ongoing. Our working hypotheses include residual signals on the function generator output or undesired ground loops. Alternatively, eddy currents induced in our aluminum shield surrounding the cell and RF coil pair could be another source of distortion. We cannot easily remove the aluminum shield to test this and measure its influence since we balance the measured optical signal without a sample but in the presence of the aluminum shield. However, eddy currents in the shield will alter the sample signal and vice versa, altering the expected effects. This could also be the reason why the simulations investigating the expected phase between RF and eddy current signal presented in Oesterle (2022) predicted -170°, while we experimentally determined -192°. Extending the simulations to include the aluminum shield might provide more insight into why we observe a phase shift exceeding the predicted -170°.

- **Coherent state preparation:**
  We are currently preparing an atomic polarization of only 97.5 %, leading to a more considerable atomic projection noise in our system than the of a coherent spin state. Improving the initial atomic polarization should improve our observed noise. Similar to the approach in the DLCZ-type experiment, a delayed pump turn-off could increase the atomic polarization at the expense of loss in the optical depth. This, at the same time, should reduce the overall signal since the number of atoms in $F = 4$ determines the strength of the interaction. We are preparing the necessary changes to measure and compare the degree of conditional spin-squeezing between our regular optical pumping and optical pumping with delayed pump turn-off. However, at the time of this thesis, the test still needs to be performed. We note that the speed of the thermalization of atoms will not change even in the case of improved coherent spin state preparation, meaning that the decoherence time of conditional spin-squeezing in our system should only marginally be altered, if it improves at all.

16.3 Next steps

Given that we have only shown a proof-of-principle experiment for the quantum-enhanced MIT, we should consider improving and more rigorously quantifying the experiment's performance. Apart from the apparent improvements required on the technical level, we want to mention two possible paths currently under consideration. Both will rely on tackling experimental limitations and challenges discussed in the previous section.

16.3.1 Biomedical applications

Following in the footsteps of previous experimental implementations of classical MIT at our group, we pursue QMIT's potential application within the field of biomedical applications in mind. While we do not plan to perform magnetocardiography as done in Jensen et al. (2018), we aim to attain a signal-to-noise level suitable for distinguishing body tissues, such as heart or brain tissue, and discriminating between aberrations from healthy tissue. For example, MIT of the heart was already proposed in Marmugi and Renzoni (2016). Considering the low conductivities involved in such tomography measurements, this will require many improvements to our initial proof-of-principle measurement using a high-conductivity sample. In the long run, one of the main goals is a portable device without the necessity for a magnetic shield allowing for non-invasive measurements discriminating between different body tissues with a suitable resolution. Using our vapor cell-based approach to detect healthy and unhealthy tissues by exploiting the different conductivities of these, QMIT and MIT offer potentially a convenient and non-invasive imaging tool. However, this relies on improving our current experimental performance based on the previously mentioned limitations. Further, easy scale-up is required, too, since often parallel measurements using arrays of sensors speed up the overall measurement time.

We emphasize that many experimental improvements are necessary to realize such a device, and some technical challenges must be solved first. In general, a portable device seems within reach, given the progress in available laser sources, precise 3D printing of the housing for such a device, and the like. However, to this end, there needs to be further investigation into whether a quantum or a classical protocol will be the most feasible route. Now we can distinguish two cases. For biomedical applications, we have two constraints. On the one hand, the overall sensitivity of a classical and a quantum-enhanced device must be sufficient to measure the task at hand. If both approaches are sufficient, the other constraint will be the overall measurement time. The total measurement time required is essential since the measurement time will matter for a patient. If the required sensitivity can be obtained much faster with the quantum-enhanced protocol, this approach will be more feasible. However, suppose the classical protocol is better or on a similar footing performance-wise to the quantum-enhanced protocol. Then, the experimental simplicity of the classical protocol will outweigh the gains from

the quantum-enhanced protocol. For now, we will proceed along both lines and evaluate later which measurement protocol will be most suited to build a usable prototype and evaluate the potential up-scaling of the approaches. A third path will be evaluated in the next section, which has yet to be pursued in our laboratory.

16.3.2 Combining continuous measurements with stroboscopic probing

A key motivation for our quantum-enhanced magnetic induction tomography was the gain in signal-to-noise from pulsed measurements exploiting back-action evasion and conditional spin-squeezing. While this is a novel approach combining these techniques with MIT, considerations such as the overall measurement duty cycle compared to the optical preparation time appear to be a limitation. Therefore, we wish to investigate yet another approach. The main culprit of our experimental sequence is that we are currently only measuring roughly 1 % of the total experimental sequence duration. In the following, we want to use some crude assumptions to motivate why this quantum-enhanced MIT protocol might have a feasibility limit when comparing ourselves with continuously operating sensors also relying on room-temperature atomic ensembles such as presented in, for example, Jensen et al. (2019).

Let us assume that both the classical and quantum-enhanced protocols allow for the required sensitivity of a specific application. In order to compare both protocols and obtain the same sensitivity for the overall same measurement duration, we have to compare the continuous operating protocol to the quantum-enhanced protocol, including its reinitialization period. If for the latter, only 1 % of the time the actual measurement is performed, we need to have a sensitivity of at least ten times that of the continuous MIT. This is because if we measure 100 times longer, we expect to improve by a factor $\sqrt{100} = 10$. For QMIT to be the better choice and the additional experimental complexity to be worth the effort compared to MIT, the sensitivity and measurement precision must be significantly better. These are only very crude assumptions, and we have yet to show similar performance for the QMIT as shown for the MIT in Jensen et al. (2019).

Overall, the limited measurement duty cycle – not to confuse with the stroboscopic probing duty cycle – is unfavorable for the QMIT protocol. At the same time, a classical magnetometer based on a single ensemble will always suffer from back-action, setting a fundamental limit on the attainable measurement sensitivity. We are considering combining two key components of the quantum and classical protocol to combine the best of both protocols. Our idea is to try and see if combining stroboscopic probing with a continuous measurement pulse sequence is possible. As for the classical MIT, optical pumping, RF magnetic field, and optical probing are continuous. The difference is that the probing should be a continuous train of stroboscopic pulses. There are some open questions on whether it is possible with such a sequence

to attain the same or at least some reduction in the back-action noise. Further, it is an open question of best analyzing the measured signal. For example, if non-flat mode functions for weighing the data are required and their respective optimization.

Chapter 17

Concluding remarks

This thesis presents different experiments relying on room-temperature spin-oscillators, exploiting the quantum-mechanical nature of cesium spins in anti-relaxation coated vapor cells. We have successfully realized an on-demand single-photon source with built-in memory. In the case of immediate retrieval after the write pulse, our source is exhibiting unmistakable single-photon character by observing a conditional auto-correlation as low as $g^{(2)}_{\mathrm{RR}\,|\,\mathrm{W}=1} = 0.20 \pm 0.07$. This value is more than four standard deviations below the two-photon Fock state auto-correlation. In addition, we verified the non-classicali-ty between the write and read light fields by observing cross-correlations exceeding the classical bound of two by observing $g^{(2)}_{\mathrm{WR}} = 10 \pm 1$. While this is a clear sign of non-classical correlations between the write and read scattered light fields, we have further verified this by violating the Cauchy-Schwarz inequality and observing $\mathcal{R} > 1$. The second key component in our write-read scheme is the successful storage and delayed retrieval of a collective excitation. In our case, we verify this by delaying the retrieval light pulse. We maintain a cross-correlation value exceeding the threshold required for potential Bell-inequality violation using entanglement between two atomic ensembles for a duration of $\tau_{\mathrm{BI}} = (0.15 \pm 0.03)$ ms. Relaxing the requirement of the memory time to maintain non-classical correlations between write and read scattered light fields, the memory time even reaches $\tau_{\mathrm{NC}} = (0.68 \pm 0.08)$ ms. These improvements, compared to previous versions of the DLCZ-type experiment at Quantop, were possible by improving the optical pumping and initial coherent spin state preparation to reduce the occupancy of the storage state to 3 % and suppressing the detrimental four-wave mixing processes during the readout by exploiting a *magic detuning*. The magic detuning of our retrieval drive light field suppresses undesired write processes during the read pulse on the D_1 line of cesium, which previously limited the protocol's performance when using the D_2 line (Zugenmaier et al. (2018); Zugenmaier (2018)).

The main limitations in the overall experiment arise mainly from the cell cavity's limited outcoupling efficiency and additional losses in the detection

setups. Losses are not a fundamental problem to our scheme but slow down the rate for successful consecutive storage and retrieval of a single-photon. Despite the spin state preparation improvements, the residual population in $|F = 4, m_F = 3\rangle$ serving as our storage state remains a primary limitation. However, even with further improvement in our coherent spin state preparation, the repopulation of atoms to $|F = 4, m_F = 3\rangle$ will remain a limit to the maximal memory time.

We discussed the results of the DLCZ-type experiment and analyzed the current limitations and their potential remedies. We further presented initial tests of our ideas, for example, by testing the cavity enhancement and performing initial tests on vapor cells with a longer channel and larger cross-sections. Additionally, we presented our efforts in increasing the relative motional averaging speed by implementing a more homogeneous intensity profile of our drive light to improve our system's time-bandwidth product.

The second main experiment presented in this thesis was quantum-enhanced MIT. We have first implemented successful conditional spin-squeezing and a significant reduction in the observed back-action noise using stroboscopic probing. Due to the finite duty cycle of the stroboscopic probing pulses, we cannot realize a real QND-type interaction but significantly reduce the introduced back-action noise compared to measuring continuously. Nevertheless, we were able to observe a maximal degree of spin-squeezing of $10\log(\xi^2) = (-4.6 \pm 0.6)$ dB. Since we are mainly interested in the potential quantum noise reduction, we found that the signal reduction was not obtained for the maximal level of conditional spin-squeezing but rather as a trade-off between the contributions arising from the shot noise and the atomic projection noise to the overall noise with the conditional spin-squeezing acting only on the noise from the contribution of the atomic projection noise.

When introducing a gap of 50 µs and sending an RF pulse to induce eddy currents in a conductive sample, the spin-squeezing degraded to $10\log\left(\xi^2\right) = (1.8 \pm 0.2)$ dB. Identifying the reasons for the drop in the degree of conditional spin-squeezing are still ongoing, and the quantum-enhanced MIT was performed using the sub-optimal conditional spin-squeezing. We demonstrated a signal-to-noise improvement when performing the proof-of-principle experiment using a highly conductive sample made of titanium. Comparing unconditional to conditional uncertainties of single-shot measurements, the SNR improved from 0.72 to 1.26 when exploiting conditional spin-squeezing. Further, we compared the quantum noise in a back-action-free measurement to our observed conditional noise exploiting conditional spin-squeezing. We observed approximately 11 % lower noise utilizing conditional spin-squeezing.

Performing a 1D scan of the sample transversely to the cell channel, we could detect the sample's presence and maintain the advantage in the reduced measurement uncertainty by taking advantage of the spin-squeezing. The center of the sample could be determined with a precision of 0.36 mm for the unconditional measurement and improved to 0.20 mm for the conditional measurement.

Following the proof-of-principle experiment, we discussed the current limitations. One of our primary concerns is the drop in the degree of conditional spin-squeezing when performing the quantum-enhanced MIT when connecting the RF coils to a function generator. Further, we addressed some intrinsic limitations of our scheme compared to continuously operating MIT protocols.

Overall, the work presented in this thesis offered two examples of experiments with room-temperature spin-oscillator systems employing anti-relaxation coated vapor cells. Further, various experimental techniques and issues were presented as a guideline for future investigations and reference for the next generations of students at Quantop.

Part V

Supplementary Information

Appendix A

Supplementary information about the cell testing

A.1 Recuring of cells

Vapro cells degrade in their performance occasionally, especially if kept in storage and lose their performance compared to the time of their respective cell testing. However, time also leads to different cell issues, such as spots of cesium on the window and a blocked connection to the channel through clogging with cesium and coating material. Sometimes, issues are not visible but are just observed in a drop in performance parameters such as the number of atoms and transmission or coherence times.

One way of counteracting (sudden) changes in cell performance is recuring of the vapor cells. Our old method for recuring vapor cells included a Peltier element generating a temperature gradient of roughly 8 °C. However, during the visit from Mikhail Balabas, a new, more reliable version was developed.

Instead of creating a temperature gradient with the Peltier element, a passive cooling method using water evaporation is employed. The vapor cell stem is placed inside a small water tray with cotton wrapped around it. The cell body is slightly elevated and not touching the wet cotton. Cell and water tray are placed inside an oven heated to 60-70 °C. A fan inside the oven ensures equal distribution of the temperature. The elevated temperature is applied for several hours. We use at least 5-6 hours on first tries and up to 12 hours in more severe cases when repeating the recuring process. The elevated temperature should evaporate the anti-relaxation coating and droplets of cesium inside the cell body. Due to the wet cotton wrapped around the stem, material deposits there as the temperature is 15-20 °C lower.

Figure A.1: Setup for recuring. View of oven with fan, elevated boxes for placing cell body along with cotton and plastic trays for the water.

Essential for avoiding depositing too much material on the windows or inside the channel, the oven is let cool down over an extended period of time, typically overnight. The cooldown ensures that the vapor cell is not subjected to a sudden temperature change. We maintain a temperature gradient during the cooling-down period.

This method of recuring has proven to be superior to our old method,

improving cells that did not improve as much using the Peltier for the temperature gradient. In general, we have had great successes in regaining cell performance after degradation during storage time, as well as a sudden deterioration in performance. In addition, recuring freshly manufactured cells seems beneficial to their performance and getting a more reliable estimate of cell performance parameters.

A.2 Overview cell testing results

For reference, we will provide an overview of the obtained measurement results from the cell testing for cells of Generation O in a tabular form.

It should be noted that we only state the values obtained in the cell lab for the transmission values. The transmission was also measured in the GWD lab for some of the cells. Usually, they are reasonably consistent. We only included the most recent value in the overview when we re-cured vapor cells due to sudden degradation or initial lousy performance. For the current recuring method used when writing this thesis, please consider the relevant description of the recuring process provided in appendix A.1.

The stated T_2 times were measured in a different experimental setup, and the data was provided by **Jun Jia** and **Ryan Yde**. Due to the complexity of this measurement, the goal was to get a relation between T_1 and T_2. We hoped that this allows estimating T_2 based on T_1 for other cells. More details can be found in the main text in section 7.4.

Some footnotes accompany some of the values for specific cells, which are related to cells either not being up to spec or having other problems.

Cell name	**Size** $[\mathbf{mm}^3]$	**Transmission [%]**	**Density** ρ $[10^{16}/m^3]$	T_1 **[ms]**	T_2 **[ms]**[a]
O1	40x1x1	94.7	(2.33 ± 0.01)	(5.7 ± 0.1)	
O2	40x1x1	96.2	no atoms	no atoms	
O3	40x1x1	96.4	(2.51 ± 0.00)	(4.7 ± 0.1)	
O4	40x1x1	96.0	(2.31 ± 0.09)	(2.5 ± 0.1)	
O11	40x1x1	95.8	(2.70 ± 0.00)	(2.8 ± 0.1)	
O22	40x1x1	94.9	(2.9 ± 0.3)	(5.9 ± 0.1)	
O5	60x1x1	96.1	(4.04 ± 0.07)	(2.4 ± 0.1)	
O6	60x1x1	87.6[b]			
O7	80x2x2	96.7	(2.65 ± 0.04)	(6.4 ± 0.2)	5.9
O8	80x2x2	96.3	(2.95 ± 0.11)	(9.1 ± 0.2)	10
O12	80x2x2	95.2	(2.77 ± 0.09)	(4.5 ± 0.1)[c]	7.8
O13	80x2x2	95.4	(2.39 ± 0.15)	(5.9 ± 0.2)	5.8
O15	80x2x2	95.8	(2.9 ± 0.1)	(7.2 ± 0.1)	9
O9	25x0.5x0.5	94.9	(0.81 ± 0.02)	(1.05 ± 0.02)	
O10	25x0.5x0.5	71[d]		(0.40 ± 0.01)	
O16	25x0.5x0.5	91.0	(2.36 ± 0.01)	(1.19 ± 0.01)	
O14	80x(4π)	96.3[e]		(16 ± 0.1)	
O17	80x(4π)	96.2	(3.7 ± 0.1)	(20 ± 0.2)	
O18	80x(4π)	96.4	(3.54 ± 0.02)	(6.5 ± 0.2)[f]	
O19	80x3x3	94.8	(3.78 ± 0.02)	(11.5 ± 0.2)	
O20[g]	80x3x3				
O21	80x3x3	95.3	(4.8 ± 0.4)	(7.0 ± 0.1)	

Table A.1: Cell properties for Generation O: Overview over obtained results for transmission measurements, atomic density at room-temperature, longitudinal spin coherence time T_1 and transverse spin coherence time T_2. Uncertainties on T_1 are obtained from fit confidence intervals. See 7 for details.

[a] These numbers were provided by Jun Jia and Ryan Yde and measured in the "GWD lab".
[b] Discarded due to bad transmission.
[c] Obtained T_1 after recuring since initial T_1 had dropped to 1 ms. Comparison between T_1 and T_2 times might not be reliable.
[d] Improved transmission after three recuring cycles. Cell discarded.
[e] After recuring, worse before. Absorption was not remeasured after recuring, therefore not stated.
[f] Before recuring: $T_1 = 8.5$ ms.
[g] Discarded due to twisted channel

Appendix B

Magnetic field optimization

The need for a homogeneous bias magnetic field is common to the experiments presented throughout this thesis. Often, a combination of different coils[1] is used to achieve this. To optimize and verify the homogeneity of the bias magnetic field, we need means of measuring its profile. For this, we use the colinear MORS method together with a cubic vapor cell of size $5\,\text{mm} \times 5\,\text{mm} \times 5\,\text{mm}$. For the colinear MORS, our probing beam simultaneously acts as a far-detuned repump laser, and no transverse optical pumping is required. To map out the magnetic field, we move the cubic cell transverse to the bias magnetic field direction along the probing direction. To enable this while not obscuring the beam path, we place the cell on a plastic rod as indicated in figure B.1. The cell is attached to a holder placed on a precision stage. The stage allows us to move the cell along the probing beam direction.

As described in chapter 6, we use polarization homodyning to record the birefringence induced by a transverse spin component. Instead of recording a time trace, we use a picoscope with a spectrum analyzer feature to directly observe the spectrum. An RF coil pair drives the transverse spin component. For the colinear MORS, we use white noise to drive all RF frequencies equally. It ensures that atoms in the vapor cell can be addressed independent of the precise Larmor frequency at the cell's current position. Then we can observe the Larmor peak in the spectrum independent of its precise value and do not require adjusting the frequency of the RF coil for each position.

Typically, we move the cubic cell in steps of 5 mm and average the spectrum many times. Since the cell will experience a slightly different magnetic field at each position if the magnetic field profile is not homogeneous, the frequency of the Larmor peak in the spectrum will depend on the magnetic field (equation (2.3)) of its respective position. We can infer the magnetic field profile and homogeneity over the covered distance directly from the observed Larmor frequency versus the cell position. Typically, we use magnetic fields with negligible quadratic splitting for this measurement.

In the following, we will first describe optimizing the coil positioning. Afterward, the current ratio is optimized to maximize the magnetic field homogeneity. To illustrate the technique, we will present the data for the coil

Figure B.1: Cell for magnetic field optimization. Illustration of cubic cell and its holder to perform colinear MORS to record the magnetic field strength profile. See text for more details.

[1] For details on the coil configurations used in the respective experiments, see the respective experimental setup descriptions in sections 9.1.1 and 13.1.

frame used to test large vapor cells of 80 mm length required for testing the spin noise spectrum of large cells for the DLCZ-type experiment (chapter 11, section 11.3.5).

First, we record the magnetic field profile for each coil pair individually. We record each profile twice - once with positive and once with negative current[2]. An example of this sweep (for the final, optimized field) is depicted in figure B.2. Since we must drive the atoms transverse to the bias magnetic field, we must also optimize the RF coils' location. To do so, we switch the roles of RF and PCB coils to get a profile for the RF coil pair. From the obtained profiles, we adjust the positioning of the coils on the frame (figure B.3). In the final step, we combine the two coils to superimpose their magnetic field

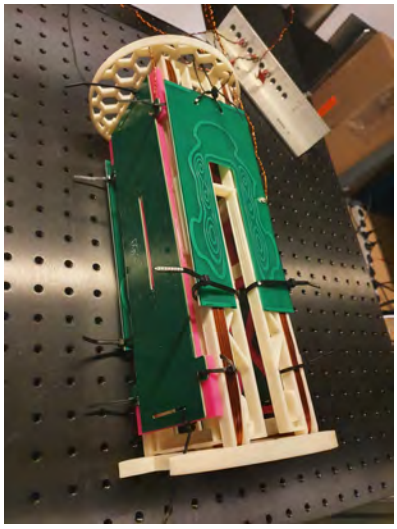

Figure B.3: Coil frame for large cells Picture of coils on a frame whose relative position and current we aim to optimize. The frame is 3D-printed. The cable binders are used to fix the coil positions preliminary. A pair of rectangular coils are wound onto the frame.

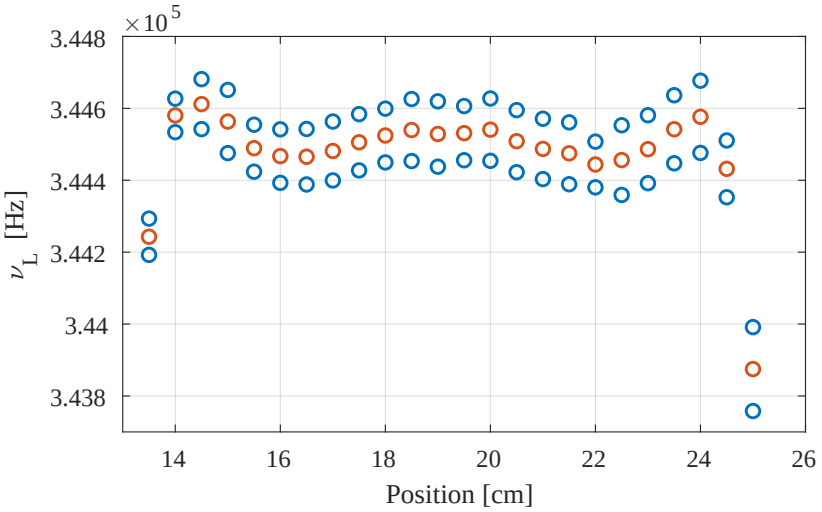

Figure B.2: Larmor frequency versus cell position. Blue: Observed center Larmor frequencies ν_L for positive and negative currents versus the position of the cubic cell. Orange: average between positive and negative current values. These values correspond to the optimal current ratio leading to the minimum homogeneity in figure B.4 for 1.1 current ratios. The relative homogeneity over 10 cm amounts to $1.3 \cdot 10^{-4}$ %.

profiles. Our goal is to find the best current ratio that minimizes the relative standard deviation of the observed Larmor frequencies. For this, we vary the current of one of the two coil pairs while keeping the other current constant. We repeat the sweep for positive and negative currents for each current ratio setting and obtain profiles as displayed in figure B.2.

We determine the mean between the positive and negative currents, as shown in orange in figure B.2. We normalize to the mean Larmor frequency and calculate using the values within the central 10 cm. This gives us the relative standard deviation for this range, which we use to quantify our magnetic field homogeneity. In figure B.4, we plot the different values for the relative standard deviation. We observe a clear minimum for a current ratio of 1.1 between bias and compensation coil, indicating only $1.3 \cdot 10^{-4}$ % relative standard deviation. Figure B.2 portrays the corresponding profile. We verify

[2] In principle, both currents should lead to the same profile. Observing a deviation in the mean Larmor frequency indicates that the magnetic shield is not "neutral". Typically, we use degaussing the magnetic shield to reset the magnetic shield and remove any residual magnetization. The approach is thoroughly explained in Stærkind (2015). Its success should allow the removal of most deviations in the center Larmor frequency between positive and negative current.

that the current ratio is optimal when increasing the Larmor frequency and observe good agreement (orange point in figure B.4).

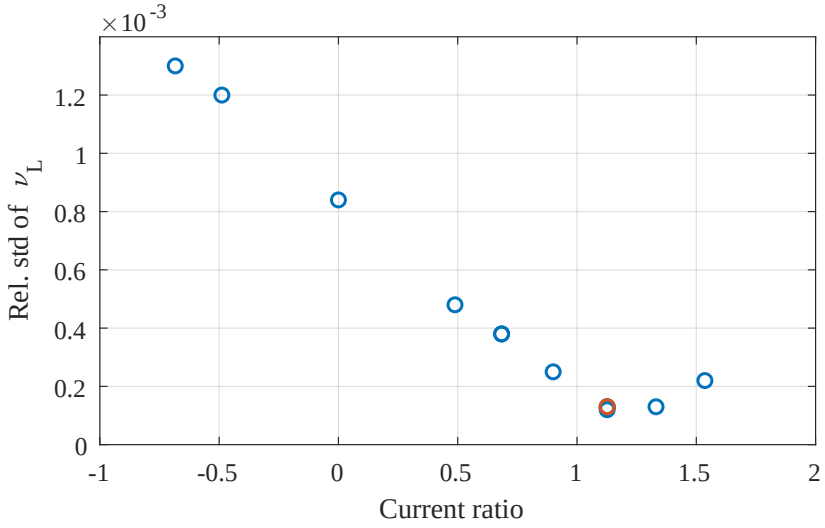

Figure B.4: Signal decay versus τ_A duration. Obtained relative standard deviation of the center Larmor frequency ν_L versus the current ratio between PCB (main) and rectangular (compensation) coil pairs. Each value refers to the length of 10 cm, measured for both current polarizations and measured in steps of 5 mm. The orange point verifies that the same current ratio still allows for the same homogeneity when doubling the currents.

While we have chosen to present the technique on the example of the magnetic field optimized for the spin noise measurement of large vapor cells (section 11.3.5), the same technique can and has been employed to optimize other coil configurations. For the QMIT, the experimental results can be found in Oesterle (2022).

Appendix C

Atomic state evolution

We have introduced in chapter 6 how we use the technique of pMORS to estimate the atomic spin polarization after optically pumping our atomic spin ensemble to prepare a coherent spin state. By introducing a variable delay between the optical pumping and the RF pulse, we can monitor the decay of the atomic spin polarization. For this reason, we performed pMORS for various delays and hyperfine manifolds. Switching between the two ground-state hyperfine manifolds can be done using the same experimental configuration but adjusting the Larmor frequency ν_L to the respective manifold. Further, to estimate the atomic polarization p, the expression in equation (6.8) has to be evaluated for the individual hyperfine and Zeeman levels. In figure C.1, we show the obtained values for p versus the delay time for both hyperfine manifolds. It should be noted that we measured these without the delayed pump turn-off. Some things are worth noting in figure C.1. First, both manifolds exhibit a high atomic spin polarization after the optical pumping. Second, the polarization of $F = 3$ first increases before it starts decreasing. This behavior we take as an indication that atoms transfer faster from $F = 4$ to $|3,3\rangle$ than from $|3,3\rangle$ to $|3,2\rangle$. Regardless, we cannot gauge the precise dynamics further, as we need more information about how many atoms there are at any time in each hyperfine manifold. Knowledge about the hyperfine occupation is vital if we want to describe our Zeeman level occupation in absolute terms to see how the population evolves. We cannot gauge this, especially for lower atomic polarization, from pMORS since it only contains information about population differences. For degrading atomic polarization, more and more "equal" distribution will be shared between Zeeman levels of a hyperfine level. This, together with the readout noise in the DLCZ when delaying retrieval (section 10.2) and how to suppress it, sparked the interest in finding means of quantifying this. We hoped that finding remedies to the growing readout noise would be easier with knowledge about the more precise dynamics of the atomic re-thermalization of the spin state.

To determine the population dynamics in absolute occupation numbers, we tried to combine the pMORS measurements for different delays to quantify the number of atoms in each hyperfine manifold. The reason is that pMORS,

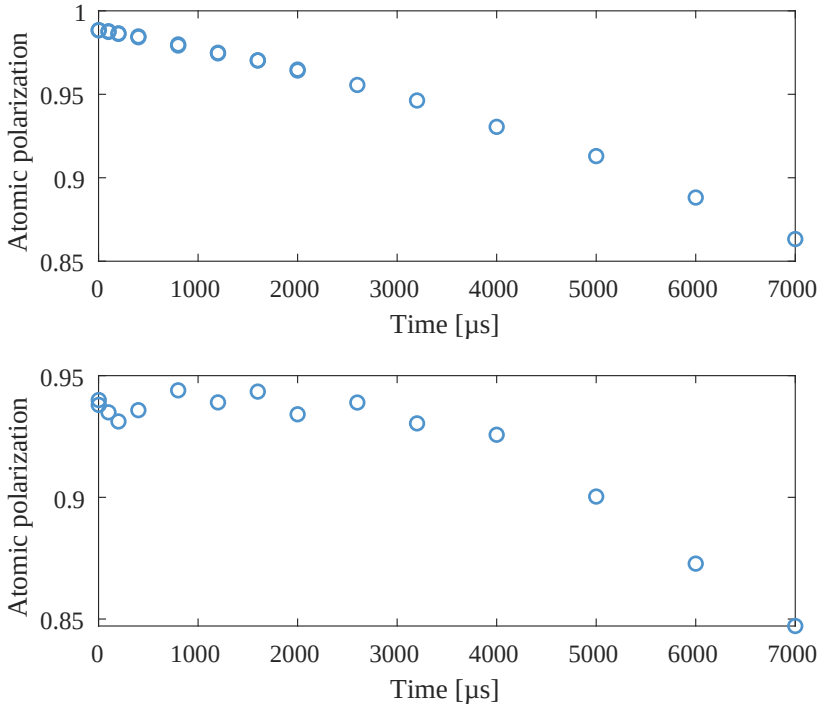

Figure C.1: Atomic polarization versus delay. Top: atomic polarization of $F = 4$ versus variable delay. Please note that multiple points are measurements from different days verifying the reproducibility. Bottom: Same for $F = 3$ manifold.

as discussed in section 6.1, only provides information about population differences between neighboring Zeeman levels but not their absolute occupation numbers. This is especially problematic when reaching non-negligible occupation numbers of lower m_F levels leading to some equilibrium population. The combined knowledge of the number of atoms in each hyperfine level and the pMORS spectra for various delays provides sufficient information to determine a common population in all Zeeman levels. While we did not yet manage to do so experimentally, I decided to address it nonetheless and include our efforts due to its potential value for future generations of master's and PhD students that hopefully benefit from the experiences we gained during our efforts.

While recording the pMORS spectra versus time is straightforward, finding practical means of quantifying the number of atoms in each hyperfine manifold is not. We know the total number of atoms N_{A}, which can be determined using the absorption measurement presented in section 7.3. In principle, one could imagine using the same approach. However, the time scales we are interested in are on the order of microseconds, which is impossible with the absorption measurement. We also investigated the model used for the absorption measurement and tried to find descriptions for different occupations to see if the method could be adjusted. While modeling was possible,

experimental tests were not reliable and fast enough.

An alternative is to use what we will refer to as the "bleaching" method. The idea is to address the atoms of a manifold with a strong on-resonance probing beam and exploit the branching ratio from the excited level for the atoms to either return to their initial manifold or the other one. Once they transition to the other, they are far-detuned from the probing laser. They do not interact with the laser anymore. Since the branching ratio is the same for all Zeeman levels within a hyperfine manifold, atoms of the same manifold interact similarly with the probe. From this, it is possible to determine the average number of photons it takes to remove an atom from one manifold to the other. Knowing this, one can monitor the transmission of the probe beam through the atomic ensemble. Due to fewer and fewer atoms in the manifold attenuating the probing beam, the transmission will increase. The total number of absorbed photons can be estimated from the area corresponding to the attenuated probe beam before all atoms are removed from the manifold. This number is then directly related to the number of atoms initially in the hyperfine level. The idea of this bleaching method originates from the supplementary material to Béguin et al. (2014) and was further explained in Béguin (2015). The method was successfully employed to gauge the number in an optical lattice.

Initially, it seemed like a very convenient way to gauge the number of atoms within a hyperfine manifold, but we soon realized that the problem was addressed too simply. We identified multiple issues. For starters, we were initially unable to use high optical power due to our highly-reflective incoupling mirror. We remedied this when we removed the incoupling mirror and replaced it with a lens to find an experimental estimate for the cavity enhancement (section 4.3). Even afterward, with high optical power speeding up the bleaching signal significantly, we did not observe the desired time scales for the process. An example of how the normalized transmission signal evolves for various optical probing powers is supplied in figure C.2. Our signal has a very fast contribution[1], and a slower response corresponds to the main slope. The behavior observed illustrates very nicely that we could not arbitrarily speed up the bleaching of the hyperfine by simply increasing the optical power.

We identified possible reasons for these issues. First, our atomic ensemble has a very high optical depth. Probing along the channel is a disadvantage. Since the light is absorbed to a large extent, the first "layers" of atoms are probed first, while atoms in the end "layers" are addressed after the initial layers lost some of their atoms to the far-detuned hyperfine level[2]. Further, we are operating at above room-temperature. Assuming that our atoms have an average velocity of $v_{\text{th}} \approx 150\ \frac{\text{m}}{\text{s}}$, we have significant Doppler-broadening ($\approx$ 100 MHz). Aiming for a measurement duration of 50 µs means that we have only 25 wall collisions where atoms change their velocity and potentially get on resonance with the light. Therefore, the technique is less easily applicable than for cold atoms in Béguin et al. (2014). While these issues caused

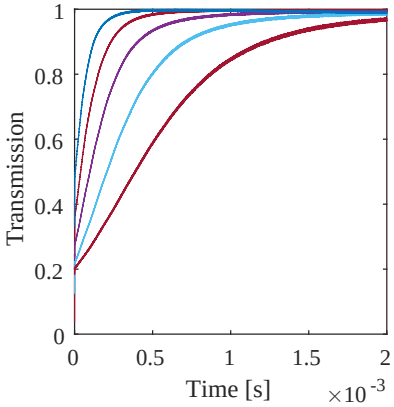

Figure C.2: Normalized transmission signals. A subset of the normalized transmission signals for probing powers ranging from 20 µW (slowest slope) to 320 µW (fastest slope), where each next faster slope corresponds to doubling the optical power.

[1] One might assume that this one is the detector response. However, when detuning the laser, we gauged the detector response to be even faster. The first swift response is therefore atomic.

[2] This is, of course, a very simplified description. It is possible to model the number of atoms and optical depth, where the expected slope is slower for more optical depth. For the sake of brevity, we refrain from presenting all details here and only provide a summary.

us to stop our efforts in finding fast means of gauging the momentary number of atoms in a hyperfine manifold, there might be options to remedy some of the observed effects. An option could be using the pump laser for optical pumping and probing the ensemble from the side. However, this comes with challenges of efficiently collecting the signal due to the highly asymmetric shape of the optical pumping beam and distortions from the cell body. Another idea to continue would be to find ways not to address all atoms in the hyperfine manifold subjected to the Doppler-broadening but rather gauge it from the on-resonance atoms. This could be implemented using a double pass configuration but would need additional calibration methods to estimate the overall number of atoms in a hyperfine manifold, together with the issue of too high optical depth.

Appendix D

Signal contribution considerations for QMIT analysis

Throughout the chapters 14 and 15, we concern ourselves with signals originating only from atoms in the 4 manifold of the ground state, as well as neglecting decoherence effects. Here, we will have a look at why we made these choices. First, we will question the decision to not include rising and falling exponential functions as mode functions during our analysis in section D.1. Also, we will consider the ratio between signal contributions arising from the two ground states to see whether we need to consider atoms in $F = 3$ as well, discussed in section D.2.

D.1 Decay of macroscopic spin

In our analysis before we have not accounted for any decoherence and therefore also do not account for it using additional mode function in the analysis as has been done for example in Vasilakis et al. (2015). Here, we will have a look at the decay of the macroscopic spin component.

Similar to our other measurements, we need to record a signal allowing us to get an estimate of the macroscopic spin decay. Therefore, we record the mean signal for a fixed duration of $\tau_B = 100\,\mu s$ used for our experiments and vary the length of the preceding τ_A. The decay of the mean signal should in this case reflect the reduction of the macroscopic spin $J_x(t) \propto J_x \exp(-t/T_1)$. In figure D.1, we plot the mean signal over 4000 measurement repetitions during $\tau_B = 100\,\mu s$ for different values of τ_A and an RF gap of $50\,\mu s$. To the resulting points we fit a simple exponential model:

$$f(\tau_A) = a \cdot \exp(-\tau_A/T_1) + c \tag{D.1}$$

which allowed us to estimate the decay time T_1 of the macroscopic spin component to be:

$$T_1 = (4.5 \pm 0.1)\ \text{ms} \tag{D.2}$$

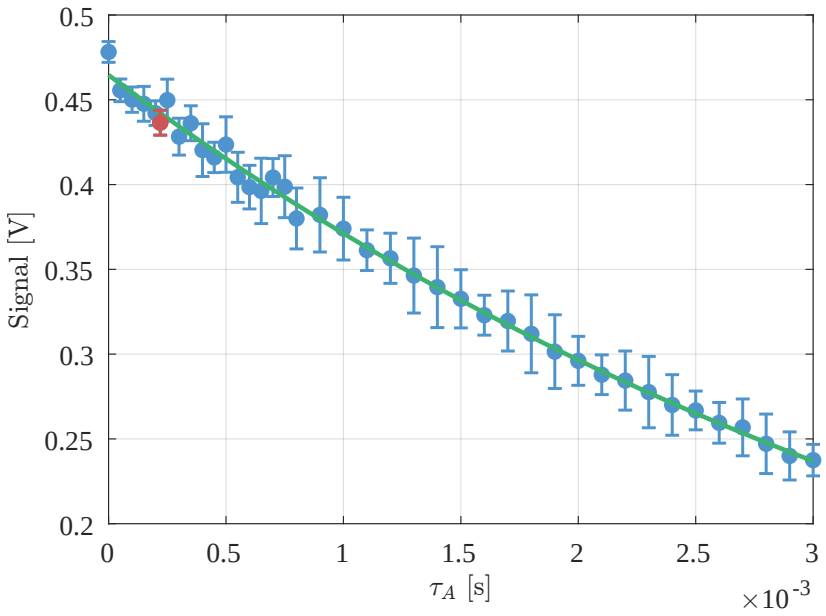

Figure D.1: Signal decay versus τ_A duration. Mean signal for $\tau_B = 100\,\mu s$ versus the duration of the squeezing preparation time τ_A. Exponential fit $f(\tau_A) = a + b\exp(-\tau_A/T_1)$ is fitted to the data. The ed point reflects our experimental choice of $\tau_B = 100\,\mu s$. Each point contains 4000 sequence repetitions, error bars reflect the resulting standard deviations of the mean. Figure re-plotted from Zheng et al. (2022).

where the uncertainty is the statistical uncertainty obtained from the fit. From this, together with the red point in figure D.1 indicating our preferred experimental timings, we deduce that the atomic decoherence is small. Our complete experimental sequence is shorter than 10 % of the T_1 time. We therefore decided to not include decoherence into our analysis in form of additional mode functions accounting for it.

D.2 Impact of 3-manifold

Throughout our experiment we mainly concern ourselves with atoms in $F = 4$ ground state manifold. However, given that we have a finite atomic polarization and minor decoherence of atoms to the $F = 3$ manifold, we wish to estimate contributions of such atoms to our overall signal[1].

In our experiment we use a probe laser locked to the second side band to the blue of the $F = 4 \rightarrow F' = 4,5$-crossover transition, corresponding to a detuning of $\Delta = -1.95\,GHz$. Here, we chose to follow the definition of negative detuning referring to blue detuning, while red detuning correspond to positive values of Δ as introduced in the theory chapter 2. For this setting, we wish to estimate the ratio between the expected contributions between atoms in $F = 3$ and $F = 4$. From equation (3.13), we know that that the atomic contribution to our signal is proportional to $\kappa^2 \propto a^2 \propto a_1^2/\Delta^2$. From

[1]The calculations presented here have been part of the supplements of Zheng et al. (2022), we elaborate here a bit more on the topic.

equations 2.27 and 2.26, we know that a_1 takes different values for the two ground state manifolds and also depend on the respective detuning of the light to the atomic transition. Calculating the respective detunings, the values for a_1 can be determined to be:

$$a_1^{F=4} \approx 1.079$$
$$a_1^{F=3} \approx -1.032$$

Of course, the detuning from the two manifold is different, it amounts to $\Delta_{45} = -1.82\,\text{GHz}$ for $F = 4 \rightarrow F' = 5$ on the D2 line for the 4 manifold, while it is $\Delta_{32} = 6.76\,\text{GHz}$ for $F = 3 \rightarrow F' = 2$:

$$\kappa^2(F=4) \propto \left(\frac{a_1^{F=4}}{\Delta_{45}}\right)^2 \approx 0.352$$
$$\kappa^2(F=3) \propto \left(\frac{a_1^{F=3}}{\Delta_{23}}\right)^2 \approx 0.023$$

The ratio between atoms contributing to a signal from the two manifolds (assuming same occupations) is roughly 15 times higher for atoms in the 4 manifold. Considering that we do have most of our atoms prepared in the CSS, the signal arising from the 3 manifold should be even smaller. We therefore deem it sufficient to consider only atoms in the 4 manifold to our signals.

Bibliography

Aharonovich, I., Englund, D., and Toth, M. (2016). Solid-state single-photon emitters. *Nature Photonics*, 10:631–641. (page 5).

Appel, J., Windpassinger, P. J., Oblak, D., Hoff, U. B., Kjærgaard, N., and Polzik, E. S. (2009). Mesoscopic atomic entanglement for precision measurements beyond the standard quantum limit. *Proceedings of the National Academy of Sciences of the United States of America*, 106:10960–10965. (page 8).

Auzinsh, M., Budker, D., and Rochester, S. (2010). *Optically Polarized Atoms: Understanding Light-atom Interactions*. Oxford University Press. (pages 11, 61).

Balabas, M. V. and Tretiak, O. Y. (2013). Comparative study of alkali-vapour cells with alkane-, alkeneand 1-nonadecylbenzene-based antirelaxation wall coatings. *Quantum Electronics*, 43:1175–1178. (page 76).

Bao, H., Duan, J., Jin, S., Lu, X., Li, P., Qu, W., Wang, M., Novikova, I., Mikhailov, E. E., Zhao, K.-F., Mølmer, K., Shen, H., and Xiao, Y. (2020). Spin squeezing of 1011 atoms by prediction and retrodiction measurements. *Nature*, 581:159–163. (pages 113, 218).

Bennett, C. H. and Brassard, G. (1984). Quantum cryptography: public key distribution and coin tossing. *Conf. on Computers, Systems and Signal Processing (Bangalore, India, Dec. 1984)*, pages 175–179. (page 7).

Béguin, J.-B., Bookjans, E., Christensen, S., Sørensen, H., Müller, J., Polzik, E., and Appel, J. (2014). Generation and detection of a sub-poissonian atom number distribution in a one-dimensional optical lattice. *Physical Review Letters*, 113:263603. (page 241).

Béguin, J.-B. S. (2015). A one-dimensional quantum interface between a few atoms and weak light. *University of Copenhagen*, PhD thesis. (page 241).

Bimbard, E., Boddeda, R., Vitrant, N., Grankin, A., Parigi, V., Stanojevic, J., Ourjoumtsev, A., and Grangier, P. (2014). Homodyne tomography of a single photon retrieved on demand from a cavity-enhanced cold atom memory. *Physical Review Letters*, 112:1–5. (page 5).

Bison, G., Castagna, N., Hofer, A., Knowles, P., Schenker, J.-L., Kasprzak, M., Saudan, H., and Weis, A. (2009). A room temperature 19-channel magnetic field mapping device for cardiac signals. *Applied Physics Letters*, 95:173701. (page 164).

Borregaard, J., Zugenmaier, M., Petersen, J. M., Shen, H., Vasilakis, G., Jensen, K., Polzik, E. S., and Sørensen, A. S. (2016). Scalable photonic network architecture based on motional averaging in room temperature gas. *Nature Communications*, 7:11356. (pages 3, 4, 42, 46, 47, 48, 49, 74, 138, 149, 151, 152).

Braginskii, V., Vorontsov, Y., and Khalili, F. (1978). Optimal quantum measurements in detectors of gravitation radiation. *JETP Lett.*, 27. (pages 29, 171).

Braginsky, V. B. and Khalili, F. Y. (1996). Quantum nondemolition measurements: the route from toys to tools. *Reviews of Modern Physics*, 68:1–11. (page 30).

Braginsky, V. B., Khalili, F. Y., and Thorne, K. S. (1992). *Quantum Measurement*. Cambridge University Press. (page 29).

Braginsky, V. B., Vorontsov, Y. I., and Thorne, K. S. (1980). Quantum nondemolition measurements. *Science*, 209:547–557. (pages 29, 30, 31, 171).

Briegel, H.-J., Dür, W., Cirac, J. I., and Zoller, P. (1998). Quantum repeaters: The role of imperfect local operations in quantum communication. *Physical Review Letters*, 81:5932–5935. (page 7).

Brown, B. J., Loss, D., Pachos, J. K., Self, C. N., and Wootton, J. R. (2016). Quantum memories at finite temperature. *Reviews of Modern Physics*, 88:1–51. (page 6).

Buser, G., Mottola, R., Cotting, B., Wolters, J., and Treutlein, P. (2022). Single-photon storage in a ground-state vapor cell quantum memory. *PRX Quantum*, 3:020349. (pages 74, 136, 151).

Buske, P., Völl, A., Eisebitt, M., Stollenwerk, J., and Holly, C. (2022). Advanced beam shaping for laser materials processing based on diffractive neural networks. *Optics Express*, 30:22798. (pages 154, 156).

Caritg, I. R. (2022). Experimental implementation of a top hat beam shaper. *University of Copenhagen*, Master thesis. (pages 73, 85, 154).

Castelletto, S. (2021). Silicon carbide single-photon sources: challenges and prospects. *Materials for Quantum Technology*, 1:023001. (page 134).

Caves, C. M., Thorne, K. S., Drever, R. W. P., Sandberg, V. D., and Zimmermann, M. (1980). On the measurement of a weak classical force coupled to a quantum-mechanical oscillator. i. issues of principle. *Reviews of Modern Physics*, 52:341–392. (pages 8, 29, 30, 31, 171).

Chalupczak, W., Godun, R. M., and Pustelny, S. (2018). Radio-frequency spectroscopy as a tool for studying coherent spin dynamics and for application to radio-frequency magnetometry. *Advances in Atomic, Molecular and Optical Physics*, 67:297–336. (page 72).

Chen, S., Reed, D. J., MacKellar, A. R., Downes, L. A., Almuhawish, N. F. A., Jamieson, M. J., Adams, C. S., and Weatherill, K. J. (2022). Terahertz electrometry via infrared spectroscopy of atomic vapor. *Optica*, 9:485. (page 73).

Chen, Z.-B., Zhao, B., Chen, Y.-A., Schmiedmayer, J., and Pan, J.-W. (2007). Fault-tolerant quantum repeater with atomic ensembles and linear optics. *Physical Review A*, 76:022329. (page 7).

Chou, C. W., Polyakov, S. V., Kuzmich, A., and Kimble, H. J. (2004). Single-photon generation from stored excitation in an atomic ensemble. *Physical Review Letters*, 92:213601. (page 52).

Clauser, J. F. (1972). Experimental limitations to the validity of semiclassical radiation theories. *Physical Review A*, 6:49–54. (page 51).

Clauser, J. F. (1974). Experimental distinction between the quantum and classical field-theoretic predictions for the photoelectric effect. *Physical Review D*, 9:853–860. (page 51).

Clauser, J. F. and Shimony, A. (1978). Bell's theorem. experimental tests and implications. *Reports on Progress in Physics*, 41:1881–1927. (page 51).

Cohen, Y., Jadeja, K., Sula, S., Venturelli, M., Deans, C., Marmugi, L., and Renzoni, F. (2019). A cold atom radio-frequency magnetometer. *Applied Physics Letters*, 114. (page 163).

Corzo, N. V., Raskop, J., Chandra, A., Sheremet, A. S., Gouraud, B., and Laurat, J. (2019). Waveguide-coupled single collective excitation of atomic arrays. *Nature*, 566:359–362. (page 5).

CPChem (2010). Alphaplus® c30+ha. *https://www.cpchem.com/sites/default/files/2020-04/AlphaPlusC30plusHA_0_0.pdf*. (page 76).

Dang, H. B., Maloof, A. C., and Romalis, M. V. (2010). Ultrahigh sensitivity magnetic field and magnetization measurements with an atomic magnetometer. *Applied Physics Letters*, 97:151110. (page 164).

Dąbrowski, M., Chrapkiewicz, R., and Wasilewski, W. (2014). Hamiltonian design in readout from room-temperature raman atomic memory. *Optics Express*, 22:26076. (page 44).

Dąbrowski, M., Parniak, M., and Wasilewski, W. (2016). Einstein-podolsky-rosen paradox in a hybrid bipartite system. *Optica*, 4:272. (page 11).

Deans, C., Marmugi, L., Hussain, S., and Renzoni, F. (2016). Electromagnetic induction imaging with a radio-frequency atomic magnetometer. *Applied Physics Letters*, 108:103503. (pages 164, 216).

Deans, C., Marmugi, L., and Renzoni, F. (2017). Through-barrier electromagnetic imaging with an atomic magnetometer. *Optics Express*, 25:17911. (page 216).

Degen, C., Reinhard, F., and Cappellaro, P. (2017). Quantum sensing. *Reviews of Modern Physics*, 89:035002. (page 164).

Derevianko, A. and Katori, H. (2011). Colloquium: Physics of optical lattice clocks. *Reviews of Modern Physics*, 83:331–347. (page 8).

Detlefsen, J. (2021). 3d-printed fiber-coupled vapor-cell magnetometer. *University of Copenhagen*, Master thesis. (page 164).

Dicke, R. H. (1954). Coherence in spontaneous radiation processes. *Physical Review*, 93:99–110. (page 17).

Dickey, F. M. and Holswade, S. C. (2000). Laser beam shaping : theory and techniques. *Marcel Dekker, Inc.*, New York, Basel. (pages 153, 154).

Dideriksen, K. B. (2014a). A laser system for a deterministic single photon source. *University of Copenhagen*, Bachelor Thesis. (page 98).

Dideriksen, K. B. (2014b). Linewidth measurement of near-infrared laser systems. *Report*, pages 1–14. (page 99).

Dideriksen, K. B. (2017). Development of a single-photon source with room-temperature atomic ensembles. *University of Copenhagen*, Master Thesis. (page 95).

Dideriksen, K. B. (2021). A room-temperature single-photon source with near-millisecond built-in memory. *University of Copenhagen*, PhD Thesis. (pages 4, 12, 43, 45, 52, 53, 54, 55, 68, 69, 70, 71, 79, 94, 95, 96, 98, 99, 102, 103, 104, 111, 112, 113, 116, 122, 130, 138, 144, 145, 147, 149).

Dideriksen, K. B., Schmieg, R., Zugenmaier, M., and Polzik, E. S. (2021). Room-temperature single-photon source with near-millisecond built-in memory. *Nature Communications*, 12:3699. (pages xiii, 3, 39, 44, 52, 68, 74, 94, 95, 109, 111, 113, 114, 115, 116, 117, 119, 122, 123, 125, 127, 128, 133, 158).

Dieks, D. (1982). Communication by epr devices. *Physics Letters A*, 92:271–272. (page 7).

Ding, X., He, Y., Duan, Z.-C., Gregersen, N., Chen, M.-C., Unsleber, S., Maier, S., Schneider, C., Kamp, M., Höfling, S., Lu, C.-Y., and Pan, J.-W. (2016). On-demand single photons with high extraction efficiency and near-unity indistinguishability from a resonantly driven quantum dot in a micropillar. *Physical Review Letters*, 116:020401. (pages 5, 134).

Dou, J.-P., Yang, A.-L., Du, M.-Y., Lao, D., Gao, J., Qiao, L.-F., Li, H., Pang, X.-L., Feng, Z., Tang, H., and Jin, X.-M. (2018). A broadband dlcz quantum memory in room-temperature atoms. *Communications Physics*, 1:55. (pages 6, 135, 151).

Downes, L. A., MacKellar, A. R., Whiting, D. J., Bourgenot, C., Adams, C. S., and Weatherill, K. J. (2020). Full-field terahertz imaging at kilohertz frame rates using atomic vapor. *Physical Review X*, 10:011027. (page 73).

Duan, L.-M., Lukin, M. D., Cirac, J. I., and Zoller, P. (2001). Long-distance quantum communication with atomic ensembles and linear optics. *Nature*, 414:413–418. (pages 5, 7, 35, 36, 39, 43, 94, 135).

Eisaman, M. D., André, A., Massou, F., Fleischhauer, M., Zibrov, A. S., and Lukin, M. D. (2005). Electromagnetically induced transparency with tunable single-photon pulses. *Nature*, 438:837–841. (pages 5, 41).

Ekert, A. K. (1991). Quantum cryptography based on bell's theorem. *Physical Review Letters*, 67:661–663. (page 7).

Elíasson, O., Heck, R., Laustsen, J. S., Napolitano, M., Müller, R., Bason, M. G., Arlt, J. J., and Sherson, J. F. (2019). Spatially-selective in situ magnetometry of ultracold atomic clouds. *Journal of Physics B: Atomic, Molecular and Optical Physics*, 52:075003. (page 163).

Enault-Dautheribes, M. (2017). Optically narrowed laser towards the implementation of a single-photon source on the d1 line of caesium. *University of Copenhagen*, Master thesis. (page 75).

Fabricant, A. (2014). Quantum-limited optical magnetometry with cesium microcells. *Univsersity of Copenhagen*, Master thesis. (pages 79, 81, 85, 97).

Felinto, D., Chou, C. W., de Riedmatten, H., Polyakov, S. V., and Kimble, H. J. (2005). Control of decoherence in the generation of photon pairs from atomic ensembles. *Physical Review A*, 72:053809. (page 41).

Finkelstein, R., Poem, E., Michel, O., Lahad, O., and Firstenberg, O. (2018). Fast, noise-free memory for photon synchronization at room temperature. *Science Advances*, 4:eaap8598. (pages 5, 135).

Fomin, A. A., Petrov, M. Y., Kozlov, G. G., Glazov, M. M., Ryzhov, I. I., Balabas, M. V., and Zapasskii, V. S. (2020). Spin-alignment noise in atomic vapor. *Physical Review Research*, 2:012008. (page 152).

Foot, C. J. (2005). *Atomic Physics*. Oxford University press. (pages 11, 12, 59, 60, 61, 78, 79).

Galinskiy, I., Tsaturyan, Y., Parniak, M., and Polzik, E. S. (2020). Phonon counting thermometry of an ultracoherent membrane resonator near its motional ground state. *Optica*, 7:718. (pages 105, 137, 148, 152).

Gerry, C. and Knight, P. (2004). *Introductory Quantum Optics*. Cambridge University Press. (pages 7, 11, 14, 19, 50, 51).

Gilmore, K. A., Affolter, M., Lewis-Swan, R. J., Barberena, D., Jordan, E., Rey, A. M., and Bollinger, J. J. (2021). Quantum-enhanced sensing of displacements and electric fields with two-dimensional trapped-ion crystals. *Science*, 373:673–678. (page 8).

Gorshkov, A. V., André, A., Lukin, M. D., and Sørensen, A. S. (2007). Photon storage in λ -type optically dense atomic media. i. cavity model. *Physical Review A*, 76:1–25. (pages 43, 49).

Graf, M. T., Kimball, D. F., Rochester, S. M., Kerner, K., Wong, C., Budker, D., Alexandrov, E. B., Balabas, M. V., and Yashchuk, V. V. (2005). Relaxation of atomic polarization in paraffin-coated cesium vapor cells. *Physical Review A*, 72:023401. (page 18).

Griffiths, H. (2001). Magnetic induction tomography. *Measurement Science and Technology*, 12:1126–1131. (page 163).

Hammerer, K. (2006). Quantum information processing with atomic ensembles and light. *Technische Universität München*, PhD Thesis. (pages 17, 26, 27).

Hammerer, K., Polzik, E. S., and Cirac, J. I. (2005). Teleportation and spin squeezing utilizing multimode entanglement of light with atoms. *Physical Review A*, 72:052313. (pages 3, 15, 26).

Hammerer, K., Sørensen, A. S., and Polzik, E. S. (2010). Quantum interface between light and atomic ensembles. *Reviews of Modern Physics*, 82:1041–1093. (pages 11, 15, 19, 20, 37, 38, 39, 40, 174, 175).

Hansch, T. and Couillaud, B. (1980). Laser frequency stabilization by polarization spectroscopy of a reflecting reference cavity. *Optics Communications*, 35:441–444. (page 98).

Heshami, K., England, D. G., Humphreys, P. C., Bustard, P. J., Acosta, V. M., Nunn, J., and Sussman, B. J. (2016). Quantum memories: emerging applications and recent advances. *Journal of Modern Optics*, 63:2005–2028. (page 6).

Holstein, T. and Primakoff, H. (1940). Field dependence of the intrinsic domain magnetization of a ferromagnet. *Physical Review*, 58:1098–1113. (page 15).

Jensen, K. (2011). Quantum information, entanglement and magnetometry with macroscopic gas samples and non-classical light. *University of Copenhagen*, PhD thesis. (pages 16, 20, 21, 23).

Jensen, K., Budvytyte, R., Thomas, R. A., Wang, T., Fuchs, A. M., Balabas, M. V., Vasilakis, G., Mosgaard, L. D., Stærkind, H. C., Müller, J. H., Heimburg, T., Olesen, S.-P., and Polzik, E. S. (2016). Non-invasive detection of animal nerve impulses with an atomic magnetometer operating near quantum limited sensitivity. *Scientific Reports*, 6:29638. (page 4).

Jensen, K. and Polzik, E. S. (2013). Quantum noise, squeezing, and entanglement in radiofrequency optical magnetometers. *Cambridge University Press: Optical Magnetometry*, pages 40–59. (page 204).

Jensen, K., Skarsfeldt, M. A., Stærkind, H., Arnbak, J., Balabas, M. V., Olesen, S.-P., Bentzen, B. H., and Polzik, E. S. (2018). Magnetocardiography on an isolated animal heart with a room-temperature optically pumped magnetometer. *Scientific Reports*, 8:16218. (pages 4, 164, 221).

Jensen, K., Wasilewski, W., Krauter, H., Fernholz, T., Nielsen, B. M., Owari, M., Plenio, M. B., Serafini, A., Wolf, M. M., and Polzik, E. S. (2011). Quantum memory for entangled continuous-variable states. *Nature Physics*, 7:13–16. (page 3).

Jensen, K., Zugenmaier, M., Arnbak, J., Stærkind, H., Balabas, M. V., and Polzik, E. S. (2019). Detection of low-conductivity objects using eddy current measurements with an optical magnetometer. *Physical Review Research*, 1:033087. (pages 4, 9, 73, 164, 204, 216, 217, 222).

Jiang, L., Taylor, J. M., and Lukin, M. D. (2007). Fast and robust approach to long-distance quantum communication with atomic ensembles. *Physical Review A*, 76:012301. (page 7).

Julsgaard, B. (2003). Entanglement and quantum interactions with macroscopic gas samples. *University of Aarhus*, PhD thesis. (pages 11, 15, 16, 19, 20, 21, 23, 24, 25, 61, 62, 63, 64, 65, 66, 68, 85, 174).

Julsgaard, B., Sherson, J., Sørensen, J. L., and Polzik, E. S. (2004). Characterizing the spin state of an atomic ensemble using the magneto-optical resonance method. *Journal of Optics B: Quantum and Semiclassical Optics*, 6:5–14. (pages 13, 63, 68).

Kaczmarek, K. T., Ledingham, P. M., Brecht, B., Thomas, S. E., Thekkadath, G. S., Lazo-Arjona, O., Munns, J. H. D., Poem, E., Feizpour, A., Saunders, D. J., Nunn, J., and Walmsley, I. A. (2018). High-speed noise-free optical quantum memory. *Physical Review A*, 97:042316. (pages 5, 135).

Katz, O. and Firstenberg, O. (2018). Light storage for one second in room-temperature alkali vapor. *Nature Communications*, 9:2074. (page 6).

Katz, O., Shaham, R., Reches, E., Gorshkov, A. V., and Firstenberg, O. (2022). Optical quantum memory for noble-gas spins based on spin-exchange collisions. *Physical Review A*, 105. (page 6).

Katz, S., Kaplan, N., and Grossinger, I. (2018). Using diffractive optical elements. *Laser Technik Journal*, 15:29–32. (page 153).

Khalili, F. and Polzik, E. (2018). Overcoming the standard quantum limit in gravitational wave detectors using spin systems with a negative effective mass. *Physical Review Letters*, 121:031101. (pages 11, 73).

Kiršanske, G., Thyrrestrup, H., Daveau, R. S., Dreeßen, C. L., Pregnolato, T., Midolo, L., Tighineanu, P., Javadi, A., Stobbe, S., Schott, R., Ludwig, A., Wieck, A. D., Park, S. I., Song, J. D., Kuhlmann, A. V., Söllner, I., Löbl, M. C., Warburton, R. J., and Lodahl, P. (2017). Indistinguishable and efficient single photons from a quantum dot in a planar nanobeam waveguide. *Physical Review B*, 96:1–11. (page 5).

Krauter, H. (2011). Generation and application of entanglement of room temperature ensembles of atoms. *University of Copenhagen*, PhD thesis. (pages 11, 15, 16, 17, 18, 19, 20, 21, 60, 66, 85, 98, 174, 183).

Krauter, H., Salart, D., Muschik, C. A., Petersen, J. M., Shen, H., Fernholz, T., and Polzik, E. S. (2013). Deterministic quantum teleportation between distant atomic objects. *Nature Physics*, 9:400–404. (page 3).

Kutluer, K., Mazzera, M., and de Riedmatten, H. (2017). Solid-state source of nonclassical photon pairs with embedded multimode quantum memory. *Physical Review Letters*, 118:210502. (page 5).

Kuzmich, A., Bowen, W. P., Boozer, A. D., Boca, A., Chou, C. W., Duan, L.-M., and Kimble, H. J. (2003). Generation of nonclassical photon pairs for scalable quantum communication with atomic ensembles. *Nature*, 423:731–734. (pages 52, 94).

Laplane, C., Jobez, P., Etesse, J., Gisin, N., and Afzelius, M. (2017). Multimode and long-lived quantum correlations between photons and spins in a crystal. *Physical Review Letters*, 118:1–5. (page 5).

Laskin, A., Kaiser, P., Laskin, V., and Ostrun, A. (2016). Laser beam shaping for biomedical microscopy techniques. *Biophotonics: Photonic Solutions for Better Health Care V*, 9887:98872E. (page 153).

Li, H., Dou, J.-P., Pang, X.-L., Yang, T.-H., Zhang, C.-N., Chen, Y., Li, J.-M., Walmsley, I. A., and Jin, X.-M. (2021). Heralding quantum entanglement between two room-temperature atomic ensembles. *Optica*, 8:925. (page 136).

Li, W., Balabas, M., Peng, X., Pustelny, S., Wickenbrock, A., Guo, H., and Budker, D. (2017). Characterization of high-temperature performance of cesium vapor cells with anti-relaxation coating. *Journal of Applied Physics*, 121:063104. (page 82).

Lidar, D. A. and Brun, T. A. (2013). Quantum error correction. *Cambridge University Press*. (page 6).

Loudon, R. and von Foerster, T. (2000). The quantum theory of light. *Oxford University press - Third Edition*. (pages 50, 51).

Lukin, M. D. (2003). colloquium : Trapping and manipulating photon states in atomic ensembles. *Reviews of Modern Physics*, 75:457–472. (page 40).

Ma, L., Slattery, O., Kuo, P., and Tang, X. (2015). Eit quantum memory with cs atomic vapor for quantum communication. *Quantum Communications and Quantum Imaging XIII*, 9615:96150D. (page 74).

Makino, K., Hashimoto, Y., Yoshikawa, J. I., Ohdan, H., Toyama, T., Loock, P. V., and Furusawa, A. (2016). Synchronization of optical photons for quantum information processing. *Science Advances*, 2:1–7. (page 6).

Marmugi, L. and Renzoni, F. (2016). Optical magnetic induction tomography of the heart. *Scientific Reports*, 6:23962. (pages 164, 221).

Mücke, M., Bochmann, J., Hahn, C., Neuzner, A., Nölleke, C., Reiserer, A., Rempe, G., and Ritter, S. (2013). Generation of single photons from an atom-cavity system. *Physical Review A*, 87:063805. (pages 5, 134).

Möhl, A., Wickenhagen, S., and Fuchs, U. (2016). Insensitive and modular gauss to top-hat beam shaping with aspheres. *Proc. SPIE 9950, Laser Beam Shaping XVII*, 995005. (page 153).

Muessel, W., Strobel, H., Linnemann, D., Hume, D., and Oberthaler, M. (2014). Scalable spin squeezing for quantum-enhanced magnetometry with bose-einstein condensates. *Physical Review Letters*, 113:103004. (page 217).

Namazi, M., Kupchak, C., Jordaan, B., Shahrokhshahi, R., and Figueroa, E. (2017). Ultralow-noise room-temperature quantum memory for polarization qubits. *Physical Review Applied*, 8:1–5. (page 151).

Neergaard-Nielsen, J. S., Nielsen, B. M., Takahashi, H., Vistnes, A. I., and Polzik, E. S. (2007). High purity bright single photon source. *Optics Express*, 15:7940. (pages 3, 5).

Neuhaus, L. and Deléglise, S. (2017). Pyrpl software. *Software available under GNU General Public License v3.0, https://pyrpl.readthedocs.io/en/latest/*. (page 105).

Nichol, B. C., Srinivas, R., Nadlinger, D. P., Drmota, P., Main, D., Araneda, G., Ballance, C. J., and Lucas, D. M. (2022). An elementary quantum network of entangled optical atomic clocks. *Nature*, 609:689–694. (page 8).

Nunn, J., Munns, J. H. D., Thomas, S., Kaczmarek, K. T., Qiu, C., Feizpour, A., Poem, E., Brecht, B., Saunders, D. J., Ledingham, P. M., Reddy, D. V., Raymer, M. G., and Walmsley, I. A. (2017). Theory of noise suppression in λ-type quantum memories by means of a cavity. *Physical Review A*, 96:012338. (page 45).

Oesterle, A. (2022). Quantum enhanced optical magnetic induction tomography through back-action evasion and conditional spin squeezing. *University of Copenhagen*, Master Thesis. (pages 165, 168, 169, 206, 220, 237).

Pal, V., Tradonsky, C., Chriki, R., Brodsky, A., Kaplan, N., and Grossinger, I. (2019). Diffractive elements for generating top-hat beams with extended depth of focus. *Proceedings of the Photonics-2018*, pages 5–7. (page 153).

Pang, X.-L., Yang, A.-L., Dou, J.-P., Li, H., Zhang, C.-N., Poem, E., Saunders, D. J., Tang, H., Nunn, J., Walmsley, I. A., and Jin, X.-M. (2020). A hybrid quantum memory–enabled network at room temperature. *Science Advances*, 6:eaax1425. (pages 6, 135, 151).

Pustelny, S., Kimball, D. F. J., Rochester, S. M., Yashchuk, V. V., Gawlik, W., and Budker, D. (2006). Pump-probe nonlinear magneto-optical rotation with frequency-modulated light. *Physical Review A*, 73:023817. (page 72).

Radnaev, A. G., Dudin, Y. O., Zhao, R., Jen, H. H., Jenkins, S. D., Kuzmich, A., and Kennedy, T. A. B. (2010). A quantum memory with telecom-wavelength conversion. *Nature Physics*, 6:894–899. (page 5).

Rambach, M., Lau, W. S., Laibacher, S., Tamma, V., White, A. G., and Weinhold, T. J. (2018). Hectometer revivals of quantum interference. *Physical Review Letters*, 121:093603. (page 137).

Raschendorfer, V. (2022). Generation of top hat laser beam for spin noise characterization. *University of Copenhagen*, Project report. (page 157).

Ripka, F., Kübler, H., Löw, R., and Pfau, T. (2018). A room-temperature single-photon source based on strongly interacting rydberg atoms. *Science*, 362:446–449. (pages 5, 134).

Rushton, L. M., Pyragius, T., Meraki, A., Elson, L., and Jensen, K. (2022). Unshielded portable optically pumped magnetometer for the remote detection of conductive objects using eddy current measurements. *Review of Scientific Instruments*, 93:125103. (page 216).

Sangouard, N., Simon, C., de Riedmatten, H., and Gisin, N. (2011). Quantum repeaters based on atomic ensembles and linear optics. *Reviews of Modern Physics*, 83:33–80. (pages 7, 8, 39, 40, 41, 52).

Saunders, D., Munns, J., Champion, T., Qiu, C., Kaczmarek, K., Poem, E., Ledingham, P., Walmsley, I., and Nunn, J. (2016). Cavity-enhanced room-temperature broadband raman memory. *Physical Review Letters*, 116:090501. (page 45).

Savukov, I., Seltzer, S., and Romalis, M. (2007). Detection of nmr signals with a radio-frequency atomic magnetometer. *Journal of Magnetic Resonance*, 185:214–220. (page 164).

Schäffer, S. A., Tang, M., Henriksen, M. R., Jørgensen, A. A., Christensen, B. T. R., and Thomsen, J. W. (2020). Lasing on a narrow transition in a cold thermal strontium ensemble. *Physical Review A*, 101:013819. (page 11).

Schliesser, A. (2016). Lecture notes for quantum optics ii. *Lecture Notes*. (page 20).

Schmidt, J., Münzenmaier, Y., Kaspar, P., Schalberger, P., Baur, H., Löw, R., Fruehauf, N., Pfau, T., and Kübler, H. (2020). An optogalvanic gas sensor based on rydberg excitations. *Journal of Physics B: Atomic, Molecular and Optical Physics*, 53:094001. (page 73).

Schmieg, R. (2018). Coherent dynamics of atomic vapors. *University of Copenhagen*, Project report. (page 79).

Schmieg, R. (2019). Observation of non-classical photon pairs from room-temperature atomic ensembles through suppression of four-wave mixing and classical noise sources. *University of Copenhagen*, Master thesis. (pages 66, 68, 70, 94, 95, 97, 98, 105, 108, 112, 113, 130, 147, 149).

Schnabel, R., Bowen, W. P., Treps, N., Ralph, T. C., Bachor, H.-A., and Lam, P. K. (2003). Stokes-operator-squeezed continuous-variable polarization states. *Physical Review A*, 67:012316. (page 14).

Schünemann, U., Engler, H., Grimm, R., Weidemüller, M., and Zielonkowski, M. (1999). Simple scheme for tunable frequency offset locking of two lasers. *Review of Scientific Instruments*, 70:242–243. (page 98).

Sekatski, P., Sangouard, N., Bussières, F., Clausen, C., Gisin, N., and Zbinden, H. (2012). Detector imperfections in photon-pair source characterization. *Journal of Physics B: Atomic, Molecular and Optical Physics*, 45:124016. (pages 50, 51, 52).

Senellart, P., Solomon, G., and White, A. (2017). High-performance semiconductor quantum-dot single-photon sources. *Nature Nanotechnology*, 12:1026–1039. (page 134).

Sewell, R. J., Koschorreck, M., Napolitano, M., Dubost, B., Behbood, N., and Mitchell, M. W. (2012). Magnetic sensitivity beyond the projection noise limit by spin squeezing. *Physical Review Letters*, 109:253605. (pages 8, 217).

Shah, V., Knappe, S., Schwindt, P. D. D., and Kitching, J. (2007). Subpicotesla atomic magnetometry with a microfabricated vapour cell. *Nature Photonics*, 1:649–652. (page 164).

Shaham, R., Katz, O., and Firstenberg, O. (2020). Quantum dynamics of collective spin states in a thermal gas. *Physical Review A*, 102:012822. (pages 42, 48).

Shaham, R., Katz, O., and Firstenberg, O. (2022). Strong coupling of alkali-metal spins to noble-gas spins with an hour-long coherence time. *Nature Physics*, 18:506–510. (page 6).

Shen, H. (2014). Spin squeezing and entanglement with room temperature atoms for quantum sensing and communication. *University of Copenhagen*, PhD Thesis. (pages 18, 23, 28, 31, 32, 190).

Sherson, J., Sørensen, A. S., Fiurášek, J., Mølmer, K., and Polzik, E. S. (2006). Light qubit storage and retrieval using macroscopic atomic ensembles. *Physical Review A - Atomic, Molecular, and Optical Physics*, 74:2–5. (page 3).

Sherson, J. F. (2006). Quantum memory and teleportation using macroscopic gas samples phd thesis. *University of Aarhus*, Phd thesis. (pages 14, 20, 21, 23, 24, 25, 26, 27).

Shor, P. (1996). Fault-tolerant quantum computation. *Proceedings of 37th Conference on Foundations of Computer Science*, pages 56–65. (page 6).

Shu, C., Chen, P., Chow, T. K. A., Zhu, L., Xiao, Y., Loy, M. M., and Du, S. (2016). Subnatural-linewidth biphotons from a doppler-broadened hot atomic vapour cell. *Nature Communications*, 7:12783. (page 5).

Sørensen, A. S. and Mølmer, K. (2001). Entanglement and extreme spin squeezing. *Physical Review Letters*, 86:4431–4434. (page 198).

Steane, A. M. (1996). Error correcting codes in quantum theory. *Physical Review Letters*, 77:793–797. (page 6).

Steck, D. A. (2007). Quantum and atom optics. *Book*, pages 143–147, 283–293,. (page 78).

Steck, D. A. (2019). Cesium d line data. *avilable online at: {http://steck.us/alkalidata} (revision 2.2.1)*. (pages 12, 13, 20, 80, 81, 96).

Stærkind, H. (2015). Magnetic bias-field coil design and characterization. *University of Copenhagen*, Project report. (pages 97, 236).

Stærkind, H., Jensen, K., Müller, J. H., Boer, V. O., Petersen, E. T., and Polzik, E. S. (2022). Precision measurement of the excited state landé g-factor and diamagnetic shift of the cesium $d_{\{2\}}$ line. (page 164).

Tanji-Suzuki, H., Leroux, I. D., Schleier-Smith, M. H., Cetina, M., Grier, A. T., Simon, J., and Vuletić, V. (2011). Interaction between atomic ensembles and optical resonators. classical description. *Advances in Atomic, Molecular and Optical Physics*, 60:201–237. (page 43).

Thomas, R. A. (2020). Optical spin-mechanics quantum interface: entanglement and back-action evasion. *University of Copenhagen*, PhD Thesis. (pages 60, 62, 79, 88, 98, 142).

Thomas, R. A., Østfeldt, C., Bærentsen, C., Parniak, M., and Polzik, E. S. (2021). Calibration of spin-light coupling by coherently induced faraday rotation. *Optics Express*, 29:23637. (page 137).

Tse, M., Yu, H., Kijbunchoo, N., Fernandez-Galiana, A., Dupej, P., Barsotti, L., Blair, C. D., Brown, D. D., Dwyer, S. E., Effler, A., Evans, M., Fritschel, P., Frolov, V. V., Green, A. C., Mansell, G. L., Matichard, F., Mavalvala, N., McClelland, D. E., McCuller, L., McRae, T., Miller, J., Mullavey, A., Oelker, E., Phinney, I. Y., Sigg, D., Slagmolen, B. J., Vo, T., Ward, R. L., Whittle, C., Abbott, R., Adams, C., Adhikari, R. X., Ananyeva, A., Appert, S., Arai, K., Areeda, J. S., Asali, Y., Aston, S. M., Austin, C., Baer, A. M., Ball, M., Ballmer, S. W., Banagiri, S., Barker, D., Bartlett, J., Berger, B. K., Betzwieser, J., Bhattacharjee, D., Billingsley, G., Biscans, S., Blair, R. M., Bode, N., Booker, P., Bork, R., Bramley, A., Brooks, A. F., Buikema, A., Cahillane, C., Cannon, K. C., Chen, X., Ciobanu, A. A., Clara, F., Cooper, S. J., Corley, K. R., Countryman, S. T., Covas, P. B., Coyne, D. C., Datrier, L. E., Davis, D., Fronzo, C. D., Driggers, J. C., Etzel, T., Evans, T. M., Feicht, J., Fulda, P., Fyffe, M., Giaime, J. A., Giardina, K. D., Godwin, P., Goetz, E., Gras, S., Gray, C., Gray, R., Gupta, A., Gustafson, E. K., Gustafson, R., Hanks, J., Hanson, J., Hardwick, T., Hasskew, R. K., Heintze, M. C., Helmling-Cornell, A. F., Holland, N. A., Jones, J. D., Kandhasamy, S., Karki, S., Kasprzack, M., Kawabe, K., King, P. J., Kissel, J. S., Kumar, R., Landry, M., Lane, B. B., Lantz, B., Laxen, M., Lecoeuche, Y. K., Leviton, J., Liu, J., Lormand, M., Lundgren, A. P., Macas, R., MacInnis, M., MacLeod, D. M., Márka, S., Márka, Z., Martynov, D. V., Mason, K., Massinger, T. J., McCarthy, R., McCormick, S., McIver, J., Mendell, G., Merfeld, K., Merilh, E. L., Meylahn, F., Mistry, T., Mittleman, R., Moreno, G., Mow-Lowry, C. M., Mozzon, S., Nelson, T. J., Nguyen, P., Nuttall, L. K., Oberling, J., Oram, R. J., O'Reilly, B., Osthelder, C., Ottaway, D. J., Overmier, H., Palamos, J. R., Parker, W., Payne, E., Pele, A., Perez, C. J., Pirello, M., Radkins, H., Ramirez, K. E., Richardson, J. W., Riles, K., Robertson, N. A., Rollins, J. G., Romel, C. L., Romie, J. H., Ross, M. P., Ryan, K., Sadecki, T., Sanchez, E. J., Sanchez, L. E., Saravanan, T. R., Savage, R. L., Schaetzl, D., Schnabel, R., Schofield, R. M., Schwartz, E., Sellers, D., Shaffer, T. J., Smith, J. R., Soni, S., Sorazu, B., Spencer, A. P., Strain, K. A., Sun, L., Szczepańczyk, M. J., Thomas, M., Thomas, P., Thorne, K. A., Toland, K., Torrie, C. I., Traylor, G., Urban, A. L., Vajente, G., Valdes, G., Vander-Hyde, D. C., Veitch, P. J., Venkateswara, K., Venugopalan, G., Viets, A. D., Vorvick, C., Wade, M., Warner, J., Weaver, B., Weiss, R., Willke, B., Wipf, C. C., Xiao, L., Yamamoto, H., Yap, M. J., Yu, H., Zhang, L., Zucker, M. E., and Zweizig, J. (2019). Quantum-enhanced advanced ligo detectors in the era of gravitational-wave astronomy. *Physical Review Letters*, 123. (page 8).

Uppu, R., Pedersen, F. T., Wang, Y., Olesen, C. T., Papon, C., Zhou, X., Midolo, L., Scholz, S., Wieck, A. D., Ludwig, A., and Lodahl, P. (2020). Scalable integrated single-photon source. *Science Advances*, 6:1–17. (pages 133, 134).

van der Wal, C. H. (2003). Atomic memory for correlated photon states. *Science*, 301:196–200. (page 94).

Vasilakis, G., Shen, H., Jensen, K., Balabas, M., Salart, D., Chen, B., and Polzik, E. S. (2015). Generation of a squeezed state of an oscillator by stroboscopic back-action-evading measurement. *Nature Physics*, 11:389–392. (pages 4, 23, 31, 32, 190, 217, 218, 243).

Vurgaftman, I. and Bashkansky, M. (2013). Suppressing four-wave mixing in warm-atomic-vapor quantum memory. *Physical Review A*, 87:063836. (page 45).

Wallucks, A., Marinković, I., Hensen, B., Stockill, R., and Gröblacher, S. (2020). A quantum memory at telecom wavelengths. *Nature Physics*, 16:772–777. (page 127).

Wan, N. H., Lu, T.-J., Chen, K. C., Walsh, M. P., Trusheim, M. E., Santis, L. D., Bersin, E. A., Harris, I. B., Mouradian, S. L., Christen, I. R., Bielejec, E. S., and Englund, D. (2020). Large-scale integration of artificial atoms in hybrid photonic circuits. *Nature*, 583:226–231. (page 5).

Wasilewski, W., Jensen, K., Krauter, H., Renema, J. J., Balabas, M. V., and Polzik, E. S. (2010). Quantum noise limited and entanglement-assisted magnetometry. *Physical Review Letters*, 104:133601. (pages 3, 9).

Weinstein, J. D., Beloy, K., and Derevianko, A. (2010). Entangling the lattice clock: Towards heisenberg-limited timekeeping. *Physical Review A*, 81:030302. (page 8).

Wickenbrock, A., Jurgilas, S., Dow, A., Marmugi, L., and Renzoni, F. (2014). Magnetic induction tomography using an all-optical {87}rb atomic magnetometer. *Optics Letters*, 39:6367. (pages 164, 216).

Wickenbrock, A., Leefer, N., Blanchard, J. W., and Budker, D. (2016). Eddy current imaging with an atomic radio-frequency magnetometer. *Applied Physics Letters*, 108:183507. (pages 164, 216).

Wildermuth, S., Hofferberth, S., Lesanovsky, I., Groth, S., Kruger, P., Schmiedmayer, J., and Bar-Joseph, I. (2006). Sensing electric and magnetic fields with bose-einstein condensates. *Applied Physics Letters*, 88. (page 163).

Willstrand, O. (2013). Intensity distribution conversion from gaussian to top-hat in a single-mode fiber connector. *Lund University*, Master Thesis. (page 153).

Wineland, D. J., Bollinger, J. J., Itano, W. M., Moore, F. L., and Heinzen, D. J. (1992). Spin squeezing and reduced quantum noise in spectroscopy. *Physical Review A*, 46:R6797–R6800. (page 218).

Wootters, W. K. and Zurek, W. H. (1982). A single quantum cannot be cloned. *Nature*, 299:802–803. (page 7).

Yde, R. (2020). Room temperature spin ensembles for pre- cision measurements. *University of Copenhagen*, Master thesis. (pages 89, 156, 168).

Zhang, C.-N., Li, H., Dou, J.-P., Lu, F., Yang, H.-Z., Pang, X.-L., and Jin, X.-M. (2022). Hong–ou–mandel interference linking independent room-temperature quantum memories. *Photonics Research*, 10:2388. (pages 135, 136).

Zhang, G. H., Braverman, B., Kawasaki, A., and Vuletić, V. (2015). Note: Fast compact laser shutter using a direct current motor and three-dimensional printing. *Review of Scientific Instruments*, 86:1–4. (page 105).

Zhang, R., Xiao, W., Ding, Y., Feng, Y., Peng, X., Shen, L., Sun, C., Wu, T., Wu, Y., Yang, Y., Zheng, Z., Zhang, X., Chen, J., and Guo, H. (2020). Recording brain activities in unshielded earth's field with optically pumped atomic magnetometers. *Science Advances*, 6:8792–8804. (page 73).

Zhao, R., Dudin, Y. O., Jenkins, S. D., Campbell, C. J., Matsukevich, D. N., Kennedy, T. A. B., and Kuzmich, A. (2009). Long-lived quantum memory. *Nature Physics*, 5:100–104. (page 41).

Zheng, W., Wang, H., Schmieg, R., Oesterle, A., and Polzik, E. S. (2022). Entanglement-enhanced magnetic induction tomography. *Preprint available at: http://arxiv.org/abs/2209.01920*. (pages xiii, 4, 31, 165, 167, 172, 173, 181, 187, 189, 192, 194, 195, 197, 198, 200, 201, 202, 203, 208, 211, 212, 214, 215, 244).

Zugenmaier, M. (2018). Towards a room temperature single photon source based on atomic vapour. *University of Copenhagen*, PhD thesis. (pages 41, 45, 48, 49, 95, 97, 98, 99, 112, 144, 145, 149, 225).

Zugenmaier, M., Dideriksen, K. B., Sørensen, A. S., Albrecht, B., and Polzik, E. S. (2018). Long-lived non-classical correlations towards quantum communication at room temperature. *Communications Physics*, 1:76. (pages 3, 4, 44, 52, 68, 76, 88, 94, 95, 100, 104, 115, 120, 148, 149, 225).